



APPROVED: 1 09 05

②

**CONTRACT #F49620-88-C-0021**  
**AIR FORCE OFFICE OF SCIENTIFIC RESEARCH**

DTIC  
ELECTE  
DEC 30 1991

**for period December 1, 1987 to August 31, 1991**

**91-19203**



Prepared by

A. Joshi, T.C. Chou and J. Wadsworth

**Lockheed Palo Alto Research Laboratory**  
**3251 Hanover Street, Palo Alto, CA 94304**

91 1227 071

Approved for public release;  
distribution unlimited.

## REPORT DOCUMENTATION PAGE

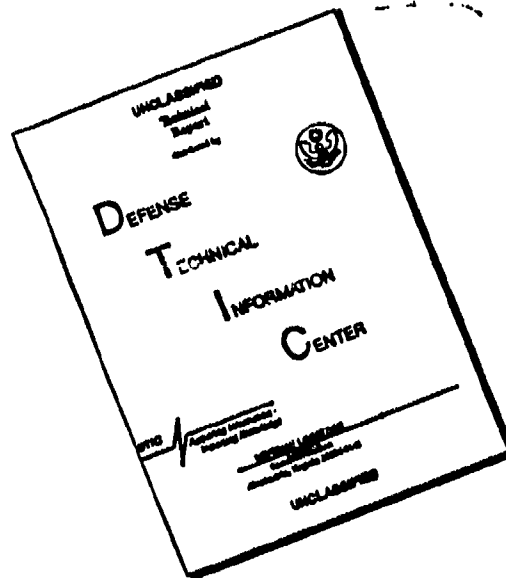
Form Approved  
OMB No. 0704-0188

1a. REPORT SECURITY CLASSIFICATION Unclassified			1b. RESTRICTIVE MARKINGS N/A		
2a. SECURITY CLASSIFICATION AUTHORITY			3. DISTRIBUTION/AVAILABILITY OF REPORT  Unlimited		
2b. DECLASSIFICATION/DOWNGRADING SCHEDULE					
4. PERFORMING ORGANIZATION REPORT NUMBER(S)  LMSC-P010621			5. MONITORING ORGANIZATION REPORT NUMBER(S)  F49620-88-C-0021		
6a. NAME OF PERFORMING ORGANIZATION  Lockheed Missiles & Space Company		6b. OFFICE SYMBOL (if applicable)	7a. NAME OF MONITORING ORGANIZATION  Air Force Office of Scientific Research		
6c. ADDRESS (City, State, and ZIP Code)  Lockheed R&D Division 3251 Hanover Street Palo Alto, CA 94304			7b. ADDRESS (City, State, and ZIP Code)  Bldg. 410-NE Bolling AFB, DC 20332		
8a. NAME OF FUNDING/SPONSORING ORGANIZATION  AFOSR		8b. OFFICE SYMBOL (if applicable)	9. PROCUREMENT INSTRUMENT IDENTIFICATION NUMBER  F49620-88-C-0021		
8c. ADDRESS (City, State, and ZIP Code)  Bldg. 410-NE Bolling AFB, DC 20332			10. SOURCE OF FUNDING NUMBERS		
	PROGRAM ELEMENT NO. 41102F	PROJECT NO. 2304	TASK NO. A1	WORK UNIT ACCESSION NO.	
11. TITLE (Include Security Classification)  High Temperature Interactions of Metallic Matrices with Ceramic Reinforcements					
12. PERSONAL AUTHOR(S) A. Joshi, T.C. Chou and J. Wadsworth					
13a. TYPE OF REPORT Final Report		13b. TIME COVERED FROM 12/1/87 TO 8/31/91		14. DATE OF REPORT (Year, Month, Day) 1991 August 31	
15. PAGE COUNT 200					
16. SUPPLEMENTARY NOTATION					
17. COSATI CODES			18. SUBJECT TERMS (Continue on reverse if necessary and identify by block number)		
FIELD	GROUP	SUB-GROUP	Nb, Co, Ni, Pt, SiC, Al <sub>2</sub> O <sub>3</sub> , Ti <sub>3</sub> Al, stainless steel, composites, metal matrix, thin films, diffusion, diffusion couples, diffusion barriers, ceramics, reinforcement kinetics, reactions, decomposition, interfaces, Auger electron spectroscopy		
19. ABSTRACT (Continue on reverse if necessary and identify by block number)  Interfacial reactions of SiC, Al <sub>2</sub> O <sub>3</sub> , and Si <sub>3</sub> N <sub>4</sub> with selected high temperature metals have been studied at temperatures between 800 and 1200 °C for various times. The metals include Nb and Ta, strong carbide formers, Co, Ni, Pt, Ti <sub>3</sub> Al, and stainless steel. Reactions of the metals with SiC in this temperature range were extensive; various metal silicides, metal carbides, ternary metal-silicon-carbides, and unreacted carbon were formed as layered reaction products in the reaction zones. Thin films of Al <sub>2</sub> O <sub>3</sub> in the 100 to 500 nm thickness range are shown to be effective in minimizing the reaction between Nb and SiC. In some systems, massive or localized interfacial melting was observed as a result of metal-silicide formation. Reactions of SiC with Ni, Co, Pt and stainless steel resulted in the formation of clustered carbon precipitates with modulated or randomly scattered characters. The nature of the C precipitation behavior depends upon the specific metal system and is a function of distance from the reaction interfaces. In contrast, no unreacted carbon was found in the SiC/Nb system. The rate limiting step for the reactions of SiC with metals is discussed in light of the decomposition of SiC, which was sluggish in all cases. In the reactions of Ti <sub>3</sub> Al with Si <sub>3</sub> N <sub>4</sub> and SiC, the diffusion kinetics of Si, as compared to N or C, at 1200 °C were strikingly different from those at 1000 °C. Titanium nitride was formed					
20. DISTRIBUTION/AVAILABILITY OF ABSTRACT <input checked="" type="checkbox"/> UNCLASSIFIED/UNLIMITED <input type="checkbox"/> SAME AS RPT <input type="checkbox"/> DTIC USERS			21. ABSTRACT SECURITY CLASSIFICATION UNCLASSIFIED		
22a. NAME OF RESPONSIBLE INDIVIDUAL A. Joshi De. Rosenstein			22b. TELEPHONE (Include Area Code) 445-484-2205 202-767-4960		22c. OFFICE SYMBOL AFOSR/NC

Abstract (Continued)

as a major reaction product at 1200°C in the reactions of  $Ti_3Al$  with  $Si_3N_4$ . Mechanisms of driving the variation of Si, N, and C diffusion behavior (as a function of temperature) and the depletion of Al from the diffusion zone are suggested. A diffusion mechanism involving self-limited diffusion kinetics by in-situ formation of a diffusion barrier is proposed to explain the reactions of  $Ti_3Al$  with  $Si_3N_4$  and SiC.

# DISCLAIMER NOTICE



THIS DOCUMENT IS BEST QUALITY AVAILABLE. THE COPY FURNISHED TO DTIC CONTAINED A SIGNIFICANT NUMBER OF PAGES WHICH DO NOT REPRODUCE LEGIBLY.



## FOREWORD

This final report was prepared by Lockheed Missiles & Space Systems Company, Inc., Palo Alto, California, under USAF contract F49620-88-C-0021. The contract is funded and administered by the Air Force Office of Scientific Research under the direction of Dr. Alan H. Rosenstein. This report covers the period December 1, 1987 to August 31, 1991 and encompasses all the activities on "High Temperature Interactions of Metallic Matrices with Ceramic reinforcements" funded under this contract.

Dr. A. Joshi is the Principal Investigator of the program. In addition to Drs. T.C. Chou and J. Wadsworth, other principal contributors include the following:

Dr. J.J. Stephens	Currently with Sandia National Laboratory, Albuquerque
Dr. D.L. Yaney	LMSC
Mr. L.J. Jesion	LMSC
Dr. H.S. Hu	LMSC
Dr. A.J. Mardinly	LMSC

The authors greatly appreciate their contributions and many helpful discussions with Dr. Alan Rosenstein.

Accession For	
NTIS	CR&I <input checked="" type="checkbox"/>
DTIC	TAU <input type="checkbox"/>
Unannounced	<input type="checkbox"/>
Justification	
By	
Distribution/	
Availability Codes	
Dist	Restrict and/or Special
A-1	



# CONTENTS

<u>Section</u>	<u>Page</u>
LIST OF FIGURES	ii
LIST OF TABLES	viii
1 INTRODUCTION	1-1
2 TECHNICAL BACKGROUND	2-1
2.1 Overview	2-1
2.2 Prior Work on Reaction Kinetics	2-3
2.3 Methods to Minimize Growth of Reaction Layers	2-7
3 SELECTION OF CANDIDATE SYSTEMS	3-1
4 EXPERIMENTAL	4-1
4.1 Preparation of Thin Film Couple	4-1
4.2 Bulk Diffusion Couples	4-3
4.3 Thermal Treatments	4-4
4.4 Characterization	4-5
5 RESULTS AND DISCUSSION	5-1
5.1 Nb/SiC System	5-1
5.2 Nb/Al <sub>2</sub> O <sub>3</sub> System	5-8
5.3 Nb/Al <sub>2</sub> O <sub>3</sub> /SiC System	5-8
5.4 Ta/SiC System	5-9
5.5 Ta/Al <sub>2</sub> O <sub>3</sub> System	5-9
5.6 Al/SiC System	5-10
5.7 Al/Si <sub>3</sub> N <sub>4</sub> System	5-12
5.8 Ni/SiC System	5-13
5.9 Ni/Si <sub>3</sub> N <sub>4</sub> System	5-14
5.10 Reactions of Co, Ni and Pt with SiC	5-15
5.11 Reactions of stainless Steel with SiC	5-25
5.12 Reactions of Ti <sub>3</sub> Al with Si <sub>3</sub> N <sub>4</sub> and SiC	5-32
6 SUMMARY	6-1
7 REFERENCES	7-1
8 PUBLICATIONS	8-1

## LIST OF FIGURES

- Fig. 2.1      Effect of  $TiB_2$  reaction layer thickness on the room temperature mechanical properties of a Ti-40A matrix with 25% boron filament reinforcement (Ref. 10).
- Fig. 2.2      Reaction kinetics of Ti/SiC composite system (Refs. 12, 13, 25, and 26).
- Fig. 2.3      Effect of Immersion time in 700°C Aluminum on UTS of Boron filaments (Ref. 26)
- Fig. 4.1      Schematic of the electrochemical set up used to measure the pin hole densities of  $Al_2O_3$  layers deposited on silicon substrates.
- Fig. 4.2      Optical micrographs showing low angle cross-sections of Nb/SiC specimens.
- Fig. 5.1      AES depth profile of 1.3  $\mu m$  Nb film on polycrystalline SiC, in the as-deposited condition.
- Fig. 5.2      AES depth profiles of Nb films (1.3  $\mu m$  thickness) on polycrystalline SiC, in (a) the as-deposited condition, and after annealing for 4 h at (b) 800°C, (c) 900°C and (d) 1000°C.
- Fig. 5.3      Isothermal section of the Nb-Si-C phase diagram at 1300°C.
- Fig. 5.4      AES profile from Nb/SiC, annealed 4 h at 1100°C.
- Fig. 5.5      Representative TEM bright field micrograph of the reaction zone between niobium and silicon carbide (hexoloy), annealed 4 h at 1100°C.
- Fig. 5.6      (a) TEM bright field micrograph, (b) convergent beam electron diffraction pattern consistent with ternary  $Nb_5Si_4C$  phase in a [1210] orientation and (c) energy dispersive x-ray spectra from grain 1.
- Fig. 5.7      (a) Bright field TEM micrograph. Grains I and II identified by electron diffraction as NbC. (b) Convergent beam electron diffraction pattern and (c) energy dispersive x-ray spectra from grain II.
- Fig. 5.8      (a) Convergent beam electron diffraction pattern and (b) energy dispersive x-ray spectra from grain 2. The electron diffraction pattern is consistent with  $\alpha-Nb_5Si_3$  in a [110] orientation.
- Fig. 5.9      Schematic illustration of ordered hexagonal structure of  $Nb_2C$ .
- Fig. 5.10      Convergent beam electron diffraction pattern from grain 3 consistent with disordered  $Nb_2C$  in a [0001] orientation.
- Fig. 5.11      Selected area diffraction patterns from (a) grain 3b, (b) grain 4, and (c) grain 5 in Fig. 5.5.
- Fig. 5.12      AES depth profile of Nb/SiC, annealed 12 h at 1100°C.
- Fig. 5.13      (a) AES spectrum and (b) depth profile from Nb/SiC, annealed 2 h at 1200°C.
- Fig. 5.14      AES depth profile of Nb/SiC, annealed 2 h at 1300°C.

- Fig. 5.15 AES profile from Nb/SiC (0001) annealed 4 h at 1100°C.
- Fig. 5.16 AES depth profile of Nb/SiC (0001) annealed at 900°C for (a) 4 h and (b) 8 h. [Ta<sub>2</sub>O<sub>5</sub> Sputter Rate = 12 nm/min].
- Fig. 5.17 Cross-sectional view SEM micrographs showing the growth of layered reaction products, from the Nb/SiC reactions at 1200°C, as annealing time increases from (a) 6, (b) 18, (c) 32, to (d) 48 h. The SiC and Nb components are indicated, and the original joining interfaces are marked by arrows.
- Fig. 5.18 Growth of the thicknesses of layers 1 and 2 in Nb/SiC diffusion couples at 1200°C.
- Fig. 5.19 AES depth profile of (a) Nb/Al<sub>2</sub>O<sub>3</sub> specimen and Nb/Al<sub>2</sub>O<sub>3</sub>/SiC specimen annealed 2 h at 1200°C, with Al<sub>2</sub>O<sub>3</sub> layer thickness of (b) 100 nm, and (c) 200 nm. [Equivalent Ta<sub>2</sub>O<sub>5</sub> sputter rate is 12 nm/min].
- Fig. 5.20 AES depth profile of Nb/Al<sub>2</sub>O<sub>3</sub>/SiC specimen annealed 2 h at 1200°C, with Al<sub>2</sub>O<sub>3</sub> layer thickness of 500 nm. [Equivalent Ta<sub>2</sub>O<sub>5</sub> sputter rate is 12 nm/min].
- Fig. 5.21 AES depth profiles of specimens (a) Nb/SiC in the as-deposited condition, (b) Nb/SiC annealed 2 h at 1200°C, and (c) Nb/500 nm Al<sub>2</sub>O<sub>3</sub>/SiC annealed 2 h at 1200°C. [Equivalent Ta<sub>2</sub>O<sub>5</sub> sputter rate is 12 nm/min].
- Fig. 5.22 AES depth profile of Al<sub>2</sub>O<sub>3</sub>/Nb/Al<sub>2</sub>O<sub>3</sub>/SiC specimen annealed 2 h at 1200°C, with Al<sub>2</sub>O<sub>3</sub> layer thickness of 20 nm for cap and 100 nm for the diffusion barrier. [Equivalent Ta<sub>2</sub>O<sub>5</sub> sputter rate is 12 nm/min].
- Fig. 5.23 AES depth profile of Ta/SiC (0001), annealed 4 h at 1100°C.
- Fig. 5.24 AES depth profile of Ta/SiC (0001), annealed 2 h at 1200°C.
- Fig. 5.25 AES depth profile of Ta/SiC (0001), annealed 4 h at 1200°C.
- Fig. 5.26 AES depth profile of Ta/Al<sub>2</sub>O<sub>3</sub>, annealed 4 h at 1200°C.
- Fig. 5.27 Al-Si-C ternary phase diagrams at 500°C and 800°C [Ref. 63].
- Fig. 5.28 The theoretical Si levels in Al required to prevent Al<sub>4</sub>C<sub>3</sub> formation [Ref. 17].
- Fig. 5.29 DSC data from Al/Si specimen.
- Fig. 5.30 AES depth profile of Al/Si specimen, in the as-deposited condition.
- Fig. 5.31 AES depth profile of Al/Si specimen, annealed 2 h at 600°C.
- Fig. 5.32 AES depth profile of Al/SiC specimen, in the as-deposited condition.
- Fig. 5.33 AES depth profile of Al/SiC specimen, annealed 2 h at 600°C.
- Fig. 5.34 AES depth profile of Al-1wt% Si/SiC specimen, in the as-deposited condition.
- Fig. 5.35 AES depth profile of Al-1wt% Si/SiC specimen, annealed 1 h at 600°C.
- Fig. 5.36 AES depth profile of Al/Si<sub>3</sub>N<sub>4</sub> specimen, in the as-deposited condition.

- Fig. 5.37 AES spectrum of  $\text{Al/Si}_3\text{N}_4$  specimen, annealed 1 h at 600°C.
- Fig. 5.38 Ni-Si-C ternary phase diagrams at 1150°C [Refs. 63,66].
- Fig. 5.39 AES depth profile of Ni/SiC specimen, in the as-deposited condition.
- Fig. 5.40 AES spectrum of Ni/SiC specimen, annealed 1 h at 1160°C.
- Fig. 5.41 AES depth profile of Ni/SiC specimen, annealed 1 h at 1160°C, peak-to-peak height data (top) and atomic concentration plot (bottom).
- Fig. 5.42 SEM micrographs of Ni/SiC specimen, annealed 1 h at 1160°C.
- Fig. 5.43 AES depth profile of Ni/SiC specimen, annealed 1 h at 725°C, peak-to-peak height data (top) and atomic concentration plot (bottom).
- Fig. 5.44 AES depth profile of Ni/Si<sub>3</sub>N<sub>4</sub> specimen, annealed 1 h at 1160°C, peak-to-peak height data (top) and atomic concentration plot (bottom).
- Fig. 5.45 SEM micrographs of Ni/Si<sub>3</sub>N<sub>4</sub> specimen, annealed 1 h at 1160°C, area in which detailed AES studies were performed.
- Fig. 5.46 SEM micrographs of Ni/Si<sub>3</sub>N<sub>4</sub> specimen, annealed 1 h at 1160°C.
- Fig. 5.47 AES survey spectra of Ni/Si<sub>3</sub>N<sub>4</sub> specimen, annealed 1 h at 1160°C, from the smooth part of precipitate (top) and from the dendrite on the precipitate (bottom).
- Fig. 5.48 (a) A cross-sectional SEM micrograph showing the Co/SiC reaction zone after annealing for 6 h at 1100°C. The location of the phase boundary is indicated by arrows. (b) A high magnification SEM micrograph showing the microstructure of the random carbon precipitation zone.
- Fig. 5.49 A SEM micrograph showing the microstructure of the ex-situ fractured SiC interface. The boundary between the unreacted and reacted regions is indicated.
- Fig. 5.50 Optical micrographs showing cross-sectional views of the Co/SiC reactions based on the reaction geometries of: (a) SiC on top of Co, and (b) Co on top of SiC after 1210°C annealing for 4 hrs. The original SiC/Co joining interface is indicated in (b).
- Fig. 5.51 A series of optical micrographs showing cross-sectional views of the Co/SiC reaction zone. (a) Co/SiC interface, (b)-(e) random C precipitation zone, (f) Co(Si) (light matrix) and Co<sub>2</sub>Si (gray areas) two phase mixture region. The dark areas, as indicated and shown on top of the (b) and (f), are voids.
- Fig. 5.52 A cross-sectional SEM micrograph of the Ni/SiC reaction zone after annealing for 6 hrs at 1100°C.
- Fig. 5.53 High magnification SEM micrographs of the Ni/SiC reaction zone.
- Fig. 5.54 Quantitative electron microprobe concentration profiles of Ni, Si, and C across the reaction zone from the Ni/SiC diffusion couple after annealing for 6 hrs at 1100°C. The relative concentrations of Ni and Si for Ni<sub>3</sub>Si and Ni<sub>5</sub>Si<sub>2</sub> are indicated. The locations of the unreacted Ni component, C-PFZ, and CPZ are marked.

- Fig. 5.55 XRD spectra of the reaction products generated from the Ni/SiC reaction at 1170°C.
- Fig. 5.56 Optical micrographs showing cross-sectional views of the Ni/SiC reaction zone after annealing for 4 hrs at 1170°C. Porosity, as a result of melting/ solidification, is noted and indicated in the reaction zone.
- Fig. 5.57 Optical micrographs showing different views of the melting/solidification phenomena from the Pt/SiC diffusion couple after annealing for 5 hrs at 900°C.
- Fig. 5.58 XRD spectra of the Pt/SiC reaction products after (a) 900, (b) 1000, and (c) 1100 °C reactions.
- Fig. 5.59 A series of SEM micrographs showing microstructure of the Pt/SiC reaction zone after annealing for 4 hrs at 1100°C.
- Fig. 5.60 SEM micrographs showing the microstructural change of the C bands, as a function of distance from the SiC reaction interface, from the as-reacted Pt/SiC diffusion couple after annealing for 4 hrs at 1100°C. As the distance increases, from (a) to (d), the thickness of the clustered C bands increases and the discrete C layers transform into C-decorated, granular Pt-silicide layers.
- Fig. 5.61 SEM micrographs showing the microstructural evolution in the reaction zone from the as-reacted Pt/SiC diffusion couple after annealing for 4 hrs at 1100°C.
- Fig. 5.62 A high magnification backscattered electron image showing the microstructure of the 3rd layer, and the morphology of the melted/solidified particulates formed on top from the as-reacted Pt/SiC diffusion couple after reactions at 1100°C for 4 hrs.
- Fig. 5.63 A series of Raman spectra from the modulated C bands precipitated in the the SiC/Pt reaction zone after annealing for 5 hrs at 1000°C. The spectrum, (a), from the SiC reaction interface indicates the existence of glassy carbon, which is characterized by the presence of a Raman peak at 1354  $\text{cm}^{-1}$ . As the locations of the C bands are farther removed from the SiC interface, from (b) to (d), graphitization of the C occurs, which is characterized by the decrease of the intensity ratio between the 1354 and 1585  $\text{cm}^{-1}$  Raman peaks.
- Fig. 5.64 A cross-sectional view SEM micrograph showing the reaction zone of a SS/SiC diffusion couple upon annealing at 1125°C for 8 h.
- Fig. 5.65 High magnification SEM micrographs showing the formation of 4 layered reaction zone. The four layers are indicated as 1, 2, 3 and 4.
- Fig. 5.66 High magnification SEM micrographs showing detailed microstructures in reaction zones 1, 2, and 3. Highly anisotropic C precipitates were observed in reaction zones 1 and 2.
- Fig. 5.67 (a) A backscattered electron image, and the corresponding elemental x-ray maps of (b) C, (c) Cr, (d) Ni, (e) Fe, and (f) Si from an area in reaction zone 1.
- Fig. 5.68 (a) A backscattered electron image, and the corresponding elemental x-ray maps of (b) C, (c) Cr, (d) Ni, (e) Fe, and (f) Si from an area in reaction zone 2.
- Fig. 5.69 (a) A backscattered electron image, and the corresponding elemental x-ray maps of (b) C, (c) Cr, (d) Ni, (e) Fe, and (f) Si from a farther area in reaction zone 2.

- Fig. 5.70 (a) A backscattered electron image, and the corresponding elemental x-ray maps of (b) C, (c) Cr, (d) Ni, (e) Fe, and (f) Si from an even farther area in reaction zone 2.
- Fig. 5.71 SEM micrographs showing (a) the Si diffusion front and the G.B.-PZ; (b) a high magnification of the grain boundary precipitates. The Si diffusion front is indicated by arrows.
- Fig. 5.72 EDS spectra collected from (a) point 1 and (2) point 2, as indicated in Fig. 5.71(a), showing the diffusion of Si is limited by the diffusion front.
- Fig. 5.73 EDS and WDS (the inset) spectra obtained from the grain boundary precipitates, as shown in Fig. 5.71(b), indicating the precipitates are Cr-carbide(s).
- Fig. 5.74 (a) A backscattered electron image, and the corresponding elemental x-ray maps of (b) C, (c) Cr, (d) Ni, (e) Fe, and (f) Si from precipitates located in a triple grain boundary junction.
- Fig. 5.75 SEM micrographs showing the locations from which systematic EDS analyses were conducted to establish the concentration gradients of Ni, Fe, and Cr.
- Fig. 5.76 (a) A TEM bright field image and (b) the corresponding electron diffraction pattern showing that the as-deposited film is polycrystalline  $\text{Ti}_3\text{Al}$ .
- Fig. 5.77 AES depth concentration profiles from (a) an as-deposited  $\text{Ti}_3\text{Al}$  film (on a  $\text{Si}_3\text{N}_4$  substrate) and (b) a bulk  $\text{Ti}_3\text{Al}$  standard.
- Fig. 5.78 (a) An ESCA and (b) an AES depth concentration profiles of the  $\text{Ti}_3\text{Al}$  films after reacting with a  $\text{Si}_3\text{N}_4$  substrate at  $1000^\circ\text{C}$  for 4 h.
- Fig. 5.79 An AES depth concentration profile of the  $\text{Ti}_3\text{Al}/\text{SiC}$  thin film diffusion couples after annealing at  $1000^\circ\text{C}$  for 4 h.
- Fig. 5.80 SEM micrographs showing the topographical characteristics of de-bonded reaction interfaces on the  $\text{Ti}_3\text{Al}$  (a and c) and the  $\text{Si}_3\text{N}_4$  (b and d) components.
- Fig. 5.81 An AES depth concentration profile of the gold-colored layer formed on the  $\text{Si}_3\text{N}_4$  substrate from a bulk diffusion couple after annealing at  $1200^\circ\text{C}$  for 6 h.
- Fig. 5.82 (a) An AES depth concentration profile of the light-brown layer formed on the  $\text{Si}_3\text{N}_4$  substrate from a thin film diffusion couple after annealing at  $1200^\circ\text{C}$  for 6 h. (b) and (c) show AES spectra from the interfaces after 33 and 120 min ion etching, respectively.
- Fig. 5.83 (a) An EDS spectrum taken from the light-brown layer formed on the  $\text{Si}_3\text{N}_4$  substrate from a thin film diffusion couple after annealing at  $1200^\circ\text{C}$  for 6 h. (b) A WDS spectra of Ti-LI and  $\text{L}_{\alpha}$  peaks, and N- $\text{K}_{\alpha}$  peak from the light-brown, TiN layer. (c) A WDS spectra of Ti-LI and  $\text{L}_{\alpha}$  peaks, and N- $\text{K}_{\alpha}$  peak from an as-deposited  $\text{Ti}_3\text{Al}$  layer.
- Fig. 5.84 SEM micrographs showing the surface characteristics of  $\text{Ti}_3\text{Al}/\text{Si}_3\text{N}_4$  thin film diffusion couples (a) after and (b) before annealing (at  $1200^\circ\text{C}$  for 6 h).
- Fig. 5.85 (a) A SEM image and the corresponding x-ray maps of (b) N- $\text{K}_{\alpha}$ , (c) Ti- $\text{K}_{\alpha}$ , (d) Al- $\text{K}_{\alpha}$ , (e) Si- $\text{K}_{\alpha}$ , and (f) Nb- $\text{K}_{\alpha}$  from an area on the de-coupled reaction interface on the  $\text{Ti}_3\text{Al}(\text{Nb})$  component after annealing at  $1200^\circ\text{C}$  for 6 h.

- Fig. 5.86 An AES depth concentration profile of the  $\text{Ti}_3\text{Al}/\text{SiC}$  diffusion couples annealed at  $1200^\circ\text{C}$  for 4 h.
- Fig. 5.87 Schematic drawings showing proposed diffusion mechanisms for the  $\text{Ti}_3\text{Al}/\text{Si}_3\text{N}_4$  reactions at (a)  $1000^\circ\text{C}$  and (b)  $1200^\circ\text{C}$ . At  $1000^\circ\text{C}$ , a discontinuous layer of TiN is formed and the out-diffusion of Si can effectively take place through the TiN-free regions. At  $1200^\circ\text{C}$ , a continuous, planar TiN layer is formed.
- Fig. 5.88 (a) A SEM micrograph showing the surface morphologies of the TiN and the de-bonded  $\text{Ti}_3\text{Al}(\text{Nb})$ . An intriguing pattern is noted on the  $\text{Ti}_3\text{Al}(\text{Nb})$  surface. (b) A high magnification SEM micrograph indicates the presence of a regular, step-like pattern on the  $\text{Ti}_3\text{Al}(\text{Nb})$  surface.



## **LIST OF TABLES**

- 2-1 Results of kinetic studies of unalloyed Ti/SiC
- 2-2 Values of parabolic rate constant at 760°C obtained for various alloy matrices of Ti in Ti alloy-B composites (Ref. 26)
- 3-1 Selection of metal/ceramic combinations
- 4-1 Representative chemical analysis of hexoloy (wt.%)
- 4-2 Target materials used in sputter deposition
- 4-3 Thin film specimens and annealing treatments
- 5-1 Phases identified by electron diffraction
- 5-2 Free energy of formation of various compounds
- 5-3 Annealing conditions, diffusion phenomena, and major reaction products for various diffusion couples
- 5-4 Gibbs free energy of decomposition of SiC at various temperatures
- 5-5 EDS analysis of the composition at various locations on the SiC and stainless steel. The compositions of the stainless steel are shown in the first row as a reference
- 5-6 Gibbs free energy of formation of selected metal carbides at 1400 K
- 5-7 Reaction patterns and reaction products formed in selected metal/SiC systems at specific temperatures
- 5-8 Characteristics of the reaction interfaces and products from various  $Ti_3Al(Nb)$  reactions with  $Si_3N_4$  and SiC
- 5-9 Gibbs free energies of formation of various compounds at 1300 and 1500 K

## Section 1

INTRODUCTION

Advanced aerospace systems require low density materials with substantially improved high temperature mechanical properties and oxidation resistance. Metal matrices with ceramic reinforcements offer such potential. From a structural viewpoint, the metal/ceramic interface controls the transfer of load between a metallic matrix and its ceramic reinforcement and thereby influences the mechanical properties of a composite. Ideally, such an interface should be a mechanical continuum, but a chemical discontinuum, implying no interdiffusion between the matrix and the reinforcement. In most practical situations, however, compound formation occurs at the interface and results in some loss in mechanical strength [1]. Improved design of metal/ceramic materials is limited by the lack of understanding of fundamental interaction mechanisms between metal matrices and ceramic reinforcements. Such an understanding is highly desired to establish a scientific basis for the future selection of metal/ceramic systems.

The primary objective of this research effort is therefore to develop a scientific understanding of the nature and extent of interactions between metal matrices and ceramic reinforcement materials at high homologous temperatures. A significant part of this study is to understand these processes sufficiently well that diffusion barriers can be selected to control the interaction. The first portion of the program involves an experimental approach to study the interactions of pure metals with selected ceramic reinforcements during high temperature exposure. The second part will examine techniques that may be used to minimize such interactions between the above metal matrices and the ceramic reinforcements. One such approach, based on a detailed understanding of the nature of the interaction and interdiffusion between the metal matrices and the ceramics, will be to select interfacial layers that will act as barriers to interdiffusion. This will require an understanding of the thermodynamics and kinetics of the baseline metal/ceramic interaction, and a determination of the rate controlling species during interdiffusion.

Most investigations on metallic matrices and ceramic reinforcements have been empirical and have emphasized bulk engineering materials. Furthermore, they have concentrated on reaction layer thicknesses which are convenient for study, i.e., in excess of 3-5  $\mu\text{m}$ , but that are not necessarily appropriate for understanding fundamental metal/ceramic interactions. Reaction layer thicknesses on the order of only 0.3-0.5  $\mu\text{m}$  can lead to significant degradation in both strength and ductility. The

present research emphasizes the use of sophisticated surface analytical techniques, which make it possible to characterize reaction layers less than  $0.1\text{ }\mu\text{m}$ , thereby providing a fundamental understanding of the early stages of the reaction kinetics. This information will be used to predict and evaluate the usefulness of selected materials as diffusion barriers in order to minimize reaction layer growth kinetics.

In most practical situations, interdiffusion or compound formation occurs at the interface during either high temperature consolidation processes or engineering applications. Since most of the refractory metal matrices contain metal species (e.g., Ti, Nb, Ni, Fe, Al, V or Co) having a high affinity for the elements present in reinforcing fibers (e.g., Si, B or C), the composite systems must be treated as non-equilibrium systems from a thermodynamic view point. In other words, the interdiffusion distance increases and the evolution of compound formation gets more complex as a function of time at elevated temperatures. Interdiffusion between the matrix and reinforcement, together with compound formation, may result in interfacial embrittlement and associated degradation of the overall properties of a composite. In order to improve the design of composites, a fundamental understanding of interfacial reactions of metal matrices with ceramic reinforcements is crucially needed.

This final report summarizes the nature of interfacial reactions between candidate matrix materials Nb, Ta, Al, Co, Ni, Pt and  $\text{Ti}_3\text{Al}$  and ceramic reinforcement materials  $\text{SiC}$ ,  $\text{Al}_2\text{O}_3$  and  $\text{Si}_3\text{N}_4$ . Emphasis was placed on understanding the nature of reaction products and the kinetics reactions occurring at elevated temperatures. Reaction studies were conducted on thin film metals sputter deposited on ceramic materials, as well as on bulk diffusion couples (for Nb, Ni, Co, Pt and stainless steel matrix materials with  $\text{SiC}$ ). The bulk diffusion couples were prepared by diffusion bonding plate-shaped  $\text{SiC}$  with pure metals and then vacuum annealing at selected temperatures. The nature and extent of interfacial reactions were evaluated using optical metallography, x-ray diffraction (XRD), Auger electron spectroscopy (AES) for surface, interface and thin film chemical characterization, and scanning electron microscopy (SEM) and transmission electron microscopy (TEM) for detailed microstructural characterization. Finally, the effectiveness of thin film diffusion barriers in minimizing the reaction between metal matrix and ceramic reinforcement was studied using Nb/ $\text{Al}_2\text{O}_3$ / $\text{SiC}$  system.

## Section 2

TECHNICAL BACKGROUND2.1 Overview

In order to understand the interaction of metallic matrices with ceramic reinforcements, it is necessary to focus on the metal/ceramic interface. For example, from a structural viewpoint, this interface will control the transfer of load between a metallic matrix and its ceramic reinforcement. The particular type of bonding at the interface will determine the shear strength, and thereby will influence the mechanical properties of a composite. Ideally, such an interface should be a mechanical continuum, i.e., one that has coherent atomic bonds across the interface, but one which is also a chemical discontinuum, implying no possible interdiffusion between the matrix and the reinforcement. In most practical situations, however, a chemical continuum exists across this interface, resulting in compound formation at the interface and some loss in mechanical strength [1]. It is useful to consider three different classes of reinforcement/matrix systems [2]: Class I, in which the reinforcement and matrix are mutually non-reactive and insoluble at either processing or service temperatures; Class II, in which the reinforcement and matrix are mutually non-reactive but have mutual solubility; and Class III, in which the reinforcement and matrix chemically react to form compounds at the interface.

2.1.1 Class I Ceramic Reinforcement/Metal Matrix System: Good examples of Class I systems are familiar to materials scientists, as they include classic dispersion strengthened metals such as nickel-thoria or copper-alumina. In these systems, the ceramic reinforcement is usually incoherent with respect to the metallic matrix, resulting in relatively poor bonding across the interface. Only small volume fractions of ceramic reinforcement can be used effectively in Class I systems. The systems are generally utilized as a result of the ability of the fine, incoherent ceramic dispersoids to inhibit the passage of dislocations at elevated temperatures. This capability is in marked contrast to the typical engineering advantages of composites with high volume fractions of ceramic reinforcements such as SiC whiskers: i.e., increased elastic stiffness as well as improvements in room temperature mechanical strength.

There are a number of dispersion strengthened materials which are usually considered Class I systems but do not strictly satisfy the criteria of nonreactive matrix and reinforcement. Examples of

this type of behavior would include mechanically alloyed, dispersion strengthened systems which contain  $Y_2O_3$  reinforcements within nickel alloy matrices containing aluminum additions. It has been documented [3,4] that the largest  $Y_2O_3$  dispersoids transform during processing to mixed ( $Y_2O_3$ - $Al_2O_3$ ) oxides. This is accompanied by some degree of coarsening of the average dispersoid size. The degradation in high temperature creep strength, however, as a result of this coarsening is only on the order of 10%, which is usually considered to be tolerable [3].

**2.1.2 Class II ceramic Reinforcements/Metal Matrix Systems:** Within the context of Metal/Ceramic hybrids, there are some very significant systems which would qualify as Class II systems. Typically, Class II systems would include eutectic systems - i.e., systems in which the matrix and the reinforcement are soluble as liquids above the eutectic temperature, but are reasonably non-reactive as solids below the eutectic temperature. Transition metal/carbon systems such as nickel-carbon, cobalt-carbon, or copper-carbon would all be examples of class II systems. These systems would be of marginal use for elevated temperature applications as they would possess limited oxidation resistance. The various directionally-solidified nickel or iron base superalloy eutectic systems would also qualify as class II systems, and these have been studied extensively for aerospace applications. Recent work in the field of directionally solidified eutectics has been summarized in a volume edited by Lemkey, et al [5]. The most serious problem facing applications of these materials is their relatively poor low cycle fatigue and thermal fatigue properties [6].

**2.1.3 Class III Ceramic Reinforcement/Metal Matrix Systems:** The vast majority of ceramic/metal systems with the ultimate potential for interesting aerospace structural applications fall under the category of Class III systems. In these composites, the reinforcement phases and matrices react to form compounds at their interfaces [2]. In general, the various metal species, which possess low density and high ductility (e.g., Al and Ti), have a thermodynamic tendency towards compound formation with the most desirable reinforcement species. As a result, carbides, borides or silicides are usually encountered in the interfacial reaction zone. It is reasonable to assume that the presence of a reaction layer implies strong interfacial bonding. As Ochiai, Murakami and co-workers have shown [7-9], however, for the case of a well-bonded reaction layer, degradation in room tensile properties of practical engineering materials such as a continuous fiber reinforced composite is to be expected. This degradation is a result of a notch effect created by the reaction product which is then exerted upon the fiber. If the kinetic growth law of the reaction layer can be determined, for a matrix/reinforcement combination at a given temperature, then it is possible using their models to predict the time required to cause a degradation in room temperature ultimate tensile strength. Unfortunately, the necessary kinetic data is often not known for a given

matrix/reinforcement combination; a further requirement would be the ability to predict the degradation in strain to fracture of these Class III systems.

By way of example, the formation of titanium diboride ( $TiB_2$ ) reaction layers (as thin as 0.4 micron in a material consisting of commercial purity titanium (Ti-40A), reinforced with 25 vol% boron filaments) has been shown to lead to significant degradation in room temperature strain to fracture, as measured by the strain to fracture of the filament [10]. This is illustrated in Fig. 2.1; also indicated in the figure is the fact that degradation in strain to fracture occurs before the largest decrease in ultimate tensile strength occurs. That is, a  $TiB_2$  layer thickness on the order of 0.7 micron can be tolerated before significant degradation is observed in the ultimate tensile strength of this particular system. These results also suggest that very small reaction layers, of less than a certain critical thickness, may lead to increased work hardening, and in this regime the filament strength controls fracture. However, when the reaction layer exceeds a certain critical thickness, it begins to act as a notch, and leads to reductions in both strength and strain-to-fracture of the composite. The degradation in properties is also aggravated by net volume changes due to reactions; net volume changes can either magnify the notch effect or degrade load transfer at interfaces due to void formation. Thus, control of interfacial reactions is essential in obtaining good mechanical properties in Class III metal/ceramic systems.

## 2.2 Prior Work on Reaction Kinetics in Class III Metal Matrix/Ceramic Reinforcement Systems

In this section we will examine critically the most important previous studies on Class III systems which have focused on the kinetics of interfacial reactions. This section was derived in part from the results of a comprehensive, computer-aided, literature survey which was performed at the Lockheed Research and Development Division in preparation for this proposal. Examples of recent studies in this class include SiC/Ti [11-13], SiC/Ti-6Al-4V [11,12,14,15], B/Ti [16], SiC/Al [17-19], C/Al [20], SiC/Ni [21], and  $Al_2O_3$ /Mg [18,22]. For the sake of brevity, we will consider only one Class III system here - the Ti-SiC system. This technologically significant system can, in terms of complexity, be considered typical for Class III composites, and has been studied intensively.

Before we examine the Ti-SiC system, it is useful to review the manner in which kinetic data is usually presented by investigators concerned with metal/ceramic interactions.

2.2.1 Presentation of Kinetic Data: It is worth noting some important points with respect to the presentation of kinetic data. The materials of interest in Class III systems are multicomponent, with

multiple reaction layer formation being thermodynamically possible. Fortunately, kinetic factors usually dictate that only a few compound species will form - this outcome is a function of factors such as diffusion rates at elevated temperature, and the free energies of formation of the compounds. With these qualifications in mind it is of value to consider, in terms of kinetic behavior, the factors expected for compound layer growth in a binary system. The Au-Sb system is a good example, as only one intermetallic species is thermodynamically stable,  $\text{AuSb}_2$  [23,24]. In general, two extremes in layer growth kinetics are possible [25]: (i) in circumstances where the interfacial reaction is rate limiting, layer growth is observed that is linear as a function of time; (ii) for cases in which diffusion of either constituent is rate limiting, parabolic kinetics will be observed, and the reaction layer thickness will be linear as a function of the square root of time.

The most general way to describe reaction layer kinetics in multicomponent systems is to independently measure the exponent,  $n$ , of time in the equation [24]:

$$x(t,T) = x_0 + k'(t)^n. \quad (2-1)$$

In eq. (2-1),  $x$  is the reaction layer thickness,  $x_0$  is the as-processed layer thickness at zero time, and  $k'$  is the reaction rate constant at a particular temperature. Thus, in order to determine whether linear or parabolic kinetics are controlling layer growth, a plot of  $\log(x)$  versus  $\log(t)$  is used to measure the reaction exponent,  $n$ . For cases where parabolic kinetics are anticipated, the relation between  $x$  and  $t$  is written as follows:

$$x^2 = (x_0)^2 + 2kt \quad (2-2)$$

where  $k$  is the parabolic rate constant, and has the same dimensions as a diffusion coefficient, i.e.,  $(\text{length})^2(\text{time})^{-1}$ . Thus,  $k$  is written explicitly as

$$k = k_0 \exp(-Q/RT) \quad (2-3)$$

and can be obtained by plotting  $\log(k)$  as a function of  $1/T$ , to yield the activation energy  $Q$  and the pre-exponential factor  $k_0$  from the slope and intercept, respectively. Whereas the value of  $k$  at a given temperature is useful for ranking the relative reaction kinetics for various systems, it is usually not possible to infer specific information regarding rate limiting mechanisms from the values of  $Q$  and  $k_0$ . This is because in most cases multiple reaction layers are formed - for example, many binary systems such as Ti-Si contain three intermediate compounds - and closed form solutions to

multiple layer growth problems are not generally available. The value of  $Q$  is thus often a composite value involving the growth of multiple reaction layers, and the specific identities of reaction layers need to be considered in interpretation of these activation energy values. Nevertheless, the method of analysis outlined above is useful for its inherent simplicity, and changes in the value of  $Q$  as a function of temperature permit some inference of changes in rate limiting mechanisms.

**2.2.2 Titanium/Silicon Carbide System:** Titanium, because of its high thermodynamic driving force for compound formation, is a worst-case metal to consider for metal matrix/ceramic systems. The major problems with compatibility investigations are readily apparent when considering Ti matrices. In performing critical evaluations of existing data, it is necessary to make a basis of comparison in order to determine the validity of a given study. The following items need to be examined closely when comparing different kinetic studies for the same Class III system (Ti-SiC is used as a typical system here):

1. Was care taken to control trace impurities in the metallic matrix? For example, if commercial purity titanium was used, was a carbon content cited?
2. Was the ceramic reinforcement a stoichiometric compound? Often, for example, silicon carbide contains excess free silicon. This would be expected to produce different kinetics from studies using stoichiometric SiC.
3. Method of sample preparation: Were thin Ti films deposited on a ceramic substrate? It is generally more common for investigators to look at bulk composite specimens, i.e., with the reinforcement present as fibers.
4. Method of kinetic analysis: Which range of thickness was used to arrive at the reaction kinetics? Recall that one would really like to look at early stage kinetics, i.e., thicknesses in the range of 0.1 to 1  $\mu\text{m}$ , because this is the thickness range in which degradation in properties can become pronounced (see Fig. 2.1).

With the above points in mind, it is useful to examine prior investigations on the Ti-SiC system. All of the investigators have either found or assumed parabolic rate kinetics, and thus plot their data according to eq. (2-2). The results for the various investigations are shown in Table 2-1 [12,13,25-27]. The first remarkable result from Table 2-1 is that except for the case of Snide et al. [25], there is reasonable agreement in the activation energy for reaction layer growth. Excluding the work of Snide et al., this average value is  $65.1 \pm 5.4$  Kcal/mole. There is, however, a very wide range of values of  $k_0$ . This suggests that there is indeed a specific, diffusion-controlled mechanism for layer growth, but different experimental geometries may influence the relative layer growth rates. The values of parabolic rate constant as a function of inverse temperature are plotted in Fig. 2-2.



It is important to note that there are potential problems with some of the previous investigations cited in Table 2-1. Klein et al.[26] and Snide et al.[25] studied continuous composite tapes of a commercial purity (Ti-40A) matrix with BORSIC filaments. The BORSIC filament is a Boron filament with an outer coating of  $0.4\text{ }\mu\text{m}$  SiC. The role of Boron on the layer growth kinetics cannot be discounted even though Klein et al. systematically omitted reaction layer thicknesses in excess of  $0.4\text{ }\mu\text{m}$  from their kinetic analysis. Ratliffe and Powell [27] employed semi-infinite layers of commercial purity (unknown grade) Ti and SiC. The SiC used, however, was not stoichiometric SiC, but contained 8% excess Si. It is also worth noting that they were the only workers (see Table 2-1) to report observations of the silicon-rich compounds,  $\text{TiSi}$  and  $\text{Ti}_3\text{Si}$ .

The two most recent studies shown in Table 2-1 - those of Martineau et al. [12], and of Chamberlain [13] - appear to be studies that have avoided the above problems. Chamberlain studied the reaction kinetics of sputtered Ti films on stoichiometric (0001)  $\alpha$ -SiC single crystals in the temperature range  $550\text{--}700^\circ\text{C}$ , using Auger electron spectroscopy. This permitted correlation of reaction layer thicknesses as small as  $0.1\text{ }\mu\text{m}$ . Chamberlain noted problems with the relatively small volumes of reaction product formed, leading to a poor detection limit when using x-ray diffraction for reaction compound identification. This suggests the need to use TEM in order to perform structural identification of reaction layers in a thin film diffusion couple experiment.

The work of Martineau et al. [12] constitutes the most extensive study of the Ti-SiC system, and included three different types of SiC fibers: 1. Stoichiometric; 2. Carbon-rich surface; 3. SiC coated with pyrolytic graphite (PG). For purposes of comparison, we have tabulated in Table 2-1 the case of stoichiometric SiC filaments in a commercial purity Ti matrix. Martineau et al. noted that a carbon-rich or PG surface increases the parabolic rate constant of the Ti-SiC system by roughly a factor of 2. Microstructural studies show that the reaction zone consists primarily of a binary mixture of  $\text{TiC}_{1-x}$  and  $\text{Ti}_5\text{Si}_3(\text{C})$ : the titanium carbide forms concentric rings around the SiC fiber. The innermost layer adjacent to the fiber is a ternary  $\text{Ti}_3\text{SiC}_2$  compound. They suggest the following sequence of events during the growth of the reaction layer in Ti/stoichiometric SiC composites: 1) Reaction and formation of  $\text{Ti}_3\text{SiC}_2$ , along with  $\text{Ti}_5\text{Si}_3(\text{C}_x)$  ( $x < 1$ ):  $\text{TiSi}_2$  was not detected; 2)  $\text{Ti}_5\text{Si}_3(\text{C}_x)$  grows by interdiffusion of both Si and C from the filament as well as by Ti from the matrix. As the  $\text{Ti}_5\text{Si}(\text{C}_x)$  becomes supersaturated with C, Titanium carbide is precipitated; leading to the observed concentric ring geometry.

The above sequence is consistent with the 1200 °C isothermal phase diagram which has been assembled by Brukl [28]. Clearly, non-stoichiometric or carbon coated SiC would complicate the above sequence. It is also interesting that, unlike Boron-reinforced titanium systems in which Boron diffuses to the Ti matrix, in this case both fiber and matrix elements participate in an interdiffusion process. The study of Martineau et al. emphasizes the need for close correlation of Auger data with SEM and electron microprobe data in order to arrive at clear conclusions on rate limiting mechanisms.

### 2.3 Methods to Minimize Growth of Reaction Layers in Class III Metal/Ceramic Composites

Two basic approaches can be used to minimize reaction layers in Class III systems: 1. the application of a thin film diffusion barrier to the reinforcement phase prior to combination with the metal matrix; 2. alloying of the metal matrix to minimize the thermodynamic driving force between the reinforcement and the matrix. Both methods seek to reduce the kinetics of reaction layer growth.

**2.3.1 Diffusion Barriers:** The diffusion barrier concept consists of placing a thin film barrier on the reinforcement phase to inhibit reaction layer formation and growth. The barrier is designed to reduce greatly the flux of the most rapidly diffusing species, and thereby limit the rate of growth of the reaction layer. For example, it has been demonstrated, by observations of Kirkendall porosity in thermally treated specimens, that Boron is the most rapidly diffusing species in the Titanium-Boron system [26]. This observation suggests that barriers which will block the outward diffusion of Boron into the Titanium matrix are required. In general, a diffusion barrier is not necessarily a reaction barrier - often, the original thin film placed on the reinforcement may react with the matrix to form a more stable compound which serves to effectively block diffusion.

One well-known example of diffusion barrier technology is the application of Boron Nitride (BN) to Boron filaments prior to their incorporation into aluminum matrix composites by means of liquid infiltration methods [29-31]. Surface nitriding of Boron filaments was used to produce BN coatings with thicknesses in the range of 0.3 to 0.4 micron. The effect of immersion of both treated and untreated B filaments, in molten aluminum at 700 °C, on filament tensile strength is shown in Fig. 2-3 [29]. Note that a 10 minute immersion of an untreated filament leads to an 80% reduction in the UTS of the filament, whereas the BN-coated filament suffered only a 20% reduction in UTS. Boron Nitride on Boron was also found to be an effective diffusion barrier for Boron filaments in Titanium and Nickel matrices [31].

Recently Koop and Tien [32,33] evaluated the effectiveness of ion implanted diffusion barriers for high temperature metal matrix applications. Diffusion couples of W-Ni were fabricated, employing ion implantations of Na, Ca and Ba into bulk tungsten substrate and subsequently sputter depositing nickel to approximately 100  $\mu\text{m}$  thickness. The diffusion couples were annealed in vacuum at 1500 K for 50 h and composition as a function of distance from the interface were evaluated. The profile from Ca-implanted diffusion couple indicated some decrease in interdiffusional kinetics, while an acceleration was observed for Ba- and to some degree for Na-implanted specimens. The mechanisms involved in these materials are under evaluation [34].

Many modern composites use some type of diffusion barrier coating in order to achieve good bonding between the matrix and reinforcement, and at the same time limit the growth of harmful reaction layers. Unfortunately, most of the details are considered proprietary by composite manufacturers [35] and the scientific basis for their selection is not documented, if indeed it ever existed.

**2.3.2 Alloying the Metallic Matrix:** In discussions of alloying of the metallic matrix to minimize the growth of reaction layers in Class III systems, it is essential to focus on the exact physical mechanisms which control the growth processes. There are two major methods by which alloying elements can lead to reductions in reaction layer growth: 1. by impeding diffusion of the rate limiting species in the matrix; 2. by means of rapid diffusion of the alloying element to the matrix/reinforcement interface, and promotion of a reaction layer. This reaction layer has a different chemical stoichiometry from the layer formed for the case of the unalloyed matrix, and it can serve as a diffusion barrier to inhibit subsequent reaction layer growth. Both mechanisms seek to inhibit reaction layer growth by making interdiffusion more difficult - however, the latter method in which a reaction layer forms is probably more effective. This is because such compound structure layers require a change in the type of vacancy mechanism needed to permit diffusion. In general, the diffusion of a divacancy pair through a compound structure is apt to be a process with a higher activation energy than mono-vacancy diffusion through a metal. In practice, experimental evidence often suggests both mechanisms occur simultaneously and it is sometimes difficult to determine which one is more important with respect to slowing reaction layer growth.

**2.3.2.1 Al- $\alpha$ -Al<sub>2</sub>O<sub>3</sub> System:** Clear examples are available in which alloying elements preferentially segregate to the matrix/reinforcement interface and form compounds which inhibit further reaction. For example, a study of slurry casting of Al alloys reinforced with discontinuous fibers of  $\alpha$ -Al<sub>2</sub>O<sub>3</sub> by

Levi et al., [36], examined the effect of Cu and Mg alloying additions on interface reactions. It was found that Mg additions formed thermodynamically stable  $\text{MgAl}_2\text{O}_4$  spinel-reaction layers around the fibers. For the case of ternary Al-Cu-Mg alloys, the  $\text{MgAl}_2\text{O}_4$  layer inhibited the formation of thick reaction layers of  $\text{CuAl}_2\text{O}_4$  spinel, which was observed in the binary Al-Cu alloy. Unfortunately, the authors only examined temperatures at which the alloys were molten; it would be of great interest to determine kinetic data for these systems at temperatures relevant to aging.

**2.3.2.2 Ti-SiC and Ti-B Systems:** There is a substantial body of data in the literature [2,12] documenting the effect of matrix alloying on reduction of the rate constant for reaction layer growth for Titanium reinforced with either Boron (B) or Silicon Carbide (SiC). It is worth examining some of this work, since the results show the difficulty of identifying exact mechanisms whereby the alloying elements inhibit diffusion. For example, Martineau et al.[12] observed a reduction by a factor of 4 in the parabolic rate constant,  $k$ , for reaction layer growth in Ti-6Al-4V alloy reinforced with SiC, by comparison with unalloyed Ti/SiC alloys. For the case of uncoated, stoichiometric SiC, in Ti-6Al-4V, Auger line scans indicated the presence of some vanadium in regions dominated by Ti and Si, suggesting the growth of ternary Titanium-Vanadium Silicides. Electron microprobe data also indicated evidence of Al enrichment within the Ti-6Al-4V matrix immediately adjacent to the reaction layer. The Al segregation could possibly make it more difficult for Ti to diffuse from the matrix into the reaction layer, but it is more probable that the diffusion of C and Si are more strongly impeded by the non-stoichiometric Titanium-Vanadium Silicides which are formed.

Klein et al. investigated the effect of various binary alloying elements on the rate constant for reaction layer growth at  $760^\circ\text{C}$  in Ti-B composites [26]. Three types of alloying elements were identified, based on their effectiveness in reducing the parabolic rate constant,  $k$ : Type A, which have no effect on the rate constant (e.g., Si, Sn); Type B, which decrease the rate constant in an amount which is proportional to their atomic percent addition (e.g., Cu, Ge); and Type C, which decrease the rate constant as a strong, non-linear function of their atomic percent addition (e.g., Al, Mo, Zr, V). Klein and co-workers observed that Al and Mo are rejected ahead of  $\text{TiB}_2$  as it grows into the matrix, which suggests that these two elements may be effective in reducing matrix diffusion of Ti. Molybdenum additions were generally more effective than Al additions in reducing  $k$  since Mo additions greater than 8 at% also lead to formation of a  $\text{MoB}_2$  inner layer reaction zone. They also observed that V and Zr tend to form ternary borides, which apparently inhibit the transport of B from the filament to the metallic matrix. This work, then, appears to indicate that the second mechanism, where alloying elements diffuse to form a diffusion barrier, is the more effective means of reducing reaction kinetics.

The various reductions in  $k$  due to particular alloying elements appeared to be additive, thereby permitting identification of more complex alloys which would be compatible with the Boron filaments. The values obtained for different Ti alloy matrices are shown in Table 2-2 [26]. Note that the best Titanium alloy matrix (Ti-13V-5Zr-2.5Al-10Mo) has a parabolic rate constant which is about a factor of 700 lower than the rate constant for unalloyed Ti.

This section has sought to demonstrate that there are useful options available to deal with controlling reaction layer growth in Class III systems. The number of components in the system, however, resulting from either alloying additions or diffusion barriers, makes the analysis of these zones complicated. Unlike the case where the matrix is a pure metal, phase diagrams are usually not available for the multicomponent systems. This makes impossible the prediction of phases that will be encountered in the reaction zone. More experimental investigations of these phenomenon will hopefully result in a better understanding of the mechanisms and hence the most effective means of controlling matrix/reinforcement interactions in Class III systems.

Table 2-1 RESULTS OF KINETIC STUDIES OF UNALLOYED Ti/SiC

<u>Investigation</u>	<u><math>(k_D)^{1/2}</math> (cm/s<sup>-1/2</sup>)</u>	<u>Q (Kcal/mole)</u>	<u>Temperature Range (°C)</u>	<u>Compound Identified</u>
1. Martineau (1984)	2.14	65.6	700-1000	TiC, Ti <sub>3</sub> Si <sub>3</sub> , Ti <sub>3</sub> SiC <sub>2</sub>
2. Chamberlain (1980)	0.249	62.8	570-700	TiC
3. Snide (1971)	0.0032	36.4	700-1050	TiC, Ti <sub>5</sub> Si <sub>3</sub>
4. Ratliff (1970)	0.0026*	72.4*	1000-1200	TiC, Ti <sub>5</sub> Si <sub>3</sub> , Ti <sub>3</sub> Si, TiSi Ti <sub>2</sub> SiC
5. Klein (1969)	0.95	59.8	650-982	-----

\*Stage I data

Notes on each of the above investigations:

- #1. "Laid up" composite: using stoichiometric polycrystalline SiC fibers.
- #2. Sputtered Ti on single crystals of stoichiometric SiC.
- #3. BORSiC filaments, commercial purity Ti matrix.
- #4. Diffusion couples - semi-infinite - of commercial purity Ti and SiC. SiC used contained 8% excess Si.
- #5. Continuous composite tapes of Ti-40A matrix with BORSiC filaments, SiC coating: 0.4  $\mu$ m thick.

**Table 2-2**      **VALUES OF PARABOLIC RATE CONSTANTS AT 760°C OBTAINED FOR  
VARIOUS ALLOY MATRICES OF TI IN TI ALLOY-B COMPOSITES (26)**

<u>Matrix</u>	<u>k (10<sup>-15</sup> cm<sup>2</sup>/s)</u>
Unalloyed Ti	68.0
Ti-6Al-4V	17.0
Ti-8Al-1Mo-1V	29.0
Ti-8V-8Mo-2Fe-3Al	6.4
Ti-13V-11Cr-3Al	4.9
Ti-11Mo-5Sn-5Zr	10.0
Ti-17V-5Mo	8.1
Ti-30Mo	9.0
Ti-13V-5Zr-2.5Al-10Mo	0.1

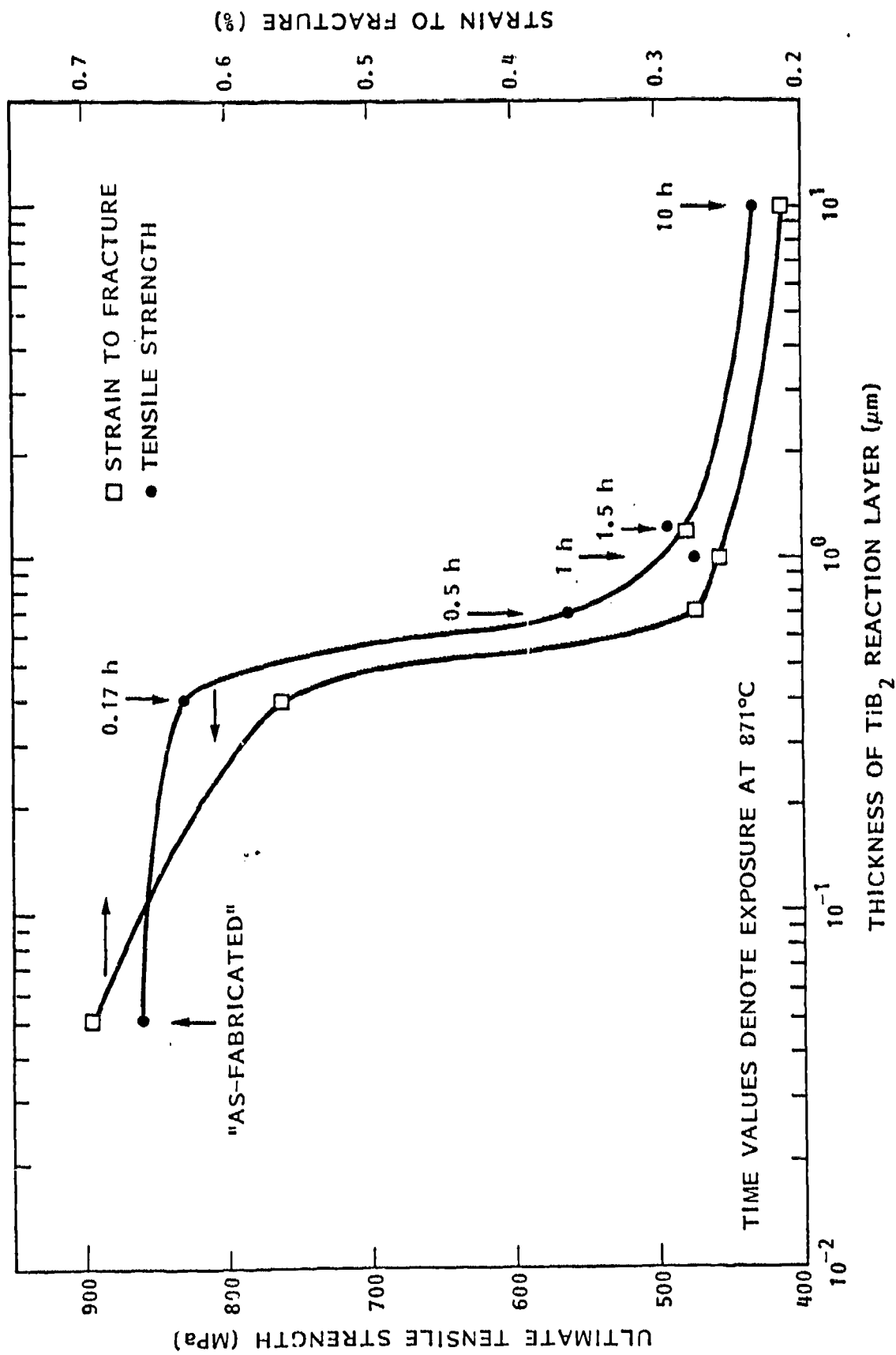


Fig. 2.1 Effect of  $TiB_2$  reaction layer thickness on the room temperature mechanical properties of a Ti-40A matrix with 25% boron filament reinforcement (Ref. 10).



# REACTION KINETICS OF Ti/SiC SYSTEM

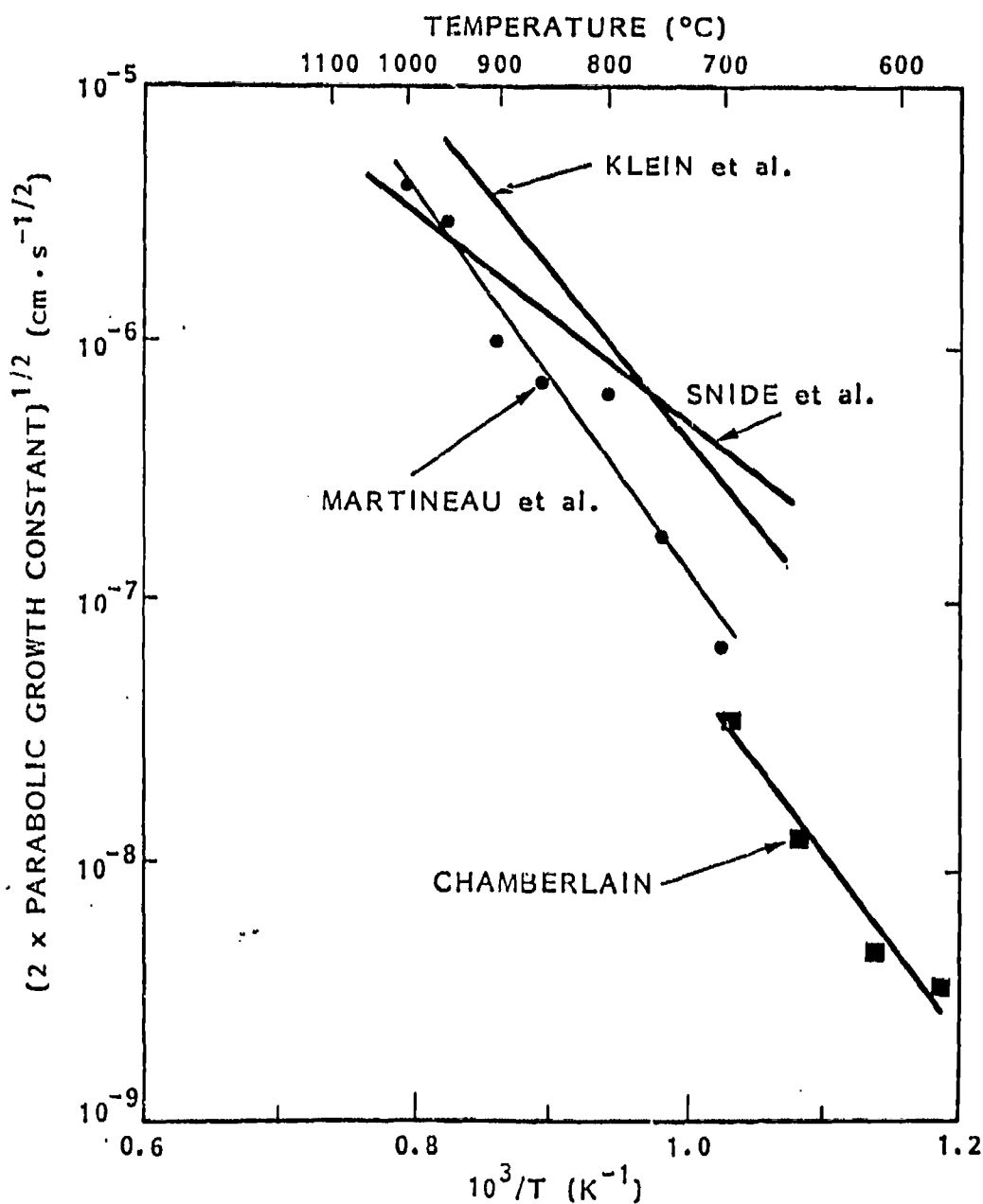


Fig. 2.2 Reaction kinetics of Ti/SiC composite system (Refs. 12, 13, 25, and 26).

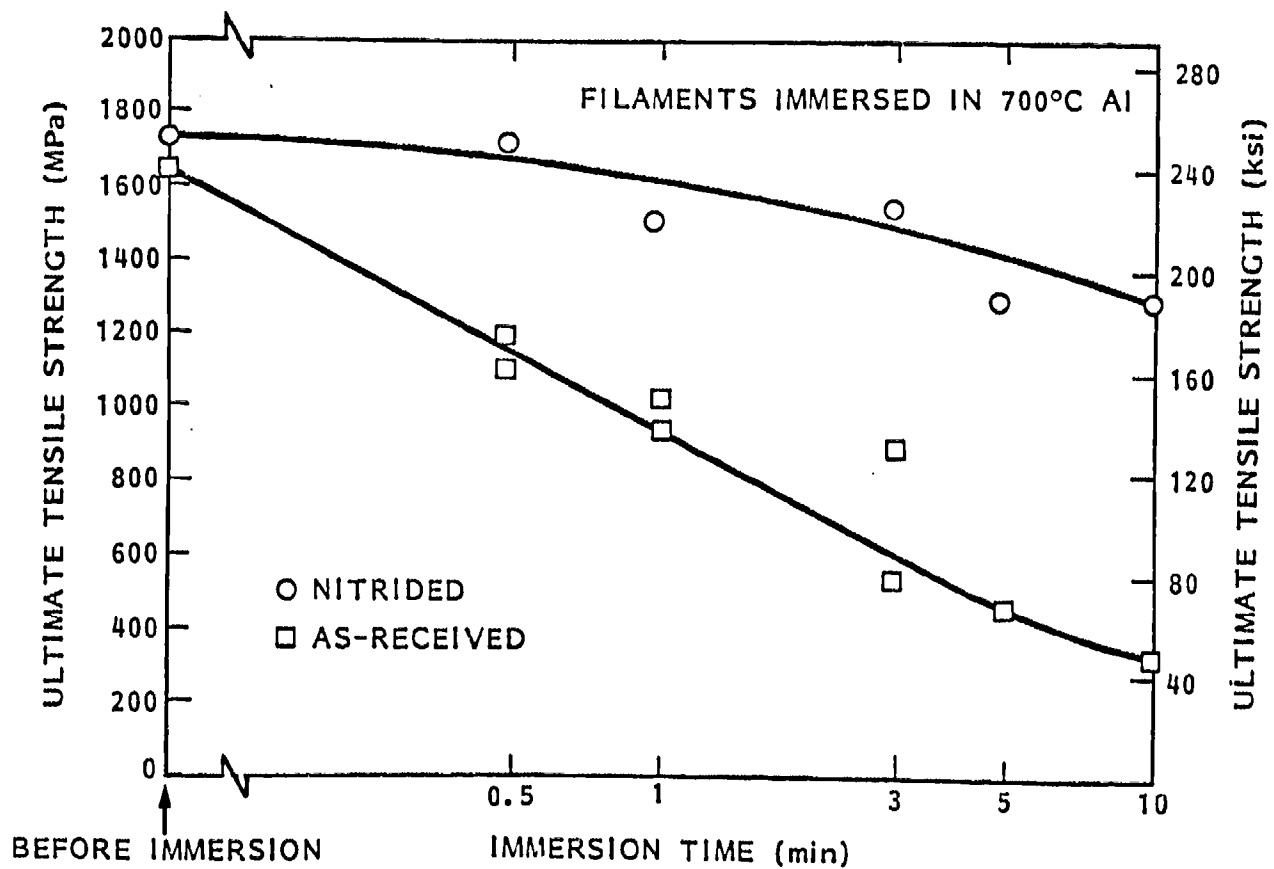


Fig. 2.3 Effect of immersion time in 700°C Aluminum on UTS of Boron filaments (Ref. 26).

## Section 3

SELECTION OF CANDIDATE SYSTEMS

A number of metal matrix materials were selected based upon their uniqueness of physical and chemical properties and crystal structures. Two FCC metal matrices have been selected: Aluminum and Nickel. Aluminum is a key element as it is likely to impart oxidation resistance to, and decrease the density of, alloys or intermetallic compounds constituting the matrix of future engineering materials. Nickel was selected as a matrix material since many existing high temperature alloys are based on a nickel matrix. Cobalt, with a similar melting point and adjacent to nickel in the periodic table, was selected as a HCP matrix candidate. Stainless steel is selected as a multicomponent matrix candidate for evaluating the possible complex reactions. Ti and Nb, have been selected because their crystal structures are HCP and BCC, respectively, and their melting points are high enough to permit elevated temperature applications. They are also under active consideration as the basis of alloys for high temperature aerospace applications. Niobium is particularly interesting among the refractory metals due to its relatively low density (by comparison with Mo, W, and Ta). At the beginning of the present program, a niobium target, required for sputter deposition, could not be procured immediately. To minimize associated delays, experimental work was undertaken using tantalum, that was readily available, and for which most diffusional and reaction aspects are expected to be very similar to niobium. Finally, an intermetallic compound  $Ti_3Al$  was selected for evaluations because it exhibits excellent elevated temperature mechanical properties and oxidation resistance and is a promising matrix material for many critical elevated temperature applications. Additional factors for selecting this system are presented in section 5.12.

SiC and  $Al_2O_3$  are two of the most common reinforcement candidates because of their low density, good mechanical strength, and thermal stability at elevated temperatures. From considerations based on metal matrices, the most popular current materials used in the aerospace industry focus on nickel-, niobium-, and titanium- based alloys. A few previous studies [12,13,37-47] have investigated the thermal compatibilities, fiber-matrix (FM) reactions, or solid state reactions of SiC with various high temperature metallic materials, e.g., Ti [12,13,37], Ni [38-40], Fe [38], Co [40], titanium aluminides [41-43], titanium alloys [42], nickel aluminides [44,45], and superalloys [46,47]. Most of these studies have been concentrated primarily on the determination of reaction products of metal/SiC reactions, and the growth kinetics of reaction layers, which were deduced from the thicknesses of reaction layers as a function of reaction time. In this work emphasis was placed on

the reactions of SiC with those elemental species which are contained in most of the refractory alloys. The reactions of SiC with multi-element metal matrices were also studied to provide a fundamental understanding of SiC reaction behavior in the presence of various elemental species. Another objective of this study is to explore several fundamentally intriguing questions, e.g., the decomposition characteristics of SiC (in the presence of various metals), the effect of metal silicide formation (on interfacial properties), the thermodynamic driving force, and carbon precipitation behavior during SiC/metal reactions at high temperatures. To address these issues, elemental metals of Nb, Ni, and Co, and alloys of stainless steel (SS), containing Fe, Ni, and Cr, were reacted with SiC. Both thin film and bulk diffusion couples with plane interfaces, rather than consolidated metal powders with reinforcing fibers, were prepared to evaluate the metal/SiC reactions.

In addition to SiC and  $\text{Al}_2\text{O}_3$ ,  $\text{Si}_3\text{N}_4$ , which does not contain the reactive elements C and O, was selected for additional evaluations. A complete list of the metal matrices and ceramic reinforcements which were examined under this program are shown in Table 3-1.

Table 3-1 SELECTION OF METAL/CERAMIC COMBINATIONS

<u>Structure</u>	<u>Matrix</u>		<u>T<sub>m</sub> (K)</u>	<u>Ceramic Reinforcements</u>
		<u>Metal</u>		
FCC		Aluminum	933	SiC, Si <sub>3</sub> N <sub>4</sub>
FCC		Nickel	1726	SiC, Si <sub>3</sub> N <sub>4</sub>
HCP		Cobalt	1768	SiC
FCC		Platinum	2045	SiC
BCC		Niobium	2741	SiC, Al <sub>2</sub> O <sub>3</sub>
BCC		Tantalum	3014	SiC, Al <sub>2</sub> O <sub>3</sub>
HEX		Ti <sub>3</sub> Al	1623	SiC, Si <sub>3</sub> N <sub>4</sub>
FCC		Stainless Steel		SiC

## Section 4

**EXPERIMENTAL**

Candidate metal matrix and ceramic reinforcement specimens were prepared in the form of (i) thin film couples containing thin metal films on ceramic substrates, or (ii) bulk diffusion couples. For some systems, both thin film and bulk couples were examined and the results were correlated. Evaluation of  $\text{Al}_2\text{O}_3$  diffusion barriers in the Nb/SiC system was conducted using thin film couple specimens.

**4.1 Preparation of Thin Film Couples**

**4.1.1 Substrate Preparation:** Ceramic substrates of SiC,  $\text{Al}_2\text{O}_3$  and  $\text{Si}_3\text{N}_4$  were obtained from various sources and prepared for metal film depositions.

SiC single crystal and polycrystalline substrates were obtained from Carborundum (formerly Standard Oil Engineered Materials). The single crystal orientation was determined to be (0001) using Laue back reflection. The polycrystalline substrates were 1 cm x 1 cm x 0.23 cm Hexoloy SA SiC tiles and were fabricated from powders, which were formed into a green product and then sintered in argon or nitrogen at temperatures exceeding 2000°C. The SiC content of the Hexoloy is typically 99.2 weight percent and a representative chemical analysis, as supplied by the manufacturer, is given in Table 4-1. Prior to metal deposition, the SiC substrates were step polished and finished with 0.25 micron diamond paste. The surface contaminants were then removed by immersion in a solution of one part concentrated HF and one part distilled water for 30 to 60 seconds. Subsequently, they were ultrasonically rinsed in methanol. The HF solution was selected as an etchant because it effectively removed surface contamination without attacking the substrate. Also, the stoichiometry of the surface composition was not affected by etching, as determined by Auger electron spectroscopy (AES).

Sapphire crystals were obtained from Crystal Systems, Inc. Crystal orientations of the substrates were (0001) and (1010). The starting material had a nominal purity of 99.996 weight percent. The crystals were supplied as 2.54 cm diameter X 0.317 cm disks with an 8050 standard optical finish. The crystals were fabricated by the Heat Exchanger Method (HEM<sup>TM</sup>). Crystal growth itself was performed in a graphite vacuum resistance furnace. A refractory metal crucible loaded with  $\text{Al}_2\text{O}_3$

chips was seated on a tungsten heat exchanger with the seed crystal centered inside. After the chamber was evacuated, the furnace was heated above 2050° C to melt the alumina charge and nucleate on the seed crystal. The seed crystal was prevented from melting by passing helium through the heat exchanger. After the crystal was grown, the temperature was lowered to just below the solidification temperature to anneal out solidification defects. Throughout the entire process, the crucible and crystal remained stationary. Prior to sputter deposition of metal, the sapphire substrates were cut into quarters, polished with 0.25 micron diamond paste, immersed in fuming sulfuric acid for 30 to 60 seconds, and ultrasonically rinsed in methanol.

Si<sub>3</sub>N<sub>4</sub> polycrystalline substrates were obtained from Norton. The substrates were 1.25 cm x 1.25 cm x 0.25 cm Noralide (NC132) tiles and were fabricated from powders by hot pressing at 1750°C in nitrogen. The Si<sub>3</sub>N<sub>4</sub> substrates were identified to be of  $\beta$ -type, which has a hexagonal crystal structure, by X-ray diffraction.

**4.1.2 Thin Film Deposition:** The metals Nb, Al, and Ni were deposited on selected substrates by sputter deposition. A Ti<sub>3</sub>Al target has been procured, bonded to the backing plate, and prepared for deposition studies.

Early efforts to deposit Nb films by evaporation yielded coatings with oxygen contents as high as ten atomic percent, which was unsatisfactory. For Phase I work involving Nb and Ta, thin films with oxygen contents of less than one atomic percent were applied via sputtering at the Scientific Coating Laboratory in Santa Clara, CA. Prior to sputter deposition, the substrates were dipped in a saltwater bath for 15 to 30 seconds, rinsed for 5 to 10 minutes in distilled water, and then rinsed in isopropyl alcohol. A Perkin Elmer Sputtering System Model 2400 was used. After loading the substrates, the chamber was evacuated to a base pressure of  $4 \times 10^{-7}$  torr. The niobium sputtering target was manufactured by Teledyne Wah Chang. Analysis of the ingot showed the target purity to be 99.9 weight percent pure Nb. The substrates were presputtered for fifteen minutes at 200 V, 3.1 amps. Coating thicknesses ranged from one to two microns.

For the phase II effort involving Nb, Al and Ni depositions, all the work was conducted at the Lockheed Research and Development facility using CVC 601 Loadlock sputter deposition system. The system is capable of RF deposition, required for insulating materials, and DC magnetron sputtering for high rate deposition of conductive materials. Nb and Al were deposited by the DC method, while Ni was deposited by RF sputtering due to its high magnetic permeability and resulting interaction with the magnetic fields from the magnetron. The purity of the target materials employed

in the sputter deposition is shown in Table 4-2. Prior to deposition the ceramic substrates SiC and Si<sub>3</sub>N<sub>4</sub> were etched with 50:50 HF:H<sub>2</sub>O solution for 30 to 45 seconds to remove any surface oxides, rinsed in water, subsequently rinsed in methanol, and inserted into the sputter deposition system. The substrates were further cleaned by reverse bias sputter etching prior to the metal deposition. Typical thickness of the deposited metal films is 1  $\mu$ m.

Aluminum oxide films were deposited from a sintered Al<sub>2</sub>O<sub>3</sub> target by RF deposition in a plasma containing argon and oxygen. The oxygen concentration in the gas, and the RF power and bias on the target were varied to obtain films of superior quality. Film quality was evaluated by pin hole density measurements in an electrochemical cell (Fig.4.1) and by x-ray photoelectron spectroscopy (XPS) for compositional analysis. Typical deposition parameters include 2000 V RF power, 100 to 200 V RF bias and 2 to 4% oxygen in the Ar+O<sub>2</sub> plasma. The base pressure prior to deposition is  $1 \times 10^{-7}$  torr and gas pressure during deposition is 10 mtorr. For diffusion barrier application aluminum oxide films with 100, 200 and 500 nm thicknesses were deposited on SiC substrates, followed by 1  $\mu$ m of niobium without exposing to ambient in between. All the films exhibited pin holes, with the least seen in the thickest of the films. Estimated pin hole density is 6 to 10 per cm<sup>2</sup> with a hole size of less than 2  $\mu$ m diameter. In order to determine the number of pin holes in an aluminum oxide film, the film deposited on a silicon substrate was made a cathode in an electrochemical cell. The electrolyte used is a 50:50 mixture of water and ethanol. A pointed copper electrode is used as an anode to probe H<sub>2</sub> evolution at the cathode. Assuming that hydrogen is evolved only from the conductive areas (or pin holes in the oxide film), the actual number of pin holes could be counted and their density estimated. This method is only semi-quantitative but was useful in quickly ascertaining the quality of the deposited films.

## 4.2 Bulk Diffusion Couples

**4.2.1 Preparation of SiC Ceramic:** The polycrystalline SiC substrates, designated as Hexoloy, were obtained from the Carborundum Corporation. The substrates were 1 cm x 1 cm x 0.23 cm, and they were formed by sintering at temperatures exceeding 2000°C. The SiC content of the Hexoloy is typically 99.2 wt%. Prior to metal deposition or diffusion bonding, the SiC substrates were step polished and finished with a 0.25 micron diamond paste. The surface contaminants were then removed by immersion in a solution of one part concentrated HF and one part distilled water for 30 to 60 s, followed by ultrasonic cleaning in methanol and drying by compressed air.



For Co, Ni and Pt couples, the polycrystalline SiC was prepared by hot pressing, and was identified by x-ray diffraction (XRD) and Raman spectra to be primarily  $\beta$ -SiC. The density of the plates was at least 99.5 % of theoretical value. The SiC plates were then cut into small pieces of approximate dimensions of 10mm x 5mm x 1.5mm, and polished with a 15 $\mu$ m diamond disc. The polished samples were ultrasonically cleaned in acetone, rinsed in water, and then dried using compressed air.

**4.2.2 Preparation of Metals:** The metals (Nb, Ni, and Co), which are 99.99% pure, were purchased from Aldrich Chemical Co. The stainless steel bulk material has an approximate bulk composition of Ni 30, Cr 24, Fe 46 (in at%), and trace amounts of Mn and Ti, as revealed by energy dispersive x-ray microanalysis. The Pt metal is 99.9% pure and was received from Engelhard Corporation. The metal pieces were cut into a similar size to that of the SiC, mechanically ground with #600 SiC papers, polished by slurries containing 1  $\mu$ m particle size alumina, fine polished with 1  $\mu$ m diamond paste, and finished by ultrasonic cleaning in methanol and drying.

**4.2.3 Formation of Bulk Diffusion Couples:** To form a diffusion couple, reactant coupons of metals and SiC were stacked together, under a slight pressure (estimated 0.5 kg/cm<sup>2</sup>) from a dead weight or by utilizing a pressure clamp, to achieve an intimate contact. For the Co, Ni and Pt couples with SiC, diffusion anneals were performed in either a tube furnace, which was flushed with He gas, or in a vacuum of  $5 \times 10^{-7}$  torr. Upon completion of the diffusion anneals, the samples were quenched in either water or liquid nitrogen. Vacuum annealed samples, however, were furnace cooled. To facilitate the measurement of reaction zone thickness, metals of a slightly different area from SiC were used so that the original joining interface could be distinguished and serve as a reference boundary. The thickness of the reaction zones on both the metal and SiC sides were measured from this reference boundary.

#### **4.3 Thermal Treatments**

The thin film and the bulk diffusion couple specimens were annealed in vacuum with a base pressure of  $5 \times 10^{-6}$  torr at temperatures ranging from 600 to 1200° C for 1 to 12 hours. The details of these anneals for various metal films are shown in Table 4-3.

#### 4.4 Characterization

Thin Film Couples: Thin film metal/ceramic diffusion couples were characterized using optical metallography, scanning electron microscopy (SEM), transmission electron microscopy (TEM) and the surface analysis techniques of Auger electron spectroscopy (AES) and X-ray photoelectron spectroscopy (XPS, also known as ESCA). Altogether, they provided detailed topographical, compositional, and structural information of the reaction products.

Specimens for optical metallography and SEM were prepared by low angle cross-sections, which provided enlarged (4:1) images of the thin film/substrate interface region. Examples of optical images for the Nb/SiC specimen cross-section are shown in Fig.4.2. The image on the left hand side is for a 1  $\mu\text{m}$  Nb film on a polycrystalline SiC substrate in the as-deposited condition and shows a relatively smooth surface. In contrast, the image on the right hand side is for the same specimen after vacuum annealing at 1100°C for 4 h and shows substantial surface roughness as well as several reaction zones. In addition, metallized surfaces were examined by SEM before and after thermal treatments. Together these studies provided information on interface roughness and layering of reaction products at the interface. The nature of the reactions between thin films and substrates, including reaction zone thicknesses and chemistry were evaluated primarily by AES in conjunction with Argon ion sputtering. The basic principles of these techniques is briefly presented below:

4.4.1 Auger Electron Spectroscopy: When a specimen is bombarded with energetic electrons (1 to 30 keV), both characteristic x-rays as well as characteristic electrons, named Auger electrons after their discoverer, Pierre Auger, are emitted. In AES, the energies of emitted electrons are precisely determined using an electron spectrometer and used to identify species on the specimen surface. The technique is highly surface sensitive, as these low energy electrons are emitted from a shallow region on the order of 5 to 20Å. The technique has the capability to detect all elements except hydrogen and helium and provides quantitative information with the help of external standards. The technique is often utilized to obtain highly localized information (using focused primary electron beams), surface chemical homogeneity information in the form of Auger elemental images, and depth-compositional information in conjunction with ion sputtering. For some elements such as Al and Mg, chemical state information may also be determined by observing small shifts in the Auger peaks due to chemical binding effects.

All the AES analyses were performed in a PHI 560 ESCA/SAM system manufactured by Perkin Elmer Corporation. Typical areas of analyses were  $\sim 250\mu\text{m} \times 250\mu\text{m}$  and thus represent a large area average in most instances. All the sputter profiling was conducted using 5 keV argon ion bombardment and the sputter rates were expressed in  $\text{Ta}_2\text{O}_5$  equivalents.

**4.4.2 Transmission Electron Microscopy:** TEM was instrumental in obtaining the microstructural details of the deposited films and the reaction products. These details include grain size, distribution of phases, and crystal structures. Specimens for TEM examination were prepared by sectioning samples with a diamond saw and gluing two specimen surfaces back to back with Perkin-Elmer Vac-seal epoxy resin. A diamond saw was used to cut a 0.3 to 0.5 mm thick transverse slice from the glued composite. Discs of 2.3 mm diameter were then cut from the transverse slice using an ultrasonic disc cutter. Care was taken to position the glue joint as close as possible to the center of the disc. The 2.3 mm disc was inserted into a 0.5 mm diameter brass ring (OD = 3 mm) and held in place with Torr Seal resin. The brass ring ensured that the Vac-Seal glue joint did not fail prior to complete thinning of the sample. The ring supported cross section was reduced in thickness to  $150\mu\text{m}$  by grinding. The final surface finish was  $1\mu\text{m}$ . One side of the sample was dimpled until the thickness of the sample at the center was approximately  $20\mu\text{m}$ . The final surface finish of the dimpled region was also  $1\mu\text{m}$ . After dimple grinding, the sample was ion milled until electron transparent. A JEOL-2000FX (200 kV) microscope, equipped with a complete Kevex Energy Dispersive X-Ray Analysis, was used for examination of the specimens. The 2000FX is capable of 2.8 Å point-to-point resolution in the transmission mode, and 10 Å resolution when operated in the STEM mode. Special image recording capabilities include a Gatan TV system and image intensifier, coupled to a quantel frame-store.

**Bulk diffusion couples:** The bulk diffusion couples were transversely sectioned and reaction zones were analyzed by optical microscopy, scanning electron microscopy with EDS (energy dispersive spectrometry) microanalysis, x-ray diffraction, and scanning Auger microprobe. Electron microprobe analysis was conducted to establish quantitative atomic concentration profiles. The carbon precipitation behavior was examined by a laser Raman microprobe. Thin film metal/ceramic diffusion couples were characterized using optical metallography, x-ray diffraction (XRD), scanning electron microscopy (SEM), transmission electron microscopy (TEM) and Auger electron spectroscopy (AES). Altogether, they provided detailed topographical, compositional, and structural information of the reaction products.

**Table 4-1      REPRESENTATIVE CHEMICAL ANALYSIS OF HEXOLOY (wt%)**

<b>SIC</b>	<b>Free Si</b>	<b>Al</b>	<b>Ca</b>	<b>B</b>	<b>Fe</b>	<b>Ti</b>	<b>Ni</b>
99.2	0.07	0.10	0.01	0.45	0.01	0.01	0.01

**Table 4-2      TARGET MATERIALS USED IN SPUTTER DEPOSITION**

<u>Material</u>	<u>Supplier</u>	<u>Purity(%)</u>
Al	DeGussa	99.999
Al-1Si	DeGussa	99.999
Al <sub>2</sub> O <sub>3</sub>	Cerac	99.99
Nb	Teledyne Wah Chang	99.9 <50 ppm O
Ni	DeGussa	99.99
Ti <sub>3</sub> Al	Cerac	99.5-99.9

Table 4-3 THIN FILM SPECIMENS AND ANNEALING TREATMENTS

<u>Coating / Substrate System</u>	<u>Temperature (°C)</u>	<u>Annealing Time (h)</u>
Ta/(0001) SiC	800	4
	900	4
		8
		12
	1000	4
	1100	4
	1200	2
		4
Ta/Sapphire	900	4
	1100	4
	1200	2
		4
Nb/(0001) SiC	800	4
	900	4
		8
	1000	4
	1100	4
Nb/Polycrystal SiC	800	1
		4
	900	4
		8
	1000	4
	1100	4
	1200	2
Nb/Sapphire	800	1
	900	8
	1100	4
	1200	2
Al/SiC, Al-1wt%Si/SiC, Al/Si and Al/Si <sub>3</sub> N <sub>4</sub>	As-deposited	
	400	2
	500	2
	600	1
	600	2
	600	4
Ni/SiC and Ni/Si <sub>3</sub> N <sub>4</sub>	As-deposited	
	725	1
	1160	1

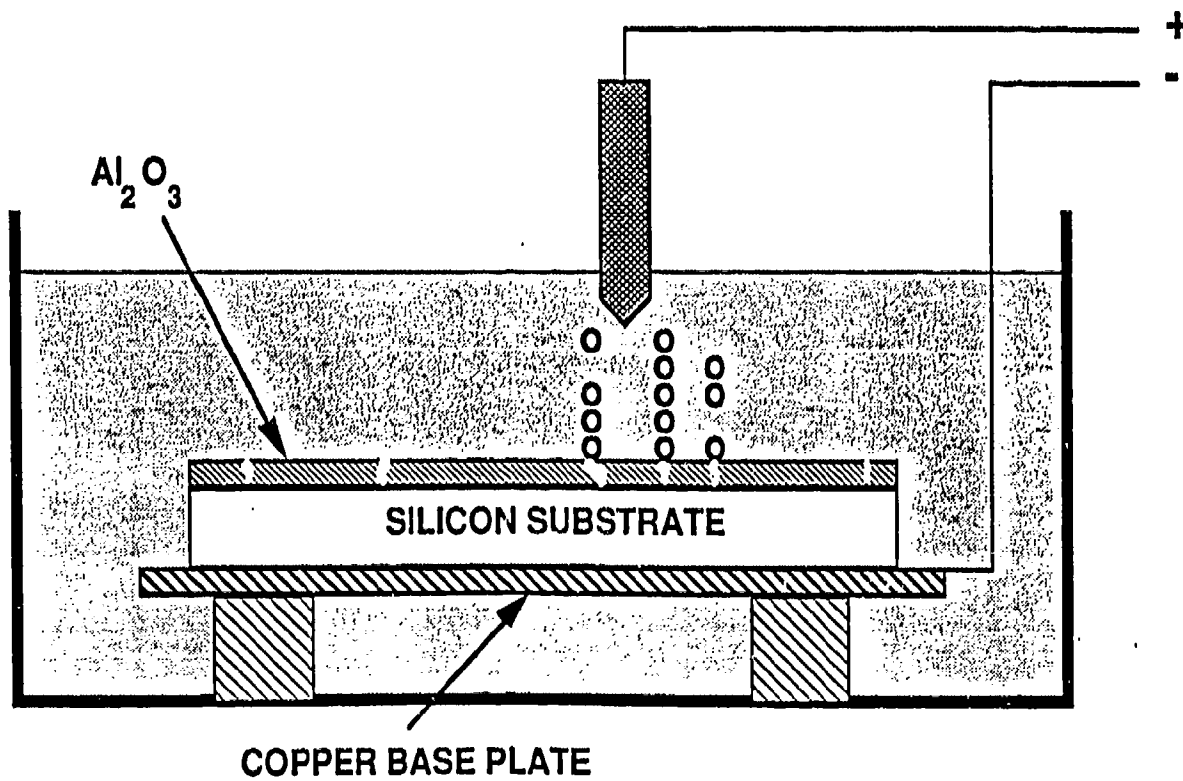


Fig. 4.1

Schematic of the electrochemical set up used to measure the pin hole densities of  $\text{Al}_2\text{O}_3$  layers deposited on silicon substrates.

AS-DEPOSITED

1100°C - 4 HRS -  $10^{-6}$  TORR

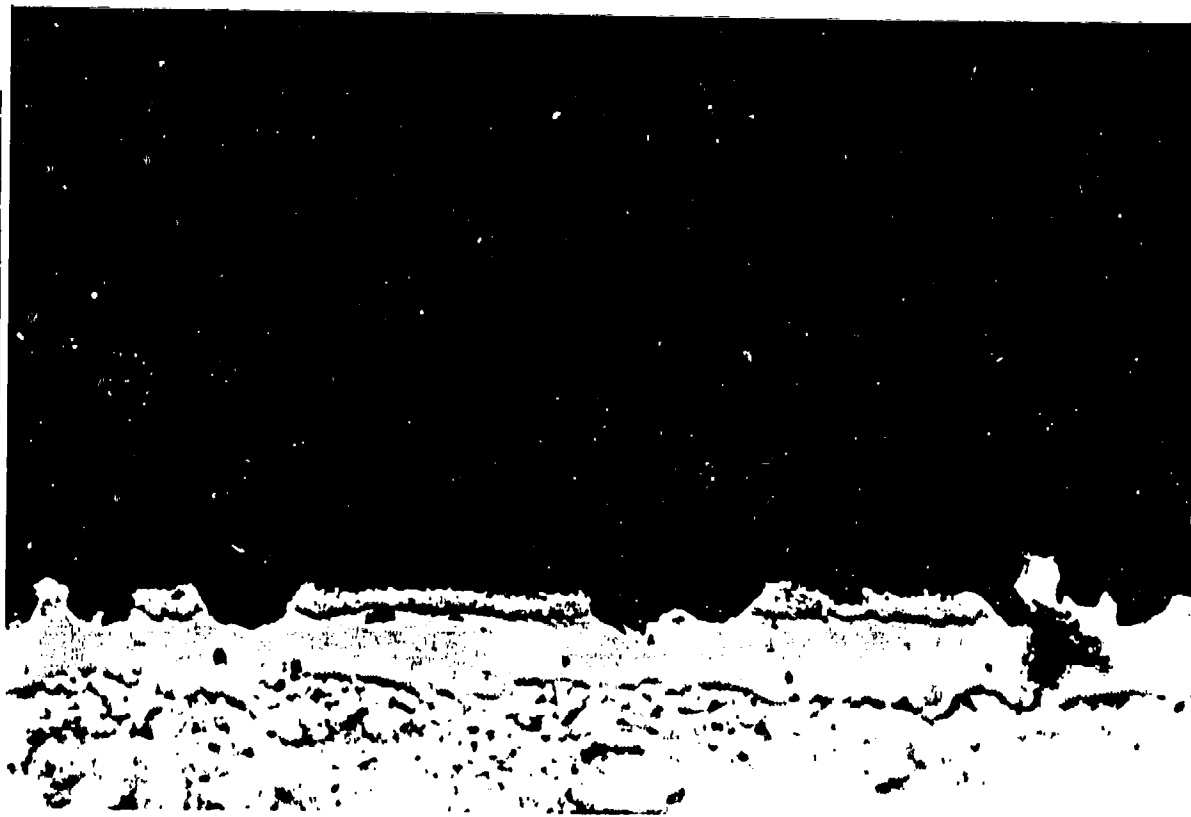
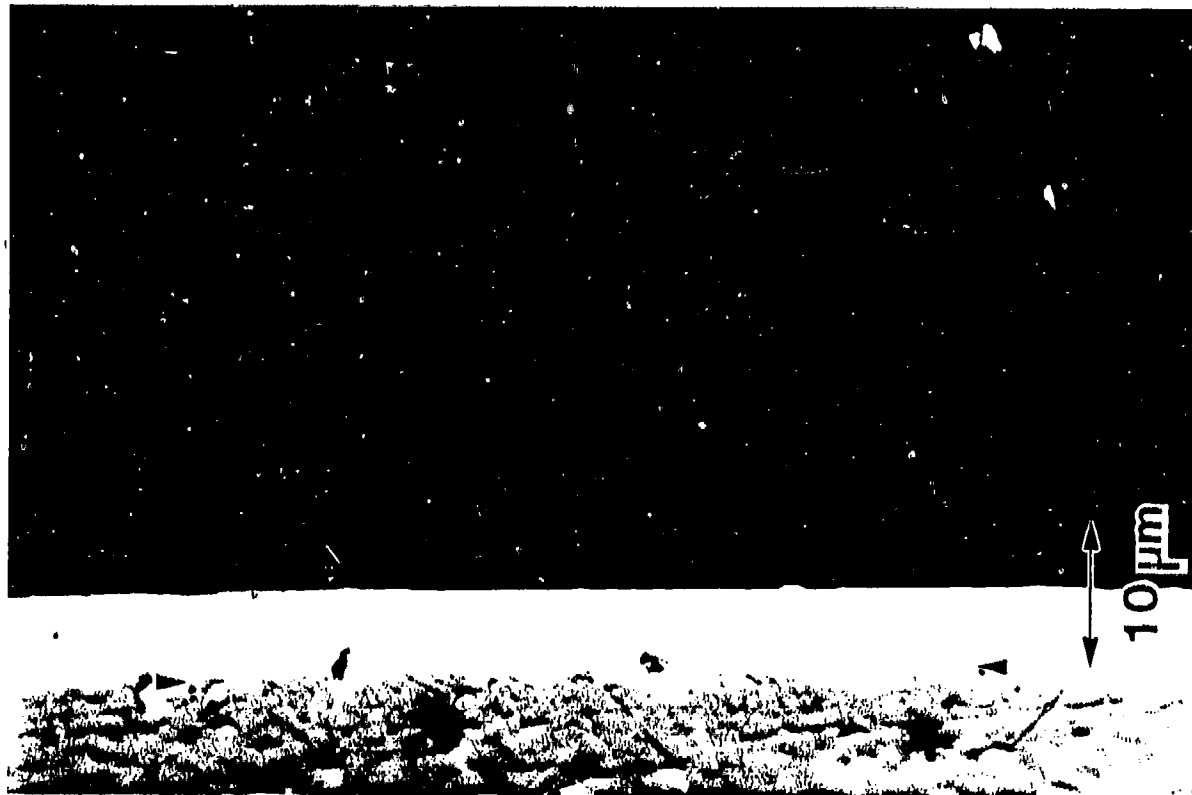


Fig. 4.2 Optical micrographs showing low angle cross-sections of Nb/SiC specimens.



## Section 5

RESULTS AND DISCUSSION

This section discusses the interfacial reactions occurring at the various metal/ceramic systems selected in the form of thin film and bulk diffusion couples. AES, SEM, TEM and optical metallographic techniques have been the primary experimental methods employed in the characterization of these materials.

### 5.1 Nb/SiC System

**5.1.1 Nb/SiC Thin Film Couples:** Niobium thin film was deposited simultaneously on a number of polycrystalline SiC (Hexoloy), single crystal SiC (0001) and  $\text{Al}_2\text{O}_3$  substrates. The thickness of the as-deposited niobium film is typically 1.3  $\mu\text{m}$ . The niobium film in the as-deposited condition is relatively clean (below the AES detectability level for O, C and N, typically 0.1 at.%) as demonstrated by the depth profile shown in Fig. 5.1. The metal/ceramic specimens were vacuum treated for selected times at various temperatures and subsequently characterized by AES. Specimens that underwent a significant degree of interfacial reaction were selected based on the AES data and subjected to detailed characterization using TEM.

**600-1000°C Reactions:** The effect of annealing temperature on the interfacial reactions in the Nb/SiC system was studied by examining specimens annealed for 4 h at various temperatures. A specimen annealed at 600°C for 4 h showed little or no interdiffusion (figure not shown) in comparison with the as-deposited specimen (Fig. 5.2a). The AES profile obtained upon heating to 800°C for 4 h (Fig. 5.2b), however, indicates some interdiffusion of Nb and C near the film/substrate interface. Also, during this anneal, the oxygen and carbon levels within the niobium film increased to the 2-3 at.% range. An examination of the nature of the profiles in various Nb/SiC thermally treated specimens, and consideration of all possible contamination sources, suggests that the elements C and O originate from the vacuum annealing system. After exposure at 900°C for 4 h, significant diffusion and reactions took place near the thin film interface, as shown in Fig. 5.2c. Formation of a distinct layer of carbon-rich niobium (possibly a  $\text{NbC}_x$  phase) was observed after about 90 minutes of sputter time (0.96  $\mu\text{m}$  depth) and a C- and Si-rich region (possibly  $\text{NbC}_x\text{Si}_y$

phase) after about 110 minutes sputter time (1.14  $\mu\text{m}$  depth). The oxygen contamination in the reacted region is very low indicating the possible rejection of oxygen from niobium during its reaction with C and Si. The reactions occurring after annealing at 1000°C for 4 h are shown in Fig. 5.2d. It is apparent that the  $\text{NbC}_x$  region has moved further toward the surface of the film and the thickness of the  $\text{NbC}_x\text{Si}_y$  region has increased.

The specimen annealed at 1000°C for 4 h was characterized in detail by TEM, in order to understand the nature of reaction products. Two phases were observed in the first reaction layer adjoining SiC. Cubic NbC was present in some areas and hexagonal ternary phase  $\text{Nb}_5\text{Si}_4\text{C}$  in the other regions. The ternary phase was seen in all the specimens as the first or second layer, followed by tetragonal  $\alpha\text{-Nb}_5\text{Si}_3$  and the ordered hexagonal  $\alpha\text{-Nb}_2\text{C}$ .  $\text{Nb}_5\text{Si}_4\text{C}$  formation is also consistent with the AES depth profiles from this specimen and various other annealed Nb/SiC (poly) and Nb/SiC (0001) specimens showed regions of compositional uniformity that contain Nb, Si, and C. The composition has an average value of approximately 64Nb-20C-16Si (in at.%). Based on the 1300°C section of the ternary phase diagram (Fig. 5.3) [48], the only ternary phase at this temperature is the T (hexagonal D $_{8g}$ ) phase with the stoichiometric formula  $\text{Nb}_5\text{Si}_4\text{C}$ . The carbon concentration in the  $\text{NbC}_x\text{Si}_y$  region in most of the AES profiles is substantially higher than the 11% corresponding to the T phase. One possibility is that at lower temperatures (such as 1000 to 1200°C), the composition of this phase changes substantially or a new ternary phase becomes more stable. Also the AES sensitivity factors employed in atomic concentration calculations may not be accurate for application to these layered compounds. To avoid any misrepresentation, the designation  $\text{NbC}_x\text{Si}_y$  will be used in the following discussions.

Reactions at 1100°C: The extent of reaction of Nb with polycrystalline SiC at 1100°C for 4 hours is shown by the AES profile in Fig. 5.4. This film consists of a layered structure that may be represented by NbC/Nb $_2$ C/ $\text{NbC}_x\text{Si}_y$ /NbC/SiC. The surface compound is likely to be the result of the pick up of carbon from the vacuum environment. The silicon content at the interface is low compared to the 1000°C annealed specimen; this is probably because of the growth of the  $\text{NbC}_x\text{Si}_y$  phase and the associated depletion of Si from the interfacial region. This reaction zone formed between niobium and silicon carbide during heating for four hours at 1100°C was further examined by TEM coupled with electron diffraction and energy dispersive x-ray analysis techniques. Several different areas were analyzed; the discussion, however, will center around the analysis of the region shown in Fig. 5.5. All grains in this region which have been analyzed are numbered for convenient identification. Immediately adjacent to the SiC, two different phases were observed: (1) the ternary hexagonal phase,  $\text{Nb}_5\text{Si}_4\text{C}$  [48,49] and cubic NbC. The ternary phase is characterized

by an extremely fine grain size (less than 100 nm) and as can be seen in Fig. 5.5, is sometimes the major reaction product between niobium and silicon carbide at 1100°C. A higher magnification bright field image of grain 1, and corresponding convergent beam electron diffraction pattern consistent with the ternary phase in a  $[1\bar{2}10]$  orientation are shown in Figs. 5.6(a) and (b), respectively. An energy dispersive x-ray spectrum taken from this grain is shown in Fig. 5.6(c). It should be noted that detection of elements with an atomic number below 11 was not possible. In another area along the interface, the phase immediately adjacent to the substrate was identified by convergent beam electron diffraction as cubic NbC. A bright field micrograph of this second region of the interface is shown in Fig. 5.7(a). Note that both grains I and II were identified as NbC. A convergent beam electron diffraction pattern from grain II which is consistent with NbC in a  $[001]$  orientation is shown in Fig. 5.7(b). The corresponding energy dispersive x-ray spectrum is shown in Fig. 5.7(c). Note the extremely small peak for silicon in comparison with that from the ternary phase in Fig. 5.6(c).

Returning to Fig. 5.6(a), the second reaction product after the ternary phase was found to be the tetragonal phase  $\alpha\text{-Nb}_5\text{Si}_3$ . The variant of  $\text{Nb}_5\text{Si}_3$  observed is reported to be stable at temperatures below 1650°C [50]. In Fig. 5.6(a), grain 2 was identified as  $\alpha\text{-Nb}_5\text{Si}_3$ . A convergent beam electron diffraction pattern from grain 2 consistent with  $\alpha\text{-Nb}_5\text{Si}_3$  in a  $[110]$  orientation is shown in Fig. 5.8(a). The corresponding energy dispersive x-ray spectrum is given in Fig. 5.8(b).

Next to  $\alpha\text{-Nb}_5\text{Si}_3$ , grain 3 was identified as  $\text{Nb}_2\text{C}$  with a hexagonal structure. According to a recent compilation of phase diagrams [51],  $\text{Nb}_2\text{C}$  exists in two forms. Below 1350°C,  $\alpha\text{-Nb}_2\text{C}$  with an orthorhombic structure is reportedly found whereas above 1350°C,  $\beta\text{-Nb}_2\text{C}$  with a disordered hexagonal structure supposedly prevails. Birla and Hoch [52] also observed this transformation from an orthorhombic to a hexagonal structure in  $\text{Nb}_2\text{C}$ . However, in their study of a Nb-0.82 at.%C-2.2 at.%Si alloy, these authors observed a transformation temperature of approximately 1200°C. In addition to the  $\alpha$  and  $\beta$  forms of  $\text{Nb}_2\text{C}$ , Terao [53] reports that like  $\text{Mo}_2\text{C}$  [54], an ordered hexagonal form of  $\text{Nb}_2\text{C}$  also exists. The structure is identical to that of  $\epsilon\text{-Fe}_2\text{N}$  and is related to the disordered hexagonal  $\text{Nb}_2\text{C}$  in the following manner:  $a(\text{ordered}) = \sqrt{3}a(\text{disordered})$  and  $c(\text{ordered}) = c(\text{disordered})$ . A schematic illustration of the structure is given in Fig. 5.9. In attempting to determine if grain 3 has the ordered or disordered structure, diffraction patterns taken in different orientations were indexed according to both structures and then atom position information was used to determine if the reflections present are allowed for each structure. A convergent beam electron diffraction pattern from grain 3 in an  $[0001]$  orientation is shown in Fig. 5.10. The pattern has been indexed according to the disordered structure. The six diffraction spots

nearest the center spot all correspond to a lattice spacing of 0.271 nm. In the disordered structure this corresponds to the spacing of the  $(\bar{1}100)$ ,  $(\bar{1}010)$  and  $(0\bar{1}10)$  planes. In the ordered structure, however, this corresponds to the spacing of the  $(\bar{2}110)$ ,  $(\bar{1}120)$  and  $(1\bar{2}10)$  planes. Diffraction spots from the  $(\bar{1}100)$ ,  $(\bar{1}010)$  and  $(0\bar{1}10)$  planes should still be visible but their spacing in the ordered structure is 0.469 nm and thus should lie inside the array of 6 spots corresponding to  $d = 0.271$  nm. Since spots corresponding to  $d=0.469$  nm were not observed, it is tempting to conclude that the structure of  $\text{Nb}_2\text{C}$  is disordered. However, the intensity of these superlattice spots may be sufficiently low that they are impossible to see in a convergent beam electron diffraction pattern. In addition to grain 3, grains 3(a) and 3(b) were also identified as  $\text{Nb}_2\text{C}$ . Selected area diffraction patterns taken from grain 3(b), and grains 4 and 5 in Fig. 5.5 are shown in Fig. 5.11. They are consistent with ordered  $\text{Nb}_2\text{C}$  (in a  $[1\bar{2}1\bar{3}]$  direction) [53], cubic  $\text{NbO}$  (in a  $[011]$  direction) and  $\text{Nb}$  (in a  $[111]$  direction) respectively. A complete listing of all phases identified by electron diffraction is given in Table 5-1. To summarize, the typical reaction layer sequence in the examined area is  $\text{SiC}/\text{Nb}_5\text{Si}_4\text{C}/\text{Nb}_5\text{Si}_3/\text{Nb}_2\text{C}/\text{NbO}/\text{Nb}$ . However, in one area of the specimen, the first reaction layer was  $\text{NbC}$  rather than  $\text{Nb}_5\text{Si}_4\text{C}$ .

The requirement of maintaining local thermodynamic equilibrium requires an interfacial phase between  $\text{SiC}$  and  $\text{Nb}_5\text{Si}_4\text{C}$ . Such a phase could be (a)  $\text{NbC}$  or (b) an extraneous one. The  $\text{NbC}$  phase was detected in some locations and no extraneous phases were observed in any of the examined areas. The situation where there was no interfacial  $\text{NbC}$  phase observed may be explained by considering (a) an extremely thin layer of  $\text{NbC}$  was present, but undetected by TEM, or (b) the formation and growth of  $\text{Nb}_5\text{Si}_4\text{C}$  phase in equilibrium with an intermediate phase, such as  $\text{SiO}_2$ . Such an  $\text{SiO}_2$  phase may have its origin from a native oxide on the starting  $\text{SiC}$  material or from oxide impurities present in  $\text{SiC}$ . In order to evaluate the thermodynamic feasibility of such an  $\text{SiO}_2$  phase, a quaternary  $\text{Nb-Si-C-O}$  phase diagram was calculated from available thermodynamic data [55,56]. A minimum (most negative) free energy of formation for the ternary compound  $\text{Nb}_5\text{Si}_4\text{C}$  of -582 kJ/mole was estimated (Table 5-2) assuming that the equilibrium between  $\text{NbSi}_2$  and  $\text{SiC}$  observed experimentally at  $1300^\circ\text{C}$  [16] also exists at  $1100^\circ\text{C}$ . The observed reaction layer sequence is in agreement with the calculated quaternary phase diagram.

Annealing for longer times at  $1100^\circ\text{C}$  increased the thickness of the ternary phase, as exemplified in Fig. 5.12 for the  $\text{Nb/SiC}$  specimen annealed for 12 hours.

Reactions at 1200 to 1300°C: At temperatures of annealing higher than 1100°C, the reaction is completed in relatively short times. An AES spectrum from the surface of a specimen annealed at 1200°C for 2 h (Fig. 5.13a) reveals that the elements Nb, O, Si, and C (in its hydrocarbon form) are at the surface. Silicon migrated to the surface by diffusing through the entire film, an observation that is also demonstrated by the AES depth profile of the same specimen in Fig. 5.13b. The carbon Auger peak shapes and positions (not shown) indicate that the surface carbon (sputtering time=0) is hydrocarbon, the carbon in the film is similar to that of a metal carbide (e.g.,  $\text{NbC}_x$ ), and is different from that of the SiC (corresponding to sputter time of 170 min). The silicon peak shapes indicate that surface silicon is present in the form of its oxide, silicon within the film is present in the form of a silicide or elemental silicon, and is different from that of the substrate SiC. The AES profile of this 2 h, 1200°C annealed specimen is consistent with a layered structure represented by  $\text{NbC}/\text{Nb}_2\text{C}/\text{NbC}_x\text{Si}_y/\text{NbC}/\text{SiC}$ .

The reaction between Nb and SiC at 1300°C for 2 hours is shown in the AES profile, Fig. 5.14. The film has C-rich NbC region at the surface followed by a shallow region of a possibly ternary phase adjacent to a C-rich NbC phase that is next to the SiC substrate. This observation suggests that a substantial amount of carbon from the annealing environment was absorbed at the metal surface, thereby forming the C-rich NbC phase through much of the film. Also the formation of a ternary phase such as  $\text{Nb}_5\text{Si}_4\text{C}$ , from the reaction of NbC with SiC, is thermodynamically unfavorable.

Reactions of Nb with Single Crystal SiC: Thin film specimens deposited on single crystal (SiC) substrates exhibited depth resolution (seen in the AES profiles) that was superior to the films deposited on polycrystalline SiC substrates. The improvement is readily seen in the as-deposited condition but is dominant in the annealed specimens. This is exemplified by the AES profile shown in Fig. 5.15 for the single crystal substrate and may be compared with Fig. 5.4 of the identically treated polycrystalline SiC substrate. In this case, the  $\text{NbC}_x$  layer forming within 4 h at 1100°C does not increase significantly in thickness upon further annealing, indicating the reaction is nearly complete. The surface has a layer of  $\text{NbO}_x$  mixed with  $\text{NbC}_x$  followed by layers of  $\text{NbC}_x$ ,  $\text{NbC}_x\text{Si}_y$ , and  $\text{NbC}_x$  all on top of the SiC (0001) substrate.

The reaction rate as a function of time was studied for selected temperatures and times using AES depth profiles from Nb/SiC specimens. For example, at 900°C the overall reaction zone thickness of  $\text{NbC}_x + \text{NbC}_x\text{Si}_y$  increased from 0.47  $\mu\text{m}$  (corresponding to 4 h annealing) to 0.65  $\mu\text{m}$  after 8 h annealing. In particular, the thickness of the  $\text{NbC}_x\text{Si}_y$  layer increased, whereas the  $\text{NbC}_x$  layer

thickness remained unchanged during this period. Similar results are seen in Nb reactions with single crystal SiC substrates, as exemplified by the reaction at 900°C (Fig. 5.16).

Standard free energies of formation of various known binary compounds of Nb, C, and Si suggest that Nb<sub>5</sub>Si<sub>3</sub> is the most stable reaction product over the entire temperature range of interest. The AES and TEM characterization results show that a ternary NbC<sub>x</sub>Si<sub>y</sub> is forming at the expense of several of the other products. As will be discussed later, in the Ta/SiC system, a similar compound of TaC<sub>x</sub>Si<sub>y</sub> forms readily at low temperatures and becomes the most dominant phase in specimens annealed at 1200°C for 4 h.

**Summary of Thin Film Nb/SiC Reactions:** The AES and TEM characterizations described above have led to an improved understanding of the reaction sequence between Nb and SiC. TEM studies indicated the presence of NbC in regions adjacent to SiC. The NbC<sub>x</sub>Si<sub>y</sub> formation identified in the AES profiles is preceded by Nb<sub>2</sub>C formation in most instances. Once this phase forms and grows to a certain thickness, it becomes self limiting, possibly because of the build-up of Si at the Nb<sub>2</sub>C/SiC interface and associated formation of the NbC<sub>x</sub>Si<sub>y</sub> phase. The AES profiles also indicate that primarily the thickness of the NbC<sub>x</sub>Si<sub>y</sub> region increases with continuing reaction (time or temperature). Thus the reaction appears to take a path Nb-Nb<sub>2</sub>C-NbC<sub>x</sub>Si<sub>y</sub>-NbC-SiC. The portion of the path Nb<sub>2</sub>C-NbC<sub>x</sub>Si<sub>y</sub>, which is not obvious in the ternary phase diagram section at 1300°C, may be understood if there is a thin region of NbC or Nb<sub>5</sub>Si<sub>3</sub> between Nb<sub>2</sub>C and NbC<sub>x</sub>Si<sub>y</sub>. The reaction path, in such an event, would be Nb-Nb<sub>2</sub>C-NbC (or Nb<sub>5</sub>Si<sub>3</sub>)-NbC<sub>x</sub>Si<sub>y</sub>-NbC-SiC. In some specimens, the AES profiles indicated NbC-Nb<sub>2</sub>C-NbC<sub>x</sub>Si<sub>y</sub>-NbC-SiC, which suggests surface carburization during annealing.

The thickness of reactions zones, as measured in the AES profiles, may also be utilized in determining the rates of reactions; also, the activation energy for the reaction may be determined through an Arrhenius plot. Such a determination indicates that the activation energy for NbC<sub>x</sub>Si<sub>y</sub> formation is 20.0 kcal/mole. Similar measurements obtained for NbC<sub>x</sub> growth in Nb/SiC indicate an activation energy of 11.6 kcal/mole. Even though the limiting step in these reactions could not be identified, these relatively small activation energies indicate the ease of formation of NbC<sub>x</sub> and NbC<sub>x</sub>Si<sub>y</sub>.

**5.1.2 Nb/SiC Bulk Diffusion Couples:** Sequential annealing was conducted on Nb/SiC bulk diffusion couples at 1200°C for 6, 18, 32, and 48 h; cross-sectional views of the reaction zones are shown in

Figs. 5.17(a), (b), (c), and (d). Two layered reaction products, as indicated by 1 and 2 in Fig. 5.17(a), were formed in the Nb/SiC reaction zone. The thicknesses of the two layers were more or less uniform across the interface. Layer 1, formed on the SiC side, was found to be thinner than layer 2 which was formed on the Nb side. In addition, a heterogeneously nucleated third phase (phase 3) was noted attached to the reaction front of layer 2.

The thicknesses ( $x$ ) of both layers 1 and 2 increased as a function of reaction annealing time ( $t$ ) and exhibited a parabolic relationship ( $x^2 = kt$ , where  $k$  is a reaction rate constant). Fig. 5.18 includes plots of  $x$  vs.  $t^{0.5}$  and shows a linear relationship for both layers 1 and 2, from which the reaction rate constants of  $6.7 \times 10^{-13}$  and  $5.3 \times 10^{-12}$  cm<sup>2</sup>/sec, respectively, were deduced. It appears that the growth rate for layer 1 is slower than that for layer 2. In contrast, the sizes of the heterogeneously nucleated phase 3 could not be directly correlated to annealing time. Nevertheless, it seems that the number of nucleating sites of phase 3 increases with annealing time. Since phase 3 was not connected to the Nb/SiC original joining interface, but rather was attached to the migrating reaction front of layer 2, it is believed that phase 3 was nucleated at a later stage of the Nb/SiC reactions.

According to both AES and WDS x-ray analyses, the chemistry of reaction products 1 and 3 were similar; both phases were relatively rich in C and Nb, but poor in Si, compared to reaction product 2. Based on these analyses and earlier research on the Nb/SiC system, the phases 1 to 3 were determined to be NbC<sub>x</sub>, NbSi<sub>y</sub>C<sub>z</sub>, and NbC<sub>x</sub>, respectively. These observations suggest that the sequence of reaction products in the 1200°C heated sample is SiC/NbC<sub>x</sub>(layer 1)/NbSi<sub>x</sub>C<sub>y</sub>(layer 2)/NbC<sub>x</sub>(phase 3)/Nb. No unreacted C was observed in the reaction zone.

The mechanism regarding the heterogeneous nucleation of NbC<sub>x</sub> is not clearly understood. It is likely to be a result of localized outward diffusion of C atoms, through interstitial sites, from layer 2 toward Nb. When the local C concentration reaches a certain supersaturation level, the NbC<sub>x</sub> phase starts to nucleate and grow. This is supported by the observation of an increase of the number of NbC<sub>x</sub> precipitates as a function of time. Also, based on an isothermal section (at 1300°C) of a Nb-Si-C ternary phase diagram [48], the Gibbs thermodynamic phase rule requires the presence of NbC<sub>x</sub> at the Nb/NbSi<sub>x</sub>C<sub>y</sub> interface. Hence, it is possible that there exists a thin but unresolved NbC<sub>x</sub> layer all along the interface, which piles up occasionally as observed. The reason why NbC<sub>x</sub> phase nucleates homogeneously at the SiC reaction front is attributable to the existence of a uniformly distributed high concentration of C from dissociated SiC.

## 5.2 Nb/Al<sub>2</sub>O<sub>3</sub> System

Interfacial reactions occurring at the interfaces of Nb films deposited on Al<sub>2</sub>O<sub>3</sub> substrates were evaluated by thermal annealing followed by AES depth profiling. There was little or no evidence of reactions in specimens annealed for up to 4 h and 1100°C (Fig. 5.19(a)). Al<sub>2</sub>O<sub>3</sub> is thermodynamically more stable than NbO, which has the lowest free energy of formation per gram mole of oxygen than any other oxide of niobium. Thus no reaction would be expected between Nb and Al<sub>2</sub>O<sub>3</sub>. These results are also in agreement with the recent high resolution electron microscopy work by Kuwabara et. al. [57], in which the Nb/Al<sub>2</sub>O<sub>3</sub> system equilibrated for 40 minutes at 1450°C exhibited atomically flat interfaces with no evidence of interfacial compounds.

The absence of a reaction between Nb and Al<sub>2</sub>O<sub>3</sub> suggests that Al<sub>2</sub>O<sub>3</sub> may be a promising diffusion barrier between Nb and SiC. A three layer system such as Nb/Al<sub>2</sub>O<sub>3</sub>/SiC, however, would also require that there be little or no reaction between Al<sub>2</sub>O<sub>3</sub> and SiC. Calculated free energies of possible reactions between these compounds suggest that compounds such as Al<sub>4</sub>C<sub>3</sub>, SiO<sub>2</sub> or 3Al<sub>2</sub>O<sub>3</sub>·2SiO<sub>2</sub> are unlikely to form, since the free energies of these reactions are all positive and large in value.

## 5.3 Nb/Al<sub>2</sub>O<sub>3</sub>/SiC System

AES profiles were obtained from Nb/Al<sub>2</sub>O<sub>3</sub>/SiC specimens containing 100, 200 and 500 nm thicknesses of interfacial Al<sub>2</sub>O<sub>3</sub> layers. Figs. 5.19(b) and (c), and 5.20 show the profiles for specimens that were vacuum annealed for 2 h at 1200°C. The niobium layer remained mostly unreacted in all cases, as indicated by the minimal build-up of silicon in the Nb film. In all instances both carbon and oxygen are seen in the films; this is likely to be a result of contamination occurring in the vacuum annealing system. Similar artifacts were observed in a number of specimens in the past. The reduction in the extent of interfacial reaction becomes more evident from a comparison of these profiles with those of Nb/SiC films in the as-deposited condition and after annealing for 2 h at 1200°C. Fig. 5.21 also includes a Nb/SiC film for comparison. In the absence of an Al<sub>2</sub>O<sub>3</sub> diffusion barrier, the reaction of Nb with SiC results in the formation of a sequence of reaction products, illustrated by Nb/Nb<sub>2</sub>C/Nb<sub>5</sub>Si<sub>4</sub>C/NbC/SiC.

Several attempts were made to minimize the contamination occurring from the vacuum system during annealing at the elevated temperatures. These included improving the vacuum integrity of



the annealing system and placing a diffusion barrier layer at the surface of the thin film specimen. A 20 nm  $\text{Al}_2\text{O}_3$  cap layer applied to various specimens to achieve a thin film structure represented by  $\text{Al}_2\text{O}_3/\text{Nb}/\text{Al}_2\text{O}_3/\text{SiC}$  was found to be quite effective. AES results from a capped specimen which was subsequently annealed at  $1200^\circ\text{C}$  for 2 hours is shown in Fig. 5.22. It is seen that both the carbon and oxygen levels in the Nb film are lower compared to the uncapped specimens. It is also noteworthy, in this film with a 100 nm  $\text{Al}_2\text{O}_3$  diffusion barrier layer, that the reaction of Nb with SiC and the associated diffusion of Si into the Nb film is also lowered. These results indicate that a thin 100 nm  $\text{Al}_2\text{O}_3$  diffusion barrier layer is effective in minimizing the interfacial reaction in the Nb/SiC system.

#### 5.4 Ta/SiC System

The reactions between Ta and SiC are, as anticipated, found to be similar to those between Nb and SiC. An example of AES data obtained upon annealing a Ta/SiC (0001) specimen at  $1100^\circ\text{C}$  for 4 h is shown in Fig. 5.23. Formation of  $\text{TaC}_x$ ,  $\text{TaC}_x\text{Si}_y$ , and a depleted Si region above the substrate, in a manner similar to Nb/SiC, is noted in this profile. Upon annealing the Ta/SiC (0001) specimen at  $1200^\circ\text{C}$  for 2 h (Fig. 5.24), a Ta-C-Si region formed at about 35 minutes of sputter time, which has different composition than the  $\text{TaC}_x\text{Si}_y$  identified at about 50 minutes of sputter time. This portion of the profile may be explained as either a result of inhomogeneity of phase distributions in-plane, or because of the formation of a separate layer of another ternary  $\text{TaC}_m\text{Si}_n$  phase. Further work utilizing TEM characterization is needed to elucidate fully these reactions. As with Nb/SiC specimens, the chemical state of carbon in the reacted film is indicated to be similar to a carbide. Upon longer time (4 h) annealing at  $1200^\circ\text{C}$ , the reaction is completed (Fig. 5.25) and a relatively uniform  $\text{TaC}_x\text{Si}_y$  phase is formed.

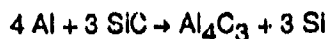
#### 5.5 Ta/ $\text{Al}_2\text{O}_3$ System

Tantalum did not react with  $\text{Al}_2\text{O}_3$  in anneals up to 4 h at  $1200^\circ\text{C}$ . An AES profile from one such specimen (Fig. 5.26) shows little or no oxygen within the tantalum film indicating little or no reaction with the  $\text{Al}_2\text{O}_3$  substrate. An interfacial layer of  $\text{Al}_2\text{O}_3$  applied between Ta and SiC, would thus appear to be a promising diffusion barrier.

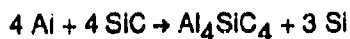
## 5.6 Al/SiC System

Aluminum is the most used light metal in aerospace structural applications. SiC particulate or whisker reinforcement is gaining prominence because of its low density, high strength, high modulus, and availability. For these reasons, Al/SiC metal matrix composites have been the subject of many recent investigations. Many of these composites are produced by the powder route, which involves blending of metal powders with the appropriate amount of reinforcing particulate followed by hot pressing consolidation. Recently developed technologies [58,59] have enabled the incorporation of the reinforcements into the melt, thereby permitting casting of the resulting composite in a conventional manner. The reinforcing particles readily react with the molten aluminum, however, resulting in their degradation.

The major reaction between Al and SiC [60,61] is given below:



The formation of  $\text{Al}_4\text{C}_3$  involves not only the consumption of the reinforcement, but it is also susceptible to corrosion and is accompanied by an increase in the Si level of the alloy, thereby modifying the composition of the metal matrix and associated properties. Even though a ternary compound [62,63] may form by the following reaction, there has been no evidence reported of such a phase.



The hypothetical ternary phase diagram of Al-Si-C [64] is shown in Fig. 5.27 and does not indicate any other phases at 500°C.

There are a number of approaches taken to minimize the interfacial reaction between Al and SiC. These include (a) employing diffusion barrier coatings between metal and reinforcement, (b) alloying the metal with solutes that reduce the driving force for interfacial reactions and (c) alloying the metal with elements that preferentially react with SiC and form an interfacial barrier layer thereby reducing the Al-SiC reaction. Candidate solute elements to be alloyed with Al using the latter approach include Zr and Ti. The diffusion barrier approach has been utilized and some proprietary coatings have been developed for the SiC particulate that act as diffusion barriers. These coatings are intended to prevent interfacial reactions during liquid phase sintering or during

stir casting operations. The second approach of alloying with elements that reduce the driving force for reaction has also been examined carefully [17]. Thermodynamic studies indicate that Si levels above 8 at.% in Al are required to stabilize the Al/SiC interface. These results of Lloyd [17] are summarized in Fig. 5.28. Other approaches to minimize the reaction include spray casting which permits rapid solidification and associated low reaction time.

The role of Si in Al in minimizing the interfacial reaction will be further examined. Whereas the above thermodynamic analysis pertains to molten Al, which has 18 at.% or higher solubility for Si, the situation is quite different for solid state reactions. The solid solubility of Si in Al is at a maximum of 1.64 at.% at 577°C and is lower than 0.5 at.% for temperatures below 450°C. This suggests that Si is likely to be very effective in reducing the interfacial reaction and formation of  $\text{Al}_4\text{C}_3$  in the solid state. The experience of Al and Al alloys in microelectronic metallization also suggests that alloying Al with Si has beneficial effects. At temperatures in the 400-450°C range used for the post deposition processing, diffusion of Si occurs from the substrate into the unalloyed Al. The diffusion of Si is lowered when Al is alloyed with approximately 1 wt% Si. Larger amounts of Si are not employed for this application because of the unacceptable lowering in the electrical conductivity of the Al metallization. These observations suggest that either the driving force for diffusion or the enthalpy (or free energy) of solution of Si in Al is a significant factor in controlling the thermal stability of the Al/Si system. There is no known evidence for the formation of  $\text{Al}_4\text{C}_3$  or other carbides in the solid state reactions between Al and SiC.

In view of the above understanding of reactions between Al and Si, and Al and SiC, it would appear to be useful to examine the reactions of Al with Si and SiC in the 400-650°C range. Of particular interest would be to learn the nature and rate of reaction of Al with SiC, with and without Si present in the aluminum. Based on this reasoning, diffusion couple specimens of Al/Si, Al-1 wt.% Si/Si, Al/SiC, and Al-1 wt.% Si/SiC have been selected for investigation. Experiments were conducted on thin film specimens of Al, and Al-1wt%Si deposited on SiC and Si substrates.

The element silicon rapidly diffuses in aluminum. For example, the time taken to diffuse through the entire 1  $\mu\text{m}$  Al film at 450°C is less than 1 second. Assuming a good metallurgical contact between Al and Si (and no oxide at silicon surface), the equilibrium concentration of Si in Al will be dictated by the phase diagram. Differential scanning calorimetry (DSC) is a suitable technique to evaluate these reactions between Al and Si, provided a measurable heat is generated or consumed during the reaction. The DSC data obtained during heating, cooling, and reheating the Al/Si specimen at 40°C/min rate are shown in Fig. 5.29. There was no major reaction seen until ~580°C, at which

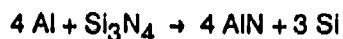
point an endotherm is seen. During cooling from 600°C, a larger and sharper exotherm is seen at 565°C. The same metallurgical reaction is seen in the following reheating curve at 580°C and indicates that the observed endotherm is likely due to eutectic melting. The measured reaction temperature is in reasonable agreement with the eutectic temperature of 577°C of the Al-Si system. Although the DSC study provided direct information on eutectic melting, the measurements were not sensitive enough to study the interdiffusion between Al and Si. AES was instrumental for this purpose. A number of Al/Si and Al/SiC specimens were vacuum annealed for selected times in the 400 to 600°C range (Table 4-3) and several examined by AES. The AES depth profile of the Al/Si specimen in the as-deposited condition is shown in Fig. 5.30 and may be compared to that annealed for 2 h at 600°C (shown in Fig. 5.31). A substantial amount of interdiffusion of Al and Si is evidenced in the profile after 600°C annealing. In contrast, the Al/SiC specimen showed (Figs. 5.32 and 5.33) little or no interfacial reaction upon vacuum annealing for 2 h at 600°C. Also, there was no indication of any  $\text{Al}_4\text{C}_3$  layer formation at the interface. AES profiles from the Al-1wt%Si/SiC specimens in the as-deposited condition and after annealing for 1 h at 600°C are shown in Figs. 5.34 and 5.35. Based upon these data and DSC studies performed on similar specimens, it is apparent there was no significant interfacial reaction in the specimen heated at 600°C. It is possible that fine precipitates of  $\text{Al}_4\text{C}_3$  may be present at the interface, which may be observable using a transmission electron microscope.

A simple calculation of free energy of formation of  $\text{Al}_4\text{C}_3$  from Al and SiC at 600°C shows that the  $\Delta G$  for the reaction is modestly positive. The experimental results to date have not indicated any  $\text{Al}_4\text{C}_3$  formation, which is in general agreement with the thermodynamic prediction.

## 5.7 Al/Si<sub>3</sub>N<sub>4</sub>

The interdiffusion and reactions between Al and  $\text{Si}_3\text{N}_4$  were studied by AES. An AES profile of a specimen in the as-deposited condition is shown in Fig. 5.36. Several specimens were annealed for 1 to 4 hours in the 400 to 600°C range as shown in Table 4-3. First, the specimen that was annealed for 1 h at 600°C was examined by AES in detail. A survey spectrum (Fig. 5.37) obtained from the surface shows the presence of Al in its oxide form at the surface. A sputter profile could not be obtained from this specimen, because of excessive electron and ion beam charging. It is believed that much of the aluminum from the thin film diffused into the substrate, or the surface oxidized to form  $\text{Al}_2\text{O}_3$ , resulting in a non-conductive surface.

The most likely reaction between Al and  $\text{Si}_3\text{N}_4$  involves the formation of AlN.



The reaction is thermodynamically favorable at 600°C and AlN is expected to form. For this reason it is presumed, for now, that Al diffused into the  $\text{Si}_3\text{N}_4$  substrate and subsequently formed AlN. Additional investigations are underway to understand the interfacial reactions in this system.

## 5.8 Ni/SiC System

There have been few studies [65,66] evaluating interfacial reactions of Ni and its alloys with ceramic reinforcements. A ternary phase diagram of the Ni-Si-C system at 1150°C [49,64] is shown in Fig. 5.38 and it suggests that the major reaction products in the Ni/SiC system are likely to be the various  $\text{NiSi}_x$  compounds. Chemical compatibility between SiC and a nickel aluminide was evaluated in a recent study [21]. Specimens of nickel aluminide, diffusion bonded to SiC fiber and sintered SiC, were annealed in the 700-1100°C range and interfacial reactions examined by optical and electron microscopy. Layered structures were observed in specimens heated above 800°C and based on an electron microprobe study, it was suggested that Ni diffusion from the matrix controls the observed reactions. It was also suggested that simple oxides such as  $\text{Al}_2\text{O}_3$  would be effective diffusion barriers to minimize diffusion of Ni and thus control the reaction. The present study aims to generate a detailed understanding of the interfacial reactions in the Ni/SiC and Ni/ $\text{Si}_3\text{N}_4$  systems.

An examination of the free energies of formation of various Ni-Si and Ni-C compounds (Table 5-2) suggests that  $\text{Ni}_7\text{Si}_{13}$  is a relatively stable compound, and its free energy of formation per gram mole is more negative than for either SiC or  $\text{Si}_3\text{N}_4$ . However, the free energy of reaction,  $\Delta G$ , of Ni with the latter substrates is positive indicating that  $\text{Ni}_7\text{Si}_{13}$  will not form. An examination of the Ni-Si-C ternary phase diagram at 1150°C (Fig. 5.38) suggests that in order for Ni to be in thermodynamic equilibrium with SiC, it would require an intermediate phase, such as  $\text{Nb}_5\text{Si}_3$ . To verify these hypotheses and evaluate interdiffusion and reactions, if any, experiments were conducted on thin film specimens of Ni deposited on SiC and  $\text{Si}_3\text{N}_4$  substrates. As described in the experimental section, Ni was RF sputter deposited to approximately 1  $\mu\text{m}$  film on the substrates. A number of these specimens were vacuum annealed for 1 h at 725°C and 1160°C. Specimens in the as-deposited and annealed conditions were investigated using SEM and AES.

Fig. 5.39 shows the AES depth profile of a 1  $\mu\text{m}$  Ni thin film on SiC in the as-deposited condition. The as-deposited specimens were vacuum annealed at two temperatures, 1160°C (0.8 x melting point of Ni) and at 725°C (-0.5 x melting point of Ni) for 1 h each, and reexamined by AES. Fig. 5.40 shows the AES survey spectrum from the surface of a film annealed at 1160°C for 1 hour. A large amount of carbon was seen at the surface in addition to Ni, O, Si and N. An AES profile (Fig. 5.41) shows that the surface oxygen and carbon (as well as nitrogen) are contaminants in the vacuum system and are readily removed upon sputtering. Si diffused into the entire metal film while carbon diffused over three-quarters of its thickness. These observations are suggestive of a layered structure such as  $\text{NiSi}_x/\text{NiSi}_xC_y/\text{SiC}$ . SEM images (Fig. 5.42) of the 1160°C annealed specimen indicate a highly non-uniform surface. An AES profile of a specimen annealed at 725°C (Fig. 5.43) also shows a layered structure similar to that from the sample annealed at 1160°C, indicating the driving force is similar. Both profiles show the top layer is composed of Ni and Si in an approximate 7:2 ratio and a very low carbon concentration within that region. The overall thickness of the reaction zone in the 725°C annealed specimen, however, is smaller indicating the slower kinetics at the lower temperature.

The second layer, designated  $\text{NiSi}_xC_y$ , in both the profiles contained a relatively high carbon concentration (estimated in the 30 to 40 at.% range) and is unaccounted by the ternary phase diagram. Additional studies of Ni/SiC system involving bulk diffusion couples are presented in section 5.10.

## 5.9 Ni/Si<sub>3</sub>N<sub>4</sub> System

As with the Ni/SiC system, a number of Ni/Si<sub>3</sub>N<sub>4</sub> specimens were prepared and annealed at 725°C and 1160°C (Table 4-3). An AES spectrum obtained from the surface of Ni/Si<sub>3</sub>N<sub>4</sub> specimen heated for 1 h at 1160°C indicated presence of Si, N, C, and O in addition to Ni. The AES profile in Fig. 5.44 shows that Si and N are present throughout the profile. AES data near the interface region is misleading, as the electron beam caused substantial charging at the insulating surface of Si<sub>3</sub>N<sub>4</sub>. The rough topography of this surface, shown in the SEM images in Figs. 5.45 and 5.46, is indicative of substantial reaction and migration at the surface. The region shown in Fig. 5.45 was investigated in detail by scanning Auger microscopy to understand the nature of these reactions. The specimen was sputter cleaned by removing approximately 10 nm from the surface and AES spectra were obtained from localized regions on and off the dendritic structure seen in the bottom

image of Fig. 5.45. The spectra (Fig. 5.47 (top)) show that the smooth regions consist of Ni and Si in an approximately 50:50 concentration. Little or no nitrogen was detected at this location, suggesting that the precipitate-like feature is likely to be  $\text{Ni}_7\text{Si}_{13}$  or some similar  $\text{NiSi}_x$  phase. The AES sensitivity factors appropriate for such a phase are not readily available and hence there is some uncertainty in the composition of this phase as determined by AES. AES spectrum from the dendritic region (Fig. 5.47 (bottom)) showed the presence of W and C, in addition to Ni and Si. Tungsten was completely removed upon sputtering approximately 120 nm, indicating it to be a relatively thin film. The source of tungsten contamination is believed to be the tungsten filament used in the vacuum annealing process. It may be pointed out this is the only specimen surface at which tungsten was observed to date.

These results suggest that extensive surface migration, associated with interfacial reactions, occurs in the  $\text{Ni/Si}_3\text{N}_4$  system. A major reaction product is  $\text{NiSi}_x$ . The AES profile of the specimen annealed at  $1160^\circ\text{C}$  also showed presence of nitrogen through out the film. This is indicative of islands of  $\text{Si}_3\text{N}_4$  present on the examined area or possibly a ternary phase. Further AES and TEM investigations are in progress to better understand these reactions.

#### 5.10 Reactions of Co, Ni and Pt with SiC

The metal/ceramic reactions give rise to layered reaction products consisting of various metal silicides (as matrices) and free unreacted carbon (as precipitates); the unreacted carbon was identified by laser Raman microprobe. No carbide formation (i.e.,  $\text{Ni}_3\text{C}$ ,  $\text{Co}_2\text{C}$ , or  $\text{Co}_3\text{C}$ ) was detected by x-ray diffraction or electron microprobe analysis with wavelength dispersive spectrometry (WDS). The formation of metal-silicides results in interfacial melting at certain temperatures. The carbon precipitates were formed either randomly or periodically in the reaction zones, depending upon the metal system as well as the location with respect to the SiC reaction interface. Detailed metal/ceramic reactions are described in the following subsections.

**5.10.1 Co/SiC reactions at 1100 and 1210°C:** A Co/SiC reaction zone after  $1100^\circ\text{C}$  annealing for 6 h is shown in Fig. 5.48(a). Immediately adjacent to the Co metal is a region relatively free from C precipitation that is designated as carbon precipitation free zone (C-PFZ). A phase boundary separating the unreacted Co and the C-PFZ was observed and is indicated in Fig. 5.48(a). Clustered voids were noted in some sections along this phase boundary. The thickness of the C-PFZ is typically less than  $10\text{ }\mu\text{m}$  and increases with annealing time. Adjacent to the C-PFZ, a

reaction layer with randomly scattered C precipitates was noted. A higher magnification SEM image of this random carbon precipitation zone (R-CPZ) is shown in Fig. 5.48(b). Concentration profiles, determined by electron microprobe analysis, of Co and Si across the reaction zone indicate the formation of Co-rich silicides ( $\text{Co}_2\text{Si}$ ). Compositional discontinuities in the Co and Si concentration profiles at the phase boundary were also observed and, furthermore, diffusion of Si into the unreacted Co was detected.

No apparent melting/solidification was observed in the Co/SiC reaction zone at  $1100^\circ\text{C}$ . Ex-situ fractured Co and SiC reaction interfaces, however, do show signs of interfacial melting. A SEM micrograph from a fractured SiC interface is shown in Fig. 5.49. Granular particles with curved and smooth surface morphologies were observed at the interface. EDS x-ray microanalysis shows the presence of Co and Si from these particulate reaction products. The morphological characteristics of the reaction products suggest a pre-occurrence of interfacial melting and solidification.

Reactions between Co and SiC at  $1210^\circ\text{C}$  are extensive. A Co sample of 2 mm in thickness, as compared to a SiC of 0.87 mm, was consumed completely after a reaction at  $1210^\circ\text{C}$  for 4 h. Massive interfacial melting followed by solidification was observed and is shown in Fig. 5.50(a) and (b), which differ by the stacking sequence of the Co metal and the SiC. Droplet-like reaction zones, as a result of a surface tension effect, were noted. Regardless of the relative position of the metal component with respect to the SiC component during diffusion bonding, the SiC reaction interface shows a concave contour. Moreover, the amount of SiC consumed during the reactions is exactly the same in the two different reaction geometries. The effect of gravity on the interface morphology, and SiC decomposition kinetics, is believed to be negligible. XRD results show that cobalt silicide ( $\text{Co}_2\text{Si}$ ), a solid solution of Si in Co [ $\text{Co}(\text{Si})$ ], and free carbon (C) were all formed in the reaction zone. Cross-sectional optical micrographs, as shown in Fig. 5.51, of the reaction zone show the presence of C-PFZ as well as random carbon precipitation zone (R-CPZ). In the areas remote from the SiC reaction interface, two coexisting phases, featured by the light and gray areas in Fig. 5.51(f), were noted. Electron microprobe analysis indicates that the light phase (as a matrix) is  $\text{Co}(\text{Si})$  while the gray one is  $\text{Co}_2\text{Si}$ . A major portion of the reaction zone is physically separated from the unreacted SiC as a result of a weak Co/SiC interface. No distinguishable C-PFZ was observed in the region close to the Co because of the complete consumption of the Co layer during the metal/ceramic reaction.

**5.10.2. Ni/SiC reactions at 1100 and 1170°C:** The Ni/SiC reactions at  $1100^\circ\text{C}$ , as shown in Fig. 5.52(a), (b) and (c), generate similar patterns to those in the Co/SiC reactions. In addition to the



formation of C-PFZ and R-CPZ, a modulated carbon precipitation zone (M-CPZ) was also generated in the region adjacent to the SiC component. High magnification SEM micrographs of the Ni/SiC reaction zone are shown in Fig. 5.53(a), (b) and (c). It is noted that the M-CPZ, see Fig. 5.53(a), is composed of patches of very fine C precipitates. At locations farther removed from the SiC reaction front, from which the C was decomposed, the C starts to redistribute and exhibit a more random pattern, as shown in Fig. 5.53(b) and (c). Moreover, the C precipitates appear more globular and to increase in size as a function of distance from the SiC reaction front. The thickness of the C-PFZ in the Ni/SiC reaction zone is in the same range as that in the Co/SiC; it also increases with annealing time. The C-PFZ is separated from the Ni component by a phase boundary which is clustered with voids.

Quantitative electron microprobe analysis across the Ni/SiC reaction zone, see Fig. 5.54, indicates that the C-PFZ is composed of  $\text{Ni}_3\text{Si}$ , while the CPZ (which includes M-CPZ and R-CPZ) is primarily  $\text{Ni}_5\text{Si}_2$  phase. An inward diffusion of Si into the Ni was also noted. No obvious compositional discontinuity, however, was observed at the phase boundary; this result is not clearly understood at this time. Thickness measurements of the reaction zone on the Ni and SiC sides show that the reaction zone on the Ni side is thicker than that on the SiC side.

The Ni/SiC reactions at  $1170^\circ\text{C}$  give rise to massive interfacial melting, which is characterized by the formation of a teardrop-shaped reaction zone and porosity as a result of solidification. The Ni sample is 2 mm in thickness, as compared to the SiC sample which is 1 mm, and was consumed completely during the reaction. In the reaction zone, non-planar reaction interfaces as well as microcracks were generated. The generation of microcracks is suggested to be a result of mismatch of the thermal expansion coefficients between the reaction products and SiC. By XRD analyses, see Fig. 5.55,  $\text{Ni}_3\text{Si}$  and C were identified to be present in the reaction zone. Cross-sectional views of the reaction zone show the formation of M-CPZ and R-CPZ, as shown in Fig. 5.56. A C-PFZ was not observed in this case because the Ni component was consumed completely during the reaction.

**5.10.3. Pt/SiC reactions at 900, 1000 and  $1100^\circ\text{C}$ :** The Pt/SiC reactions at 900, 1000 and  $1100^\circ\text{C}$  were found to be very similar to each other. Interfacial melting was observed, as marked by arrows in Fig. 5.57, for all the samples annealed in these temperature regimes. This suggests that either the melting point of the reaction product(s) is lower than the respective annealing temperatures, or that the enthalpy of Pt/Si solid state intermixing is high. XRD analysis of the Pt/SiC reaction zones

shows the formation of  $\text{Pt}_3\text{Si}$ ,  $\text{Pt}_2\text{Si}$ , and a mixture of Pt-silicides upon annealing at temperatures 900, 1000 and 1100 °C, respectively. The XRD spectra are shown in Fig. 5.58 (a), (b) and (c).

Cross-sectional views of the Pt/SiC reaction zones show three distinguishable reaction layers. SEM micrographs of a Pt/SiC reaction zone after 1100 °C annealing are shown in Fig. 5.59. Starting from the Pt reaction interface [Fig. 5.59(a)], a 1st layer containing alternate Pt-silicide/C-decorated Pt-silicide bands [Fig. 5.59(b),(c) and (d)] is followed by a 2nd layer with clustered discrete C bands [Fig. 5.59(e) and (f)], and a 3rd layer consisting of randomly scattered C precipitates in the areas adjacent to the SiC interface [Fig. 5.59(f)]. In the areas adjacent to the Pt component, a large volume of porosity was generated. There is also a microcrack, running parallel to the reaction interface, formed within the 2nd layer.

It is noted in Fig. 5.59 that the frequency of the presence of the discrete C bands, which formed in the 2nd layer, decreases as a function of distance from the Pt reaction interface. As the Pt interface is approached, see Fig. 5.60(a), (b), (c), and (d), clustered discrete C bands disappear and C-decorated granular Pt-silicide layers evolve. The granular microstructure develops as a result of the formation and subsequent grain growth of Pt-silicide. Carbon is found to decorate the microstructure either along grain boundaries or within the grains, presumably on defect sites. The thickness and grain growth phenomena of the granular layers become more prominent at locations farther away from the SiC reaction front. The transition from discrete C layers into C-decorated granular layers was noted and is evident in Fig. 5.60(b) and (c). As the reaction temperature decreases, similar phenomena were also observed, but to a much lesser extent than those at high temperature.

The pre-occurrence of melting/solidification during the Pt/SiC reactions is evidenced by the microstructure in the reaction zone from as-reacted Pt/SiC samples. A typical example is shown in Fig. 5.61 of the microstructural change as a function of distance from a Pt/SiC diffusion couple after reaction at 1000 °C. A dendritic-shaped reaction zone ( $\text{Pt}_2\text{Si}$ ) was noted to be generated in front of a microcrack, which is adjacent to alternating layers of Pt-silicide and C. The dendrites are oriented perpendicular to the reaction interface. In other words, the growth orientation of the dendrites is parallel to the direction of thermal conduction during the cooling of the interfacial melt.

In the area (which corresponds to a 3rd layer in a Pt/SiC diffusion couple) immediately adjacent to the unreacted SiC, clustered granular particles were noted to form on a matrix which has a similar granular microstructure to the SiC. A high magnification backscattered electron image of the 3rd

layer is shown in Fig. 5.62. A brighter contrast was observed from this layer than from the SiC, indicating that the average atomic density of the layer is greater. Inward diffusion of Pt into the 3rd layer was detected by EDS. The smooth surface morphology of those clustered particles suggests that they have undergone melting/solidification. Based on EDS microanalyses, the particles were identified as having a chemistry close to  $\text{Pt}_2\text{Si}$ .

A similar microstructure between the 3rd layer and the unreacted SiC suggests that the phase transition from SiC to Pt-silicides in the 3rd layer is incomplete. Raman microprobe analyses from the 3rd layer, however, indicates the presence of C only. Neither SiC nor Si characteristic peaks were detected.

A list of major reaction products and interfacial phenomena observed from the samples which were diffusion annealed at various temperatures for different times is given in Table 5-3. For all the Co/SiC, Ni/SiC, and Pt/SiC reactions, Raman microprobe analyses indicate that C precipitates exist in a mixed glassy/graphitic state. A series of Raman spectra are shown in Fig. 5.63 (a),(b),(c), and (d), which were obtained from C precipitates, located both in regions close to the SiC and farther away, in the Pt/SiC reaction zone after diffusion annealing at  $1000^\circ\text{C}$ . In the regions close to the SiC reaction interface, the C exists primarily in a glassy state. Graphitization of the C occurs, however, as its location is farther removed from the SiC interface. The formation of glassy carbon is characterized by the presence of a Raman peak at  $1354\text{ cm}^{-1}$ , whereas graphitization of the glassy carbon is indicated by a decrease of the intensity ratio between the  $1354$  and  $1585\text{ cm}^{-1}$  Raman peaks [67].

**5.10.4 Reaction products and interfaces:** Co, Ni and Pt metals are known to react with Si and to form various silicides. According to the present experimental results, these metals also react with SiC ceramics and form various silicides. In addition, free unreacted C is also generated as a result of the metal/ceramic reactions. It is clear that the source of Si atoms originates from a decomposition of the SiC. The decomposition of the SiC therefore provides not only Si but also C. The decomposed Si atoms readily react with the metals to form silicides, whereas no carbide formation was detected. This may be attributed to a lower reaction affinity of the respective metals for carbon than for silicon. Thermochemistry data [68] show that the Gibbs free energies of  $\text{Co}_2\text{C}$  and  $\text{Ni}_3\text{C}$  formation at 1100 and 1200, and  $727^\circ\text{C}$  are +1090 and +880, and +6410 cal/mole, respectively. No data are available for Pt-carbides and  $\text{Co}_3\text{C}$ , or  $\text{Ni}_3\text{C}$  formation at temperatures above  $727^\circ\text{C}$ . The present study indicates that only metal-rich silicide phases were formed during the metal/ceramic reactions between 900 and  $1200^\circ\text{C}$ . The reaction is sluggish at temperatures

below 900°C. However, the temperature at which decomposition of SiC can occur during a metal/SiC reaction has been reported to be as low as 500°C based on interfacial reactions between Ni and Pd thin films, of about 100 nm in thickness, on SiC substrates [39].

Considering the overall reactions between SiC and the metals of interest,  $\text{SiC} + \text{M (Ni, Co, Pt)} \rightarrow \text{M}_x\text{Si}_y + \text{C}$ , a negative Gibbs free energy of the reaction is necessary to assure the formation of metal silicides as well as of C. The decomposition of SiC into Si and C exhibits positive Gibbs free energies at all the temperatures being studied. In addition, the presence of unreacted C precipitates, which appear to be an inert species within these material systems, in the metal silicide matrices requires the formation of interfacial energy. Both the positive Gibbs free energy of the SiC decomposition, and the total interfacial energy required between the C precipitates and metal silicide matrices, are factors that inhibit the metal/ceramic reactions. In order for the reactions to proceed, it is clear that Gibbs free energy of metal silicide formation must be highly negative in order to provide the thermodynamic driving force for the metal/ceramic reactions. Table 5-4 lists calculated Gibbs free energy for the decomposition of SiC at different temperatures. Experimental thermochemistry data for those metal silicides which were formed in the present studies, however, were not available.

According to the present results, two types of interfacial morphologies were observed. Planar interfaces were observed when solid state interdiffusion occurs alone. On the other hand, non-planar interfaces were generated when interfacial melting occurs. The non-planar interfaces show a concave contour with respect to the SiC component. Analogous to the grain growth phenomenon, the presence of a curved grain boundary (interface) is always associated with a net driving force ( $\Delta P$ ) which drives atomic diffusion fluxes from the convex side (positive curvature) toward the concave side (negative curvature). The driving force can be expressed by  $\Delta P = \gamma_l/r_l + \gamma_j/r_j$ , where  $\gamma_{l,j}$  and  $r_{l,j}$  are the interfacial energy and radius of curvature, respectively, of two orthogonal contours (l and j) of an interface. The presence of curved interfaces is expected to affect the interdiffusion rates of the constituents from either side of the concave reaction interface. Based on the interface morphologies observed in the present study, it is suggested that diffusion rates of the metal species (which lie in a positive curvature side) is further assisted by the creation of a non-planar interface.

It has been reported [69] that molten metals (i.e., Ni, Co, Pt, Fe, and Cr) attack SiC ceramic regardless of its high degree of chemical stability. Although no further details on the attack phenomenon and mechanism were given, it is believed that the attack is mediated through the

formation of low melting point eutectic silicides. All of the listed metals are well-known to form various silicides across wide compositional ranges. It is suggested that once the silicide phase forms, which gives rise to interfacial melting and concave interfaces in SiC, the metal/SiC reaction is expedited and propagates until the SiC is consumed.

To understand the rate limiting step for the present metal/ceramic reactions, the thicknesses of the reaction zones on metal and ceramic sides were measured and correlated with the reaction time. When no interfacial melting occurs, it is noted that the thickness of the reaction zone on the SiC side is thinner than that on the metal side. In most cases, a parabolic growth rate law ( $x^2 = kt$ , where  $x$  is the thickness of reaction zone,  $k$  the reaction rate constant, and  $t$  the annealing time) is not obeyed according to the measured thickness of the reaction zone as determined from the SiC side. When interfacial melting occurs, the thickness of the reaction zone on the center of SiC, which shows the greatest thickness due to a concave interfacial morphology, is still much thinner than that of metal counterpart. Based upon these observations, it is suggested that the metal/ceramic reaction is limited by the decomposition of SiC rather than interdiffusion of the constituents. This is further supported by the fact that the diffusion rates of metal and Si constituents in the reaction zone, which exists in a molten (or partially molten) state, are not expected to be slow.

In contrast to the present results, a diffusion limited parabolic growth rate was reported in the SiC/Ni [70] at 800 °C, SiC/Ni alloys [47] at temperatures between 700 and 1150 °C, and SiC/Ni and SiC/Co-1wt%Cu composites [40] at temperatures ranging from 1000 to 1200 °C. It is not clear why there is a discrepancy in the relationship between the thickness of reaction zone and reaction time among the different studies. It is believed that the conflicting results may originate from the surface characteristics (e.g., order and stoichiometry) as well as crystal structure of the SiC being used. For example, the formation of Al carbide ( $Al_4C_3$ ) has been reported in an annealed Al thin film on  $Ar^+$ -ion bombarded single crystalline  $\alpha$ -SiC [71] but not in an Al film on ordered and stoichiometric  $\beta$ -SiC(001) [72] under similar conditions. In view of the fact that interfacial melting was observed in Ni/SiC and Co/SiC systems in the present study, but not in those of previous studies in a similar temperature region, a direct comparison of the data from different studies is difficult.

A thinner reaction zone in the SiC than in the metal suggests that the diffusion distance of metal atoms is shorter than that of Si atoms. This raises an interesting question regarding the predominant diffusing species during high temperature metal/ceramic reactions. It was reported that the Ni atoms are more mobile than the Si atoms during Ni/SiC reactions at 850 °C [38], in which

similar reaction products of  $\text{Ni}_3\text{Si}$ ,  $\text{Ni}_5\text{Si}_2$ ,  $\text{Ni}_2\text{Si}$  and C were generated. Assuming that Ni is at least as mobile as Si at higher temperatures, a comparable or greater reaction zone thickness in the SiC side (as compared to that in the metal side) would be expected providing that SiC is readily decomposed. A shorter diffusion length of Ni atoms suggests that the interaction between metal atoms and SiC at the SiC reaction interface may be a rate limiting step for the metal/ceramic reactions. This may well explain why the thickness of the reaction zone on the SiC side is smaller than that on the metal side.

In all of the three metal/ceramic systems, the silicide phases formed in the reaction zones at various temperatures are metal-rich. No Si-rich silicide phases (e.g.,  $\text{CoSi}_2$ ,  $\text{NiSi}_2$ , and  $\text{PtSi}$ ) as reported in the metallization of Si for contact and/or interconnect applications were detected. The reason why metal-rich silicides, rather than Si-rich silicides, are formed during the M/SiC reactions is primarily attributed to the presence of metal-rich sources, as compared to the Si source (i.e., SiC). In contrast, during metallization of Si in VLSI technology, the amount of the existing metal source is limited as a thin film form. Based on the present results, however, as the location of the reaction zone changes from the metal side toward the SiC side, the relative concentration of Si to metal increases. In the Ni/SiC diffusion couple, layered reaction products of  $\text{Ni}_3\text{Si}$  and  $\text{Ni}_5\text{Si}_2$  were formed from the Ni component toward the SiC component after reaction for 6 hrs at  $1100^\circ\text{C}$ .

**5.10.5 Interfacial melting:** The formation of metal silicides gives rise to interfacial melting during the metal/ceramic reactions in certain temperature ranges. The interfacial melting can be attributed to a combination of the formation of a low melting point silicide phase and a large enthalpy of mixing between the metals and Si. The former contribution may cause massive interfacial melting, while the latter one can only give rise to localized partial melting unless the reaction interface migrates at a fast rate. The contribution from the presence of C is believed to be minimal because of its inert activity in the systems. Considering the cases where overwhelming melting phenomena were observed, the formation of low melting point silicide phases is believed to be a major contributing factor. In the cases where localized melting was observed, a large enthalpy of solid state atomic intermixing may be responsible.

According to binary phase diagrams of Co/Si, Ni/Si and Pt/Si, eutectic reactions exist at various composition ranges. Specifically, the reaction products of  $\text{Co}(\text{Si})+\text{Co}_2\text{Si}$  at Co75-Si25 (at%),  $\text{Ni}_3\text{Si}$  and  $\text{Pt}_3\text{Si}$  have melting points either lower than or comparable to the respective diffusion annealing temperatures in which they were formed. Their formation in the reaction zone may well explain the observed massive interfacial melting. Exceptional cases, nevertheless, were noted in the Co/SiC

and Pt/SiC reactions at 1100 and 1000°C, respectively, in which localized and massive interfacial meltings were noted. In both systems, the melting points of the reaction products, namely Co<sub>2</sub>Si and Pt<sub>2</sub>Si respectively, are about 100°C higher than their respective formation temperatures. From the Pt/Si binary phase diagram, the stoichiometric Pt<sub>2</sub>Si compound melts congruently at 1100°C. Nevertheless its liquidus line decreases drastically, as its composition deviates from stoichiometry, from 1100°C to around 850°C (the melting point of Pt<sub>3</sub>Si). Since the formation of reaction products during a solid state reaction is facilitated through atomic interdiffusion, the effects of off-stoichiometry of the reaction product, and formation of a low melting point metastable phase on interfacial melting, cannot be ignored. A reasonable explanation for the massive interfacial melting observed in the Pt/SiC at 1000°C is that the Pt<sub>2</sub>Si is not the first phase formed during the reaction. It is believed that Pt<sub>3</sub>Si is the first phase formed during the Pt/SiC reaction at 1000°C. This hypothesis is supported by the observation that Pt<sub>3</sub>Si forms first at 900°C. The Pt<sub>3</sub>Si phase has a much lower melting point, 850°C, than the annealing temperature of 1000°C, which in turn gives rise to massive interfacial melting. The Pt<sub>2</sub>Si phase is formed through further atomic interdiffusion. In the molten state, atomic diffusion rates of the constituents are expected to be high. In addition, the large enthalpy of Pt<sub>2</sub>Si formation,  $\Delta H = -44$  kcal/mole [73], is also expected to contribute to the interfacial melting. Assuming that the heat capacity ( $C_p$ ) of Pt<sub>2</sub>Si is similar to that of Ni<sub>2</sub>Si,  $C_p = 20$  cal/deg-mole [68], the temperature rise at the reaction interface resulting from Pt<sub>2</sub>Si formation is on the order of  $10^3$  degree K, which alone is sufficient to cause interfacial melting during the Pt/SiC reactions at 1000°C.

On the other hand, the minor localized interfacial melting in the Co/SiC at 1100°C is believed to be primarily attributed to a large enthalpy of Co<sub>2</sub>Si formation. The standard enthalpy of Co<sub>2</sub>Si formation has been reported [68] to be about 28 kcal/mole. Assuming that  $C_p$  of Co<sub>2</sub>Si is similar to that of Ni<sub>2</sub>Si, the temperature rise at the reaction interface resulting from the formation of Co<sub>2</sub>Si is in the range of 700 K which is sufficient to cause local interfacial melting. Moreover, it was recently reported that self-propagating, explosive, silicide formation in a room temperature environment is feasible in certain metal/Si multilayer structures, e.g., Rh/ $\alpha$ -Si [74], Ni/ $\alpha$ -Si [75], and Zr/ $\alpha$ -Si [76] multilayers. The thermal driving force for such an explosive reaction originates from a sufficient amount of enthalpy from the silicide formation and, to a lesser extent, the crystallization of  $\alpha$ -Si. The amount of enthalpy of silicide formation may be large enough to result in melting of Ni<sub>2</sub>Si ( $T_{m.p.} = 1565$  K) at room temperature [75].

**5.10.6 Carbon precipitation behavior:** An intriguing phenomenon during the metal/ceramic reactions is that of the carbon precipitation behavior. In the Co/SiC and Ni/SiC systems, a C-PFZ is noted in

the areas immediately adjacent to the metal component. Following the C-PFZ, a R-CPZ and M-CPZ were observed in the Ni/SiC samples, while only a R-CPZ was observed in the Co/SiC samples. In the Pt/SiC samples, both M-CPZ and R-CPZ were generated but no C-PFZ was formed. Although both M-CPZ and R-CPZ were generated in the Pt/SiC and Ni/SiC diffusion couples, there is a major difference in the locations of the M-CPZ and R-CPZ. In the Ni/SiC, the M-CPZ is formed adjacent to the SiC component. In the Pt/SiC, on the other hand, the M-CPZ is formed adjacent to the metal component. Furthermore, the microstructure of C precipitation layer is different between Pt/SiC and Ni/SiC.

The reaction patterns formed during the metal/ceramic reactions can be summarized as follows: Co/SiC  $\rightarrow$  Co/C-PFZ/R-CPZ/SiC; Ni/SiC  $\rightarrow$  Ni/C-PFZ/R-CPZ/M-CPZ/SiC; Pt/SiC  $\rightarrow$  Pt/M-CPZ/R-CPZ/SiC. The reason why the C precipitation behavior varies as a function of metal system, and position from the reaction interface is not clearly understood. It may involve several competing kinetic processes, e.g., overall nucleation and growth rate of silicide phases, rejection rate of C from the reaction front (which is also influenced by its solid solubility in various silicides), growth (or condensation) rate of C clusters, and diffusion rates of metals and Si. All these kinetic processes are known to be position and concentration dependent.

The structure of C precipitates also varies as a function of their location from the SiC reaction interface. Based on Raman spectroscopy, C precipitates exist in a mixed glassy/graphitic state. The position-dependent structural change of C is believed to result from the time sequence of their formation. Consider that C atoms originate from the decomposition of SiC. In the areas adjacent to SiC interface, C is freshly decomposed and, therefore, exhibits primarily a disordered state. For those C precipitates which form in areas farther from SiC reaction interface, they are decomposed earlier and therefore experience a longer heat treatment (i.e., a pyrolytic process). As a result, the C precipitates experience a longer structural rearrangement period, and tend to be more ordered.

The duration of thermal exposure of C precipitates also affects their microstructure as well as their distribution pattern, as a function of distance from the SiC interface. Experimentally, the microstructure of the C precipitates changes from fine-sized clusters in the areas close to the SiC interface into randomly-scattered, larger particulates in remote areas. The reason why discrete C layers form in the areas close to the SiC reaction interface, whereas C-decorated granular silicide layers form in remote areas, in the Pt/SiC reaction zone is attributable to the redistribution of C in the Pt-silicide matrix upon prolonged thermal annealing in the remote areas. The distribution pattern of carbon precipitates in the areas adjacent to the SiC reaction front may represent the



decomposition behavior of SiC, since thermal relaxation and diffusion (rejection) of decomposed C is not significant.

**5.10.7 Summary of Co, Ni and Pt Reactions with SiC:** The reactions of the metals Co, Ni and Pt with ceramic SiC were studied in the temperature range 800 to 1200°C. The metal/ceramic reactions generate metal-silicides and C as reaction products. The silicides are primarily metal-rich instead of silicon-rich. The C, precipitated out in metal-silicide matrices, is found to exist in an unreacted form rather than a carbide form. The formation of metal-rich silicides gives rise to either massive or local interfacial melting at certain temperatures. Either planar or non-planar reaction interfaces are generated, depending upon the characteristics of metal/ceramic reactions. The thickness of the reaction zone on the metal side is always greater than that on the SiC side; a parabolic relationship between the thickness of the SiC reaction zone and annealing time is not observed. The kinetics of the metal/ceramic reactions are believed to be controlled by the decomposition of SiC, rather than by the interdiffusion of Si or metals. The patterns of the reaction products formed in the metal/ceramic reaction zones are different depending upon the specific metal system and their location from the reaction interface. A C-PFZ is generated in the Ni/SiC and Co/SiC, but not in the Pt/SiC. Although a CPZ is formed in all the Co/SiC, Ni/SiC, and Pt/SiC systems, both M-CPZ and R-CPZ are noted in the Ni/SiC and Pt/SiC systems. In contrast, only a R-CPZ is formed in the Co/SiC. The structure of the C precipitates varies as a function of their distance from the SiC reaction interface. The C existing close to the SiC interface is primarily in a glassy state. With increasing distance from the SiC interface, the C particulate size increases and forms a more graphitic structure. The structural evolution of the C precipitates is attributed to the duration of thermal exposure after they are dissociated from the SiC.

## **5.11 Reactions of stainless Steel with SiC**

Solid state reactions of SiC with stainless steel produced layered structures of reaction zones. The nature of those solid state reaction products and the accompanying decomposition of SiC are discussed in the following sub-sections.

**5.11.1 Solid State Reactions of SS/SiC:** The 1st and 2nd layers consisted of C precipitates. Massive interfacial melting was observed in the SS/SiC samples annealed at 1125°C for 8 h. Fig. 5.64 shows a typical cross-sectional view SEM micrograph of SS/SiC reaction pattern. The SiC reaction interface is noted to exhibit non-planar characteristics. Some areas of the reaction zone broke loose,

as a result of weak bonding caused by melting/solidification. during sample preparation for characterization; horizontal cracks caused by melting/solidification shrinkage were found in the SS component. In the reaction zone, four reaction layers are clearly distinguishable and indicated in Fig. 5.65. Starting from the unreacted SiC component, the four reaction layers can be characterized as: (1) modulated precipitation zone, (2) random precipitation zone, (3) multiple phase mixture zone, and (4) grain boundary precipitation zone. Fig. 5.66(a), (b), and (c) show high magnification SEM micrographs on the details of the microstructure in reaction zones 1, 2, and 3. It is found that multiple phases, as revealed by the regions with different contrast, start to appear in reaction zone 2.

X-ray analysis from the bulk SS/SiC reaction zone, in a powder form, indicated the presence of  $\gamma$ -iron, (Fe,C), which is the only phase detected from the as-received SS, and  $\text{Cr}_{23}\text{C}_6$ . In addition, a few unidentified minor peaks were also detected. EDS x-ray microanalysis indicated that the precipitates in reaction zones 1 and 2 were primarily carbon, while the metal matrices were rich in Ni and Fe but poor in Cr. In zone 3, four alloy phases, as revealed by backscattered electron micrographs, with varying concentrations of Ni, Cr, Fe, and Si were identified. These alloy phases are believed to contribute to those aforementioned unidentified x-ray peaks from the reaction products. One of these four alloy phases contained primarily Cr and Fe (with a small amount of Ni but no Si), while the rest of the three phases contained at least 20 at% Si. It is believed that these three phases are primarily metal silicides. Because of the complexity of these metal reaction products in the system, for convenience, the metal reaction products formed in the reaction zone will be represented by  $(\text{Ni,Fe})_x\text{Cr}_y\text{Si}_z$  throughout this discussion. In zone 4, chromium carbide(s) precipitates were found to form along the grain boundaries of stainless steel.

Some precipitates in the reaction zone 2 were found to be Cr-rich. On the other hand, the amount of Fe and Ni contained in all the precipitates was fairly small which failed to substantiate the formation of  $\text{Fe}_3\text{C}$  or  $\text{Ni}_3\text{C}$ . To gain a better statistical ground for the determination of C precipitates, area x-ray mapping was performed on the C precipitates which were located progressively away from the SiC reaction front and shown in Figs. 5.67 through 5.70. It is clear that none of the precipitates can be attributed to either  $\text{Ni}_3\text{C}$  or  $\text{Fe}_3\text{C}$ . It is important to point out in Fig. 5.68 that the areas showing Cr-rich actually originate from the light areas, as indicated by the arrows in Fig. 5.68, rather than from the darker precipitates. For precipitates farther away from the SiC, some overlapping of C and Cr starts to show, as seen in Figs. 5.69 and 5.70. In some cases, nevertheless, the Cr and C signals were not generated from the same region. It appears that the

formation of Cr-carbides in reaction zone 2 is rather scarce. In summary, the tendency of forming Cr-carbide(s) appears to increase as a function of distance from the SiC reaction interface.

Reaction zones 3 and 4 were found to separate from each other by a diffuse boundary, as shown in Fig. 5.71(a). In the reaction zone 3, which is on the right of the boundary, Si was detected. In contrast, no Si was detected in the zone 4 which is located on the left of the boundary. Fig. 5.72(a) and (b) show EDS spectra obtained from the spots 1 and 2, respectively, shown in Fig. 5.71(a). Also noted in Fig. 5.71(a) are areas with grain boundary precipitates. EDS and WDS analyses of one of these G. B. precipitates, magnified in Fig. 5.71(b), are shown in Fig. 5.73. The G. B. precipitates were found to contain primarily Cr and C, and small amounts of Ni and Fe. To understand the elemental distribution in the G. B. precipitates, x-ray mapping was conducted on precipitates located at a triple grain boundary junction. Fig. 5.74(a) through (f) show a backscattered electron image of one such region and the corresponding x-ray maps for elements C, Cr, Ni, Fe, and Si, respectively. It is clear that the grain boundary precipitates are enriched in C and Cr, but depleted in Ni and Fe. No Si was detected in this region. Quantitative analyses of these precipitates suggested that they were likely to be  $\text{Cr}_{23}\text{C}_6$ .

It is interesting to note in Fig. 5.66 that both the distribution pattern and the size of C precipitates vary as a function of distance from the SiC reaction interface. In the areas adjacent to the SiC, alternating layers of C precipitates and metal phases were noted. The C precipitates show increasingly random scattering and larger particle size as their locations farther away from the SiC reaction front. Similar behavior has been observed during the solid state reactions of SiC with Ni, Co, Fe, and Pt [38,77,78]. Nevertheless, the C precipitates formed in the SS/SiC reaction zone exhibited highly anisotropic morphology, which is rather different from what was observed in the Pt/SiC [77], Ni/SiC [78], Co/SiC [78], and Fe/SiC [38]. In those previously studied systems, C precipitates showed more-or-less irregular shape.

There is an interesting correlation among the elemental distributions in Figs. 5.68 through 5.70. It is noted that the areas enriched of Cr are depleted of Ni, Si, and Fe. Furthermore, Ni and Si are present, more or less, in the same regions while Fe is primarily present in the other regions. It is suggested that Si has a stronger affinity for Ni, than for Fe, which in turn gives rise to an overwhelming Ni-Si reaction and the formation of Ni-based complex metal silicides (which has some solubilities for Fe and Cr) in the reaction zones 1 and 2. The formation of Ni-based complex metal silicides is believed to contribute to the observed massive interfacial melting because of the low melting point of nickel-rich silicides [69].

Interfacial melting as a result of solid state reactions has been previously observed in Pt/SiC, Co/SiC, and Ni/SiC systems [77,78] at reaction temperatures much lower than the melting points of the respective constituents. The interfacial melting can be attributed to either the formation of low melting point eutectic metal silicides in the reaction product(s), or a large negative enthalpy of the metal/Si solid state reactions. To result in a massive interfacial melting phenomenon, it is believed that the former contribution is predominant. Recently, explosive, self-propagating silicide formation in a room temperature environment has been reported in some metal/Si multilayer structures, e.g., Rh/ $\alpha$ -Si [74], Zr/ $\alpha$ -Si [76], and Ni/ $\alpha$ -Si [75] systems. The standard enthalpies of formation of common metal silicides in Ni-Si, Co-Si, and Pt-Si systems are typically in the range of -20 to -50 kcal/mole [68,73,75]. Assuming that the heat capacity ( $C_p$ ) values of these metal silicides are comparable to that of Ni<sub>2</sub>Si ( $C_p = 15.8 + 0.00329 T$  cal/deg-mole) [68], under the condition of adiabatic heating, the temperature rise associated with the formation of a silicide at the reaction interface may be estimated to be in the range of  $10^2$  degree K. Clearly, the contribution from highly exothermic metal/silicon reactions to interfacial melting occurring in metal/SiC solid state reactions can not be underestimated.

A strong Ni-Si chemical affinity is expected to give rise to a fast diffusion rate of Ni from the SS toward the SiC, which can result in enrichment of Ni (as compared to Fe and Cr) in the areas adjacent to the SiC reaction front. Table 5-5 shows a list of EDS analyses on the concentrations of Si, Ni, Fe, and Cr at locations 1 through 6, as indicated in Fig. 5.75, from the SiC to reaction zone 1 (M-CPZ). It is noted in the reaction zone 1 that Ni concentration increases progressively toward the SiC interface; an uphill concentration gradient was noted. In contrast, both Cr and Fe show an expected decreasing concentration gradient. The amount of Cr diffusing through the M-CPZ is much less than Fe or Ni, which is caused by the prevailing selective formation of Cr-carbides in the G.B. precipitation zone.

The selective reaction of C with Cr, rather than with Ni and Fe, is believed to originate from the highly negative Gibbs free energy of Cr-carbide formation. It is known that there exist four different types of Cr-carbides, namely Cr<sub>23</sub>C<sub>6</sub>, Cr<sub>7</sub>C<sub>3</sub>, Cr<sub>3</sub>C<sub>2</sub>, and Cr<sub>4</sub>C. According to thermochemistry data [68,79], the Gibbs free energy of formation of various selected metal carbides were calculated and listed in Table 5-6. It appears that the most likely carbide to form in the present system is Cr<sub>23</sub>C<sub>6</sub>. The positive free energy of formation of Fe<sub>3</sub>C suggests that its formation is not thermodynamically favored. Moreover, according to Marsh [80], and Brewer et al. [81], the addition

of Ni and Si to C-Fe system further destabilizes the  $\text{Fe}_3\text{C}$  phase, although the cementite is already thermodynamically metastable.

The strong affinity of C for Cr gives rise to a faster apparent diffusion rate of C atom (than Si) toward the SS, which is characterized by the trailing of the Si diffusion front to the G.B.-PZ, as shown in Fig. 5.71(a). The diffusion of C atom proceeds from the SiC (a diffusion source), through the reaction zone, and into the SS (a diffusion sink). In view of the widespread C precipitation, the diffusion of C atom is believed to take place via both lattice and grain boundary. The reason why  $\text{Cr}_{23}\text{C}_6$  precipitates form preferentially along the grain boundaries of SS may be attributed to the combination of minimizing the strain energy associated with their formation and the ease of nucleation at the grain boundaries. In contrast, the diffusion rate of C atom was identified to be slower in the Ni/SiC, Co/SiC, and Fe/SiC systems [38,78]; the diffusion front of Si atom was found to lead that of C, which is characterized by the formation of a carbon precipitation free zone (C-PFZ) adjacent to the metals. In the present SS/SiC system, however, no C-PFZ was formed. A slower diffusion rate of C in the Ni/SiC, Co/SiC, and Fe/SiC systems is supported by the fact that all the Ni-carbide ( $\text{Ni}_3\text{C}$ ), Co-carbide ( $\text{Co}_2\text{C}$ ), and Fe-carbide ( $\text{Fe}_3\text{C}$ ) are thermodynamically unstable [78,81] at elevated temperatures, and were not formed in the Ni/SiC, Co/SiC, and Fe/SiC systems, respectively.

**5.11.2 Discontinuous decomposition of SiC:** The formation of modulated (periodical) C precipitation in the present SS/SiC system is of great scientific interest. A similar structure was also generated during the solid state reactions in Ni/SiC [38,78] and  $\text{Ni}_3\text{Al/SiC}$  [77]. Since modulated C precipitation occurs only in areas immediately adjacent to the SiC, the amount of time provided for the dissociated C atoms (from the SiC) to redistribute within these regions is not expected to be sufficient. In contrast, the C precipitation exhibited a completely random pattern in areas remote from the SiC reaction interface. It is suggested that the modulation of C precipitation is directly related to the decomposition characteristics of the SiC when reacting with certain metal species, e.g., Ni.

Considering an overall reaction equation,  $\text{SiC} + \text{SS}(\text{Ni, Fe, Cr}) \rightarrow (\text{Ni,Fe})_x\text{Cr}_y\text{Si}_z + \text{Cr}_{23}\text{C}_6 + \text{C}$ , a driving force resulting from a negative total Gibbs free energy of the reaction is required to proceed the SiC/SS reaction. In view of the global formation of the complex metal-silicides,  $(\text{Ni,Fe})_x\text{Cr}_y\text{Si}_z$ , as compared to the localized formation of  $\text{Cr}_{23}\text{C}_6$ , the driving force for the SiC/SS reactions is believed to originate from the negative free energy of the metal-silicides formation. Furthermore, it is important to consider that a prior decomposition of the SiC is required in order to proceed the

SiC/SS reactions. Since SiC is thermally stable at the temperatures of study, the decomposition of SiC requires a certain amount of activation barrier to be overcome in addition to the thermodynamic driving force. The driving force is the negative free energy of the metal-silicides formation. To surmount the activation barrier for the decomposition of SiC, however, there exists a nucleation period. Without the presence of metal atoms on SiC interface, which is analogous to the case of thermal decomposition of SiC, the incubation time for SiC decomposition may be infinitely long. It is proposed that SiC exhibits discontinuous decomposition behavior when reacting with such metals as pure Ni or rich Ni-containing alloys, but not with Co or Fe. Recent studies on the reactions of SiC with pure Ni [38,78],  $\text{Ni}_3\text{Al}$  [77], and Ni alloys [47] indicated the formation of alternating layers of C and Ni-based metal silicides in the reaction zones. On the other hand, when SiC reacted with Pt [77], Co [78], and Fe [38], the C precipitation in the areas adjacent to the SiC was completely random.

According to ternary phase diagrams of Ni-Si-C [38] and Nb-Si-C [48], SiC is not in equilibrium with pure metals or metal-rich silicides. In other words, a metal-rich or even a pure metal layer next to the SiC is required for the continuation of the (Ni,Nb)/SiC reactions, i.e., the decomposition of SiC. It is believed that a similar requirement also applies to other systems, e.g., Co-Si-C, Fe-Si-C, Pt-Si-C, etc. Our previous studies of Ni/SiC [78] also indicated that the Ni-silicide formed adjacent to the SiC was Si-rich compared to other Ni-silicides formed in the reaction zone. Clearly, the presence of a Ni-rich layer at the SiC reaction interface is a prerequisite to keep the system in a non-equilibrium state, which in turn promotes the decomposition of SiC and thereby continue the Ni/SiC solid state reactions. It is suggested that there exists a critical level of Ni concentration, above which the decomposition of SiC is possible. When the concentration of Ni falls below such a level, the decomposition of SiC is kinetically sluggish or essentially stop.

To explain the formation of a periodic structure during solid state reactions [82-84], the "supersaturation theory" proposed by Ostwald [85] is commonly adopted. According to the theory, the critical elements to constitute the formation of periodic C precipitates in metal/SiC reactions are: (1) a strong affinity of the metal specie for Si, but not C, to form a thermodynamically stable metal-silicide; (2) a critical metal concentration ( $C_m$ ) at the SiC reaction interface is to be satisfied for the decomposition of SiC; (3) a low solid solubility (or rejection rate) of C atom in the silicide matrix. Based upon these criteria, periodic C precipitation is not expected to occur when SiC reacting with strong carbide forming metals, such as Nb, Ti, or Cr. On the other hand, although Ni, Co, Fe, or Pt have low affinity for C to form stable carbide at the temperatures of interest, periodic C precipitation occurred only in the Ni/SiC system. This may be attributed to the variation of the C rejection rate in

those metal-silicide matrices. In this respect, the data of solid solubility or diffusivity of C in those metal silicides, although not available, is valuable to sort out the discrepancy. Table 5-7 summarizes a list of microstructural evolution in the reaction zone from selected metal/SiC reactions.

By examining the reaction zones of Ni/SiC under Raman microprobe, the first thin layer immediately adjacent to the unreacted SiC is found to be primarily carbon, while no free unreacted Si was detected. In the SS/SiC system, based on SEM micrographs, the immediate layer adjacent to the SiC was also found to contain predominantly C clusters. It is suggested that once a layer of SiC is decomposed, Si atoms, decomposition products of SiC, readily diffuse away and react with Ni to form a layer of Ni-silicide in front of the constituent C region. As a result, the Ni concentration at the SiC reaction interface decreases drastically, which in turn makes continuous decomposition of SiC more difficult. In order to further decompose SiC, a critical level of Ni concentration is to be satisfied, which takes time to establish. Concurrently, the dissociated C atoms, in front of the SiC reaction interface, form small clusters and aggregate as a layer to minimize their interfacial energy. The continuation of this process will give rise to the formation of alternating Ni-silicide and carbon layers. The boundary defining the layered structure, however, can be obscured by the diffusion kinetics of constituents and/or solid solubility of C in the matrices, which are known to be dependent upon metal systems, annealing parameters, and local concentration of the constituents (which is a function of distance from the reaction front). To give an example on the effects of those variables on the C precipitation behavior, our recent studies [86] of the NiAl/SiC reactions at 1300°C showed that the C precipitation in the reaction zone was completely random although modulating C precipitation has been observed during the solid state reactions of SiC with Ni<sub>3</sub>Al [77] and Ni alloys (containing 70 at.% Ni, 20 at.% Cr, and 10 at.% Al) [47].

**5.11.3 Summary of SS/SiC Reactions:** Solid state reactions of SiC with stainless steel produced four layered reaction zones. The 1st and 2nd layers consisted of C precipitates embedded in Ni-based metal silicides matrices. The 3rd layer contained multiple alloy phases. The 4th layer showed grain boundary precipitation of Cr<sub>23</sub>C<sub>6</sub>. On the basis of thermodynamic Gibbs free energy, C has the strongest affinity for Cr, which gives rise to a faster diffusion rate of C atom (as compared to Si) toward the stainless steel. As a result, the Si diffusion front trailed behind the C diffusion front, which prevented the formation of a C-PFZ adjacent to the SS, and Cr<sub>23</sub>C<sub>6</sub> precipitates formed along the grain boundaries of the SS. On the other hand, it is demonstrated that Ni, Co, and Fe do not form thermodynamically stable carbides, which resulted in a slower C diffusion rate and was characterized by the formation of a C-PFZ in Ni/SiC, Co/SiC, and Fe/SiC systems. Ni

atoms were found to have a strong affinity for Si and resulted in the formation of Ni-based metal silicides, which attributed to the observed massive interfacial melting. It has been found, so far, that the presence of Ni species in metals is essential to promote the formation of alternating C and metal-silicide layers in the reaction zone during metal/SiC reactions. Moreover, it appears that modulating C precipitation occurs only in systems which have a high Ni concentration; alternating carbon and nickel silicide layers were observed in Ni/SiC, Ni<sub>3</sub>Al/SiC, and Ni alloys (containing 70 at.% Ni)/SiC, but not in NiAl/SiC. Based on Ni-Si-C and Nb-Si-C ternary phase diagrams, it is suggested that a critical concentration of Ni at the SiC reaction interface has to be satisfied in order to maintain the SiC at a nonequilibrium state. The formation of alternating carbon and nickel silicide layers in the reaction zone was explained in terms of discontinuous decomposition of SiC, as a result of the interplay of nickel silicide formation and a dynamic, time-dependent building up of the critical Ni concentration at the SiC reaction interface.

#### 5.12 Reactions of Ti<sub>3</sub>Al with Si<sub>3</sub>N<sub>4</sub> and SiC

Titanium-based alloys are currently widely used as a high temperature structural material for aerospace applications (such as airframe and jet engine components) because of their relatively lower densities, higher strength-to-weight ratios and excellent corrosion resistance compared with steel and nickel-based alloys. As the designs for advanced aerospace vehicles call for an improved specific strength at a higher operating temperatures, titanium-aluminide intermetallic compounds, such as Ti<sub>3</sub>Al( $\alpha_2$ ), TiAl( $\gamma$ ), and TiAl<sub>3</sub>( $\tau$ ) [87], are receiving much attention lately [87-89]. Compared to conventional titanium alloys, titanium aluminides have better creep resistance, higher modulus and strength, and better oxidation resistance at both room and elevated temperatures [89]. Like most of intermetallic compounds, however, titanium aluminides also suffer from low ductility and brittle intergranular fracture at ambient temperature.

One approach to achieve high temperature strength with improved room temperature fracture toughness is composite technology. By incorporating high strength and stiffness reinforcements into a titanium aluminide matrix, a further improvement in its mechanical properties is anticipated. It has long been recognized that during both consolidation and application of a composite, interfacial reactions can occur between the matrix and the reinforcement. The kinetics of reactions as well as the properties of reaction products critically influence the overall properties of the composite. It is important to understand the nature of those interfacial reactions so that properties of the composite can be controlled.



SiC,  $\text{Si}_3\text{N}_4$ , and  $\text{Al}_2\text{O}_3$  are the most common reinforcement candidates because of their low density, and good mechanical strength as well as thermal stability at elevated temperatures. In titanium aluminide matrix composites, SiC fibers are the most frequently used reinforcements. As a result, reactions between titanium aluminides and SiC have been studied quite extensively in the past [90-96,12]. In those studies, the reaction products were found to be quite complex and contained multiple elements; however, they can be classified into carbides and silicides. Conversely, interfacial reactions of titanium aluminides with  $\text{Si}_3\text{N}_4$  and  $\text{Al}_2\text{O}_3$  are rarely studied. In this work, we concentrate on the solid state interfacial reactions between  $\text{Ti}_3\text{Al}$  and  $\text{Si}_3\text{N}_4$ . In addition, limited studies were also conducted on the reactions between  $\text{Ti}_3\text{Al}$  and SiC. Both thin film and bulk diffusion couples with planar interfaces, rather than consolidated metal powders with reinforcing agents, were prepared to evaluate the interfacial reactions.

For the preparation of the bulk diffusion couples, the titanium aluminide [ $\text{Ti}_3\text{Al}(\text{Nb})$ ], containing Ti68-Al21-Nb11 (at.%), were received from the Alta Group. Energy dispersive x-ray microanalysis indicated that the alloy contained Ti, Al, and Nb; x-ray diffraction analysis confirmed that the alloy had a hexagonal,  $\text{Ti}_3\text{Al}$  crystal structure (JCPDS# 9-98). The metallic samples were cut into appropriate sizes, mechanically ground on SiC papers, fine polished with 1  $\mu\text{m}$  diamond paste, and finished by ultrasonic cleaning in methanol and drying. To form a diffusion couple, reactant coupons of  $\text{Ti}_3\text{Al}(\text{Nb})$  and  $\text{Si}_3\text{N}_4$  (or SiC) were stacked together, under a slight pressure (estimated 50 kPa) from a dead weight, to produce contact.

For preparation of thin film couples,  $\text{Ti}_3\text{Al}$  films were deposited onto  $\text{Si}_3\text{N}_4$  and SiC substrates, using a CVC 601 system, by d.c. co-sputtering of Ti and Al targets. The purities of both of the target materials were at least 99.99%. The base pressure of deposition chamber was about  $1 \times 10^{-7}$  torr. Prior to the deposition of  $\text{Ti}_3\text{Al}$  films, both the  $\text{Si}_3\text{N}_4$  and SiC substrates were further cleaned by reverse bias sputter etching. During deposition He gas was introduced and its pressure was maintained at 5 mtorr. In order to produce  $\text{Ti}_3\text{Al}$  films, the deposition rates of Ti and Al were pre-calibrated and controlled (based on their atom concentrations) with a ratio of 3.2 : 1. Composition and structure of the resulting films were examined by Auger electron spectroscopy (AES), transmission electron microscopy (TEM, JEOL 2000FX), and grazing angle x-ray diffraction. According to both AES depth concentration profiles and energy dispersive x-ray microanalysis (with TEM), the average composition of the films is 75.5Ti-24.5Al (at.%). Both electron diffraction and x-ray diffraction indicated that the film had a hexagonal,  $\text{Ti}_3\text{Al}$  crystal structure (JCPDS #9-98). Figures 5.76(a) and 1(b) show a TEM bright field image and its corresponding electron diffraction pattern of an as-deposited  $\text{Ti}_3\text{Al}$  film; structural texture along the {002} and {201} is noted. Based

on this study, the  $\text{Ti}_3\text{Al}$  films were thermally stable up to at least  $1200^\circ\text{C}$ . The typical thickness of the  $\text{Ti}_3\text{Al}$  films made for this study was  $1\ \mu\text{m}$ .

The bulk diffusion couples were annealed in a vacuum furnace ( $10^{-7}$  torr) at  $1000$  and  $1200^\circ\text{C}$  for various times. The thin film diffusion couples were encapsulated in fused quartz tubes, which were flushed with Ar, and annealed under the same conditions as those for the bulk diffusion couples. Upon finishing the thermal treatments, both AES and x-ray photoelectron spectroscopy (XPS) were used to obtain depth- composition profiles of the various reaction products. AES is preferred for obtaining depth profiles because of good signal/noise (S/N) ratio and depth resolution. However, it has the problem of peak overlap between Ti and N; the kinetic energies of the primary N peak and the secondary Ti peak occur at  $379\ \text{eV}$  and  $387\ \text{eV}$ , respectively.[97] As a result, ESCA was also used in some instances to supplement the depth concentration profiles. The sensitivity factors of Ti, Al, and N used in AES were pre-determined based on  $\text{Ti}_3\text{Al}$  and  $\text{TiN}$  standards. Due to the problems of peak overlap and the stoichiometries of the  $\text{SiC}$  and  $\text{Si}_3\text{N}_4$  ceramics, several of the AES profiles were recombined to show estimated N, Ti, Si, and C concentrations in the diffusion zones. The regions with estimated concentration is represented by dotted lines in the concentration profiles.

X-ray diffraction was also used to characterize the reaction products. In addition, scanning electron microscopy (SEM) with both energy and wavelength dispersive spectrometries (EDS and WDS) x-ray microanalysis were used to characterize the surfaces and reaction interfaces. An OV80 layered synthetic crystal ( $2d = 8.14\ \text{nm}$ ) was used for the WDS analysis.

**5.12.1 As-deposited Films:** Auger depth concentration profiling from an as-deposited  $\text{Ti}_3\text{Al}$  film, as shown in Fig. 5.77(a), indicates that the film has a relatively uniform composition of 76 Ti and 24 Al (at.%) throughout the thickness. This result is in good agreement with that obtained from the  $\text{Ti}_3\text{Al}$  standard, as shown in Fig. 5.77(b). The composition of the film is consistent with that obtained from the EDS microanalysis by TEM. According to a Ti-Al binary phase diagram [98],  $\text{Ti}_3\text{Al}$  exists in a composition range  $78\text{Ti}22\text{Al} - 65\text{Ti}35\text{Al}$  (at.%).

**5.12.2  $\text{Ti}_3\text{Al}$  Reactions at  $1000^\circ\text{C}$ :** In this section the reactions of  $\text{Ti}_3\text{Al}$ , in both bulk and thin film forms, occurring at  $1000^\circ\text{C}$  with  $\text{Si}_3\text{N}_4$  and  $\text{SiC}$  substrates are discussed.

**Ti<sub>3</sub>Al/Si<sub>3</sub>N<sub>4</sub> reactions:** Annealing of Ti<sub>3</sub>Al(Nb)/Si<sub>3</sub>N<sub>4</sub> bulk diffusion couples at 1000°C for 4 h showed negligible reactions; no metallurgical bonding or evidence of reactions between the couples was observed. This may be attributable to the lack of intimate contact between the couples, because of the relatively low applied pressure compared to the yield strength of Ti<sub>3</sub>Al. Annealing of the Ti<sub>3</sub>Al/Si<sub>3</sub>N<sub>4</sub> thin film diffusion couples under the same conditions revealed that the Ti<sub>3</sub>Al films have reacted with the Si<sub>3</sub>N<sub>4</sub> substrates. Fig. 5.78(a) shows ESCA depth concentration profiles of Ti, Si, N, Al, and C of a thin film diffusion couple annealed at 1000°C for 4 h. It is noted that, starting from the free surface, three layered reaction products were formed. The 1st layer contains primarily Si-rich titanium silicide(s) with a very small amount of N and Al, the 2nd layer contains Ti-rich titanium silicide(s) with a greater amount of both N and Al, and the 3rd layer contains essentially equal amounts of Ti, Si, and N. It is important to note that the amount of Al existing in the layered reaction products is much smaller than that in the Ti<sub>3</sub>Al.

Consistent results were obtained from another diffusion couple annealed under the same conditions, except that the sample was encapsulated in a fused quartz tube flushed with Ar. Figure 5.78(b) shows an AES depth concentration profile of the thin film diffusion couple after annealing at 1000°C for 4 h. It is clearly noted that the Al is depleted in the near-surface layer; this phenomenon is more pronounced in the AES profiles than in the ESCA due to better S/N ratio and depth resolution in the AES data. It appears that the layered reaction products formed are primarily titanium silicide(s), titanium-silicon aluminide (with some O<sub>2</sub>), and titanium-silicon nitride.

The chemical states of Ti and Si in the reaction product(s) was determined from the precise positions of Ti and Si binding energies from the interfaces after 12 minutes of ion etching. The formation of titanium nitride is evidenced by the 455 eV binding energy of the Ti-2p<sub>3/2</sub> peak based on a TiN standard [99]. According to the binding energy of the Si-2p peak, the Si in the reaction product is suggested to be present as a titanium silicide. The binding energy of Al-2p was measured to be 74.2 eV, compared to 72.65 eV of pure Al, and it may be present as an oxide and/or hydroxide [99]. It is important to point out that the amount of Al existing in those reaction products varies from 5 to 10 at.%, which is significantly lower than that (24.5 at.%) in the as-deposited state. The origin of Al-depletion will be discussed later.

**Ti<sub>3</sub>Al/SiC reactions:** Fig. 5.79 shows an AES depth concentration profile of the thin film diffusion couples after annealing at 1000°C for 4 h. The reaction products were found to be mainly titanium-silicon carbide, next to the SiC substrate, and titanium silicide(s) with some Al and C. The reaction

products seem to form in a layered fashion. It is interesting to note, similar to the results from the  $\text{Ti}_3\text{Al}/\text{Si}_3\text{N}_4$  reactions, that the Al was also depleted from the reaction products, and the amount of Si present is richer in the near-surface layer.

Based upon the above results, it is clear that  $\text{Ti}_3\text{Al}$  reacted with  $\text{Si}_3\text{N}_4$  and SiC at  $1000^\circ\text{C}$ ; the reaction products are titanium silicide(s), titanium-silicon aluminide and titanium-silicon nitride for the  $\text{Ti}_3\text{Al}/\text{Si}_3\text{N}_4$  reactions, and titanium silicide (with some Al and C) and titanium-silicon carbide for the  $\text{Ti}_3\text{Al}/\text{SiC}$  reactions. Both ESCA and AES concentration profiles indicated layered characteristic of these reactions along with some mixing of reaction products in each of the layers.

**5.12.3  $\text{Ti}_3\text{Al}$  Reactions at  $1200^\circ\text{C}$ :** In this section the reactions of  $\text{Ti}_3\text{Al}$ , in both bulk and thin film forms, occurring at  $1200^\circ\text{C}$  with  $\text{Si}_3\text{N}_4$  and SiC substrates are discussed.

**$\text{Ti}_3\text{Al}/\text{Si}_3\text{N}_4$  reactions:** Annealing of the bulk diffusion couples at  $1200^\circ\text{C}$  for 6 h gave rise to a drastically different reaction characteristic as compared to that at  $1000^\circ\text{C}$ . Metallurgical bonding was established uniformly across the contact interfaces. Nevertheless the bonding was poor and the diffusion pairs often de-coupled. Figures 5.80(a) and (b) show low magnification SEM micrographs of the reaction interfaces on the de-bonded  $\text{Ti}_3\text{Al}(\text{Nb})$  and  $\text{Si}_3\text{N}_4$  components, respectively. Higher magnification SEM micrographs of the reaction interfaces are illustrated in Figs. 5.80(c) and (d). Gold-colored reaction product, indicative of the formation of a titanium nitride (TiN), was observed at all the interfaces on the de-bonded  $\text{Si}_3\text{N}_4$  components. In some cases, when the reaction product was more adherent to the  $\text{Ti}_3\text{Al}(\text{Nb})$  component, islands of the gold-colored reaction product were noted at the interfaces on the de-bonded  $\text{Ti}_3\text{Al}(\text{Nb})$  components.

Figure 5.81 shows AES depth concentration profiles of Ti, N, Al, and Si from the gold-colored reaction product formed on the de-coupled  $\text{Si}_3\text{N}_4$  component (as shown in Fig. 5.80(b)). It is noted that the reaction product is essentially a single layer of TiN. Based on the binding energy of the  $\text{Ti-2p}_{3/2}$  peak by ESCA, the layered reaction product was further confirmed to be titanium nitride. The TiN layer is found to contain a small amount of Si, whereas the amount of Al and Nb present in the layer is almost negligible. As the titanium nitride layer was dynamically etched away, the Si is detected only at the TiN/ $\text{Si}_3\text{N}_4$  interface.

Prolonged annealing of the bulk diffusion couples at 1200°C for 16 and 48 h resulted in essentially the same results; bonding between  $\text{Ti}_3\text{Al}(\text{Nb})$  and  $\text{Si}_3\text{N}_4$  was established and gold-colored reaction product was observed mainly at the interfaces on the de-bonded  $\text{Si}_3\text{N}_4$  components. X-ray diffraction was employed to identify the structure of the reaction product from a de-coupled  $\text{Si}_3\text{N}_4$  component after annealing for 48 h, because the amount of the reaction product formed under this condition is expected to be the greatest among all. By using  $\text{Cr-K}_\alpha$  radiation ( $\lambda = 0.22909 \text{ nm}$ ), both the (111) and (200) peaks of TiN (JCPDS #6-642) were detected at  $2\theta = 55.8$  and  $65.4^\circ$ , respectively. In addition, various diffraction peaks originating from the  $\beta\text{-Si}_3\text{N}_4$  substrate were also detected. Based on the XRD results and the fact that the Ti/N ratio in the AES profiles is close to 1:1, the titanium nitride reaction product formed between  $\text{Ti}_3\text{Al}$  and  $\text{Si}_3\text{N}_4$  at 1200°C is believed to be TiN.

Annealing of the  $\text{Ti}_3\text{Al}/\text{Si}_3\text{N}_4$  thin film diffusion couples at 1200°C for 4 h resulted in changing of the colors of the  $\text{Ti}_3\text{Al}$  film from metallic (in an as-deposited state) to light-brown. AES depth concentration profiling, as shown in Fig. 5.82(a), of the reacted  $\text{Ti}_3\text{Al}$  film indicates the formation of a TiN layer. It is further noted that the TiN layer is essentially free of both Si and Al. Figures 5.82(b) and (c) illustrate the AES spectra obtained from the interfaces after 33 and 120 min ion sputtering, respectively. It is clear that the Si peak (as indicated) is detected only in the region close to the  $\text{TiN}/\text{Si}_3\text{N}_4$ . On the other hand, no Al peak is observed throughout the TiN layer.

The sample was further examined by EDS and WDS x-ray microanalyses in a scanning electron microscope. Figure 5.83(a) shows an EDS spectrum from the light-brown, reacted  $\text{Ti}_3\text{Al}$  film. Both the Ti and Si characteristic peaks are observed, while no Al peak is found. Peak search for  $\text{Al-K}_\alpha$  in WDS mode confirmed the absence of Al. Figure 5.83(b) shows a WDS spectrum collected from the  $\text{Ti}_3\text{Al}$  film after reacting with the  $\text{Si}_3\text{N}_4$  substrate. It is noted that both  $\text{Ti-L}_\alpha$  ( $\lambda=27.42 \text{ \AA}$ ) and  $\text{Li}$  ( $\lambda=31.36 \text{ \AA}$ ) peaks at 94.3 and 107.9 mm (spectrometer's position), respectively, are clearly visible. Furthermore, a  $\text{N-K}_\alpha$  ( $\lambda=31.6 \text{ \AA}$ ) peak at 108.7 mm is also present, although it overlaps with the  $\text{Ti-Li}$  line. As a comparison, a WDS spectrum of Ti peaks from an as-deposited  $\text{Ti}_3\text{Al}$  film was also collected and is shown in Fig. 5.83(c). The higher intensity of the  $\text{Ti-Li}$  peak than the  $\text{Ti-L}_\alpha$  peak in Fig. 5.83(b), as compared to Fig. 5.83(c), is attributed to the presence of N (from the TiN reaction product) in the reacted  $\text{Ti}_3\text{Al}$  film. It has been reported [100] that the  $\text{Ti-L}_\alpha$  line is heavily absorbed by nitrogen and is about one-third as intense as that from pure Ti. The  $\text{Ti-Li}$  emission, however, is only slightly absorbed by nitrogen. As a result, the combined intensity of the  $\text{Ti-Li}$  and  $\text{N-K}_\alpha$  lines from the TiN layer is much higher than that of the  $\text{Ti-L}_\alpha$  line. SEM micrograph of the reaction-

formed TiN film, as shown in Fig. 5.84(a), indicates that the film contains a granular microstructure as compared to the smooth characteristic of a  $\text{Ti}_3\text{Al}$  film before the reaction, see Fig. 5.84(b).

Similar results were also obtained from the TiN layer formed on the de-coupled  $\text{Ti}_3\text{Al}(\text{Nb})$  and  $\text{Si}_3\text{N}_4$  bulk diffusion samples after annealing at  $1200^\circ\text{C}$  for 6 h. According to EDS spectra collected from the TiN layer formed on the de-coupled  $\text{Ti}_3\text{Al}(\text{Nb})$  component, the overall intensity of the Ti-L $\alpha$  and N-K $\alpha$  lines is also significantly greater than that of the Ti-L $\alpha$  line. Moreover, no Al was detected, suggesting that the amount of Al existing in the TiN layer is below the EDS detection limit, and the contribution to the EDS x-ray intensity of the Al-K $\alpha$  line from the  $\text{Ti}_3\text{Al}(\text{Nb})$  substrate is negligible. Figures 5.85(a) to (f) show a SEM image and Ti-K $\alpha$ , N-K $\alpha$ , Al-K $\alpha$ , Si-K $\alpha$ , and Nb-K $\alpha$  x-ray maps, respectively, of an area containing both the reacted (i.e., TiN) and unreacted  $\text{Ti}_3\text{Al}(\text{Nb})$  regions. It is clear that the reacted region contains essentially Ti, N, and Si, but no Al or Nb is noted. Based on the AES depth concentration profiles that no Si is present within the TiN layer, except at the TiN/ $\text{Si}_3\text{N}_4$  interface, the Si observed by x-ray analysis is believed to be associated with the surface of the TiN layer as a result of debonding from the  $\text{Si}_3\text{N}_4$  component. The inability of detecting Al and Nb from the substrate indicates that the TiN layer formed on the  $\text{Ti}_3\text{Al}(\text{Nb})$  has a finite thickness. By tilting the sample at  $87^\circ$ , the thickness of the TiN layer was measured to be about 5000 Å.

$\text{Ti}_3\text{Al}/\text{SiC}$  reactions: The thin film diffusion couples annealed at  $1200^\circ\text{C}$  for 4 h resulted in more extensive reactions than those annealed at  $1000^\circ\text{C}$ . Based on the AES concentration profiles, shown in Fig. 5.86, the reaction product appears to be a simple layer of titanium-silicon carbide, and the amount of Al existing in the reaction product is negligible. It is further noted that the concentration of Si in the reaction product formed at  $1200^\circ\text{C}$  is significantly lower than that in the reaction product formed at  $1000^\circ\text{C}$  (see Fig. 5.79). This phenomenon is similar to what was observed in the  $\text{Ti}_3\text{Al}/\text{Si}_3\text{N}_4$  reactions (see Figs. 5.78(b) and 5.82(a)).

**5.12.4 Discussion of  $\text{Ti}_3\text{Al}$  Reactions:** A detailed description of the characteristics of the reaction interfaces and reaction products from the various  $\text{Ti}_3\text{Al}/\text{Si}_3\text{N}_4$  and  $\text{Ti}_3\text{Al}/\text{SiC}$  diffusion couples annealed at 1000 and  $1200^\circ\text{C}$  are listed in Table 5-8.

To visualize the reactions between the  $\text{Ti}_3\text{Al}$  and  $\text{Si}_3\text{N}_4$  (or SiC), it is important to bear in mind that either the intermetallic compound or the ceramic should be in a dissociated state in order for a

reaction to propagate. Since the results from the  $\text{Ti}_3\text{Al}/\text{SiC}$  reactions are quite similar to those from the  $\text{Ti}_3\text{Al}/\text{Si}_3\text{N}_4$  reactions, we will focus the discussion on the latter reactions.

Based on the results from both the bulk and thin film diffusion couples of  $\text{Ti}_3\text{Al}/\text{Si}_3\text{N}_4$  annealed at 1000 and 1200°C, with titanium silicide(s) formed in the near-surface layer at 1000°C and a single titanium nitride layer formed at 1200°C, it appears that the diffusion kinetics of Si and N are drastically different in  $\text{Ti}_3\text{Al}$  at those temperatures and they are strongly temperature-dependent. Since a Si-enriched near-surface layer is consistently observed in the samples annealed at 1000°C, it is believed that Si is sufficiently mobile at this temperature. This is further supported by the fact that various titanium silicides ( $\text{Ti}_5\text{Si}_3$ ,  $\text{TiSi}$ , and  $\text{TiSi}_2$ ) start to form at temperatures ranging from 500 to 750°C during the reactions of Ti thin films with either polycrystalline Si films or single-crystalline Si substrates. On the other hand, N is suspected to be less mobile than Si at 1000°C in  $\text{Ti}_3\text{Al}$ , and a monotonically decreasing concentration profile of the N from the  $\text{Si}_3\text{N}_4$  substrate toward the free surface was observed.

The mobility of Si at 1200°C is expected to be no less than that at 1000°C. The inability of Si to diffuse toward the near-surface region at 1200°C is suggested to be related to the formation of a uniform layer of TiN during the  $\text{Ti}_3\text{Al}/\text{Si}_3\text{N}_4$  reactions, since titanium nitride is a good diffusion barrier for most of the elemental species. The reason why a uniform layer of TiN is not formed at 1000°C may be attributable to the slower diffusion kinetics of the N and the sluggish nucleation and growth (N/G) kinetics of the TiN. The out-diffusion of N may be strongly dependent upon the intimacy of interfacial contact (i.e., an interface-controlled reaction), and the N/G of TiN is highly heterogeneous and the reaction front is nonplanar. As a result, at 1000°C, the dissociated Si (from the  $\text{Si}_3\text{N}_4$  substrates) can effectively transport through the discontinuous TiN reaction product and form the titanium silicide(s) in the near-surface layer, while the titanium-silicon nitride is formed in the near-substrate layer (see Fig. 5.87(a)). At 1200°C, by contrast, the out-diffusion of N (toward the  $\text{Ti}_3\text{Al}$ ) is believed to be sufficiently fast and more homogeneous, and the N/G kinetics of the TiN also increases. As a result, a single layer of TiN is formed as a reaction product (see Fig. 5.87(b)), which may serve as an effective diffusion barrier, thereby retarding the outward diffusion of Si. Consequently, the amount of Si that can be present in the reaction product is reduced.

A similar argument can also be applied to the  $\text{Ti}_3\text{Al}/\text{SiC}$  reactions. In this case, the titanium-silicon carbide is formed in the near-substrate layer, while the titanium silicide(s) is formed in the near-surface layer. Furthermore, the amount of Si existing in the reaction products formed at 1200°C

appears to be much less than that in the products formed at 1000°C. These observations suggest that Si diffuses faster than C in the  $\text{Ti}_3\text{Al}$  layer.

An important phenomenon being noted from the  $\text{Ti}_3\text{Al}/\text{Si}_3\text{N}_4$  thin film diffusion couples annealed at 1200°C is the depletion of Al from the titanium nitride reaction product. A similar phenomenon was also noted from the samples annealed at 1000°C; Al-depletion was found to occur in the near-surface layer (see Fig. 5.78(b)). By performing an annealing at 1200°C for 4 h, it was found that the amount of residual Al decreased. It appears that the depletion of Al is a kinetically-driven process. This leads us to believe that the loss of Al may be attributable to evaporation when the  $\text{Ti}_3\text{Al}$  decomposes driving reaction with  $\text{Si}_3\text{N}_4$ . The depletion of Al also occurs in the  $\text{Ti}_3\text{Al}/\text{SiC}$  thin film diffusion couples; the titanium-silicon carbide reaction products were found to contain only a small amount of Al (see Figs. 5.79 and 5.86), although some Al is still present in the near-surface region in the samples annealed at 1000°C.

It is noted that the vapor pressure of Al at 1200°C is in the order of  $10^{-2}$  torr.[101] Such a high vapor pressure is adequate to result in its loss through evaporation under the present vacuum annealing condition ( $10^{-7}$  torr). Without a prior decomposition,  $\text{Ti}_3\text{Al}$  is expected to be stable (in an inert environment) at 1200°C. To verify that the evaporation of Al is not caused by the metastability of the vapor-deposited  $\text{Ti}_3\text{Al}$  films at elevated temperatures, free standing films of 50 nm in thickness were produced (by depositing on water-soluble NaCl crystals, and then the substrates dissolved in water and the films retrieved by Mo grids) and annealed between 300 and 1200°C, under the same vacuum environment, for various times. It was found that both the composition and structure of the films are stable. For example, the average composition of the films annealed at 1200°C for 6 h was measured to be 76.4Ti-23.6Al (at.%).

In the bulk diffusion couples, however, since the reaction product was sandwiched between the  $\text{Ti}_3\text{Al}(\text{Nb})$  and  $\text{Si}_3\text{N}_4$ , the available surface area of the  $\text{TiN}_x$  layer permitting the evaporation of Al is limited. As a result, some amounts of Al are still retained in the TiN layer. Aluminum is known to form a ternary compound ( $\text{Ti}_2\text{AlN}$ ) with Ti and N, the reason why Al did not form a compound with Ti and N in the present study may be related to the thermodynamic stability of the compound (compared to the TiN) and/or competing kinetics between the evaporation of Al and the formation of  $\text{Ti}_2\text{AlN}$ .

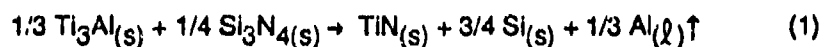
As a comparison, the vapor pressure of Si at 1200°C is about  $4 \times 10^{-6}$  torr [101] which is four orders of magnitude lower than that of Al. In addition, Si is known to strongly react with Ti to form



various titanium silicides at temperatures ranging from 500 to 750 °C. As a result, the absence of Si in the TiN layer is unlikely to result from its evaporation but, instead, attributable to its low solid solubility therein.

According to the topographies of the reaction interfaces on the de-bonded bulk diffusion couples, the surface level of the unreacted  $\text{Si}_3\text{N}_4$  region is lower than that of the reacted one (which has a TiN layer on top). Moreover, the TiN layer was mainly formed on the de-bonded  $\text{Si}_3\text{N}_4$  component, although TiN islands were occasionally noted on the  $\text{Ti}_3\text{Al}(\text{Nb})$  component, the adhesion of TiN with  $\text{Si}_3\text{N}_4$  appears to be better than with  $\text{Ti}_3\text{Al}(\text{Nb})$ . It is worth pointing out that the  $\text{Ti}_3\text{Al}(\text{Nb})$  surface at the fractured TiN/ $\text{Ti}_3\text{Al}(\text{Nb})$  interface exhibit interesting characteristic compared to the  $\text{Si}_3\text{N}_4$  surface at the fractured TiN/ $\text{Si}_3\text{N}_4$  interface. The former one shows a regular step-like pattern (see Fig. 5.88), while the latter one shows a granular morphology which essentially replicates the microstructure of the  $\text{Si}_3\text{N}_4$ . It is not yet understood that why the fractured  $\text{Ti}_3\text{Al}(\text{Nb})$  surface takes such a strange, but regular pattern.

It is worth highlighting the thermodynamic driving force for the solid state reactions of  $\text{Ti}_3\text{Al}$  with  $\text{Si}_3\text{N}_4$ . Since the reaction at 1200 °C gives rise to a simple reaction product (i.e., TiN), we will use that as an example. Considering a  $\text{Ti}_3\text{Al}/\text{Si}_3\text{N}_4$  reaction at 1500 K:



a negative Gibbs free energy is required for the reaction to take place. Based on thermochemistry data [102-105], the Gibbs free energies of formation of various compounds were calculated and listed in Table 5-9. Since the decomposition of  $\text{Si}_3\text{N}_4$  exhibits positive Gibbs free energy, in addition, the free energy for the dissociation of  $\text{Ti}_3\text{Al}$  is also expected to be positive (although its value at 1500 K is not available), it is clear that the thermodynamic driving force for the reaction is the negative Gibbs free energy of the TiN formation. Based upon a thermodynamic criterion that the total free energy of the reaction has to be a negative value, one can test the validity of those independently determined free energies of formation of the constituents, as listed in Table 5-9. According to Samokhval et al's thermochemistry data for  $\text{Ti}_3\text{Al}$  at 960 K,  $\Delta H = -96 \text{ KJ/mole}$ ,  $\Delta S = -15.2 \text{ J/mole-K}$  [104,105], the Gibbs free energy of formation of  $\text{Ti}_3\text{Al}$  at 960 K is about -19 kcal/mole; a lower, or comparable, free energy value is expected at 1500 K. As a result, the overall Gibbs free energy of the reaction in Eq.(1) has a negative value. In other words, the formation of a TiN reaction product is thermodynamically favored.

**5.12.5 Summary of  $Ti_3Al$  Reactions:** Solid state interfacial reactions of  $Ti_3Al$  with  $Si_3N_4$  and SiC were studied at 1000 and 1200 °C. At 1000 °C, titanium silicide(s), titanium-silicon aluminide, and titanium-silicon nitride were formed in the  $Ti_3Al/Si_3N_4$  diffusion couples; titanium silicide(s) (with some C and Al) and titanium-silicon carbide were formed in the  $Ti_3Al/SiC$  couples. At 1200 °C, simple reaction products were formed, TiN in the former system and titanium-silicon carbide in the latter one. The interfacial reactions in both the  $Ti_3Al/Si_3N_4$  and  $Ti_3Al/SiC$  systems were consistent and showed that a Si-enriched surface layer was formed at 1000 °C, while a lesser amount of Si diffused into the reaction products at 1200 °C. Moreover, the depletion of Al from the reaction product was noted and it exhibited temperature-dependent kinetics. A unified diffusion mechanism is proposed to explain the observed phenomena. It is suggested that the diffusion of N (or C) in the  $Ti_3Al$  and the N/G kinetics of the TiN (or titanium-silicon carbide) reaction product are less effective at 1000 °C. As a result, Si can diffuse rather easily through the discontinuous TiN and react with Ti to form titanium silicide(s) in the near surface regions. At 1200 °C, on the other hand, the diffusion of N (or C) becomes significant and the N/G kinetics of TiN (or titanium-silicon carbide) are effective. As a result, a single-layered reaction product of TiN (or titanium-silicon carbide) was formed in the near-substrate region. The planar TiN (or titanium-silicon carbide) layer may serve as a diffusion barrier which retards the out-diffusion of Si, thereby reducing the presence of Si in the reaction product. The amount of Si that can be present in the TiN may be limited by its solid solubility therein. The depletion of Al in the reaction product is suggested to result from evaporation due to its high vapor pressures at the temperatures studied. According to the interfaces from the de-bonded bulk diffusion couples, the adhesion of the TiN layer to the  $Si_3N_4$  appears to be better than to the  $Ti_3Al$ ; most of the diffusion couples de-bonded by exposing the bare  $Ti_3Al(Nb)$ . The thermodynamic driving force for the  $Ti_3Al/Si_3N_4$  solid state reactions at 1200 °C is attributed to the negative Gibbs free energy of the TiN formation. Based on literature thermochemistry data, the overall free energy of the reaction has a negative value.

Table 5-1 PHASES IDENTIFIED BY ELECTRON DIFFRACTION

<u>Compound</u>	<u>Lattice Type</u>	<u>Lattice Parameters</u>	<u>Space Group</u>
Nb <sub>5</sub> Si <sub>4</sub> C	Hexagonal	$a_0=b_0=0.7536 \text{ nm}$ $c_0=0.5249 \text{ nm}$ $\alpha=\beta=90^\circ, \gamma=120^\circ$	P6 <sub>3</sub> /mcm
Nb <sub>5</sub> Si <sub>3</sub>	Orthorhombic	$a_0=b_0=0.6570 \text{ nm}$ $c_0=1.1884 \text{ nm}$ $\alpha=\beta=\gamma=90^\circ$	I4/mcm
Nb <sub>2</sub> C (Disordered)	Hexagonal	$a_0=b_0=0.3129 \text{ nm}$ $c_0=0.4920 \text{ nm}$	P6 <sub>3</sub> /mmc
Nb <sub>2</sub> C (Ordered)	Hexagonal	$a_0=b_0=0.5240 \text{ nm}$ $c_0=0.4920 \text{ nm}$	P6 <sub>3</sub> /mmc
NbO	Cubic	$a_0=b_0=c_0=0.4210 \text{ nm}$ $\alpha=\beta=\gamma=90^\circ$	Pm3m
Nb	Cubic	$a_0=b_0=c_0=0.3300 \text{ nm}$ $\alpha=\beta=\gamma=90^\circ$	Im3m
$\alpha$ -SiC	Hexagonal	$a_0=b_0=0.3081 \text{ nm}$ $c_0=1.5117 \text{ nm}$ $\alpha=\beta=90^\circ, \gamma=120^\circ$	P6 <sub>3</sub> mc
C, Graphite	Hexagonal	$a_0=b_0=0.2464 \text{ nm}$ $c_0=0.6711 \text{ nm}$ $\alpha=\beta=90^\circ, \gamma=120^\circ$	P6 <sub>3</sub> /mmc

Table 5-2 FREE ENERGY OF FORMATION OF VARIOUS COMPOUNDS

<u>Compound</u>	<u>Temperature (°C)</u>	<u><math>\Delta G_f</math> (kJ/mole)</u>	<u>Reference</u>
SiO <sub>2</sub> (glass)	1100	-607.1	55
SiO <sub>2</sub> (quartz)	1100	-632.6	55
NbO	1100	-291.4	56
NbO <sub>2</sub>	1100	-552.9	56
NbSi <sub>2</sub>	1100	-130.2	56
Nb <sub>5</sub> Si <sub>3</sub>	1100	-468.6	56
Nb <sub>2</sub> C	1100	-177.6	56
NbC	1100	-136.8	56
SiC	1100	-62.4	56
Nb <sub>5</sub> Si <sub>4</sub> C	1100	-582	est.
SiC	1160	-62.0	56
Si <sub>3</sub> N <sub>4</sub>	1160	-271.1	56
Ni <sub>7</sub> Si <sub>13</sub>	1160	-564.1 (est.)	56
NiSi	1160	-84.7 (est.)	56
SiC	725	-65.3	56
Si <sub>3</sub> N <sub>4</sub>	725	-413.5	56
Ni <sub>7</sub> Si <sub>13</sub>	725	-611.1	56
NiSi	725	-83.3	56
SiC	600	-66.2	56
Si <sub>3</sub> N <sub>4</sub>	600	-455.8	56
Al <sub>4</sub> C <sub>3</sub>	600	-184.0	56
AlN	600	-228.8	56

**Table 5-3 ANNEALING CONDITIONS, DIFFUSION PHENOMENA, AND MAJOR REACTION PRODUCTS FOR VARIOUS DIFFUSION COUPLES**

<u>Diffusion Couple</u>	<u>Annealing Temperature</u>	<u>Annealing Time (h)</u>	<u>Diffusion Phenomena</u>	<u>Reaction Product</u>
Nb/SiC	1000°C	4	Planar interfaces	Nb <sub>2</sub> C, Nb <sub>5</sub> Si <sub>3</sub> C, NbC, Nb <sub>5</sub> Si <sub>4</sub> C
Nb/SiC	1100°C	4	Planar interfaces	Nb <sub>2</sub> C, Nb <sub>5</sub> Si <sub>4</sub> C, Nb <sub>5</sub> Si <sub>3</sub> C,
Nb/SiC	1200°C	6, 18, 32, 48	Planar interface, Homo- and heterogeneous nucleation/growth of reaction products	NbC <sub>x</sub> , NbSi <sub>y</sub> C <sub>z</sub> , NbC <sub>x</sub>
Co/SiC	1100°C	6	Localized interfacial melting, Planar interface, C-PFZ and R-CPZ	Co <sub>2</sub> Si, C
Co/SiC	1210°C	4	Interfacial melting, Non-planar interface, C-PFZ and R-CPZ	Co(Si), Co <sub>2</sub> Si, C
Ni/SiC	1100°C	6	Localized interfacial melting, Planar interface, C-PFZ, R-CPZ and M-CPZ	Ni <sub>3</sub> Si, Ni <sub>5</sub> Si <sub>2</sub> , C
Ni/SiC	1170°C	4	Interfacial melting, non-planar interface, C-PFZ, R-CPZ and M-CPZ	Ni <sub>31</sub> Si <sub>12</sub> , C
Pt/SiC	800°C	12	Limited reactions No bonding	----
Pt/SiC	900°C	5	Interfacial melting, non-planar interface, M-CPZ and R-CPZ	Pt <sub>3</sub> Si, C
Pt/SiC	1000°C	5	Interfacial melting, non-planar interface, M-CPZ and R-CPZ	Pt <sub>2</sub> Si, C
Pt/SiC	1100°C	4	Interfacial melting, non-planar interface, M-CPZ and R-CPZ	Pt <sub>3</sub> Si, Pt <sub>12</sub> Si <sub>5</sub> Pt <sub>2</sub> Si, PtSi, C
SS/SiC	1125°C	8	Interfacial melting non-planar interface, M-CPZ, R-CPZ and G.B.-CPZ	Cr <sub>23</sub> C <sub>6</sub> , C, (Ni,Fe)Cr <sub>x</sub> Si <sub>y</sub>

G.B.-CPZ: grain boundary carbide precipitation zone

Table 5-4      GIBBS FREE ENERGY OF DECOMPOSITION OF SiC AT VARIOUS TEMPERATURES

<u>Reaction</u>	<u>Temperature(°C)</u>	<u>ΔG (kcal/mole)</u>
SiC → Si + C	800	12.1
	900	12.0
	1000	11.9
	1100	11.8
	1200	11.7

**Table 5-5 EDS COMPOSITIONAL ANALYSIS OF SIC AND STAINLESS STEEL.**  
(All values in wt%)

<u>STAINLESS STEEL</u>		<u>MODULATED CARBON PRECIPITATION ZONE</u>			<u>SILICON CARBIDE</u>		
(Location): ----->		6	5	4	3	2	1
	(Bulk comp.)						
Si	0	28.24	29.41	29.29	49.96	49.97	50.00
C	0	0	0	0	49.94*	49.97*	49.98*
Fe	44.8	32.35	28.78	23.38	0.04	0.03	0
Ni	30.1	35.45	39.10	45.52	0.06	0.03	0.02
Cr	23.73	3.96	2.72	1.81	0	0	0
Ti	0.5	0	0	0	0	0	0
Mn	0.9	0	0	0	0	0	0

\* The concentration of C was obtained by ZAF calculations based on an assumption of stoichiometric SiC

**Table 5-6**      **GIBBS FREE ENERGY OF FORMATION OF SELECTED METAL CARBIDES AT 1400 K**

<u>Carbides</u>	<u>Gibbs Free Energy (Kcal/mole)</u>
$\text{Cr}_{23}\text{C}_6$	-111
$\text{Cr}_4\text{C}$	- 23
$\text{Cr}_7\text{C}_3$	- 17
$\text{Cr}_3\text{C}_2$	- 3
$\text{Fe}_3\text{C}$	+ 6
$\text{Co}_2\text{C}$	+ 2 at 1200 K data not available at $T > 1200 \text{ K}$
$\text{Ni}_3\text{C}$	+ 7 at 1000 K data not available at $T > 1000 \text{ K}$



**Table 5-7 REACTION PATTERNS AND REACTION PRODUCTS FORMED IN SELECTED METAL/SiC SYSTEMS AT SPECIFIC TEMPERATURES<sup>#</sup>**

- 
1. SS/SiC  $\rightarrow$  SS/ G.B.-PZ ( $\text{Cr}_{23}\text{C}_6$ )/ C-PFZ ( $(\text{Ni,Fe})\text{Cr}_x\text{Si}_y$ )/ R-CPZ ( $(\text{Ni,Fe})\text{Cr}_x\text{Si}_y$ )/ SiC
  2. Ni + SiC  $\rightarrow$  Ni/ C-PFZ ( $\text{Ni}_3\text{Si}$ )/ R-CPZ ( $\text{Ni}_5\text{Si}_2$ )/ M-CPZ ( $\text{Ni}_5\text{Si}_2$ )/ SiC
  3. Co + SiC  $\rightarrow$  Co/ C-PFZ ( $\text{Co}_2\text{Si}$ )/ R-CPZ ( $\text{Co}_2\text{Si}$ )/ SiC
  4. Fe + SiC  $\rightarrow$  Fe/ C-PFZ ( $\text{Fe}_4\text{Si}_1$ )/ R-CPZ ( $\text{Fe}_7\text{Si}_2$ )/ SiC
  5. Nb + SiC  $\rightarrow$  Nb/  $\text{NbC}_x$ /  $\text{NbSi}_y\text{C}_z$ /  $\text{NbC}_x$ / SiC
  6.  $\text{Ni}_3\text{Al}$  + SiC  $\rightarrow$   $\text{Ni}_3\text{Al}$ /  $\text{NiAl}^*$ / C-PFZ ( $\text{Ni}_{5.4}\text{Al}_1\text{Si}_2$ )/ M-CPZ ( $\text{Ni}_{5.4}\text{Al}_1\text{Si}_2$ )/ SiC
  7.  $\text{NiAl}$  + SiC  $\rightarrow$   $\text{NiAl}^*$ / R-CPZ ( $\text{Ni}_{14}\text{Al}_9\text{Si}_2$ )/ SiC
- 

<sup>#</sup> Reaction temperatures ( $^{\circ}\text{C}$ ): 1 (1200), 2 (1100), 3 (1100), 4 (850), 5 (1200), 6 (1000), 7 (1300)

\* significant amount of Si diffused into the NiAl phase

@ references: 4 (Ref.38), 6 (Ref.45), 7 (Ref.86).

**Table 5-8** CHARACTERISTICS OF THE REACTION INTERFACES AND PRODUCTS FROM VARIOUS  $Ti_3Al(Nb)/Si_3N_4$  AND  $Ti_3Al(Nb)/SiC$  DIFFUSION COUPLES ANNEALED UNDER DIFFERENT CONDITIONS

Type of diffusion couples*	Annealing conditions	Color of reaction interfaces/ reaction products
$Ti_3Al(Nb)/Si_3N_4$	1000°C/4h	white
$Ti_3Al/Si_3N_4$	1000°C/4h $TiSi_yN_z$	white/ $TiSi_y(Al,N)_z$ , $Ti(Si,N)_yAl_z$
$Ti_3Al(Nb)/Si_3N_4$	1200°C/6h	gold/TiN
$Ti_3Al(Nb)/Si_3N_4$	1200°C/16h	gold/TiN
$Ti_3Al(Nb)/Si_3N_4$	1200°C/48h	gold/TiN
$Ti_3Al/Si_3N_4$	1200°C/4h	light brown/TiN
$Ti_3Al/Si_3N_4$	1200°C/6h	light brown/TiN
$Ti_3Al(Nb)/Si_3N_4$	1300°C/12h	gold/TiN
$Ti_3Al/SiC$	1000°C/4h	metallic/ $TiAl_xSi_y$ , $TiSi_xC_y$
$Ti_3Al/SiC$	1200°C/4h	metallic/ $TiSi_xC_y$

**Table 5-9 GIBBS FREE ENERGIES OF FORMATION OF VARIOUS COMPOUNDS AT 1300 AND 1500 K**

Compound	Gibbs free energy* (kcal/mole)	Reference
$1/3 \text{ Si}_3\text{N}_4 \rightarrow \text{Si} + 2/3 \text{ N}_2(\text{g})$	+25 (1300 K), +20 (1500 K)	101 and 102
$\text{SiC} \rightarrow \text{Si} + \text{C}$	+12, +12	101 and 102
$\text{Ti}_3\text{Al} \rightarrow 3 \text{ Ti} + \text{Al}(\text{l})$	N.A. ; +19 (960 K)@	; 103
$\text{TiAl} \rightarrow \text{Ti} + \text{Al}(\text{l})$	+14, +13; +16 (960 K)@	102; 103
$\text{TiAl}_3 \rightarrow \text{Ti} + 3 \text{ Al}(\text{l})$	+24, +21; +34 (298 K)@	102; 103
$\text{Ti} + 1/2 \text{ N}_2(\text{g}) \rightarrow \text{TiN}$	-51, -47	102 and 102
$\text{Ti} + 2 \text{ Si} \rightarrow \text{TiSi}_2$	-30, -30	102
$\text{Ti} + 3/5 \text{ Si} \rightarrow 1/5 \text{ Ti}_5\text{Si}_3$	-28, -28	102
$\text{Ti} + \text{Si} \rightarrow \text{TiSi}$	-31, -31	102
$\text{Ti} + \text{C} \rightarrow \text{TiC}$	-41, -40	101 and 102

\* The values were round off to their nearest 1 kcal

@ Values calculated based on  $\Delta G = \Delta H - T\Delta S$

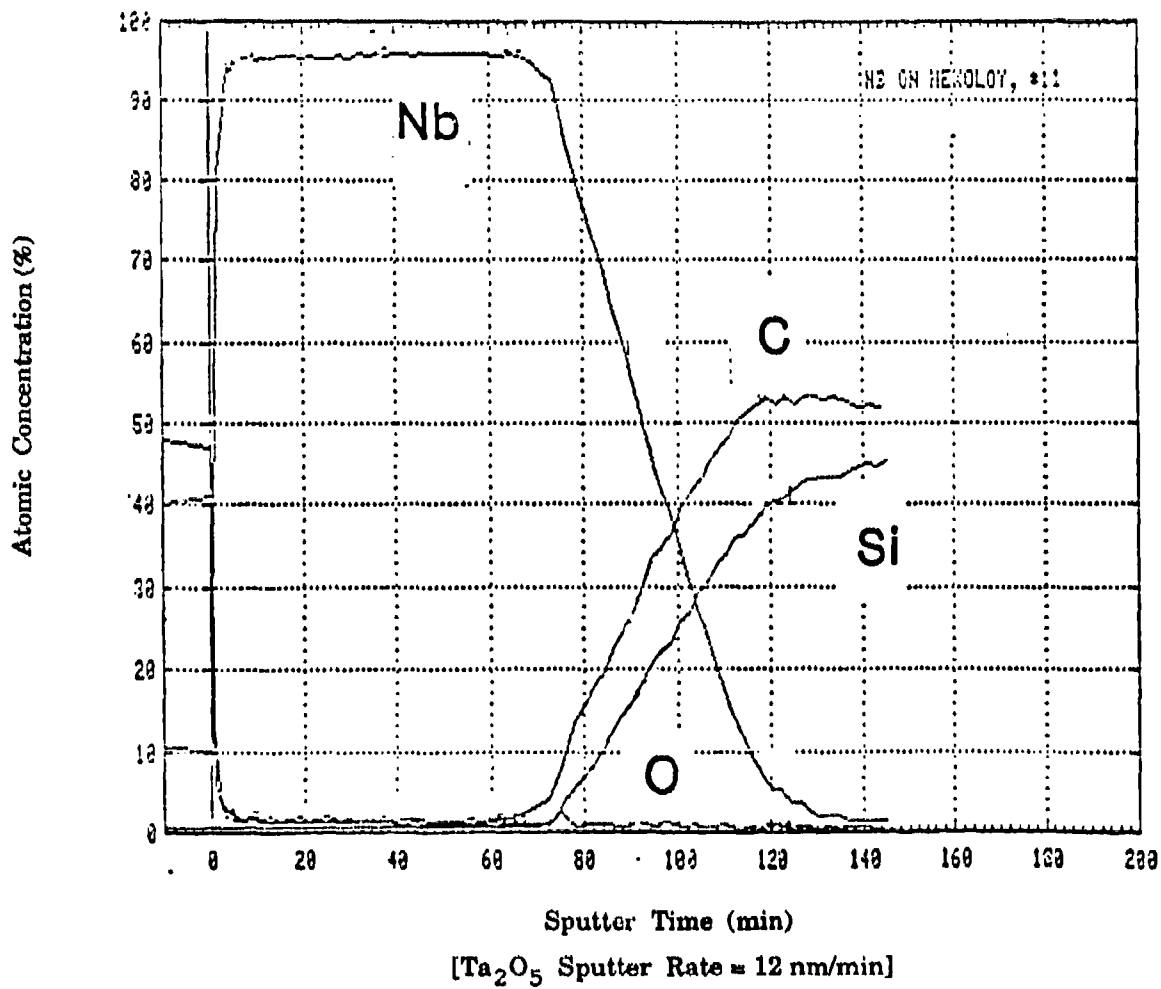


Fig. 5.1 AES depth profile of 1.3  $\mu\text{m}$  Nb film on polycrystalline SiC, in the as-deposited condition.

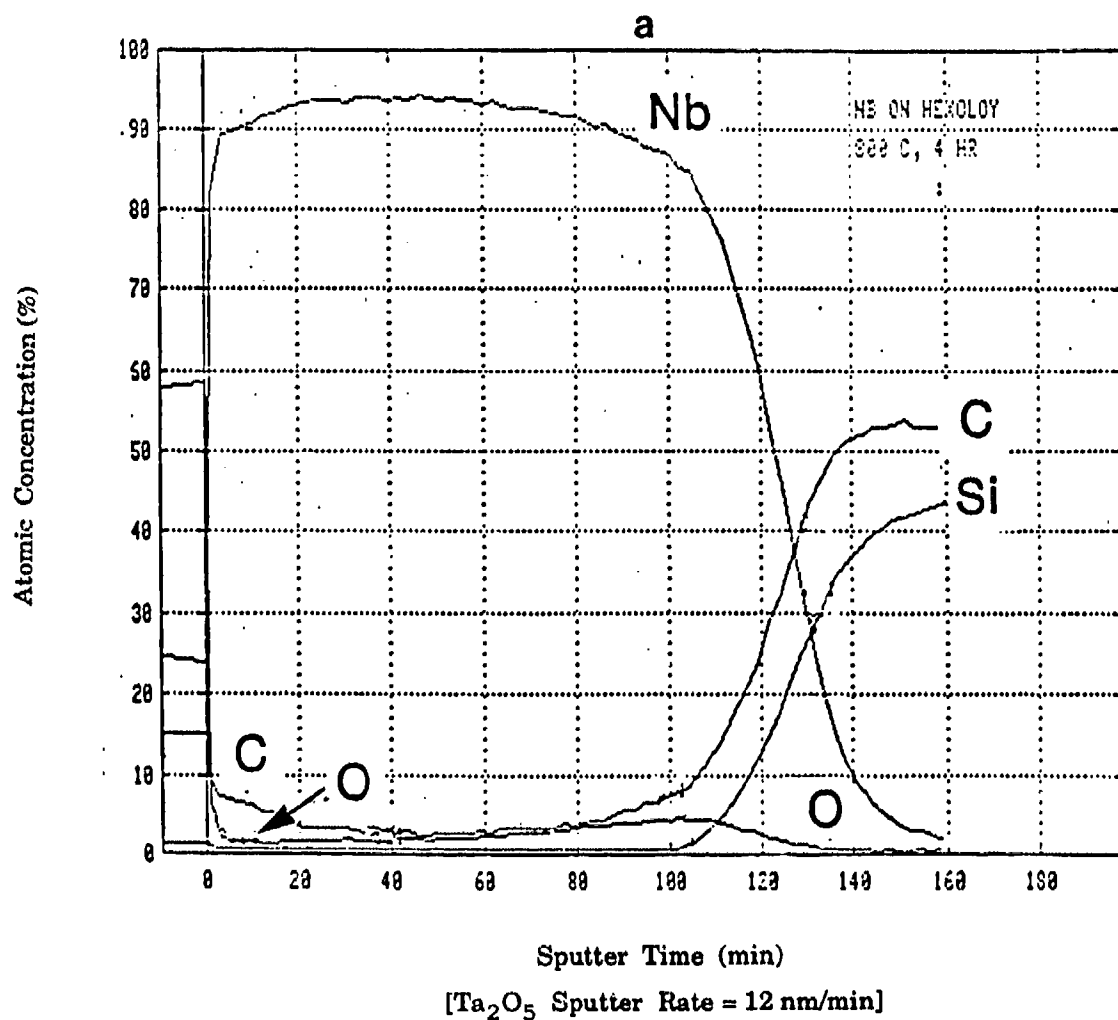
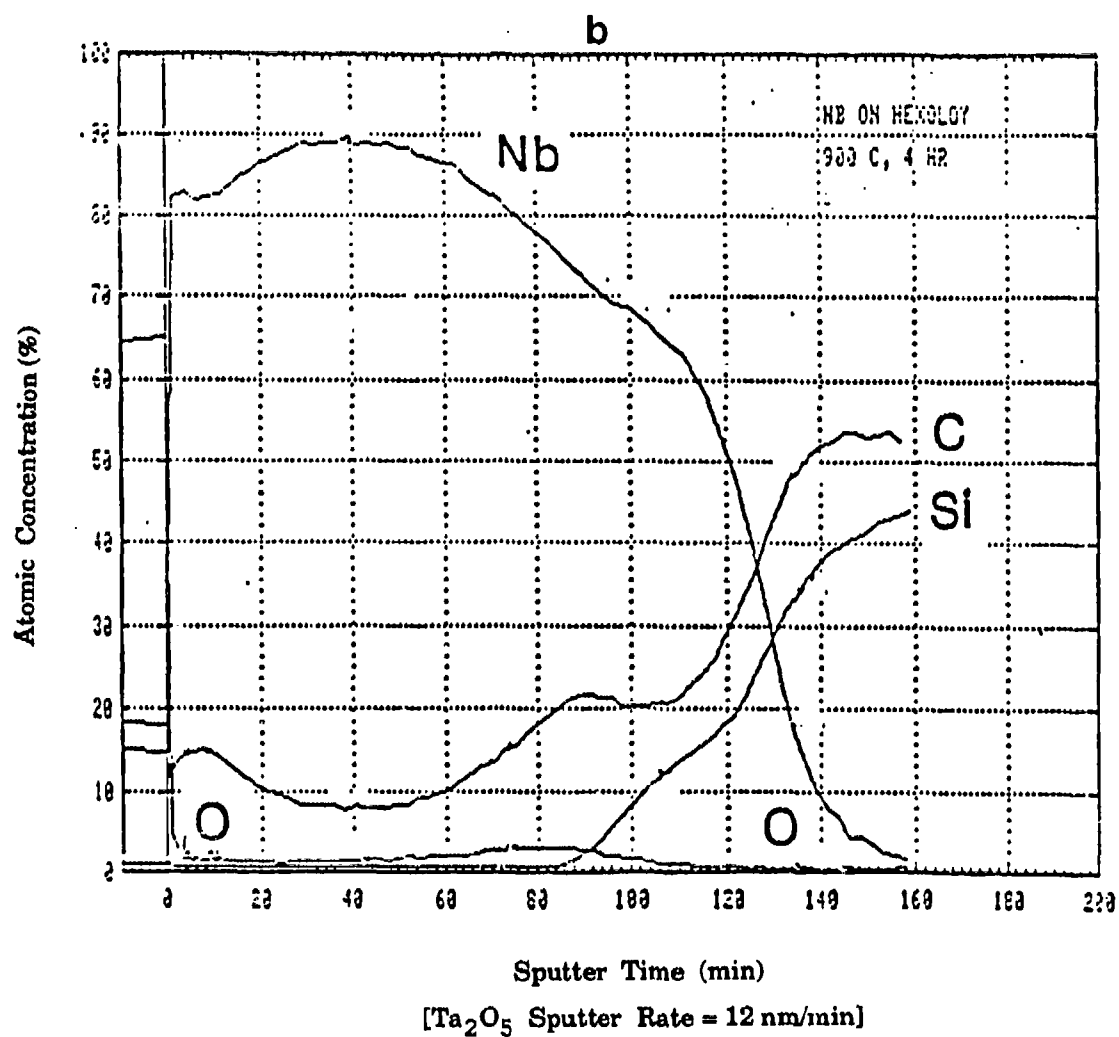
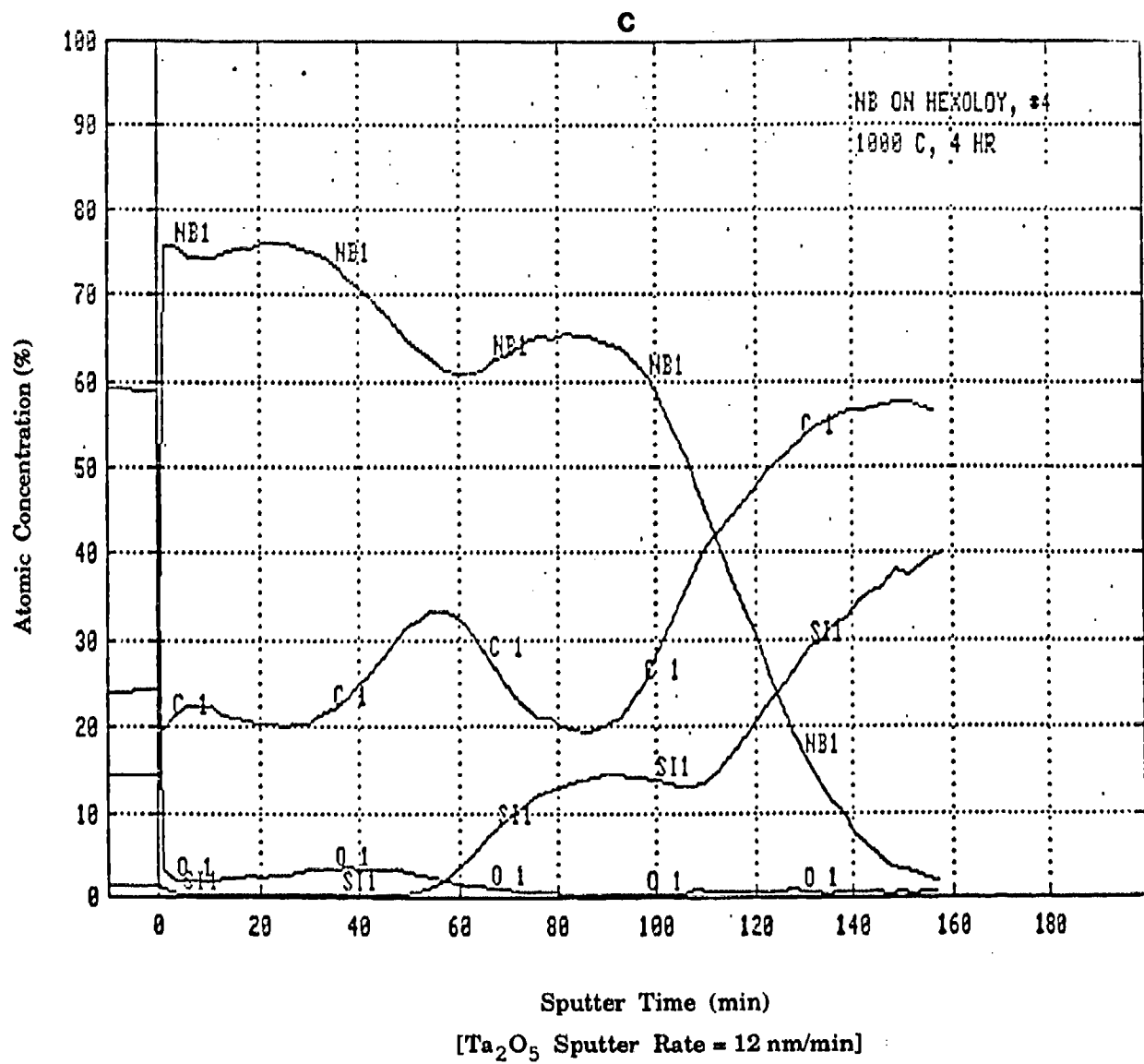


Fig. 5.2

AES depth profiles of Nb films (1.3  $\mu\text{m}$  thickness) on polycrystalline SiC, in (a) the as-deposited condition, and after annealing for 4 h at (b) 800°C, (c) 900°C and (d) 1000°C.





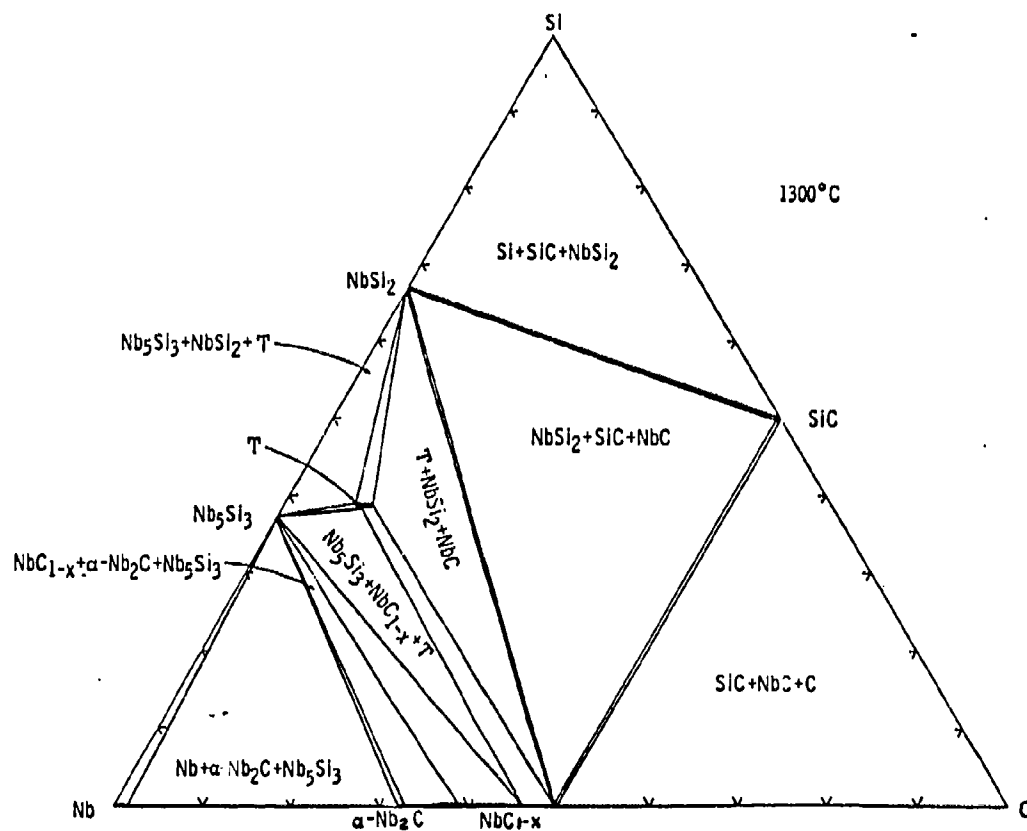


Fig. 5.3 Isothermal section of the Nb-Si-C phase diagram at 1300°C.



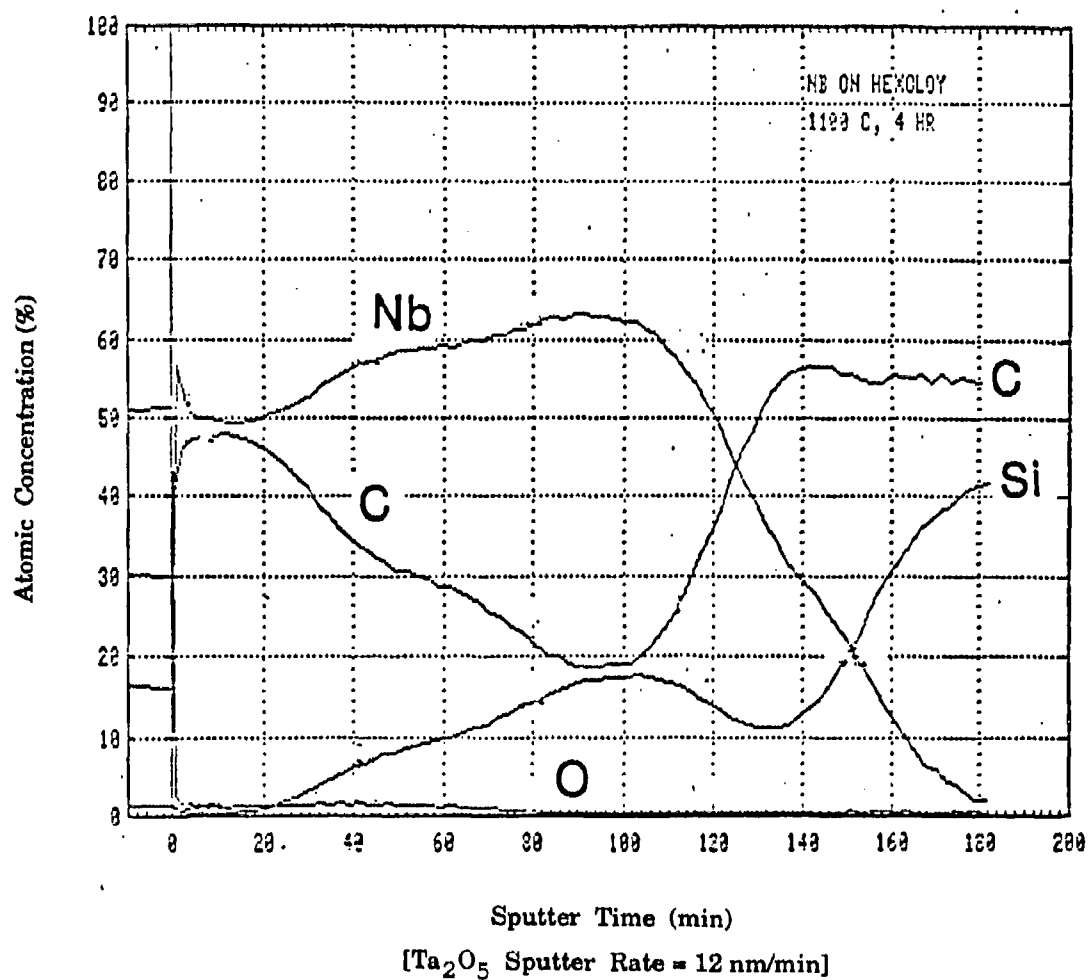


Fig. 5.4 AES profile from Nb/SiC, annealed 4 h at 1100°C.

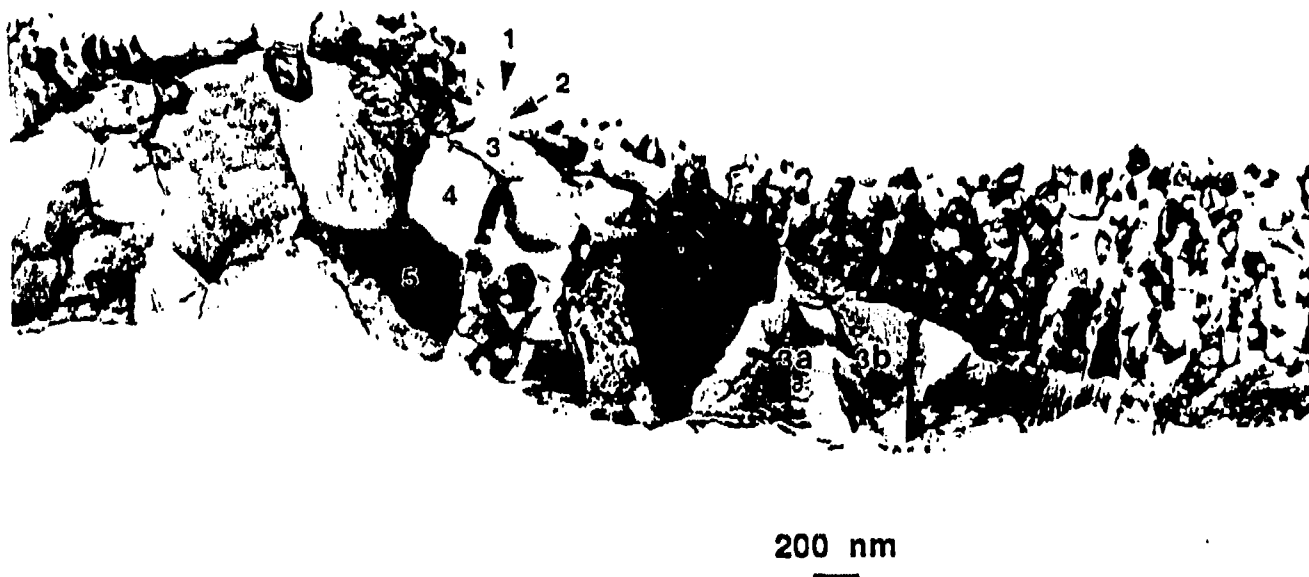


Fig. 5.5 Representative TEM bright field micrograph of the reaction zone between niobium and silicon carbide (hexoloy), annealed 4 h at 1100°C.

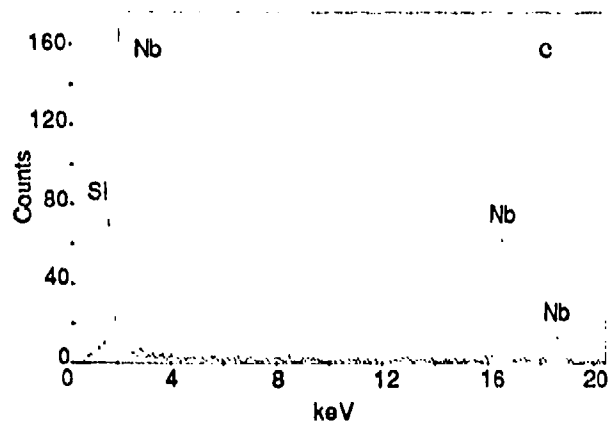
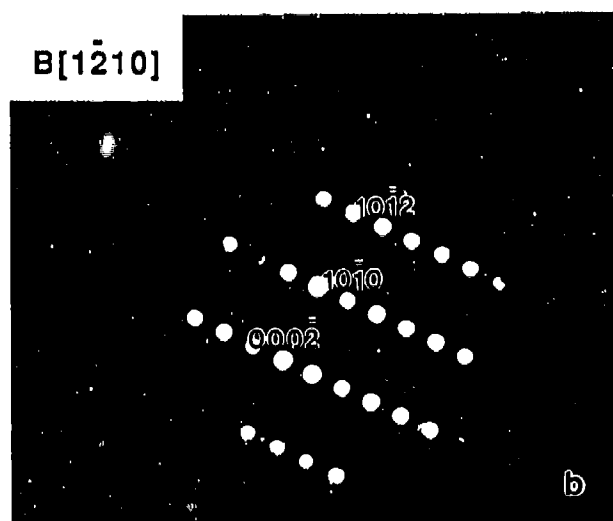


Fig. 5.6

(a) TEM bright field micrograph, (b) convergent beam electron diffraction pattern consistent with ternary  $\text{Nb}_5\text{Si}_4\text{C}$  phase in a  $[1210]$  orientation and (c) energy dispersive x-ray spectra from grain 1.

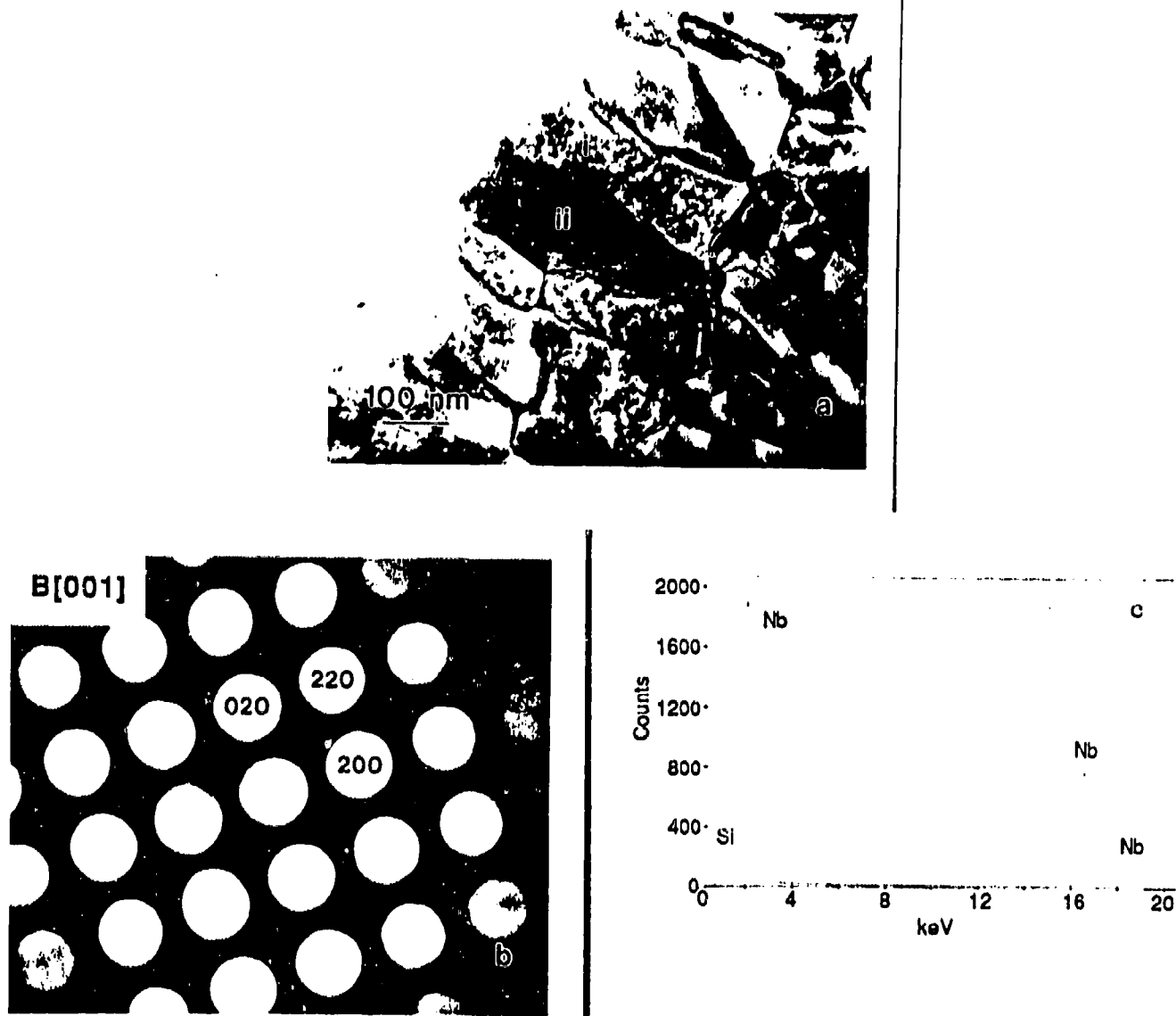


Fig. 5.7

(a) Bright field TEM micrograph. Grains I and II identified by electron diffraction as NbC. (b) Convergent beam electron diffraction pattern and (c) energy dispersive x-ray spectra from grain II.

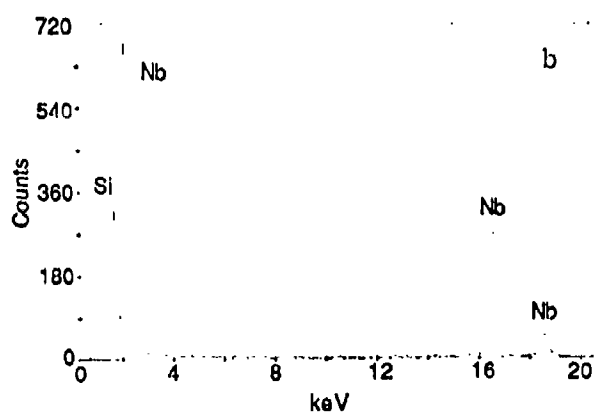
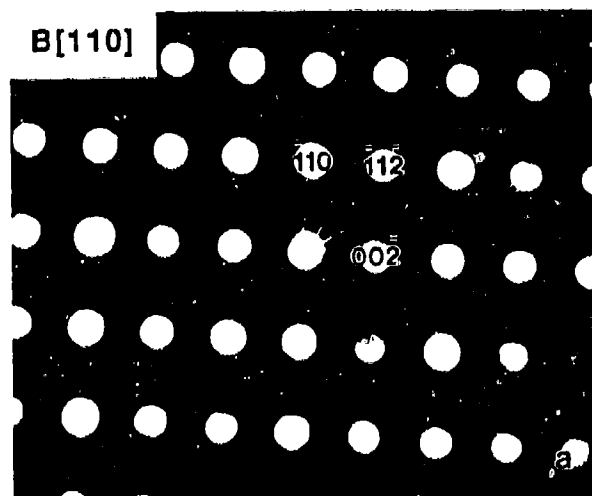


Fig. 5.8

(a) Convergent beam electron diffraction pattern and (b) energy dispersive x-ray spectra from grain 2. The electron diffraction pattern is consistent with  $\alpha$ -Nb<sub>5</sub>Si<sub>3</sub> in a [110] orientation.

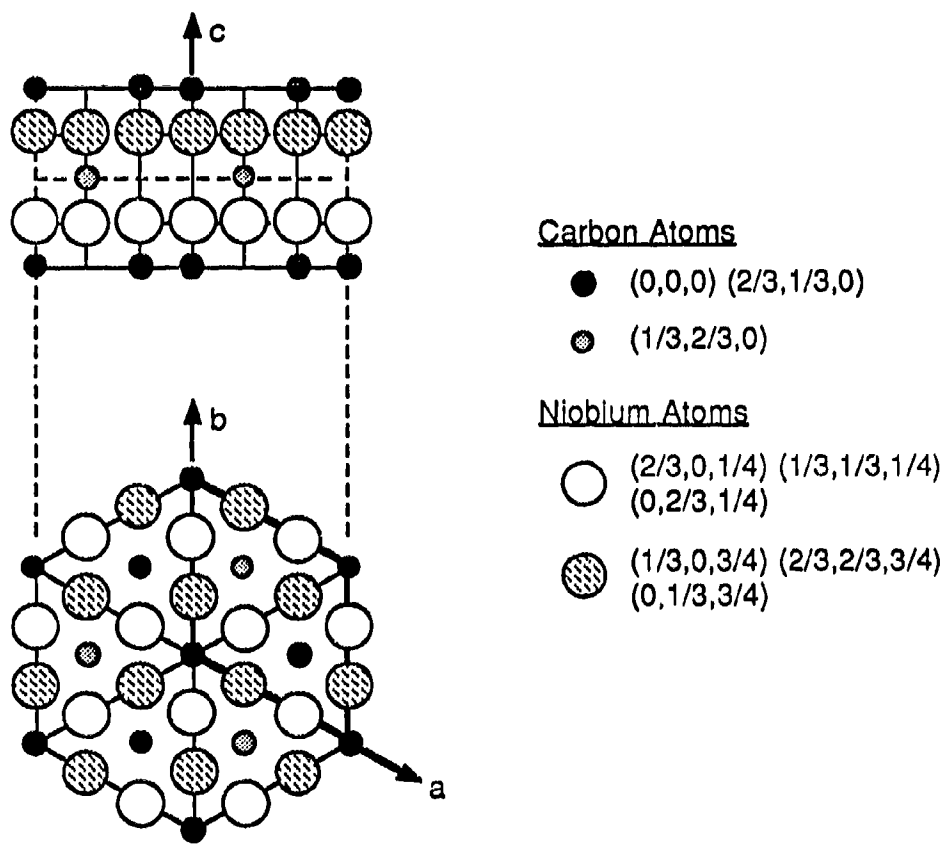


Fig. 5.9 Schematic illustration of ordered hexagonal structure of  $\text{Nb}_2\text{C}$ .

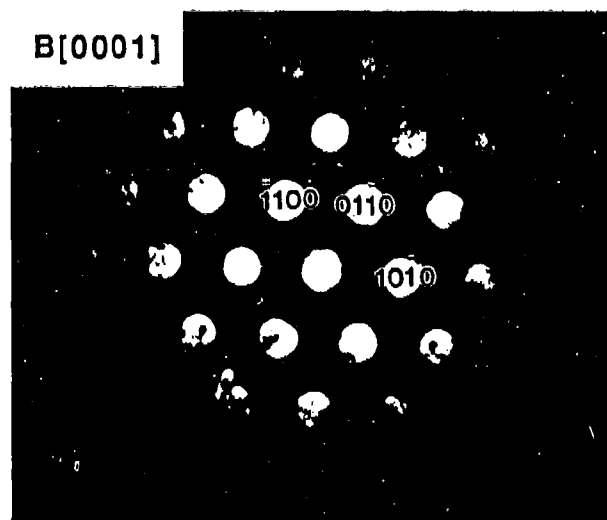


Fig. 5.10 Convergent beam electron diffraction pattern from grain 3 consistent with disordered  $\text{Nb}_2\text{C}$  in a  $[0001]$  orientation.

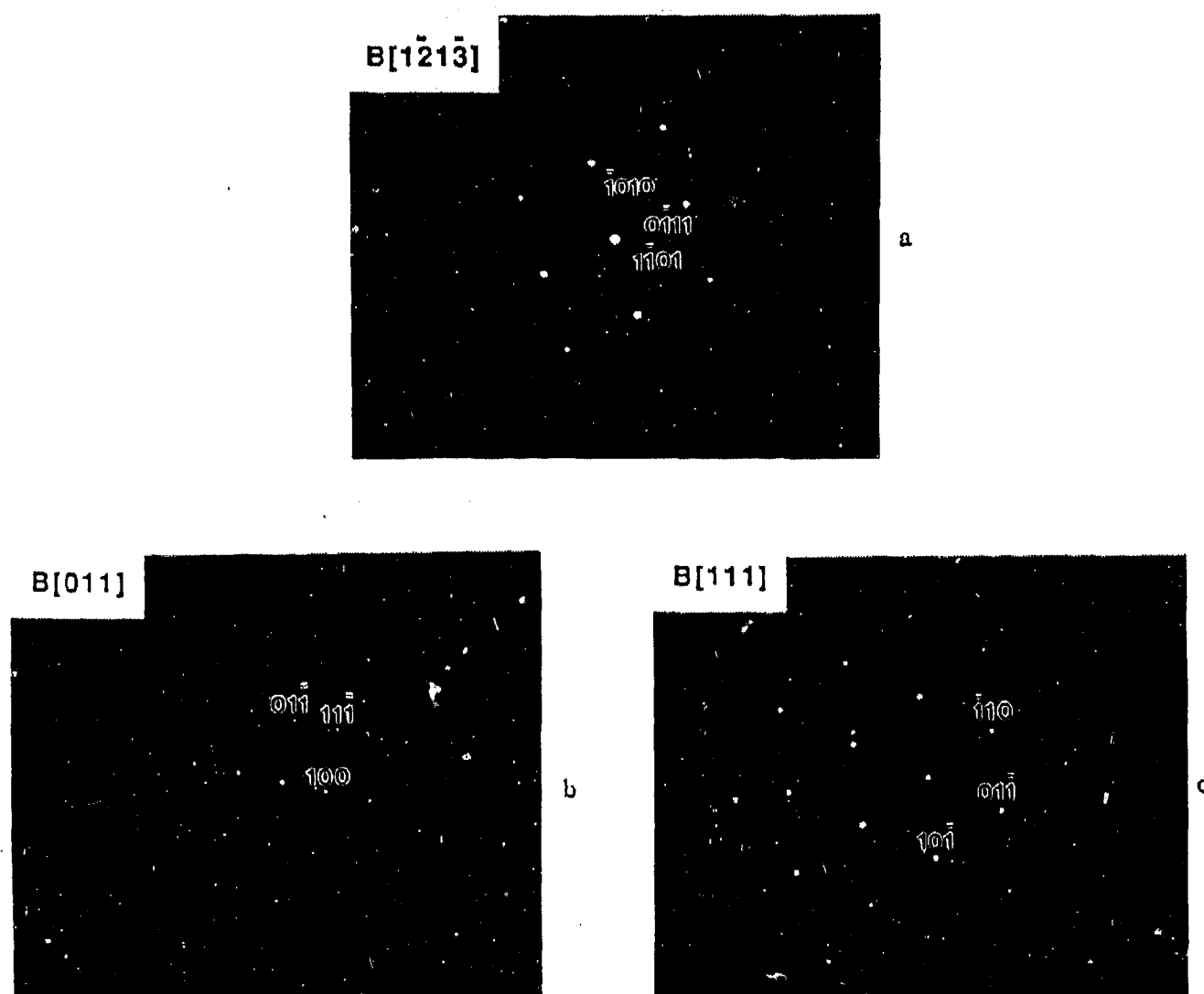


Fig. 5.11 Selected area diffraction patterns from (a) grain 3b, (b) grain 4, and (c) grain 5 in Fig. 5.5.



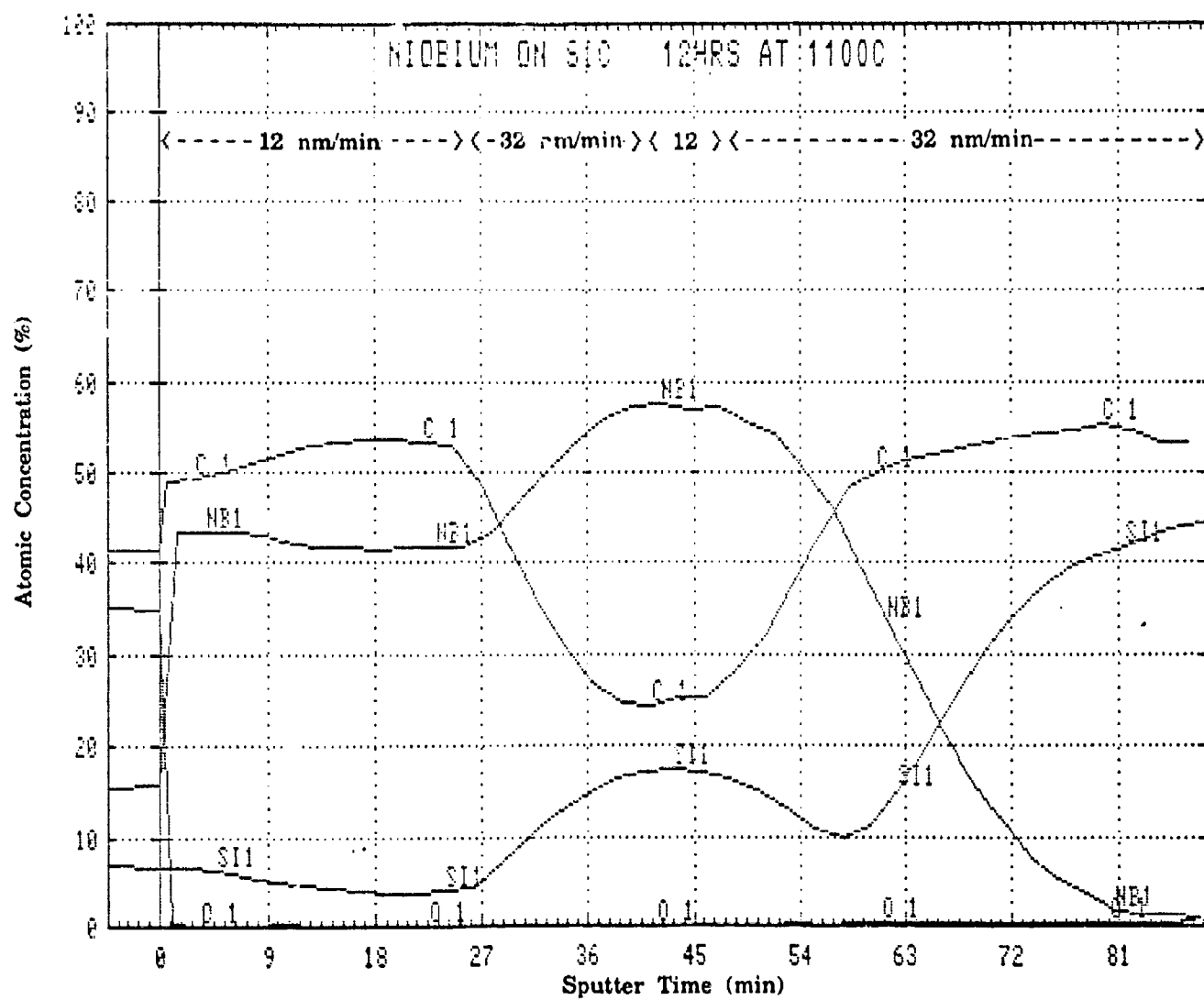


Fig. 5.12 AES depth profile of Nb/SiC, annealed 12 h at 1100°C.

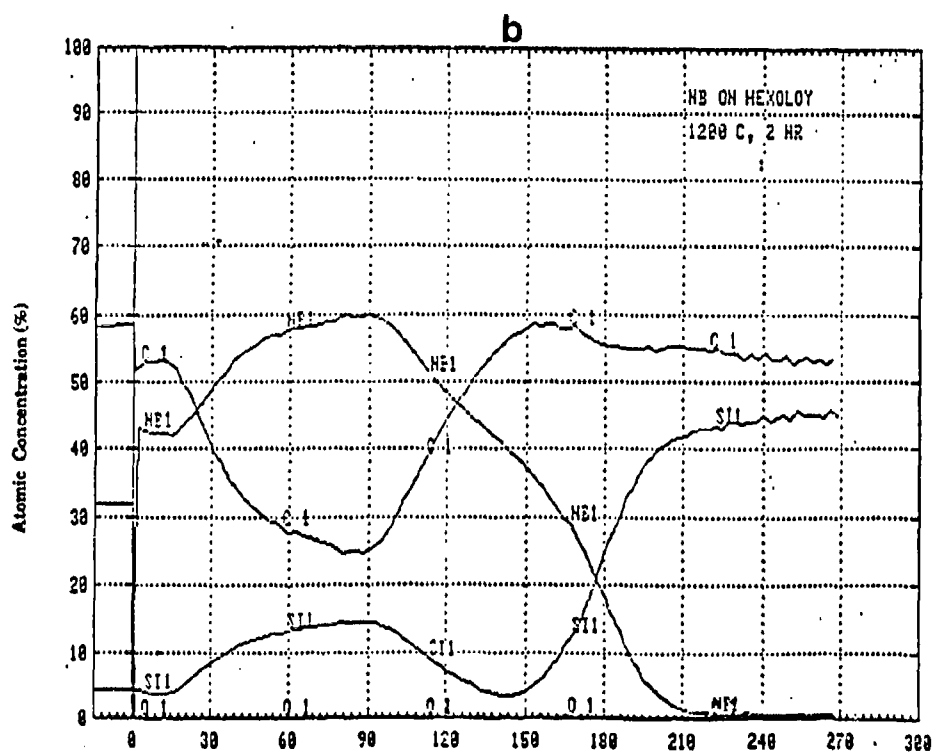
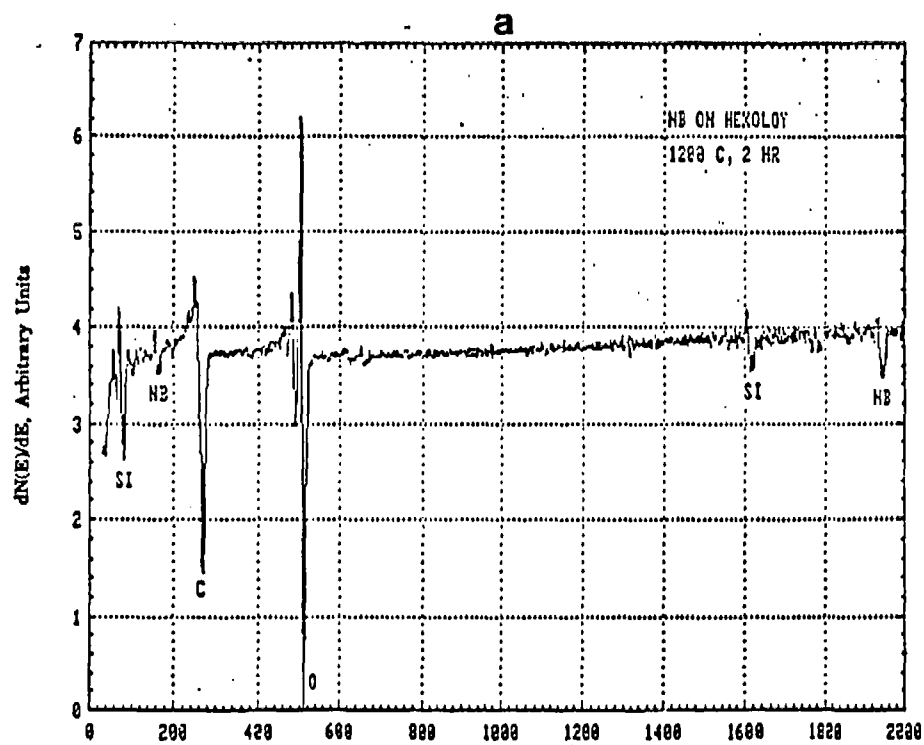


Fig. 5.13 (a) AES spectrum and (b) depth profile from Nb/SiC, annealed 2 h at 1200°C.

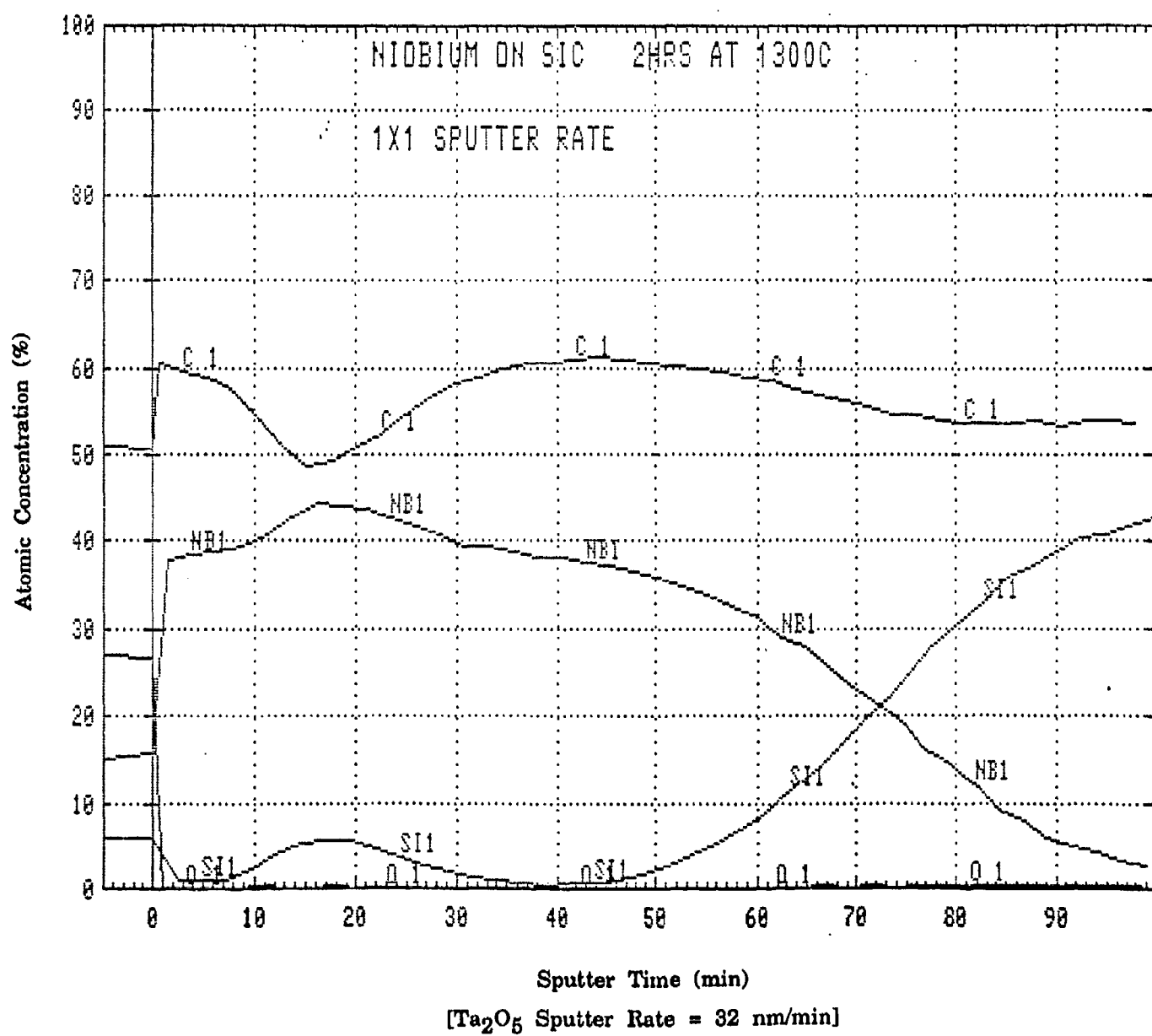


Fig. 5.14 AES depth profile of Nb/SiC, annealed 2 h at 1300°C.

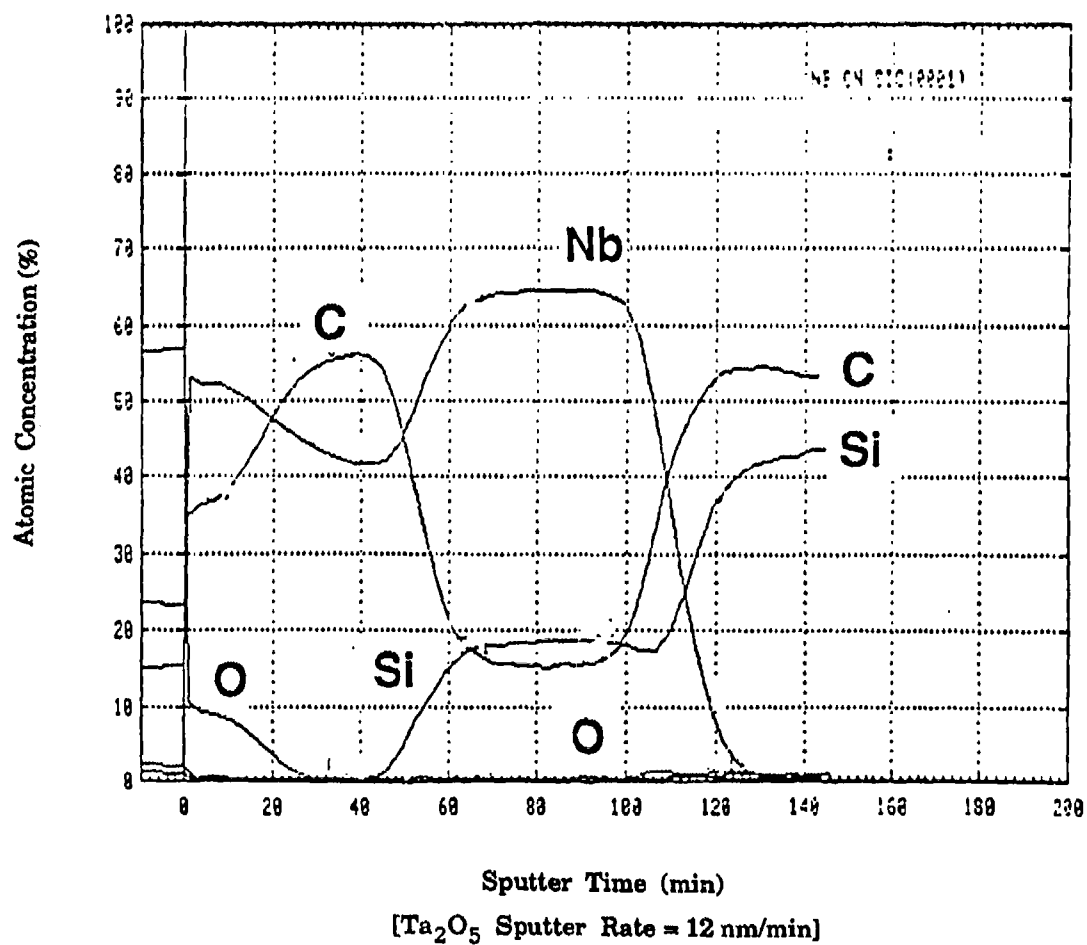


Fig. 5.15 AES profile from Nb/SiC (0001) annealed 4 h at 1100°C.

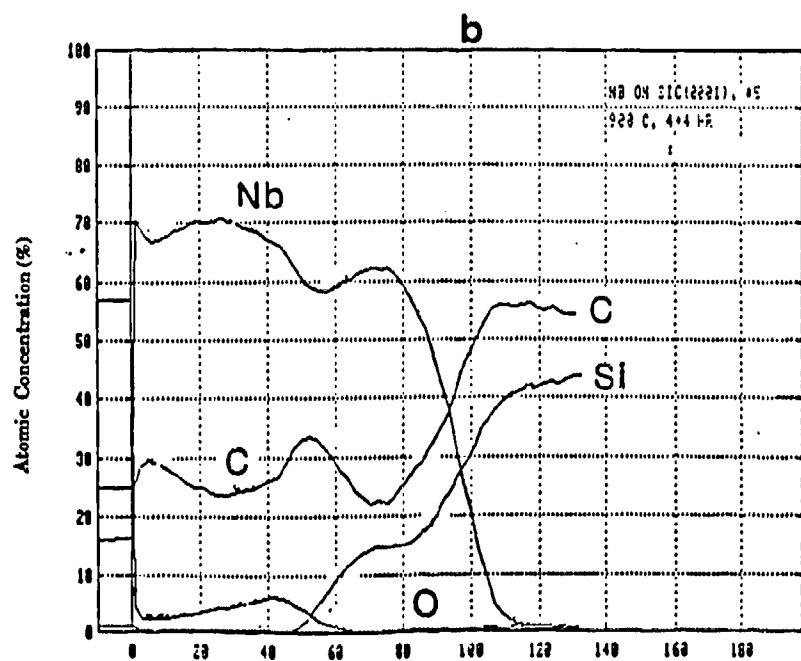
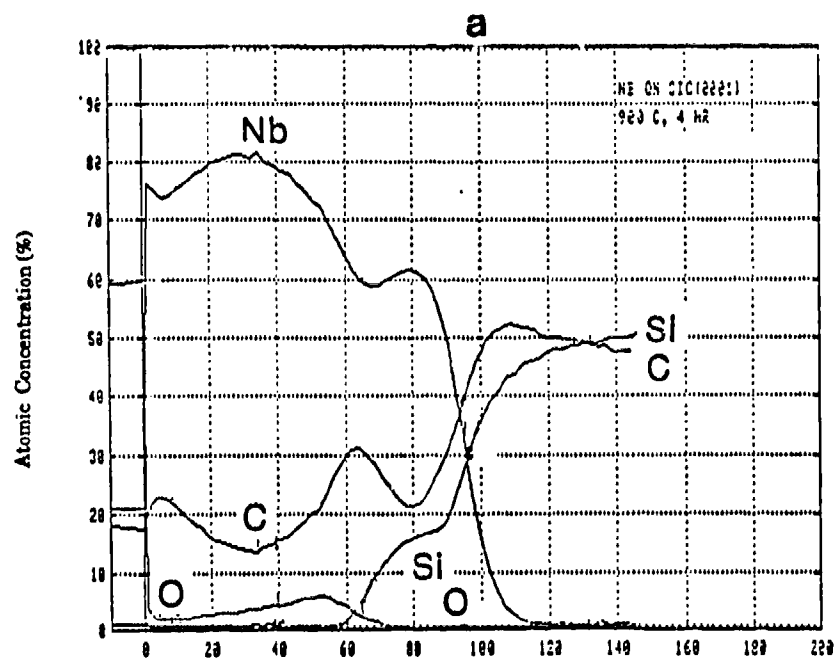


Fig. 5.16

AES depth profile of Nb/SiC (0001) annealed at 900°C for (a) 4 h and (b) 8 h. [ $\text{Ta}_2\text{O}_5$  Sputter Rate = 12 nm/min].

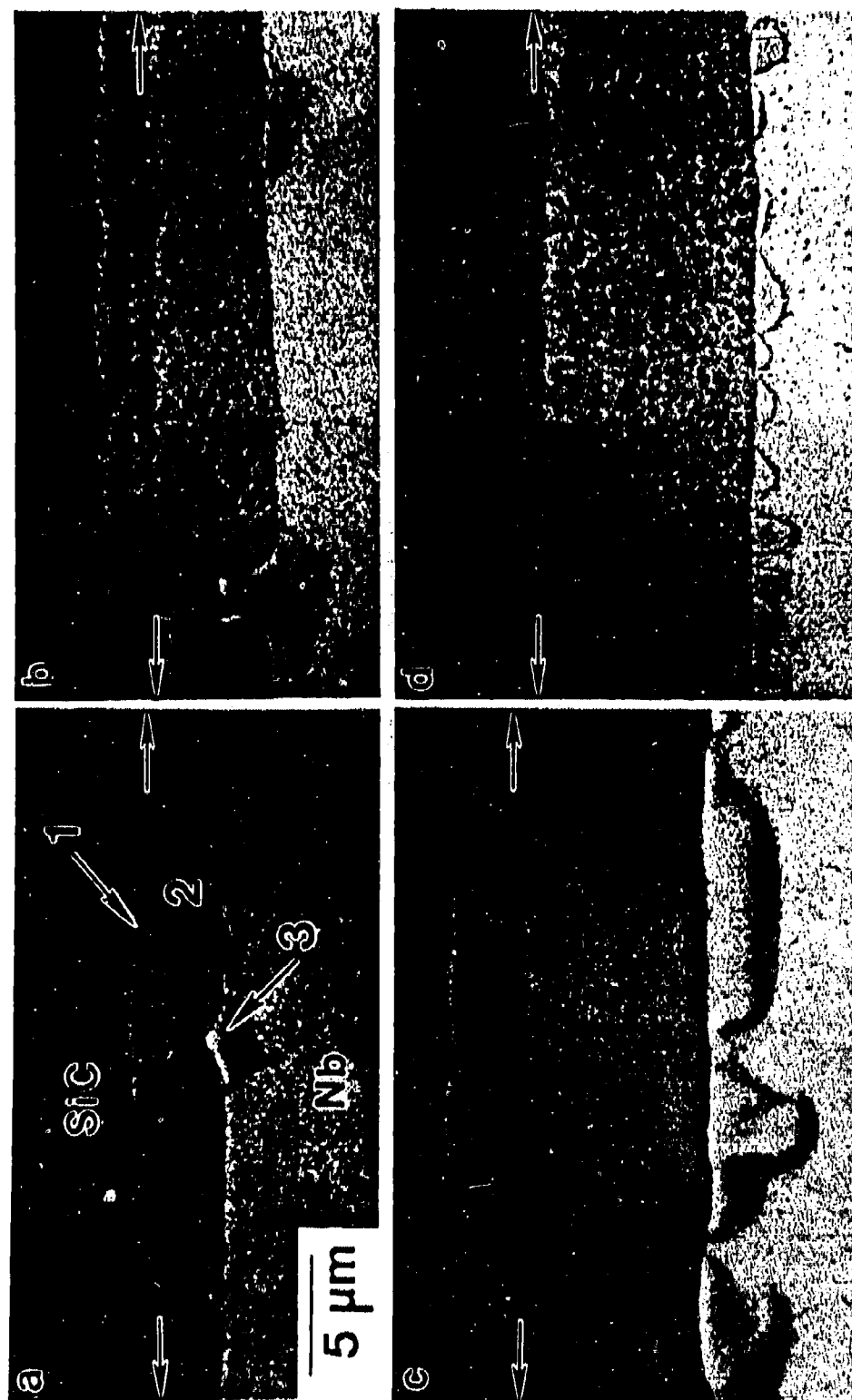


Fig. 5.17 Cross-sectional view SEM micrographs showing the growth of layered reaction products, from the Nb/SiC reactions at 1200°C, as annealing time increases from (a) 6, (b) 18, (c) 32, to (d) 48 h. The SiC and Nb components are indicated, and the original joining interfaces are marked by arrows.

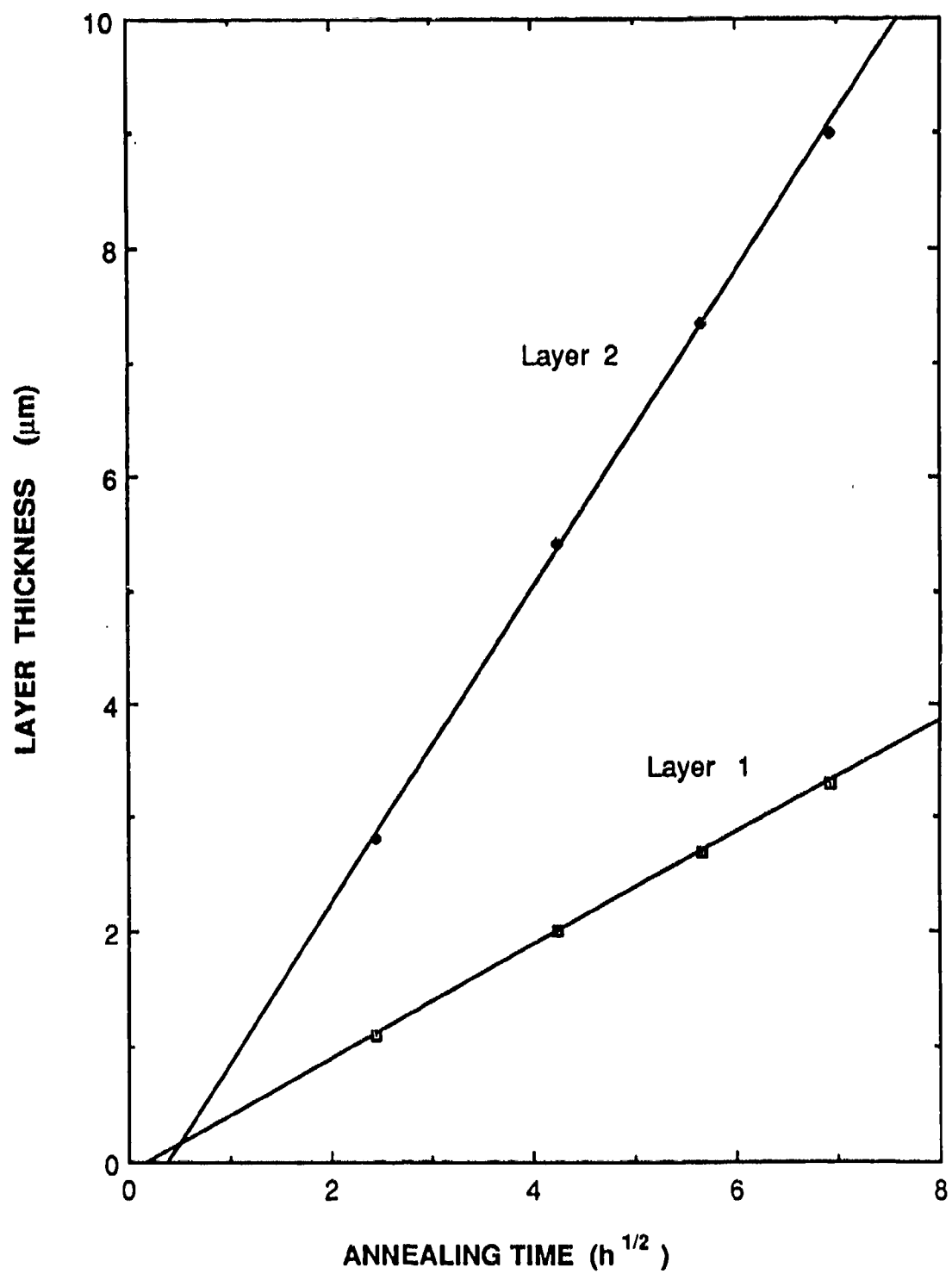


Fig. 5.18 Growth of the thicknesses of layers 1 and 2 in Nb/SiC diffusion couples at 1200°C.

## AES PROFILE OF Nb/Al<sub>2</sub>O<sub>3</sub> SPECIMEN

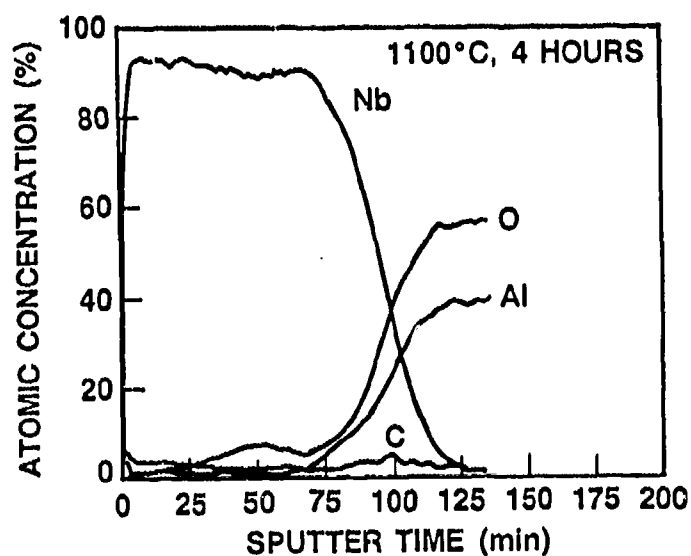
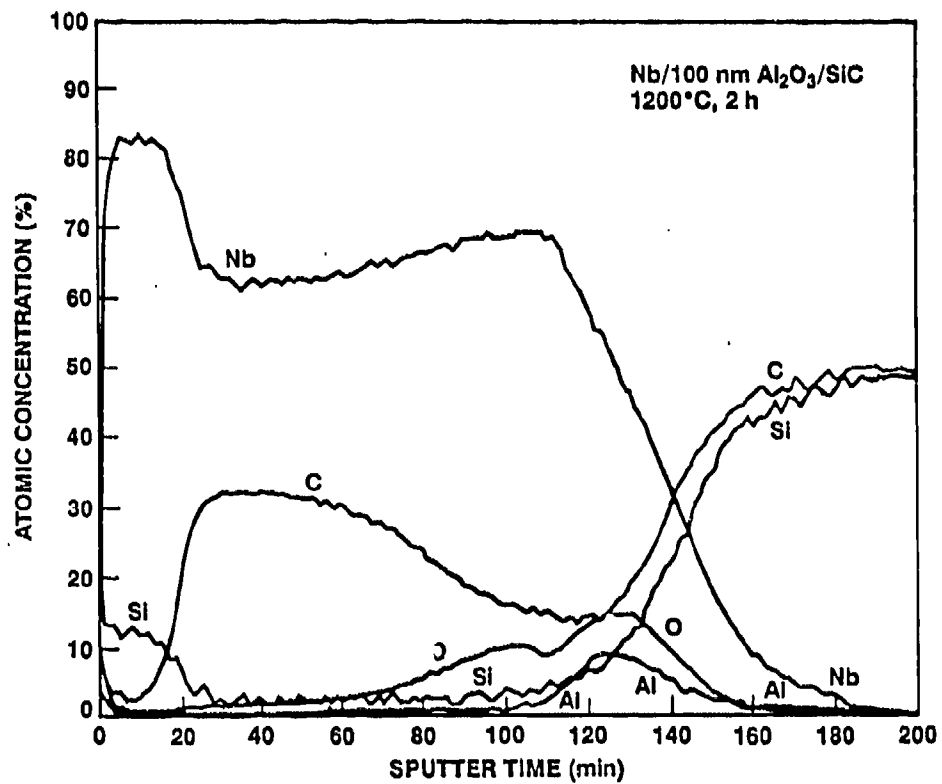
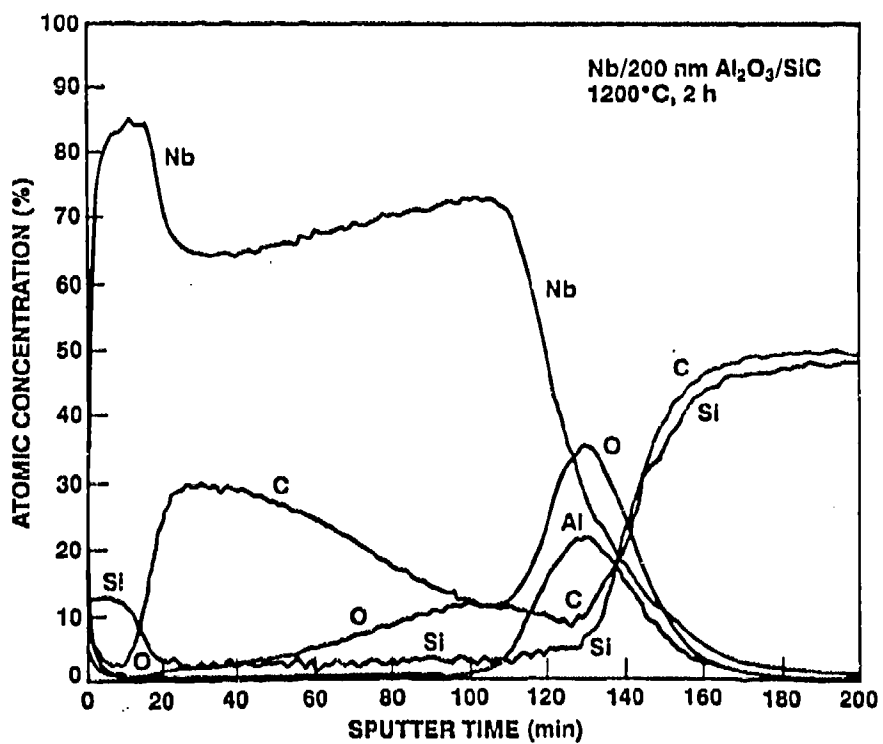


Fig. 5.19 AES depth profile of (a) Nb/Al<sub>2</sub>O<sub>3</sub> specimen and Nb/Al<sub>2</sub>O<sub>3</sub>/SiC specimen annealed 2 h at 1200°C, with Al<sub>2</sub>O<sub>3</sub> layer thickness of (b) 100 nm, and (c) 200 nm. [Equivalent Ta<sub>2</sub>O<sub>5</sub> sputter rate is 12 nm/min].





b



c

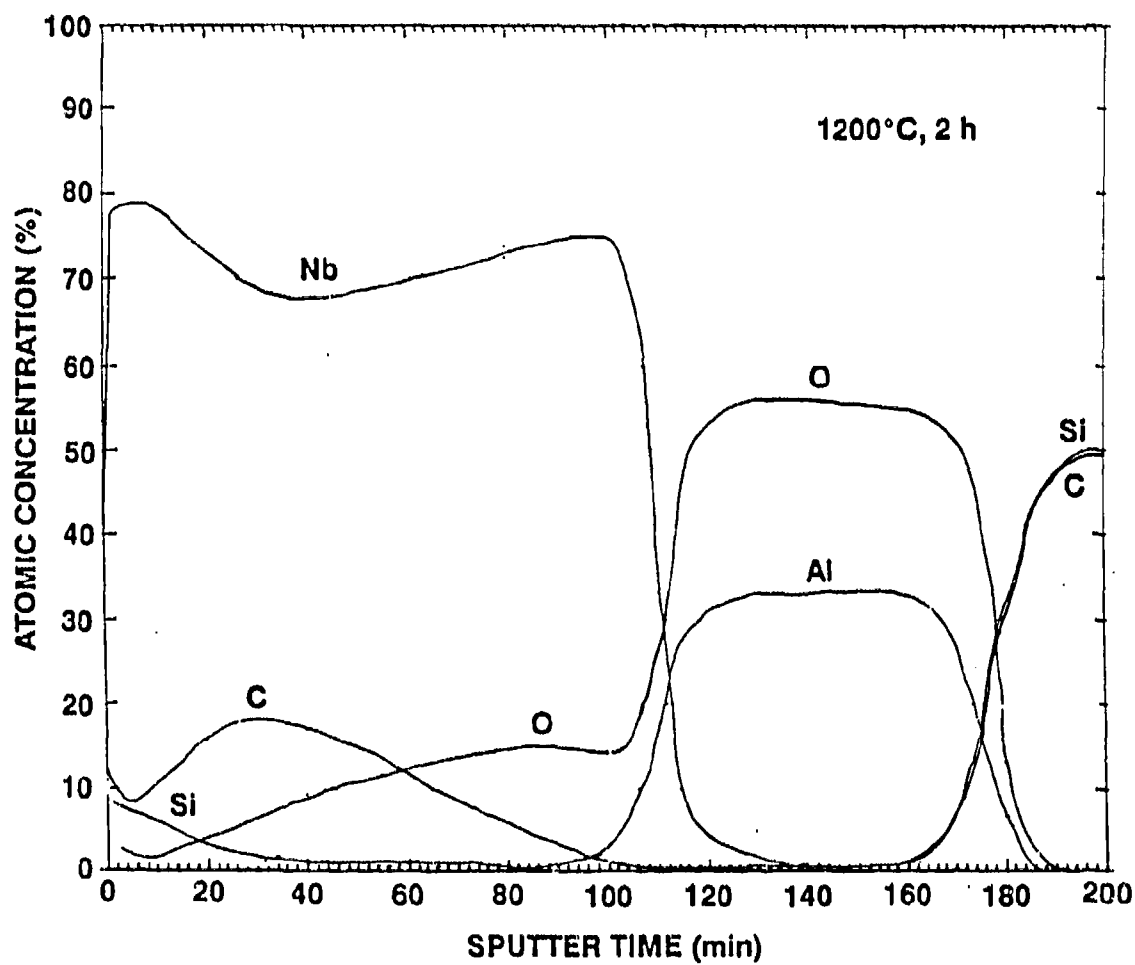


Fig. 5.20 AES depth profile of Nb/Al<sub>2</sub>O<sub>3</sub>/SiC specimen annealed 2 h at 1200°C, with Al<sub>2</sub>O<sub>3</sub> layer thickness of 500 nm. [Equivalent Ta<sub>2</sub>O<sub>5</sub> sputter rate is 12 nm/min].



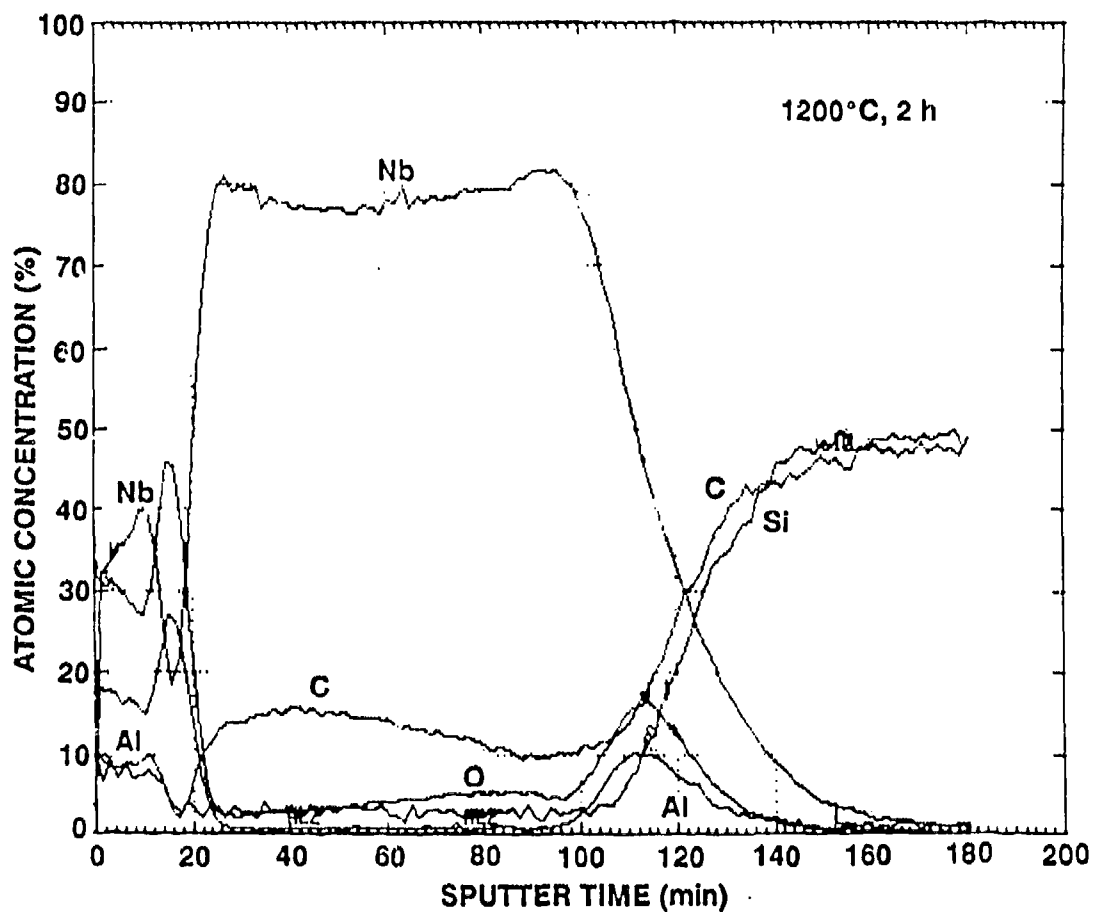


Fig. 5.22

AES depth profile of  $\text{Al}_2\text{O}_3/\text{Nb}/\text{Al}_2\text{O}_3/\text{SiC}$  specimen annealed 2 h at  $1200^\circ\text{C}$ , with  $\text{Al}_2\text{O}_3$  layer thickness of 20 nm for cap and 100 nm for the diffusion barrier. [Equivalent  $\text{Ta}_2\text{O}_5$  sputter rate is 12 nm/min].

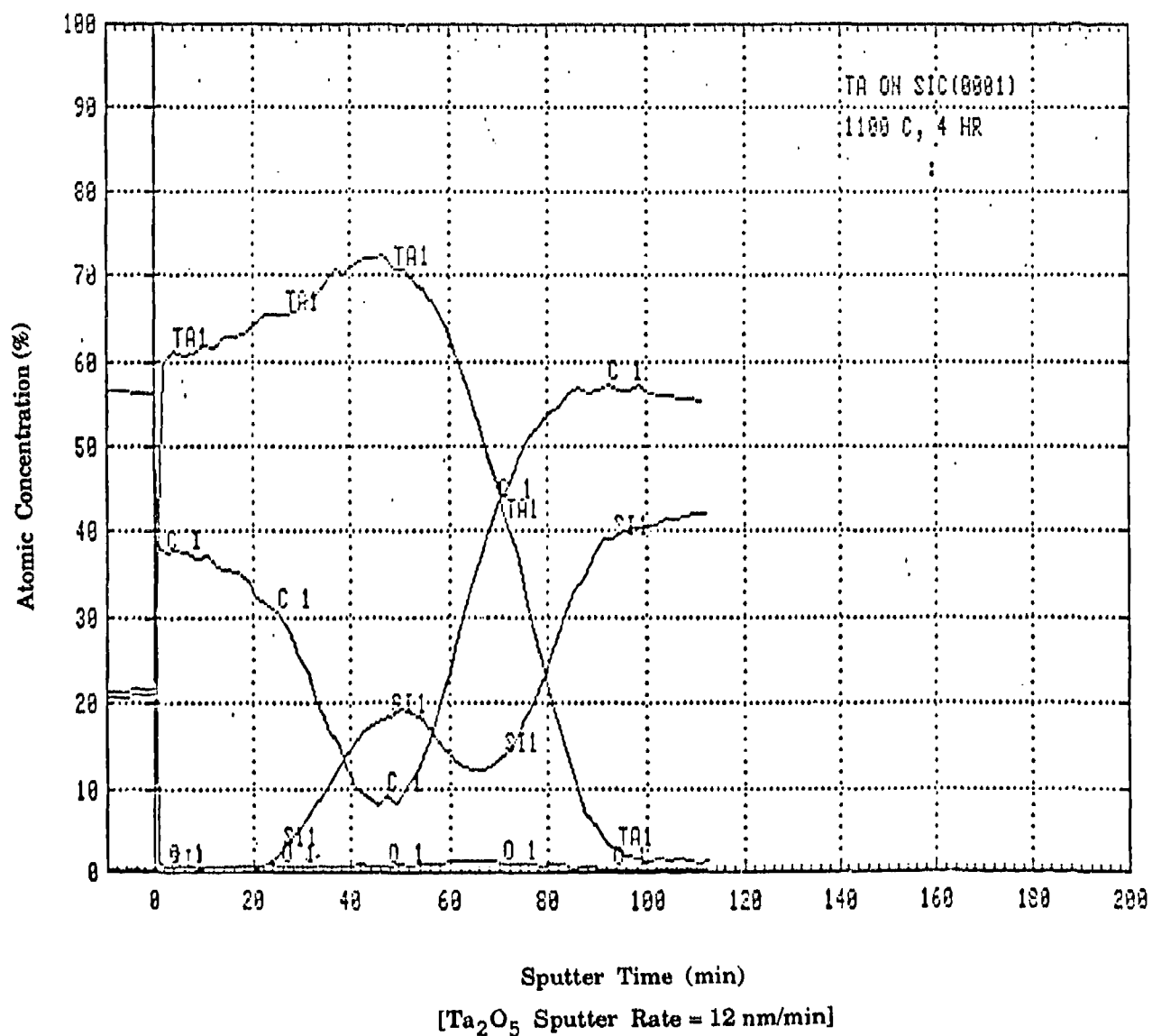


Fig. 5.23 AES depth profile of Ta/SiC (0001), annealed 4 h at 1100°C.

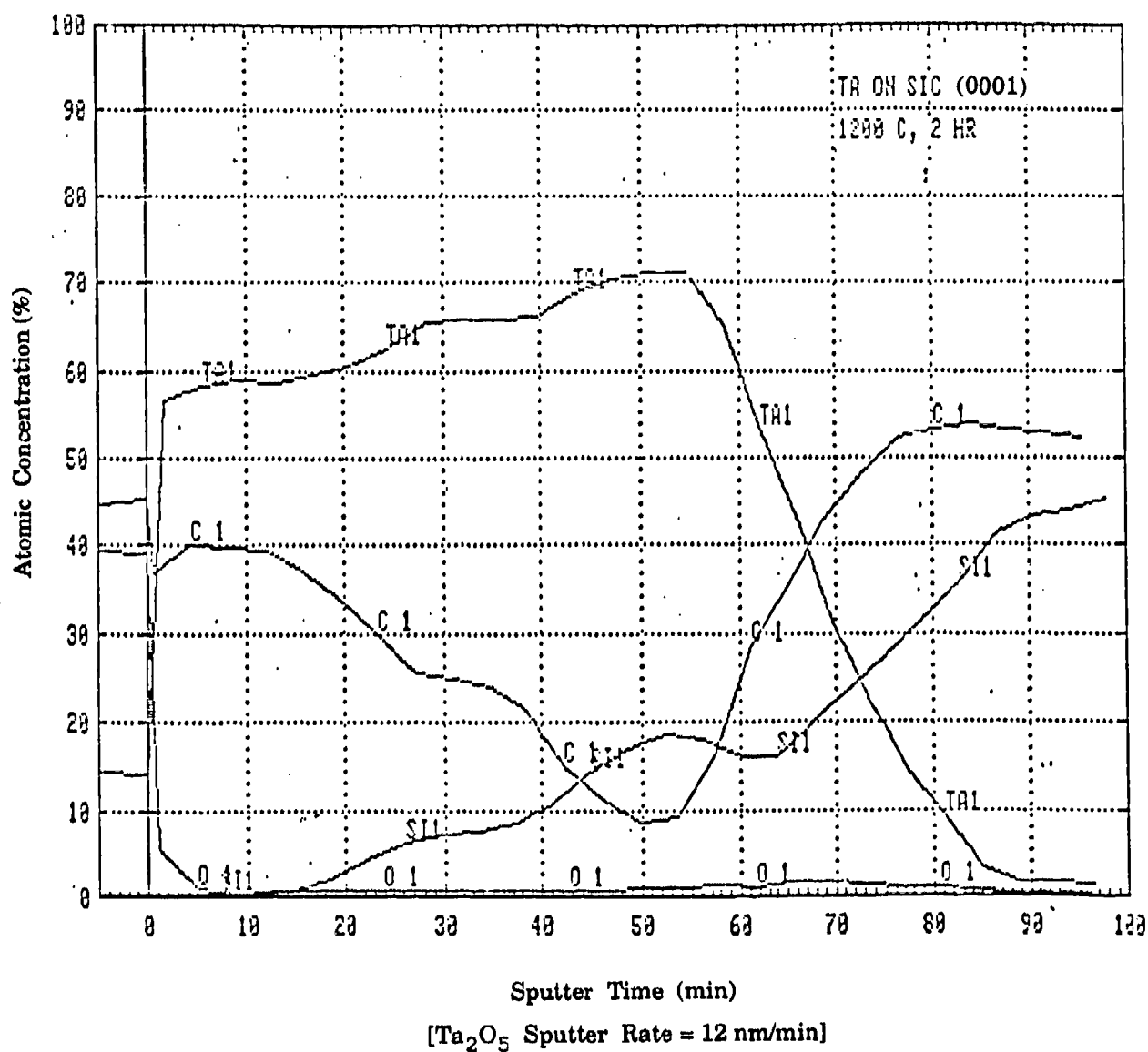


Fig. 5.24 AES depth profile of Ta/SiC (0001), annealed 2 h at 1200 °C.

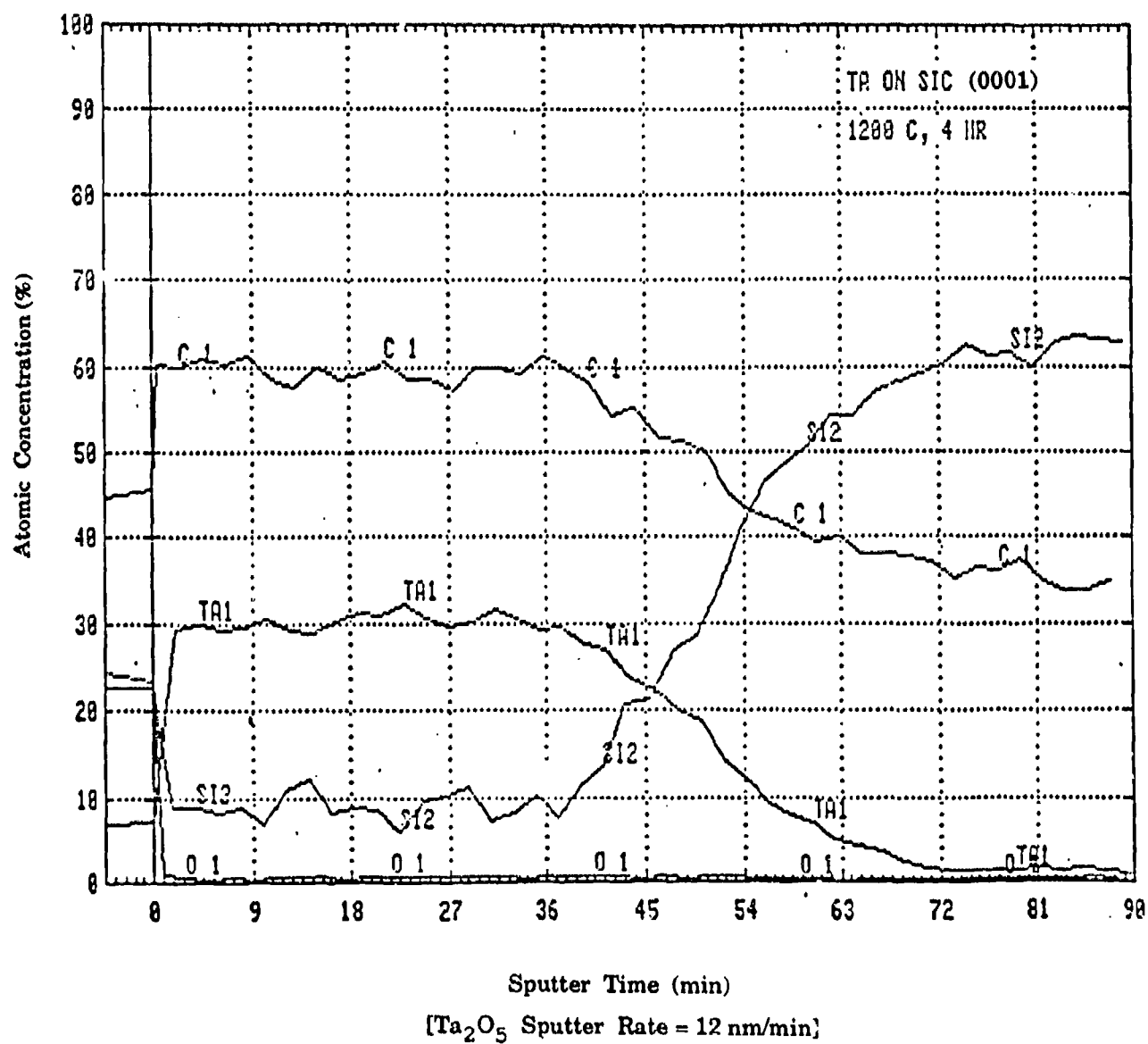


Fig. 5.25 AES depth profile of Ta/SiC (0001), annealed 4 h at 1200 °C.

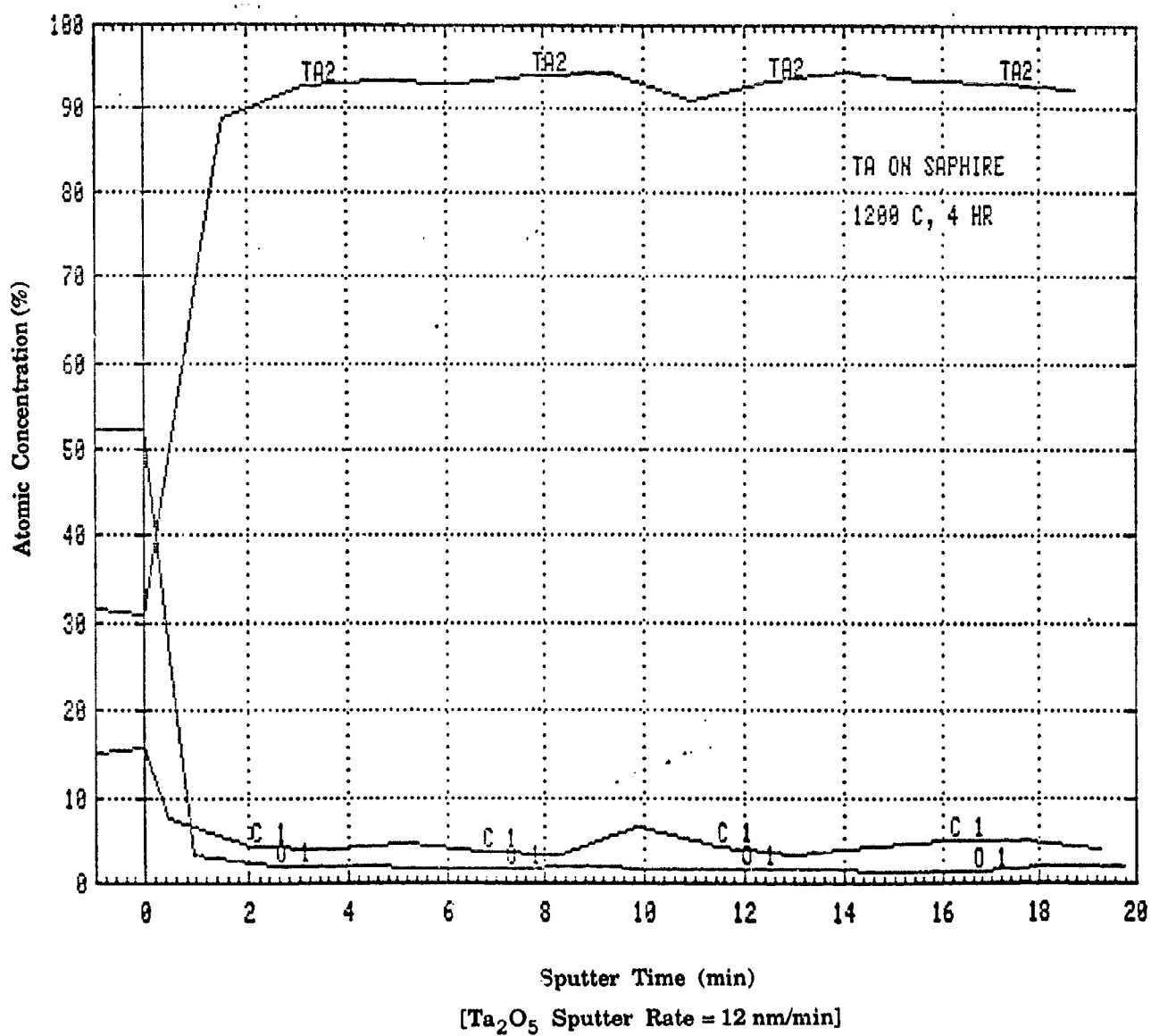


Fig. 5.26 AES depth profile of Ta/AI<sub>2</sub>O<sub>3</sub>, annealed 4 h at 1200°C.



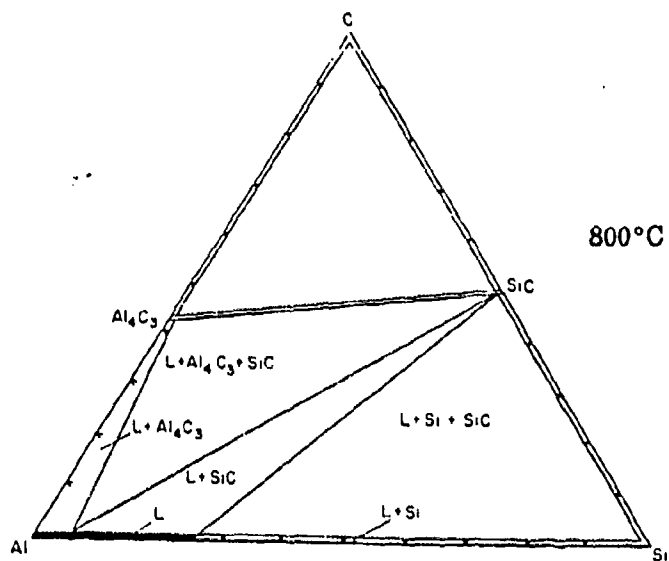
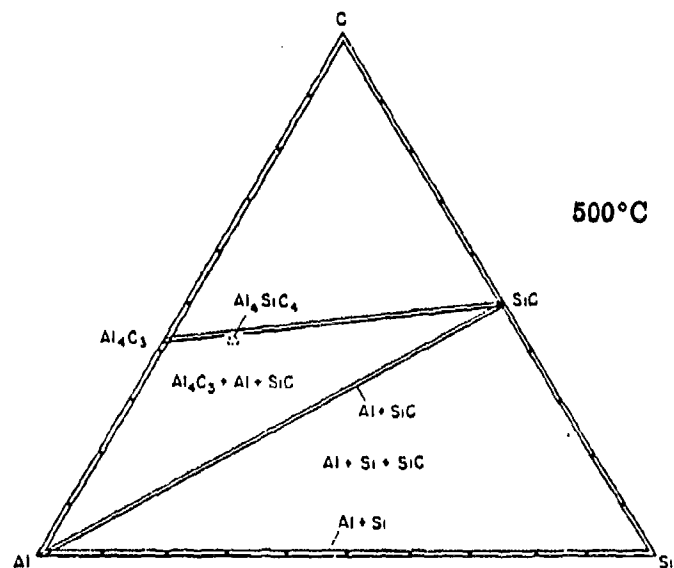


Fig. 5.27 Al-Si-C ternary phase diagrams at 500°C and 800°C [Ref. 63].

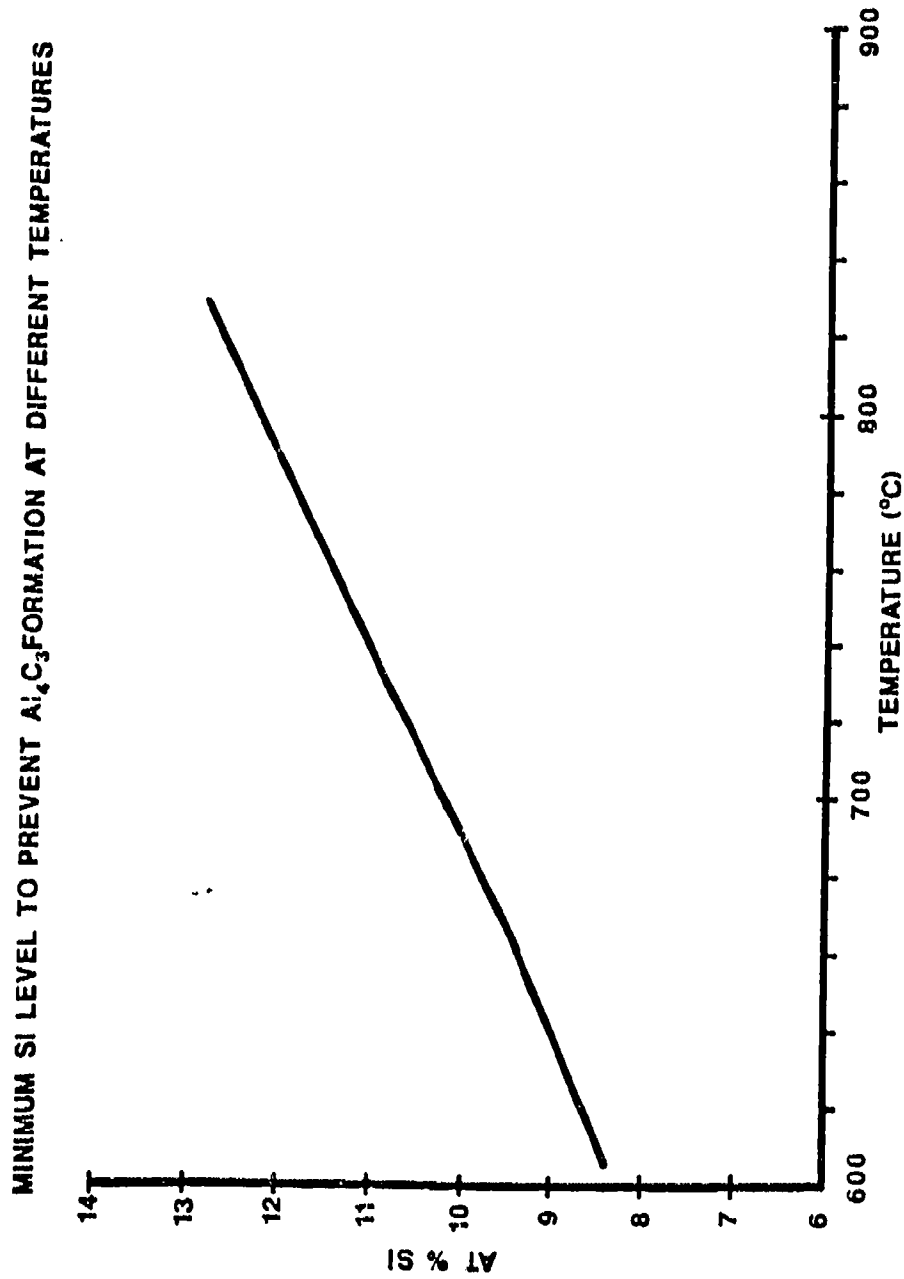


Fig. 5.28 The theoretical Si levels in Al required to prevent  $\text{Al}_4\text{C}_3$  formation [Ref. 17].

DSC Data File: als15

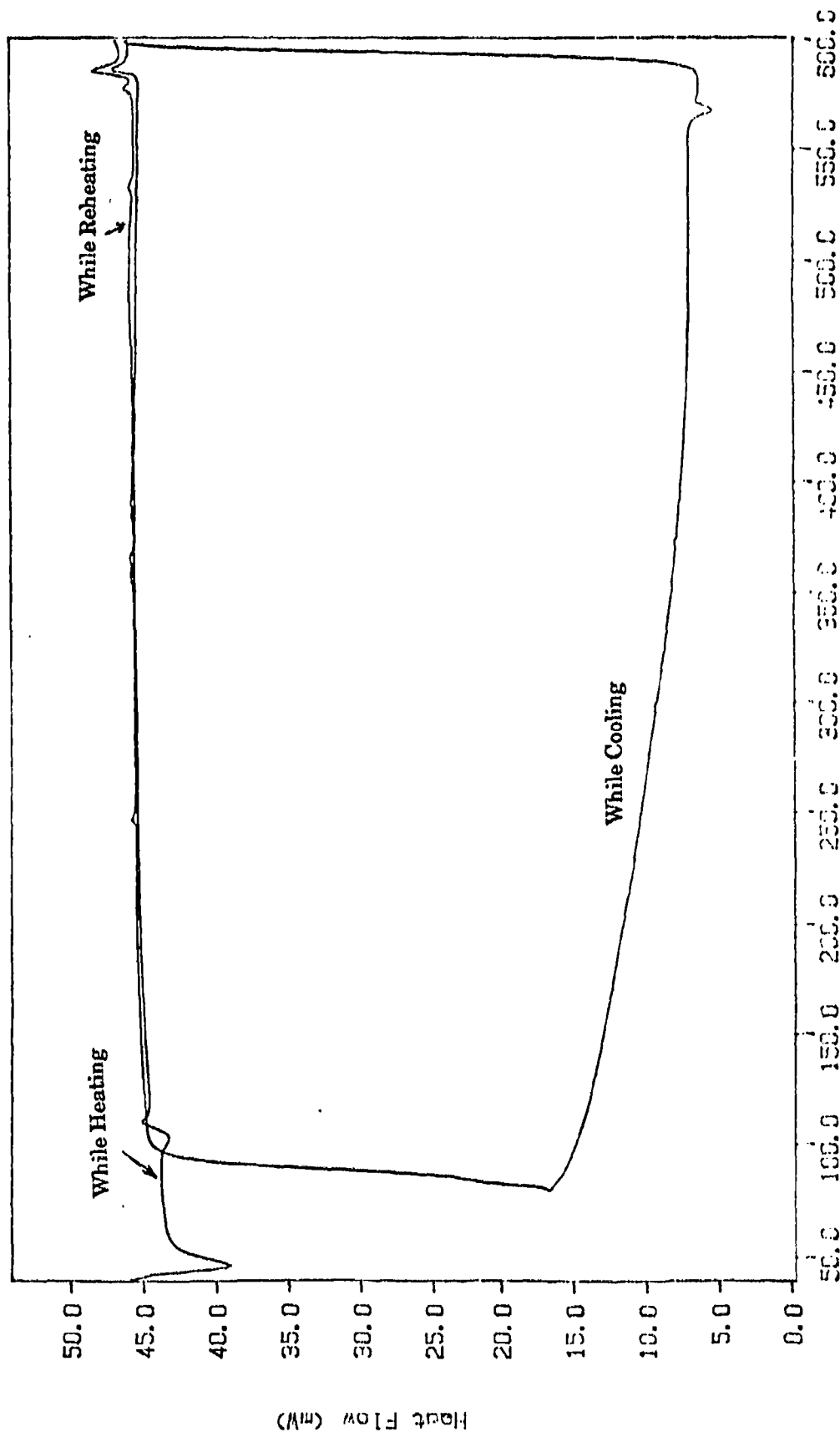
Sample Weight: 38.770 mg

Thu Feb 23 09:59:15 1989

AlSi Run #5

PERKIN-ELMER

7 Series Thermal Analysis System



B/L Used (cups) 99.999 Ar. (1cc)

TIME	1:	2:	3:	4:
TIME 1:	0.0 min	0.0 min	0.0 min	0.0 min
TIME 2:	0.0 min	0.0 min	0.0 min	0.0 min
TIME 3:	0.0 min	0.0 min	0.0 min	0.0 min
TIME 4:	0.0 min	0.0 min	0.0 min	0.0 min

RATE 1: 40.0 C/min

RATE 2: 40.0 C/min

RATE 3: 40.0 C/min

RATE 4: 40.0 C/min

Fig. 5.29 DSC data from Al/Si specimen.

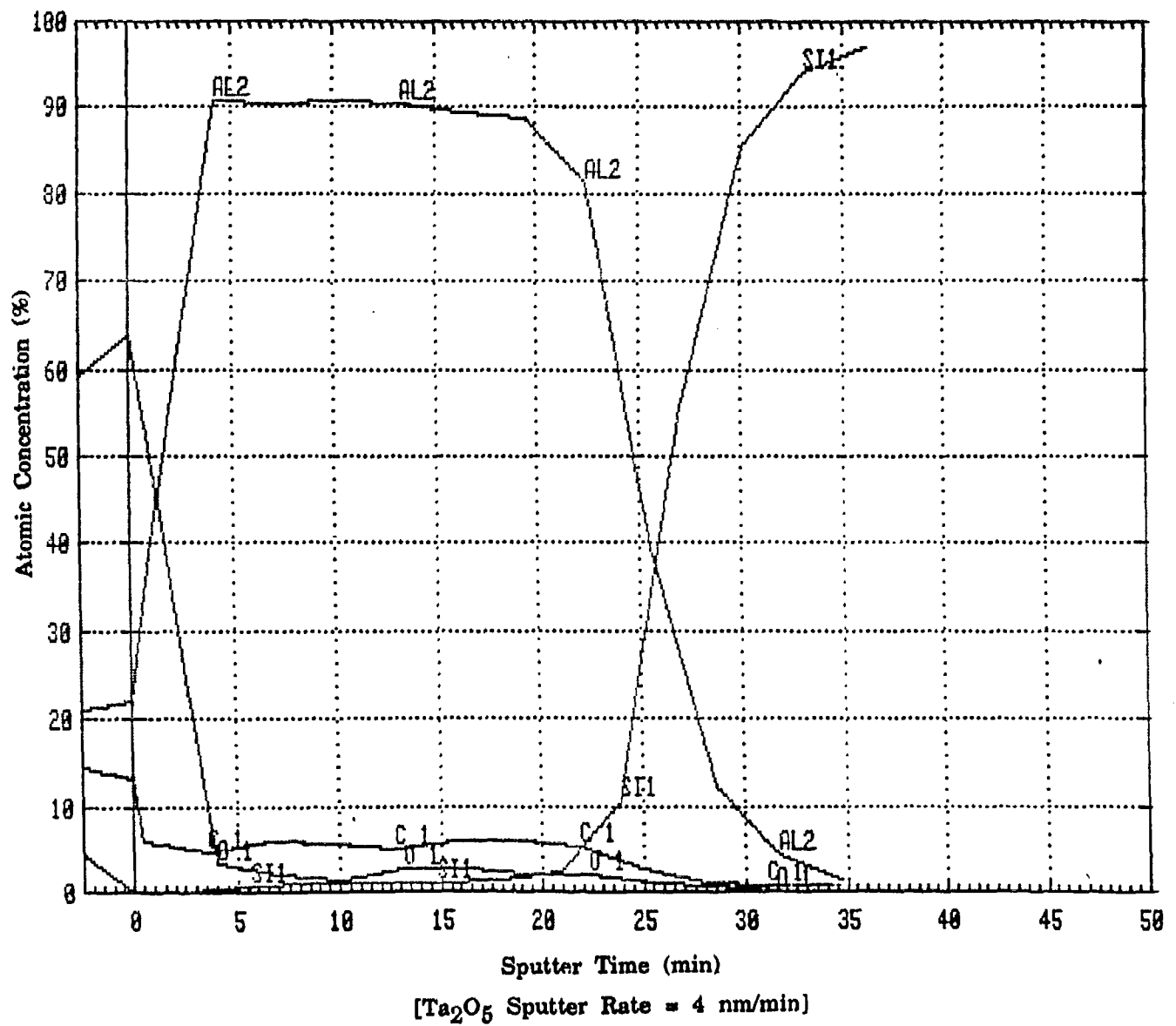


Fig. 5.30 AES depth profile of Al/Si specimen, in the as-deposited condition.

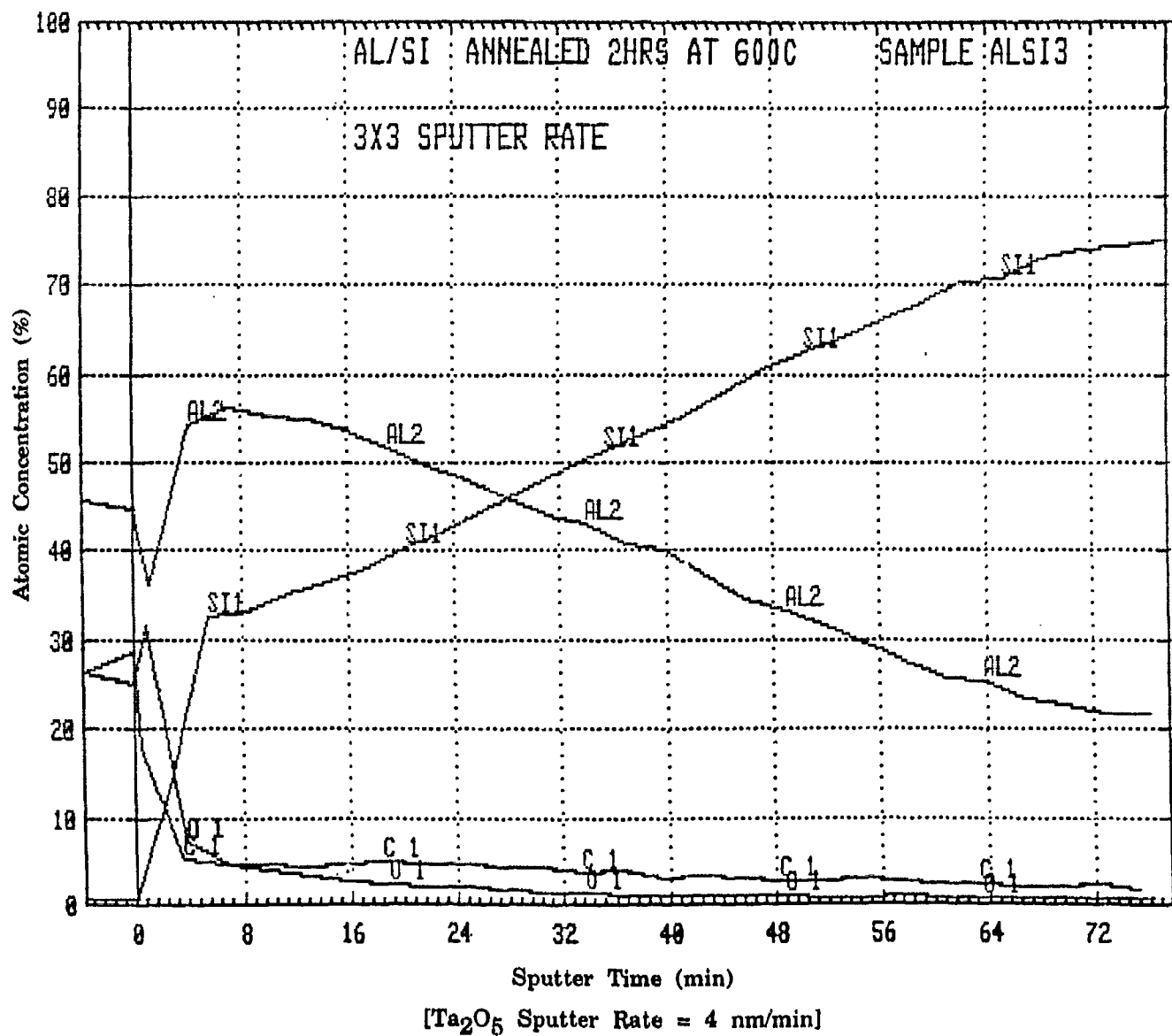


Fig. 5.31 AES depth profile of Al/Si specimen, annealed 2 h at 600°C.



**Fig. 5.32** AES depth profile of Al/SiC specimen, in the as-deposited condition.

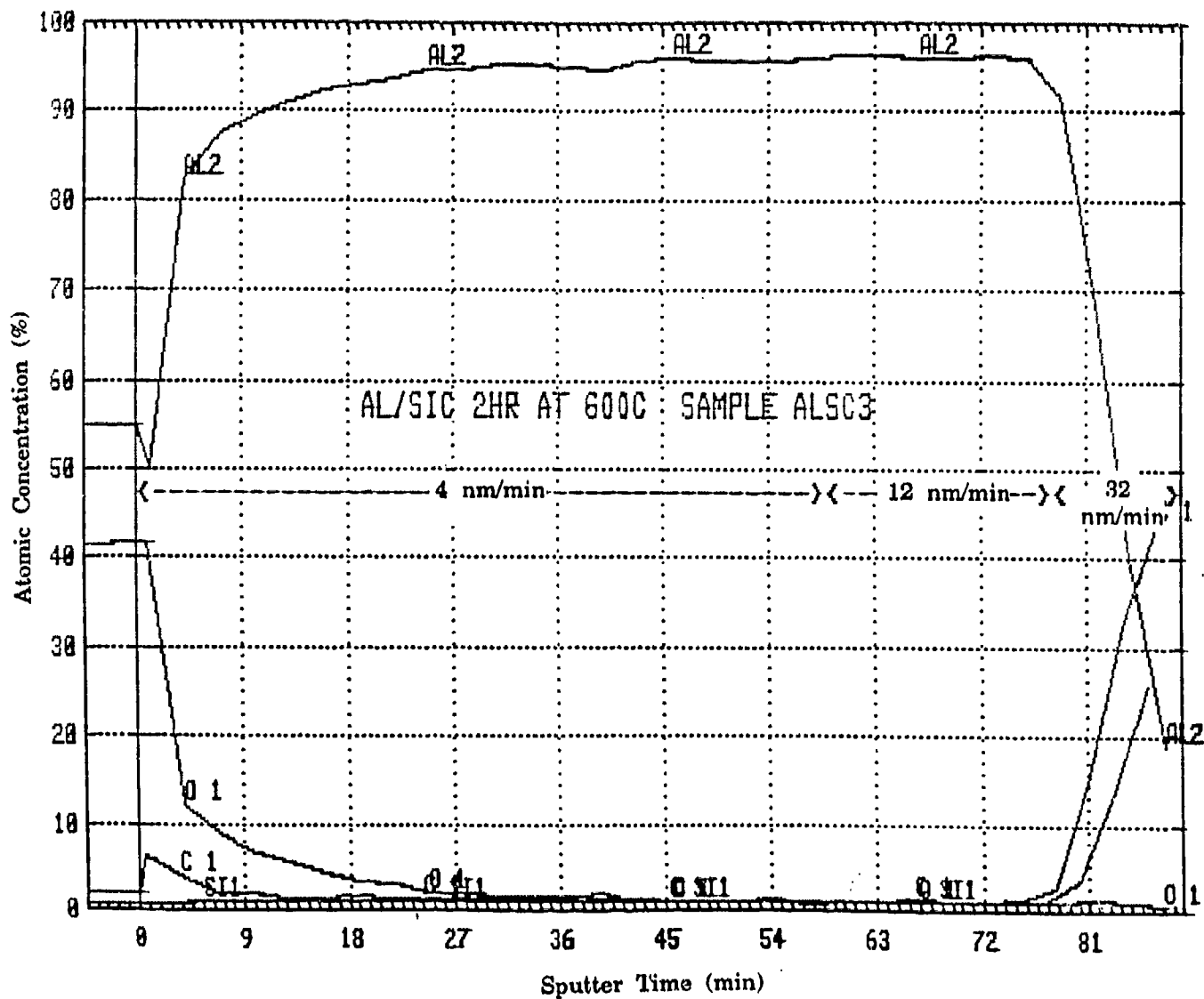


Fig. 5.33 AES depth profile of Al/SIC specimen, annealed 2 h at 600°C.

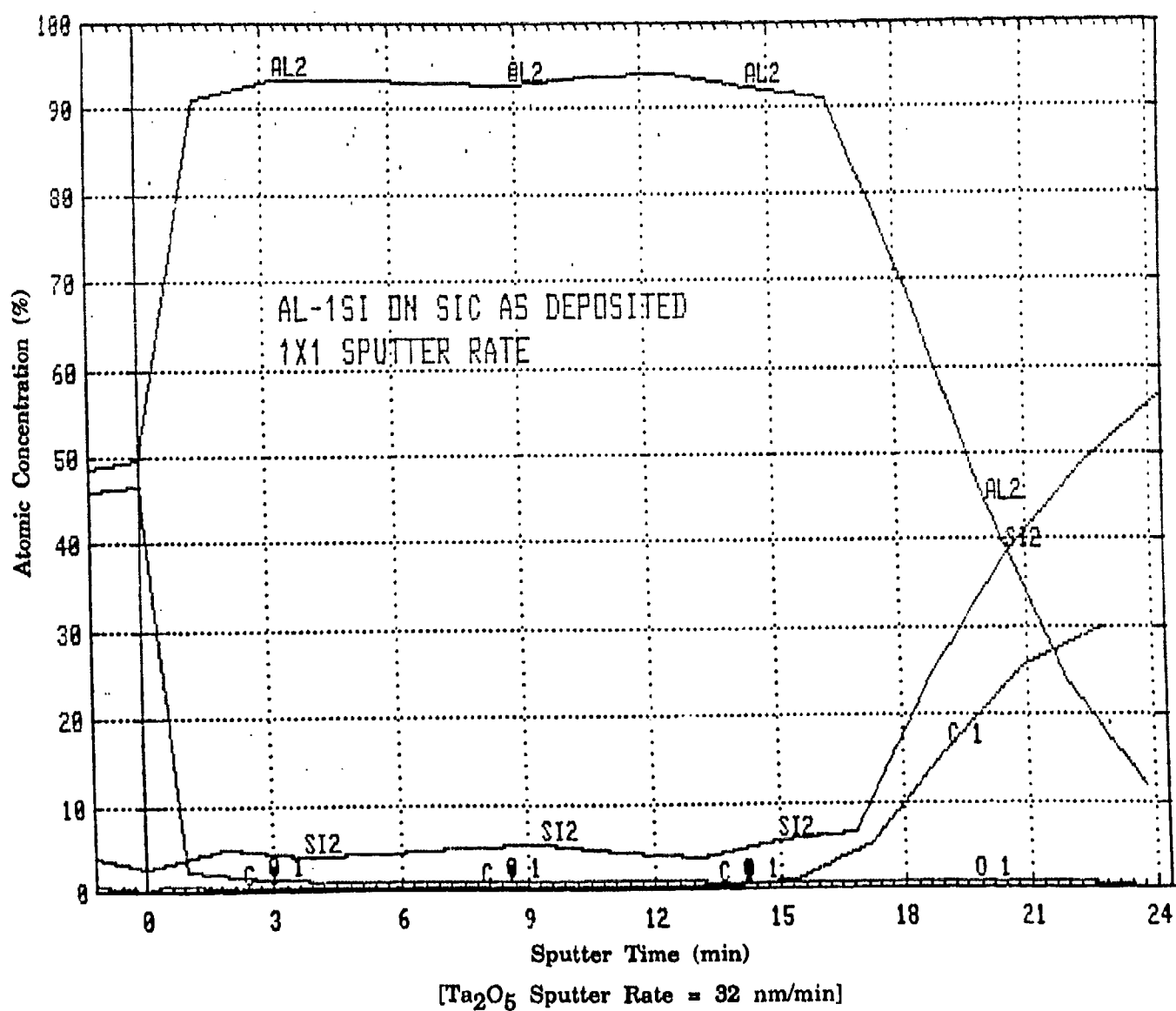


Fig. 5.34 AES depth profile of Al-1wt% Si/SiC specimen, in the as-deposited condition.



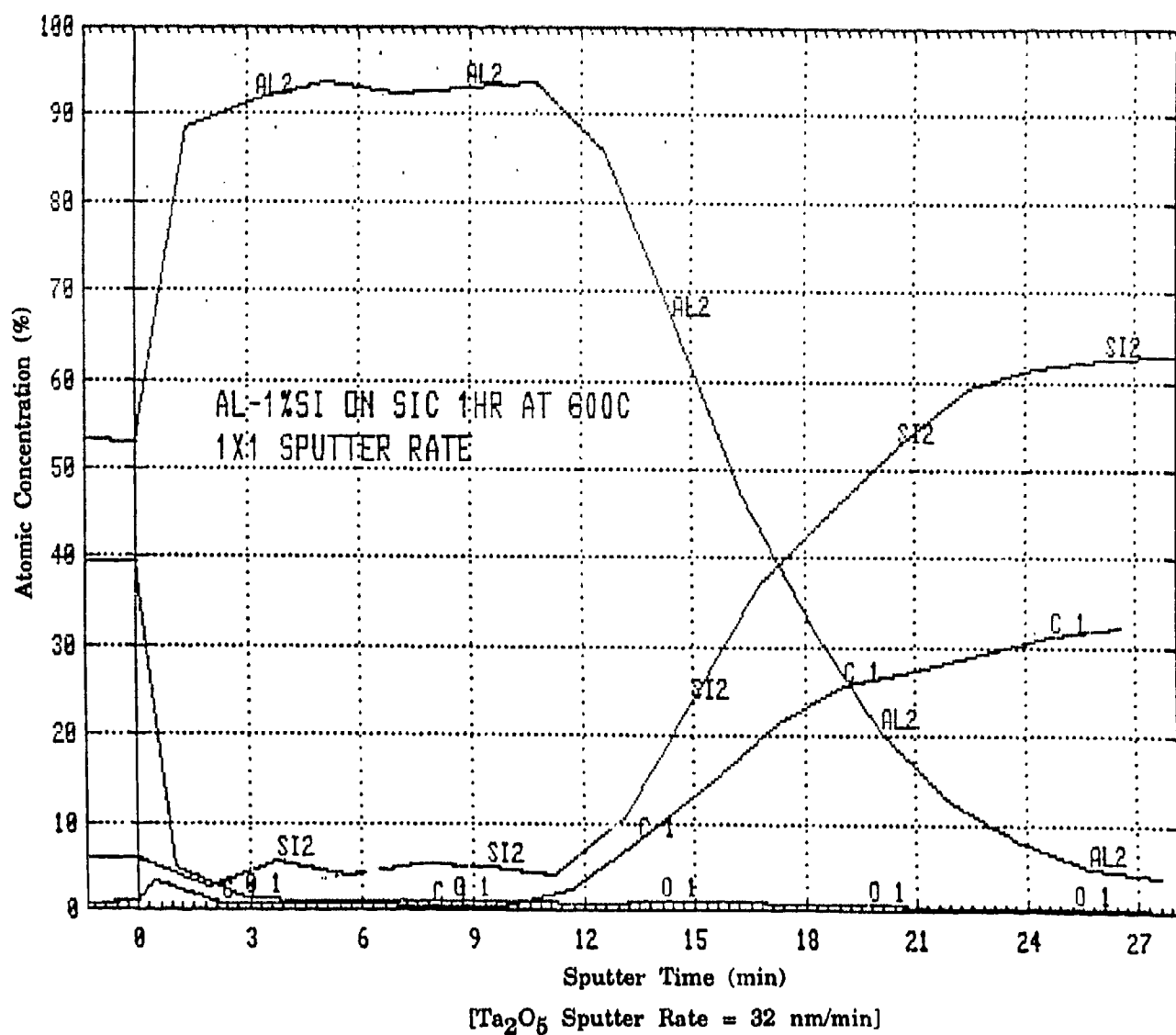


Fig. 5.35 AES depth profile of Al-1wt% Si/SiC specimen, annealed 1 h at 600°C.

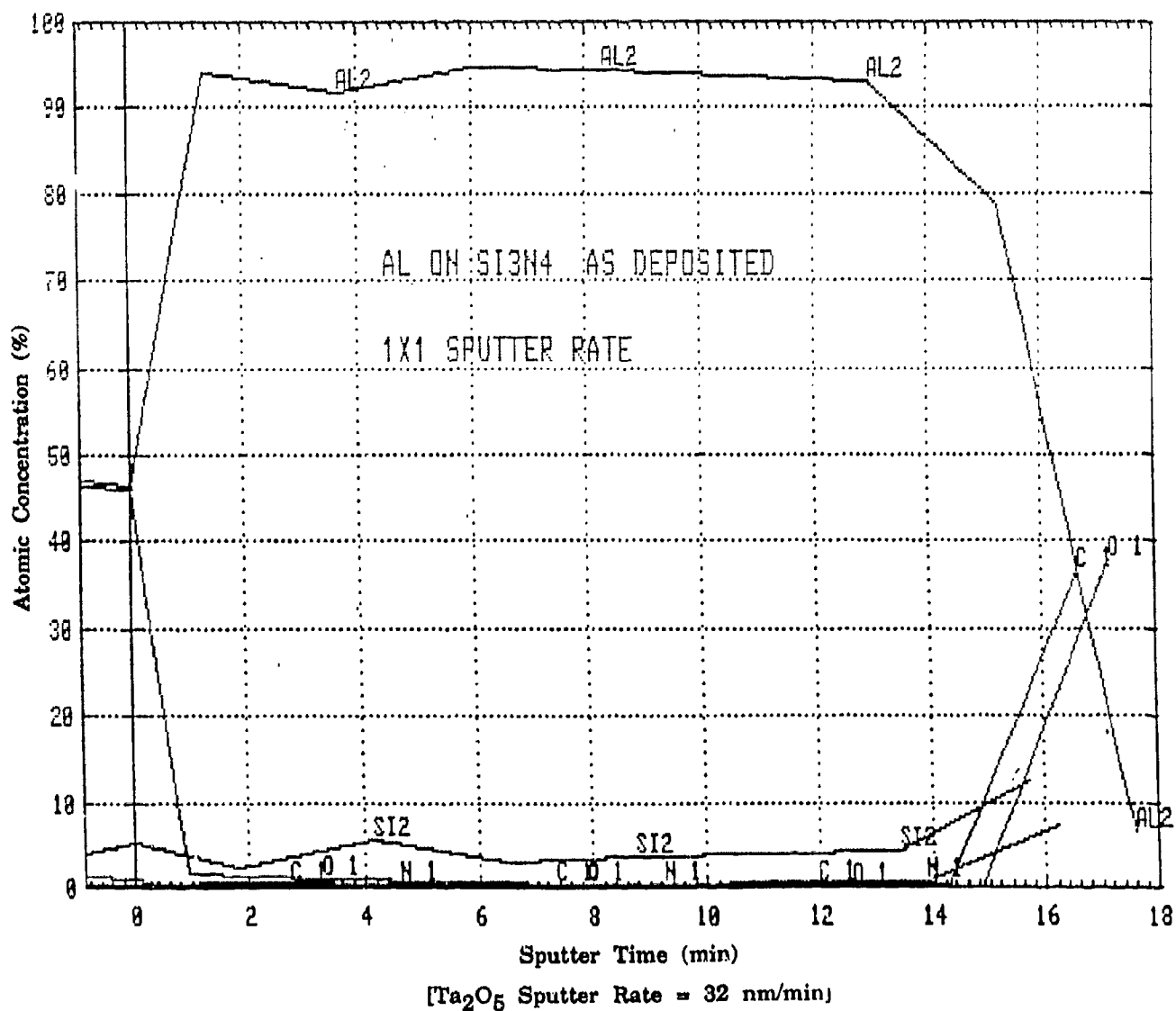


Fig. 5.36 AES depth profile of Al/Si<sub>3</sub>N<sub>4</sub> specimen, in the as-deposited condition.

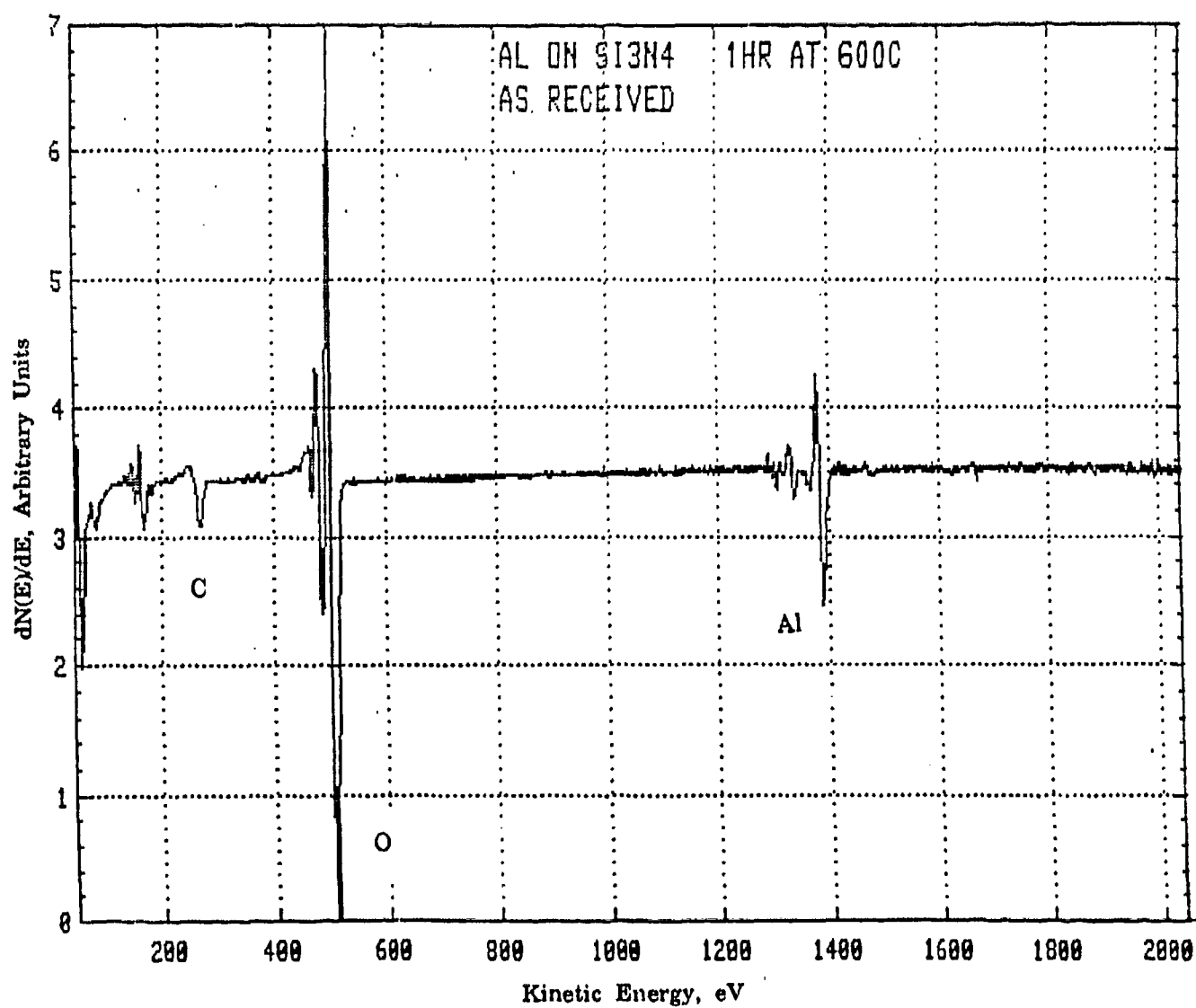


Fig. 5.37 AES spectrum of Al/Si<sub>3</sub>N<sub>4</sub> specimen, annealed 1 h at 600°C.

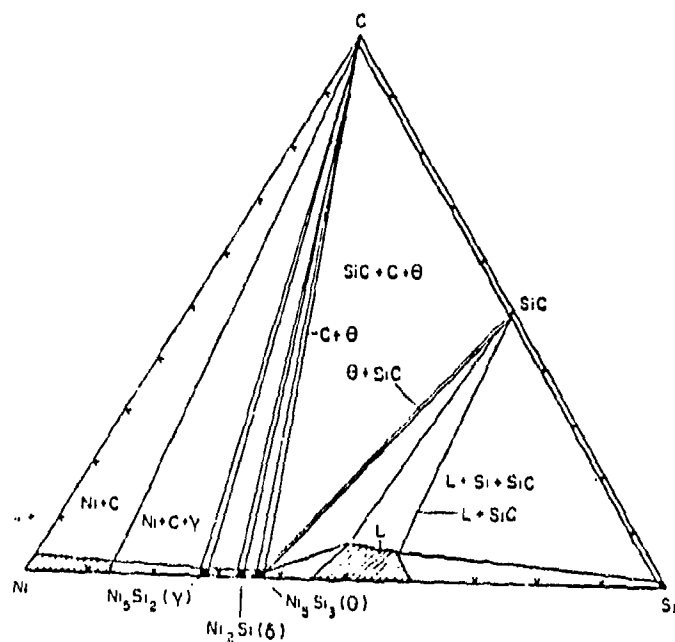


Fig. 5.38 Ni-Si-C ternary phase diagrams at 1150°C [Refs. 63,66].

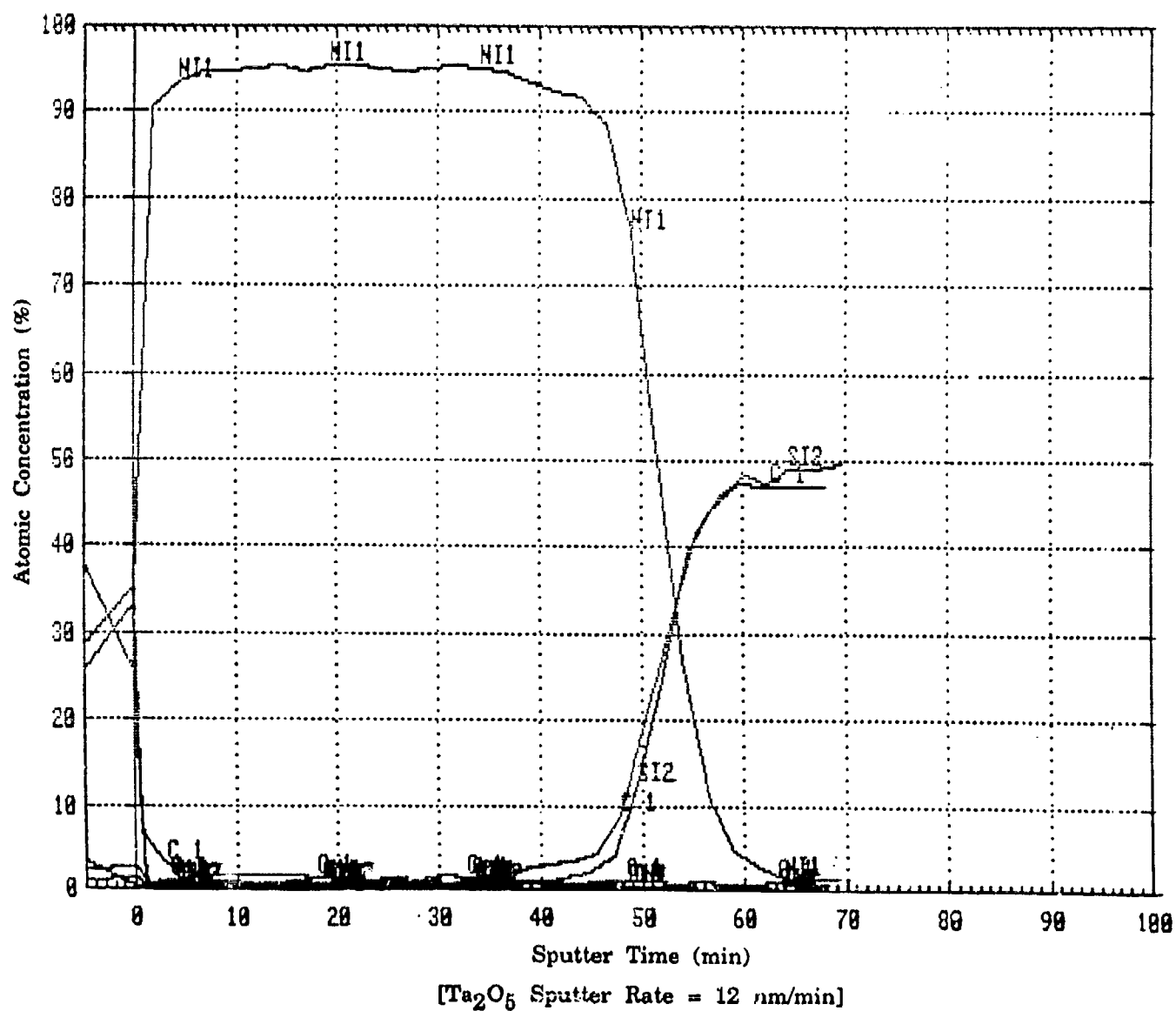


Fig. 5.39 AES depth profile of Ni/SiC specimen, in the as-deposited condition.

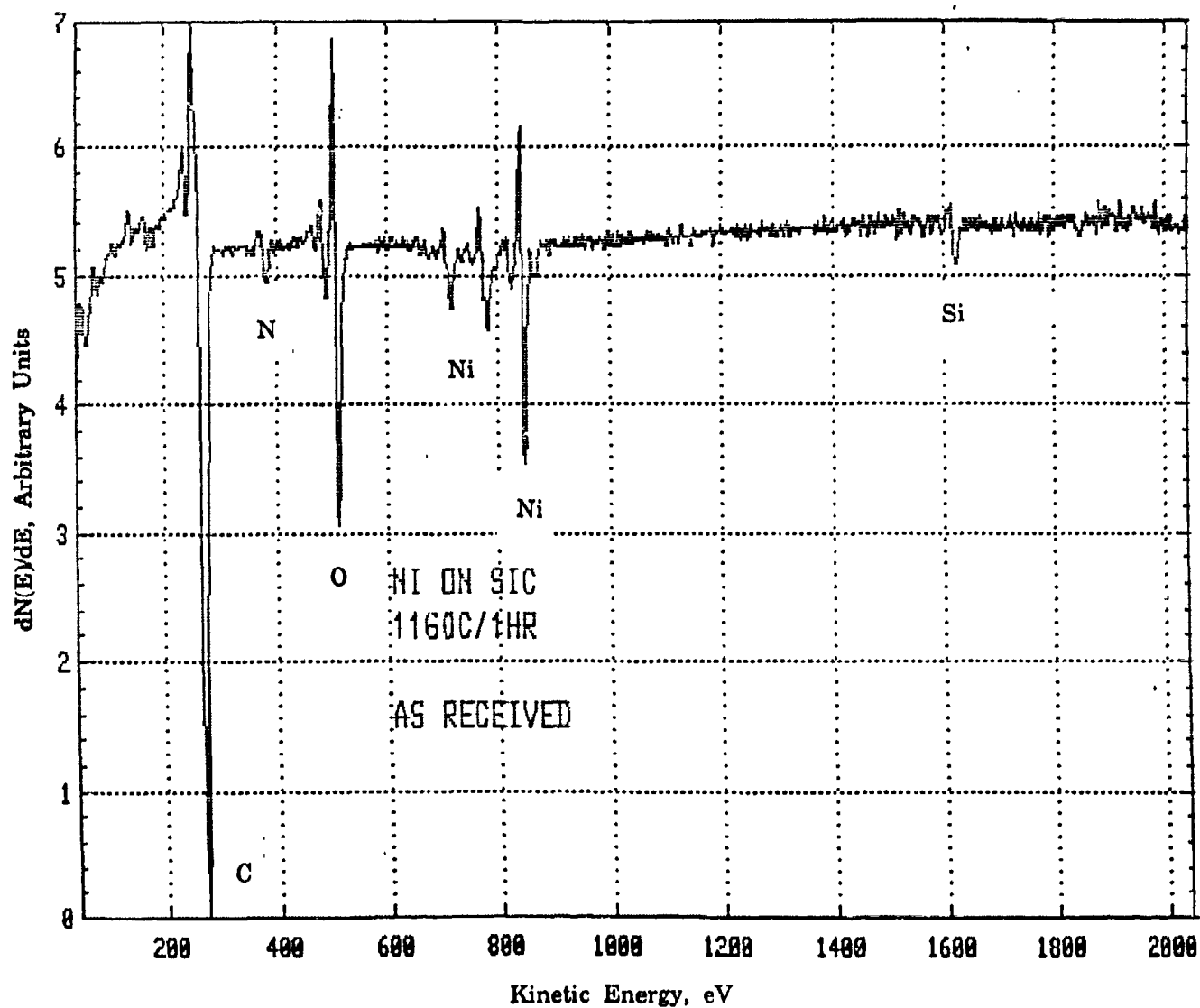


Fig. 5.40 AES spectrum of Ni/SiC specimen, annealed 1 h at 1160°C.

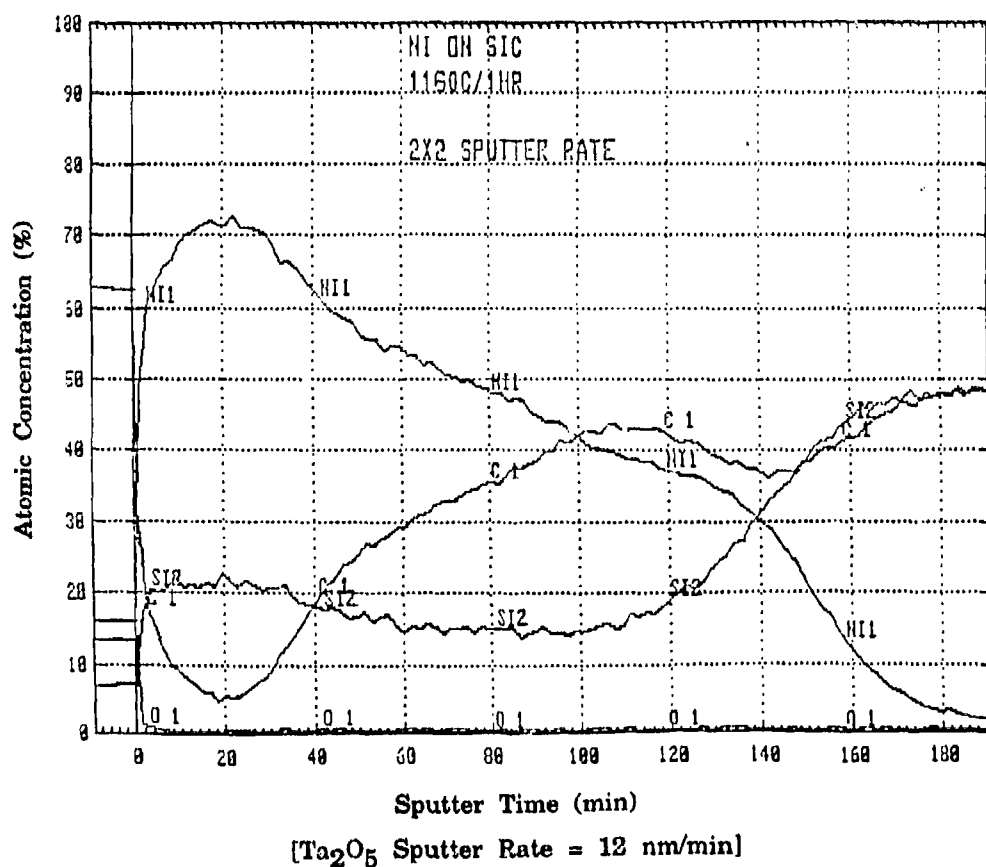
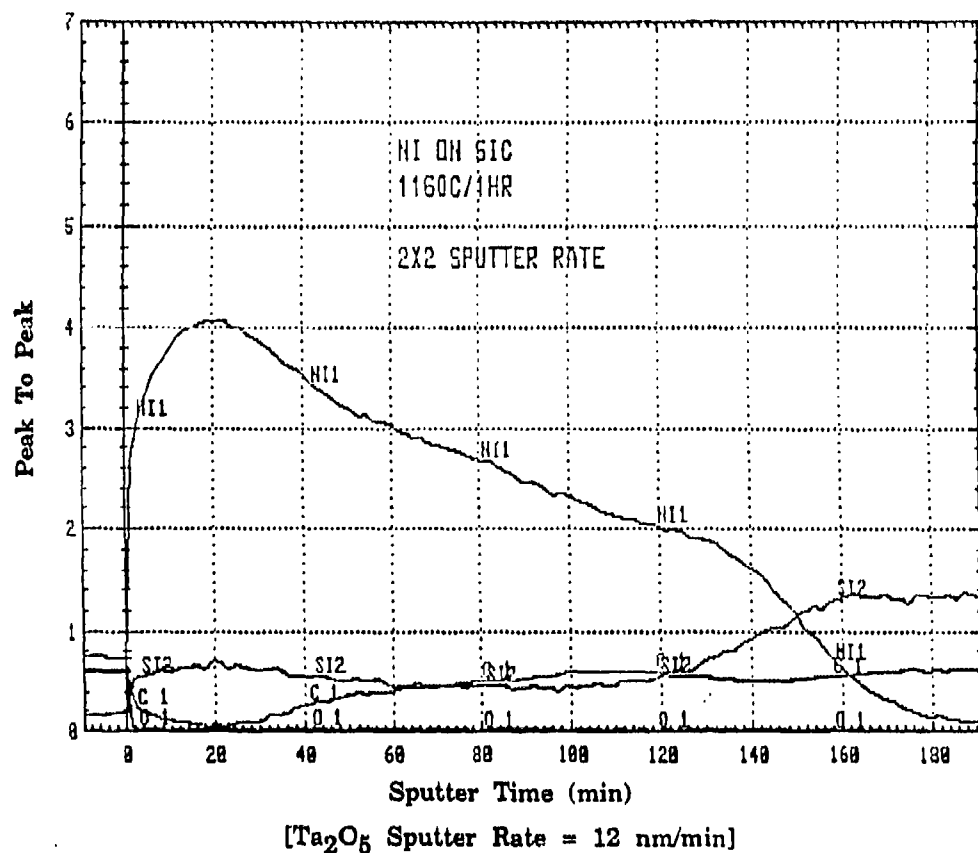


Fig. 5.41

AES depth profile of Ni/SiC specimen, annealed 1 h at 1160°C, peak-to-peak height data (top) and atomic concentration plot (bottom).

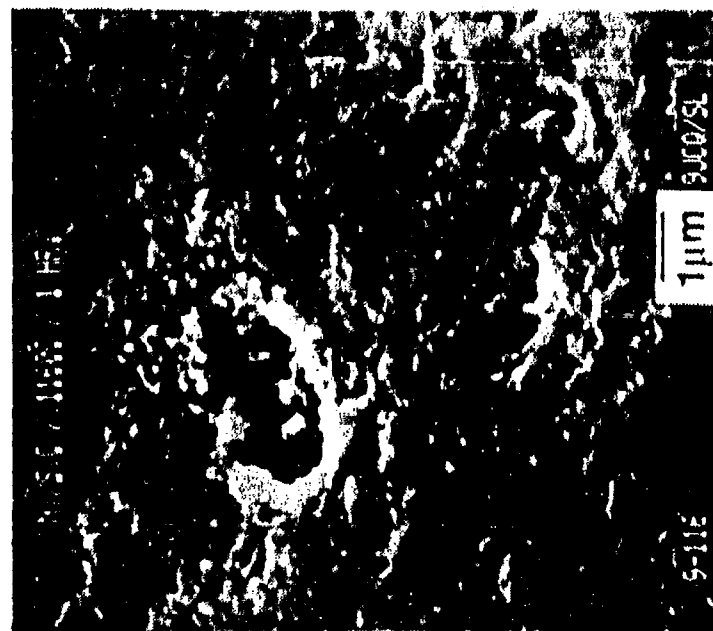


Fig. 5.42 SEM micrographs of Ni/SiC specimen, annealed 1 h at 1160°C.



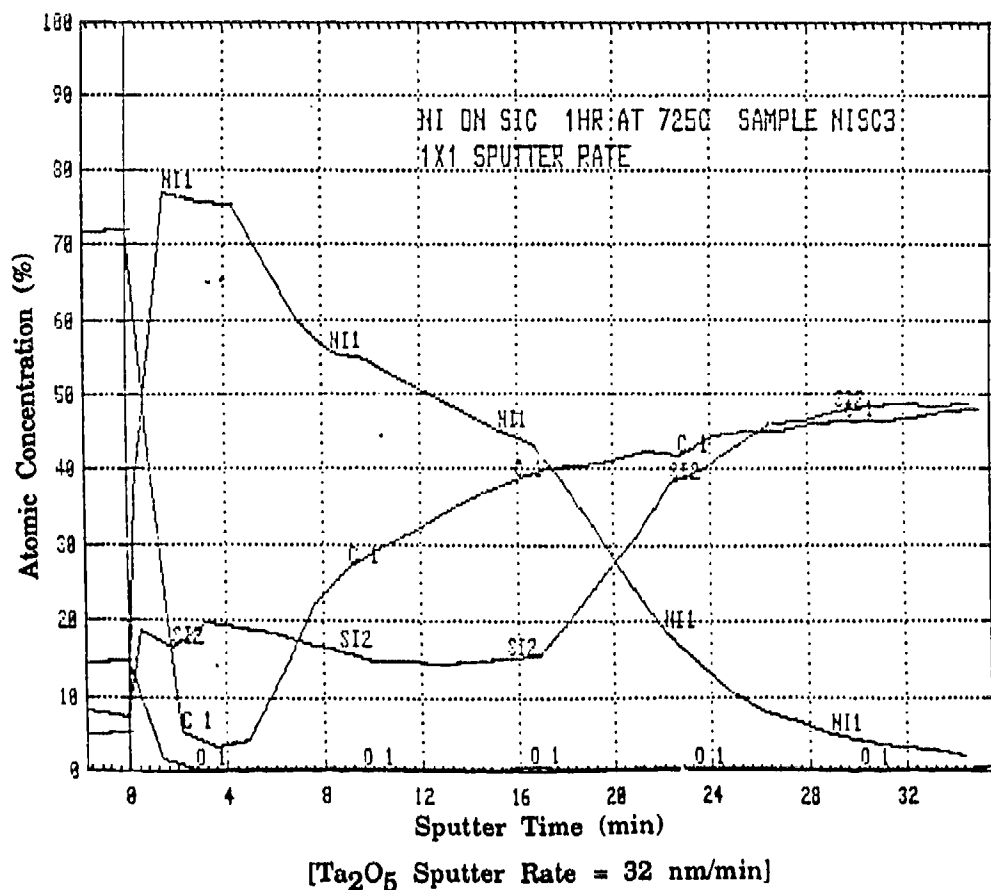
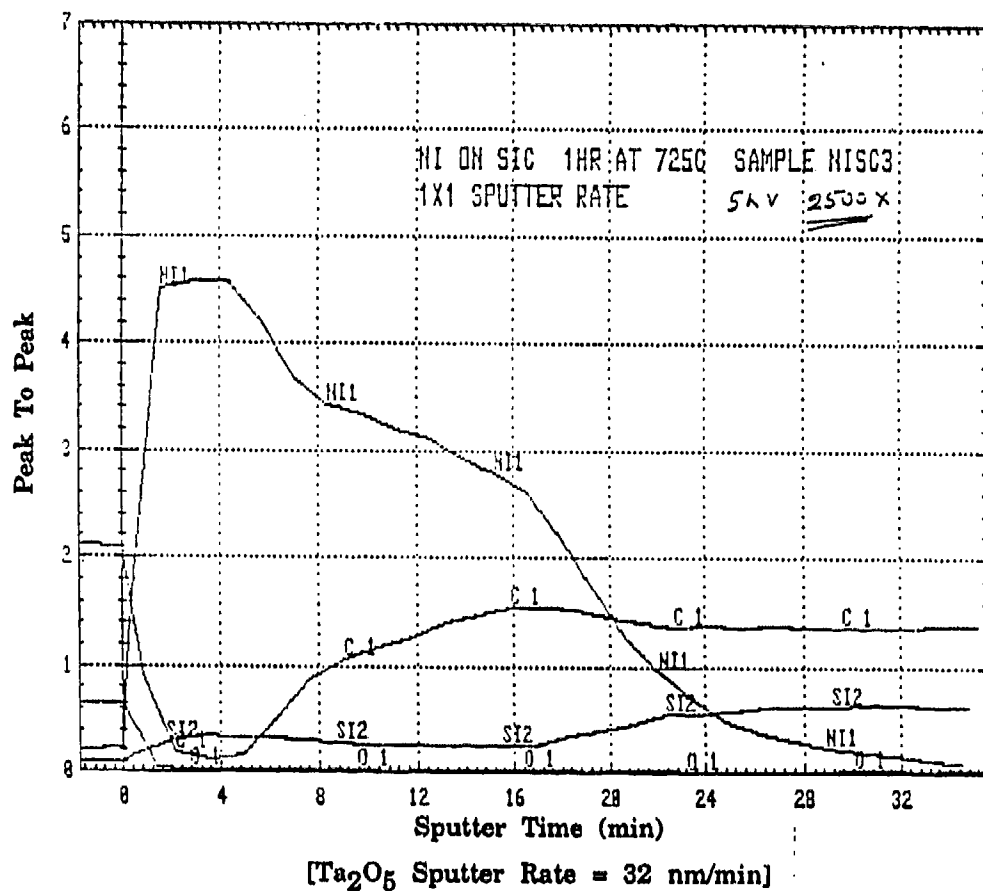


Fig. 5.43

AES depth profile of Ni/SiC specimen, annealed 1 h at 725°C, peak-to-peak height data (top) and atomic concentration plot (bottom).

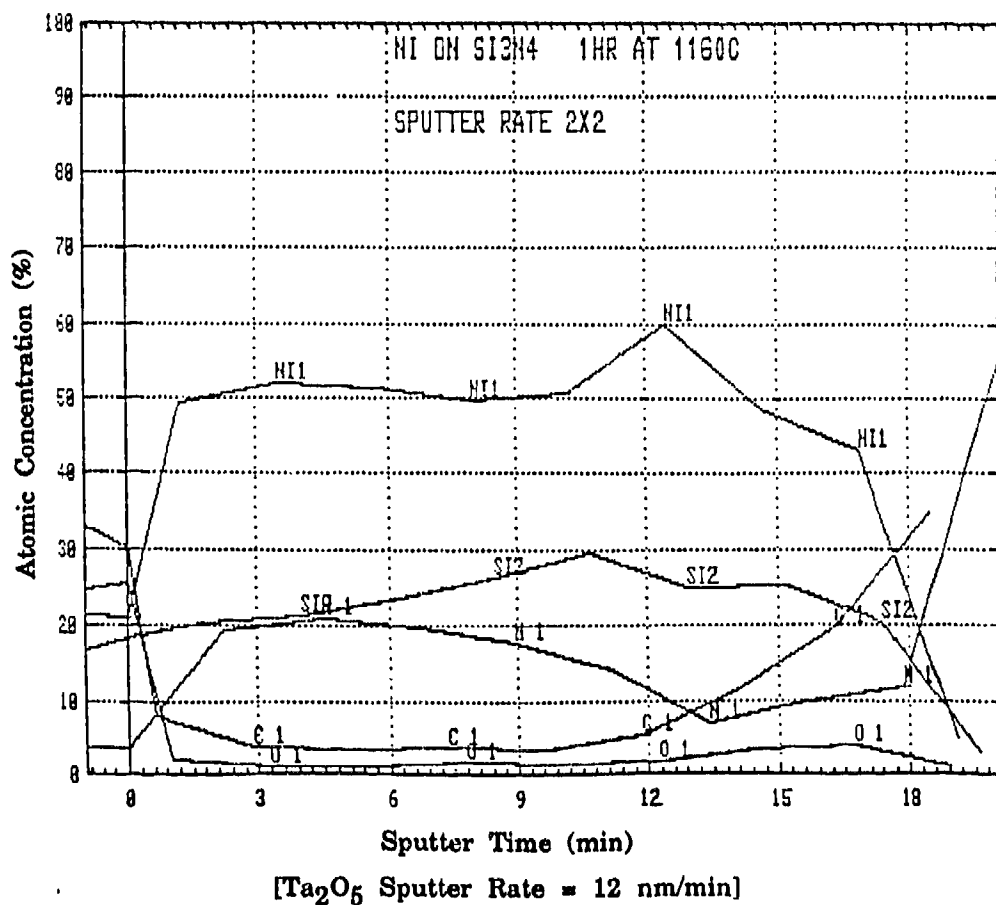
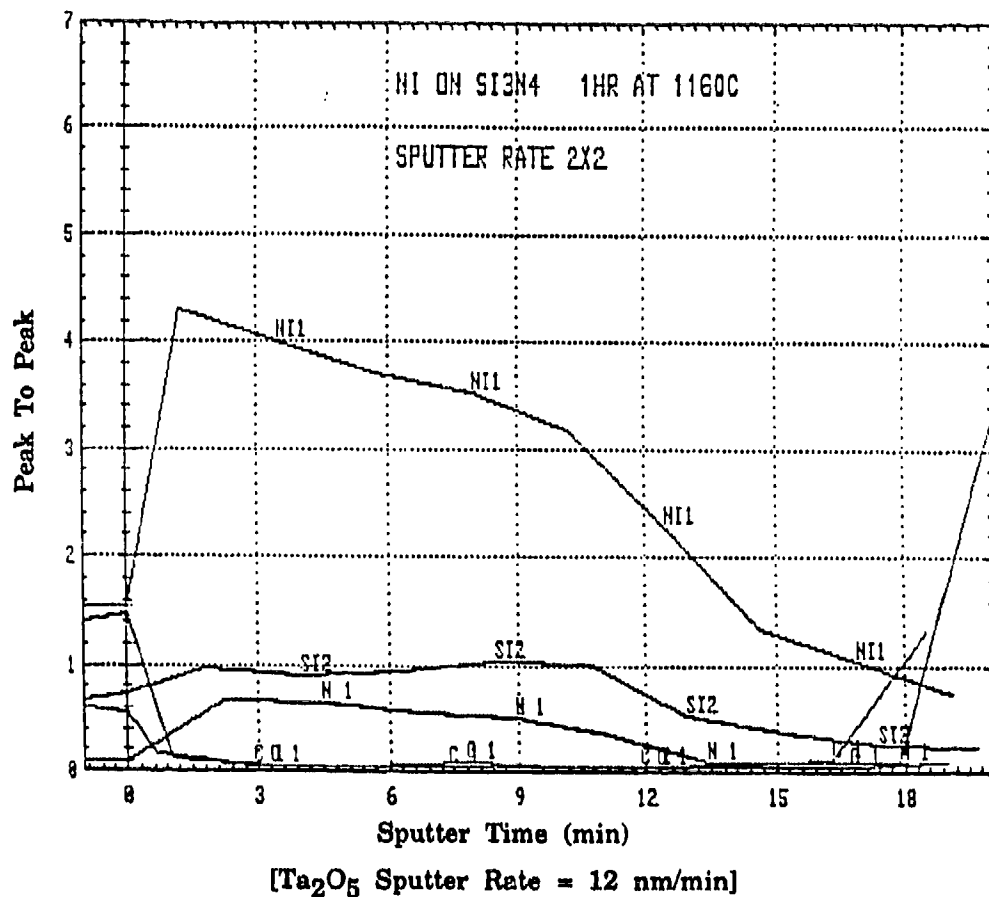


Fig. 5.44

AES depth profile of Ni/Si<sub>3</sub>N<sub>4</sub> specimen, annealed 1 h at 1160°C, peak-to-peak height data (top) and atomic concentration plot (bottom).

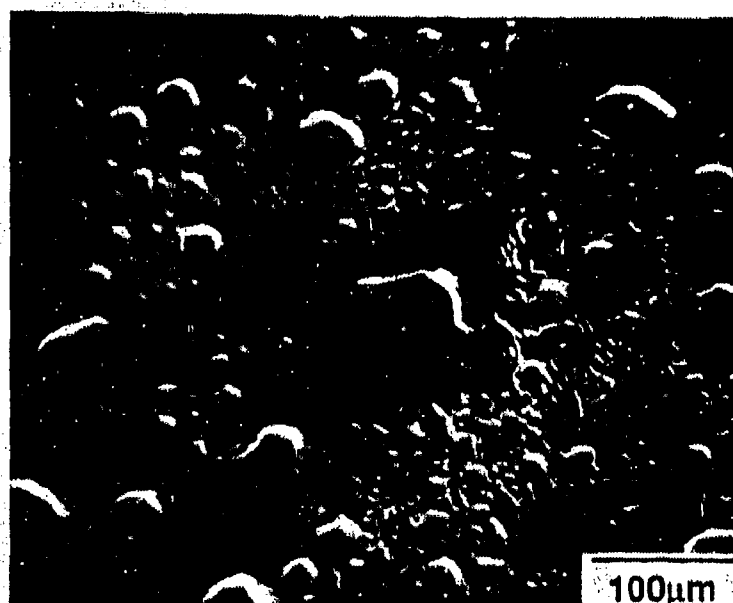


Fig. 5.45 SEM micrographs of Ni/Si<sub>3</sub>N<sub>4</sub> specimen, annealed 1 h at 1160°C, area in which detailed AES studies were performed.

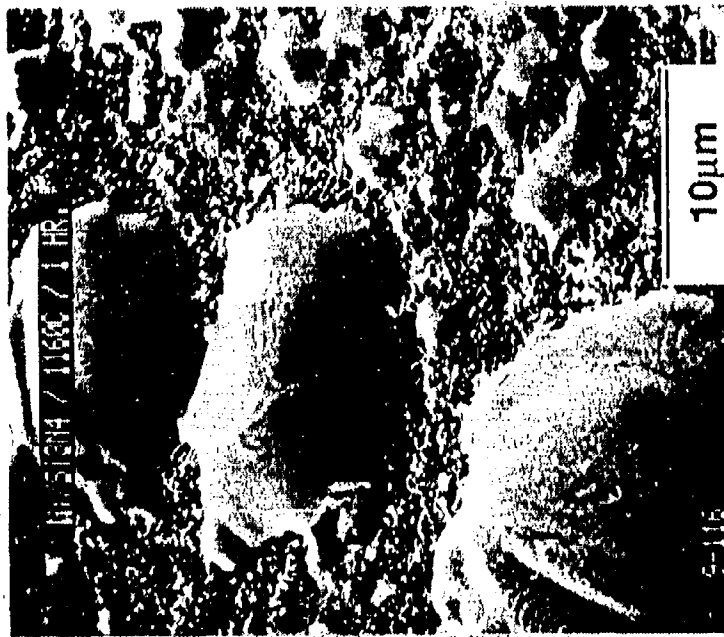
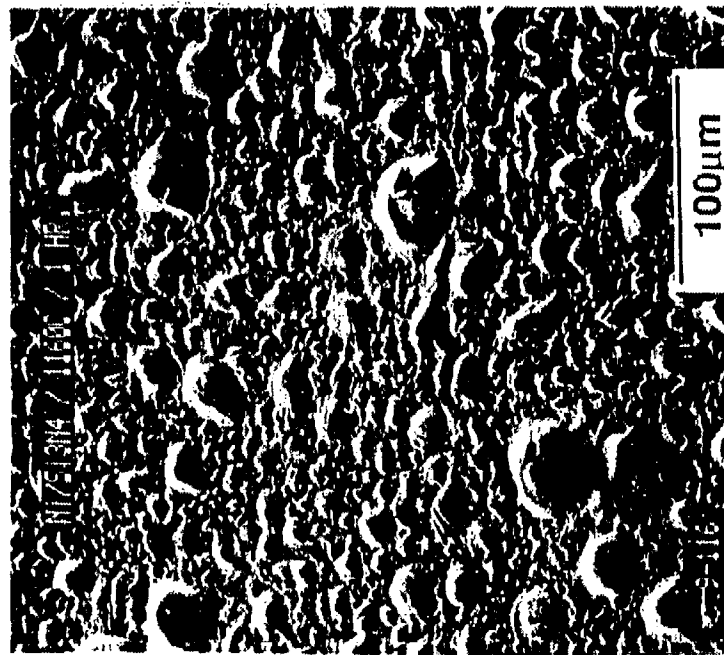


Fig. 5.46 SEM micrographs of Ni/Si<sub>3</sub>N<sub>4</sub> specimen, annealed 1 h at 1160°C.

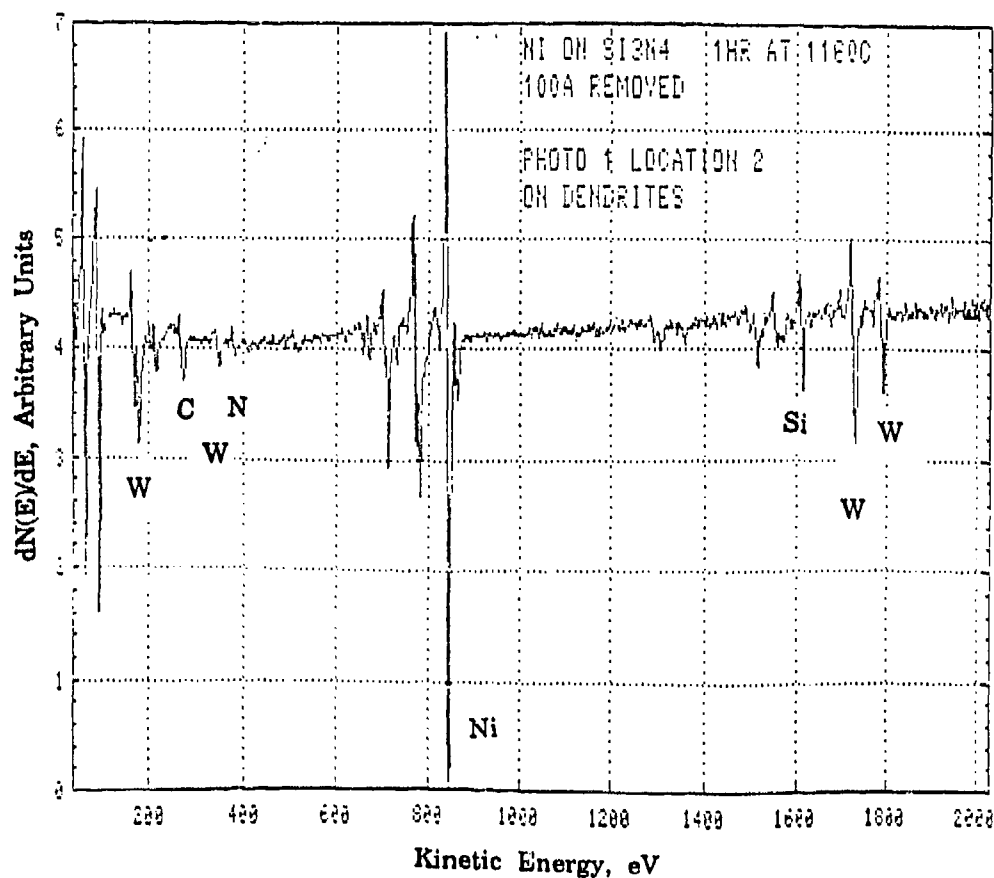
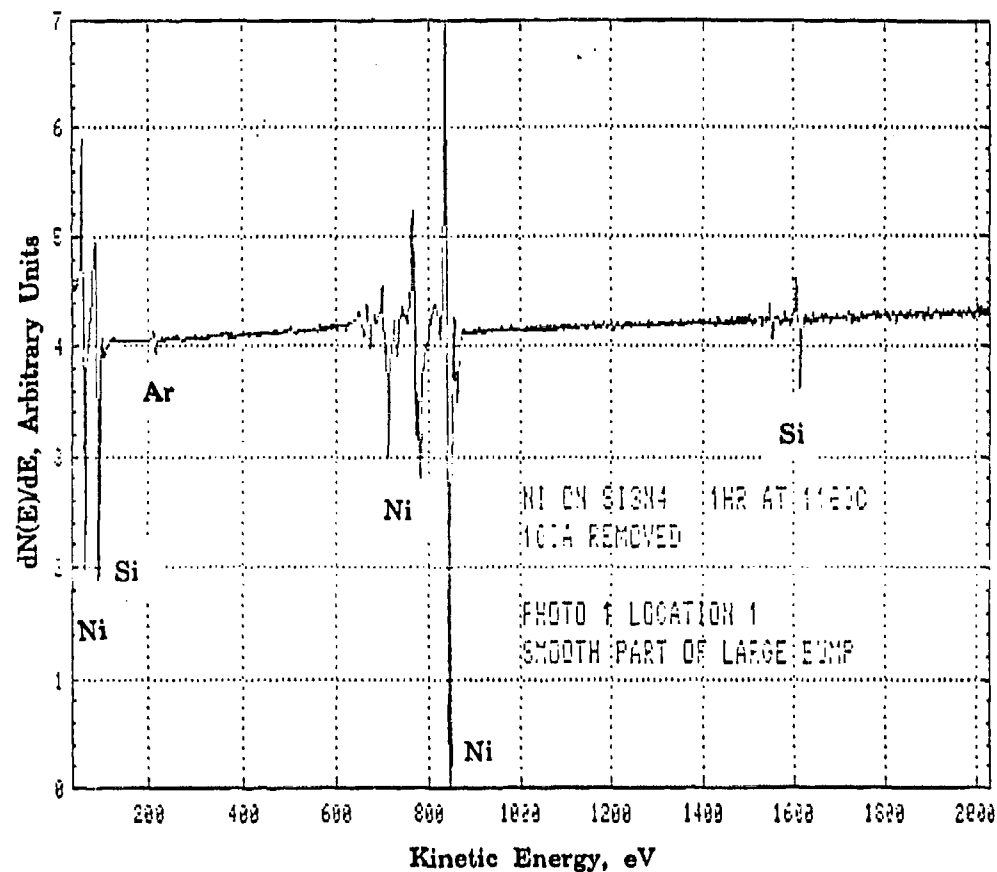


Fig. 5.47 AES survey spectra of  $Ni/Si_3N_4$  specimen, annealed 1 h at 1160°C, from the smooth part of precipitate (top) and from the dendrite on the precipitate (bottom).

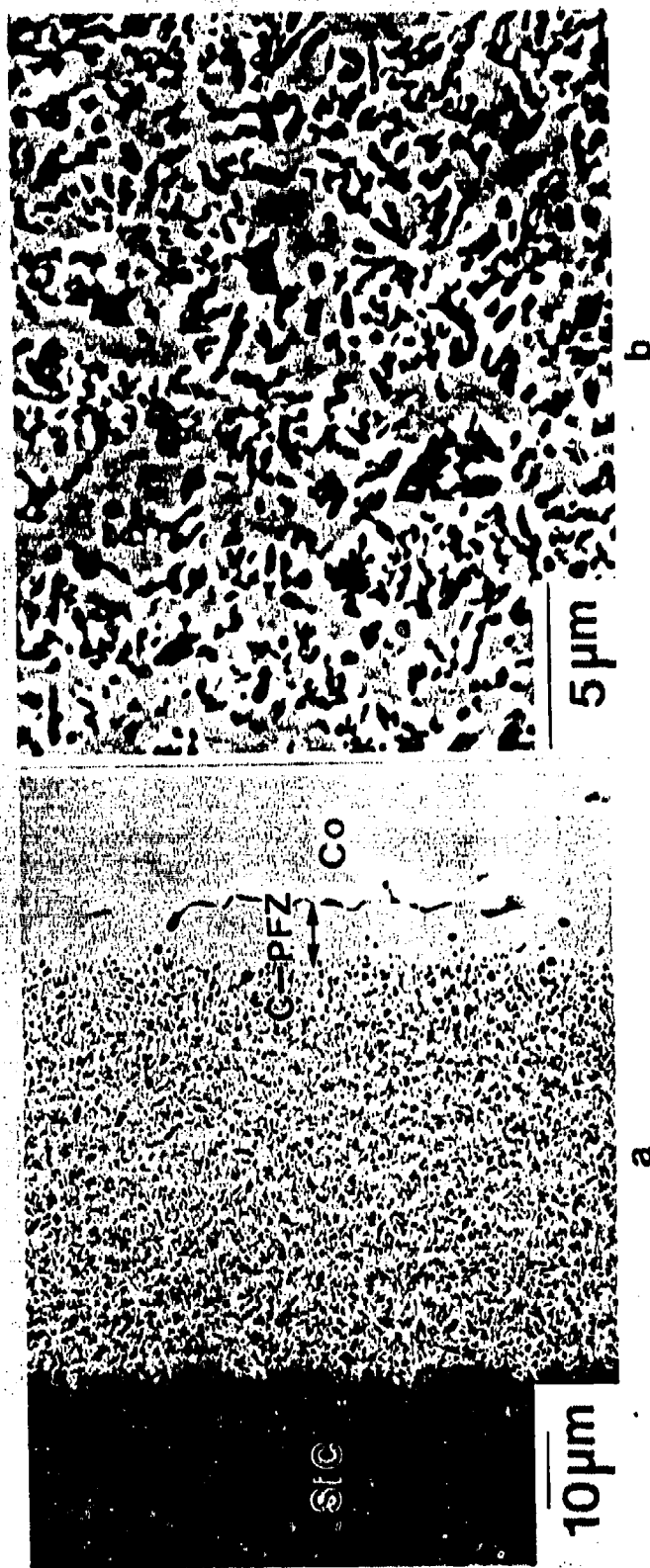


Fig. 5.48 (a) A cross-sectional SEM micrograph showing the Co/SiC reaction zone after annealing for 6 h at 1100 °C. The location of the phase boundary is indicated by arrows. (b) A high magnification SEM micrograph showing the microstructure of the random carbon precipitation zone.



Fig. 5.49 A SEM micrograph showing the microstructure of the ex-situ fractured SiC interface. The boundary between the unreacted and reacted regions is indicated.

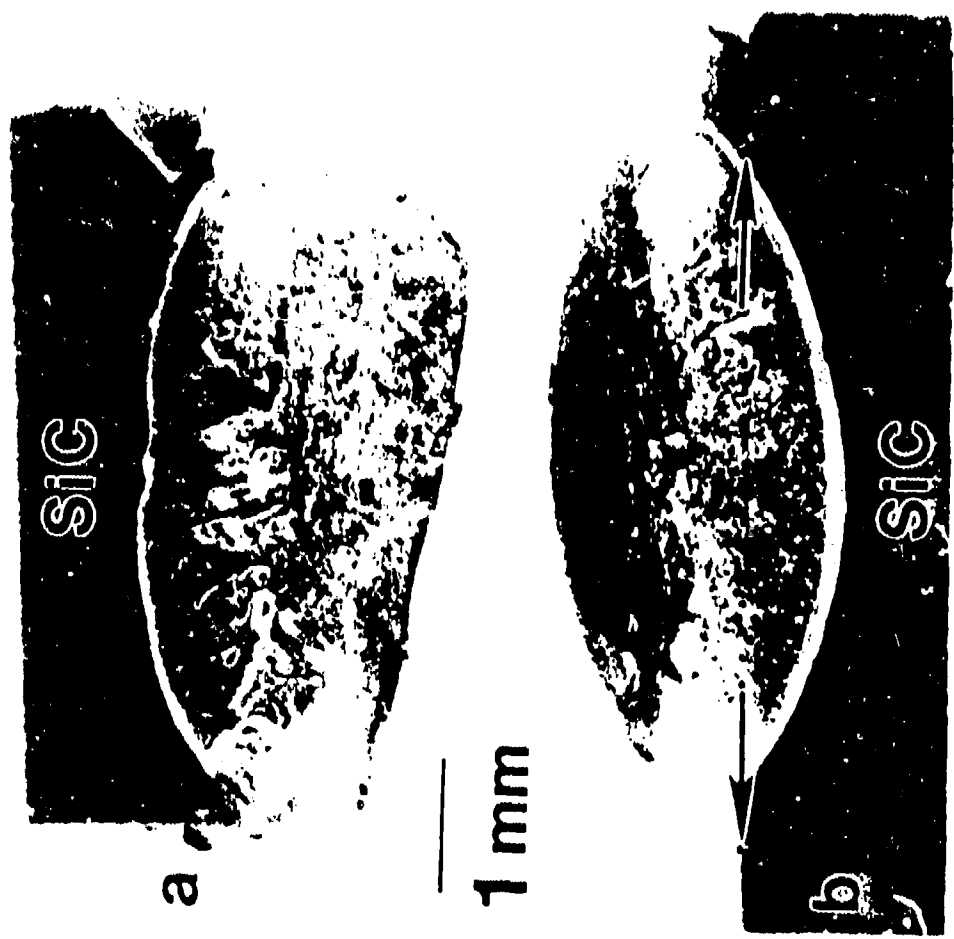


Fig. 5.50 Optical micrographs showing cross-sectional views of the Co/SiC reactions based on the reaction geometries of: (a) SiC on top of Co, and (b) Co on top of SiC after 1210°C annealing for 4 hrs. The original SiC/Co joining interface is indicated in (b).



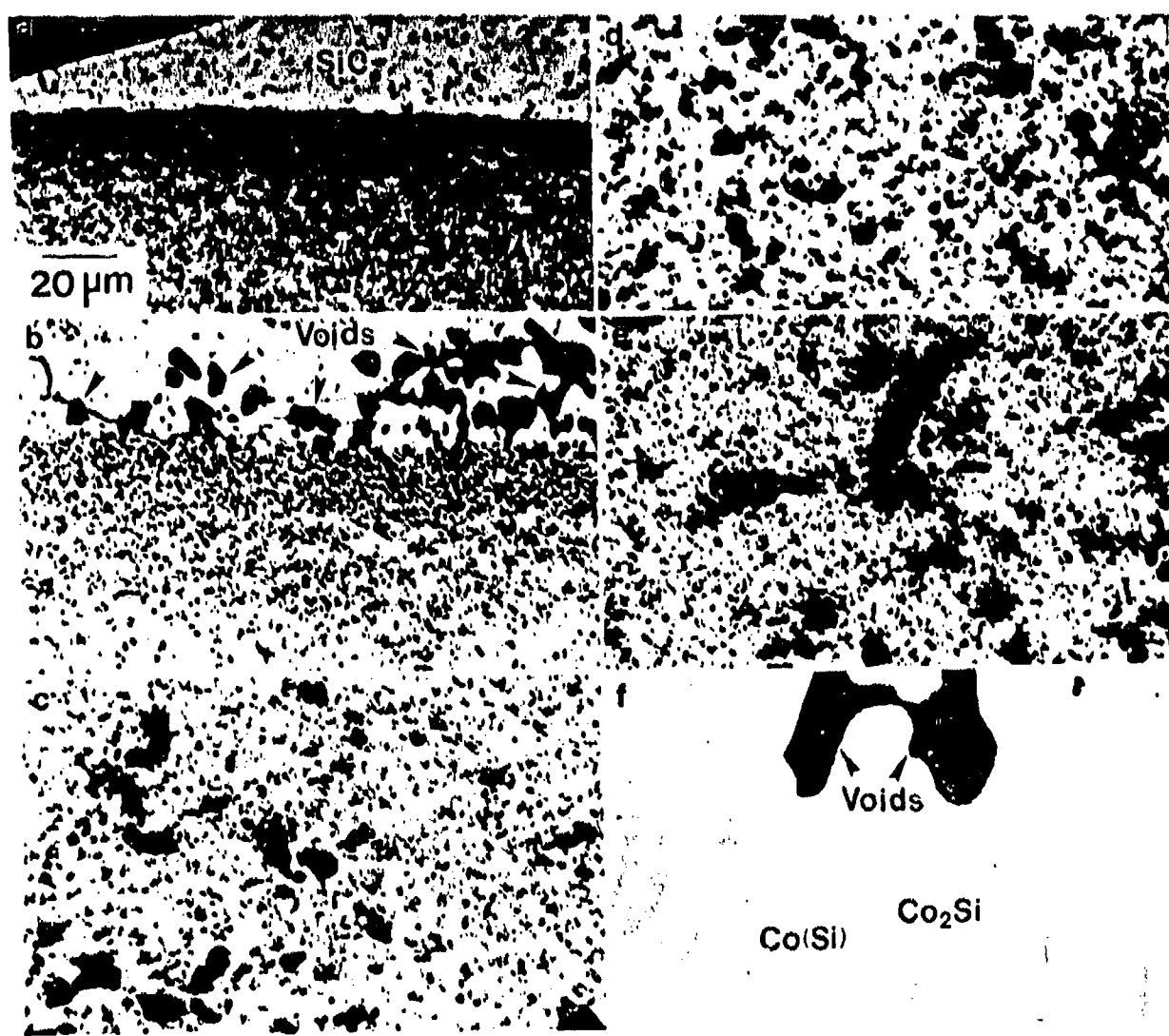


Fig. 5.51 A series of optical micrographs showing cross-sectional views of the Co/SiC reaction zone. (a) Co/SiC interface, (b)-(e) random C precipitation zone, (f) Co(Si) (light matrix) and Co<sub>2</sub>Si (gray areas) two phase mixture region. The dark areas, as indicated and shown on top of the (b) and (f), are voids.

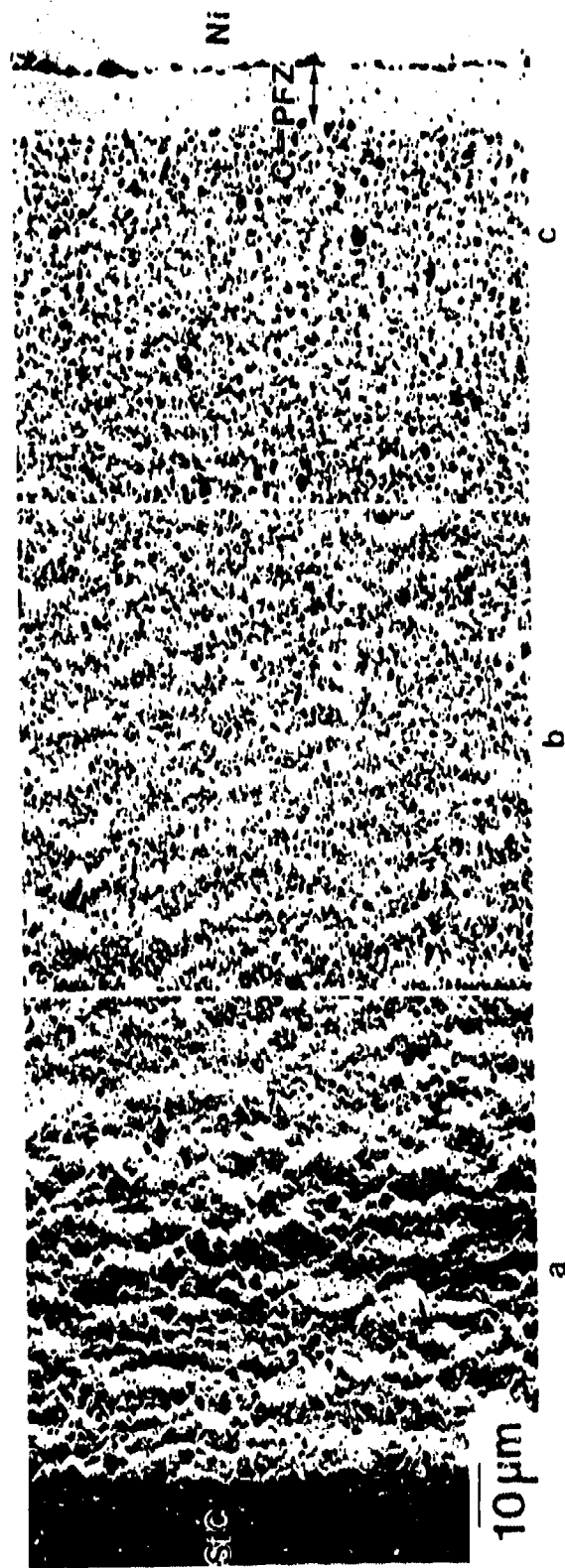


Fig. 5.52 A cross-sectional SEM micrograph of the Ni/SiC reaction zone after annealing for 6 hrs at 1100°C.



Fig. 5.53 High magnification SEM micrographs of the Ni/SiC reaction zone.

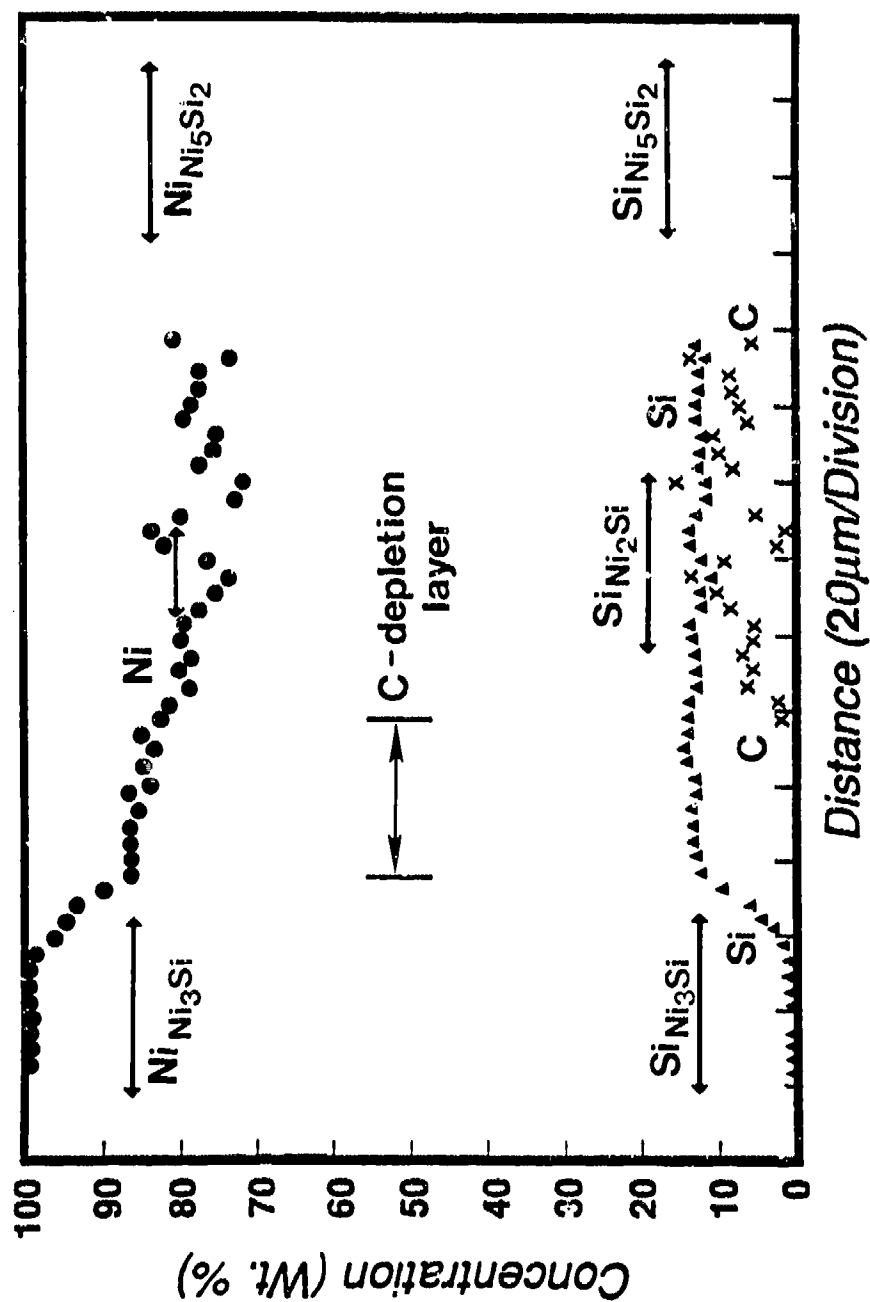


Fig. 5.54

Quantitative electron microprobe concentration profiles of Ni, Si, and C across the reaction zone from the Ni/SiC diffusion couple after annealing for 6 hrs at 1100 °C. The relative concentrations of Ni and Si for Ni<sub>3</sub>Si and Ni<sub>5</sub>Si<sub>2</sub> are indicated. The locations of the unreacted Ni component, C-PFZ, and CPZ are marked.

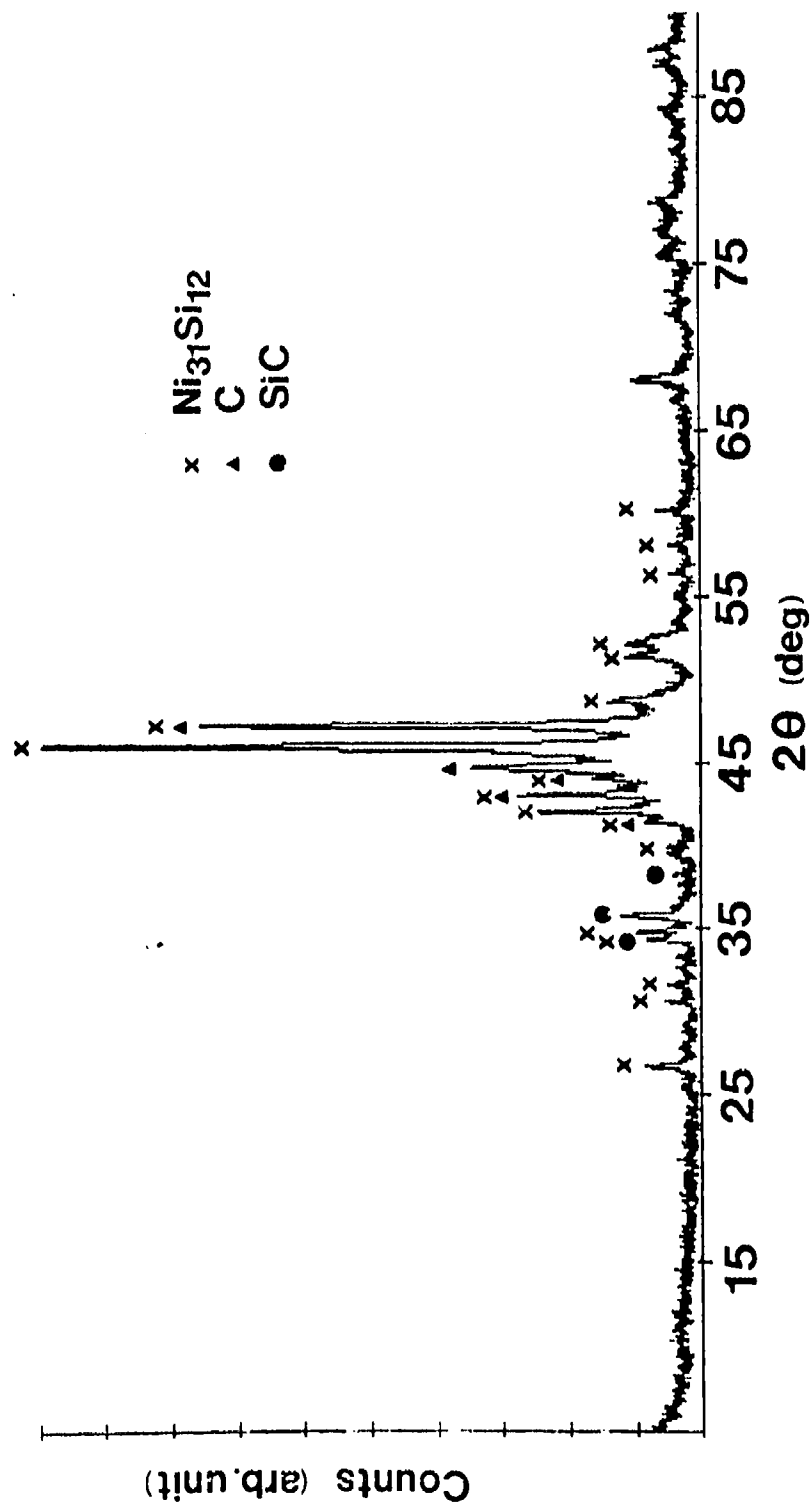


Fig. 5.55 XRD spectra of the reaction products generated from the Ni/SiC reaction at 1170°C.

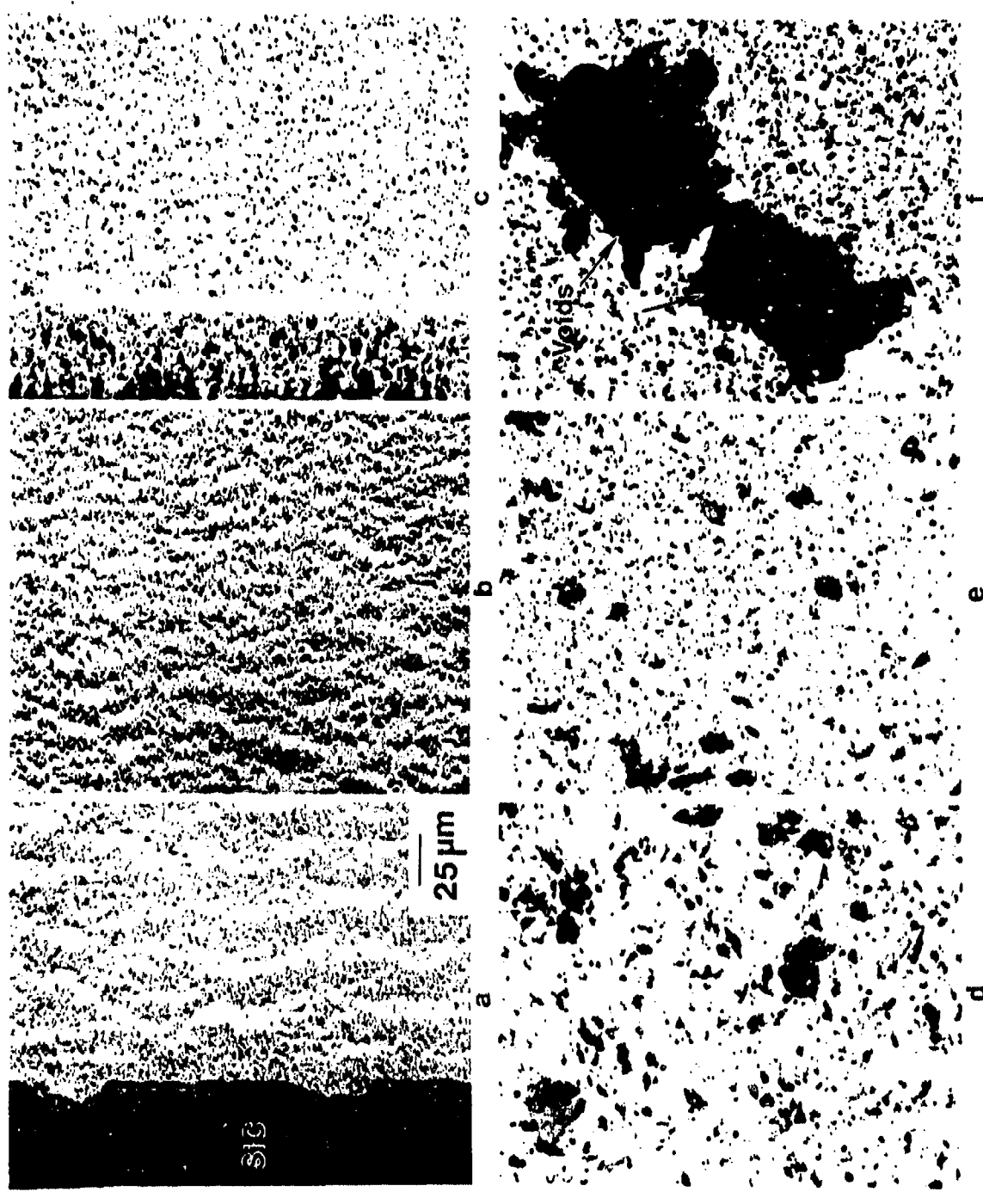


Fig. 5.56 Optical micrographs showing cross-sectional views of the Ni/SiC reaction zone after annealing for 4 hrs at 1170°C. Porosity, as a result of melting/ solidification, is noted and indicated in the reaction zone.

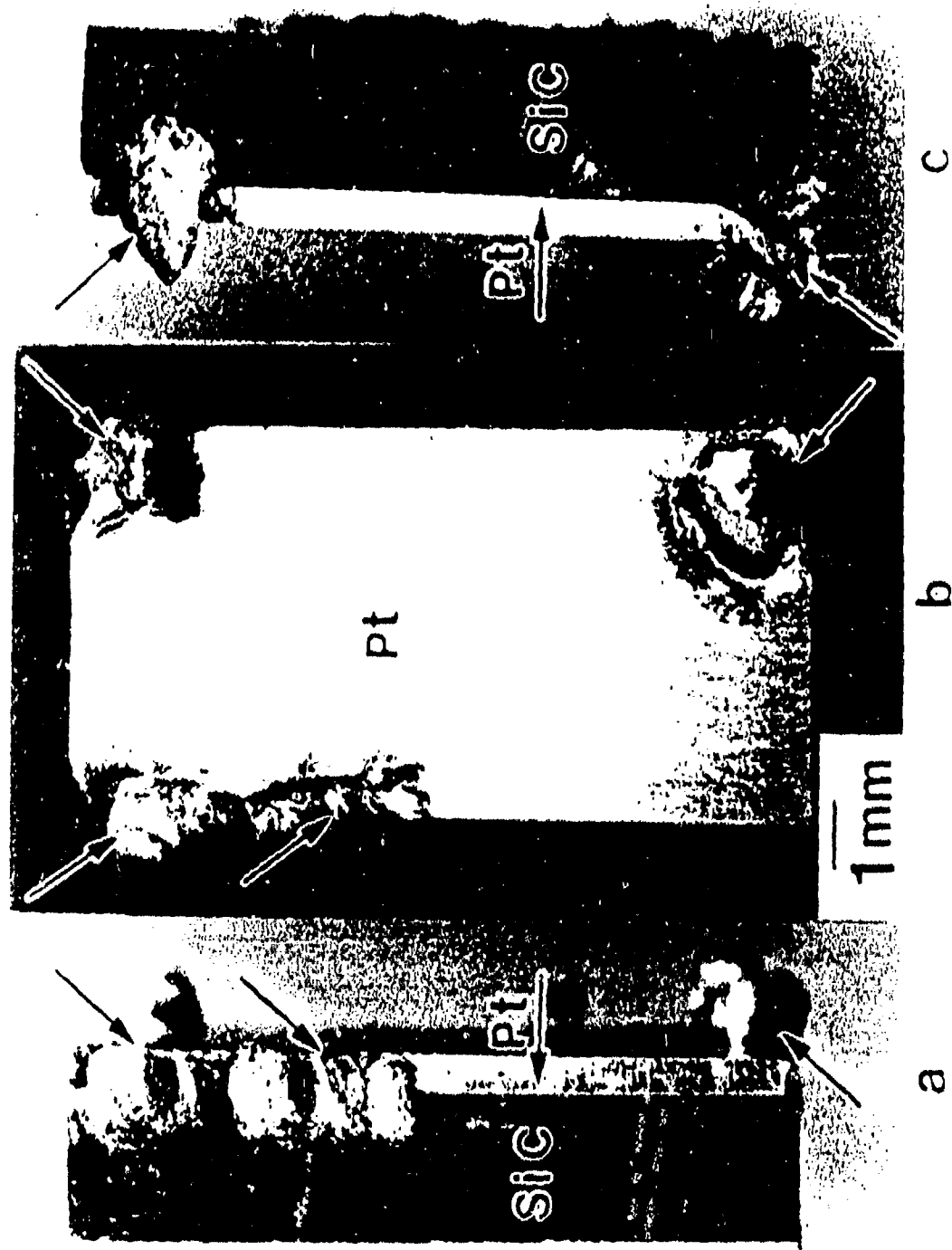


Fig. 5.57 Optical micrographs showing different views of the melting/solidification phenomena from the Pt/SiC diffusion couple after annealing for 5 hrs at 900°C.

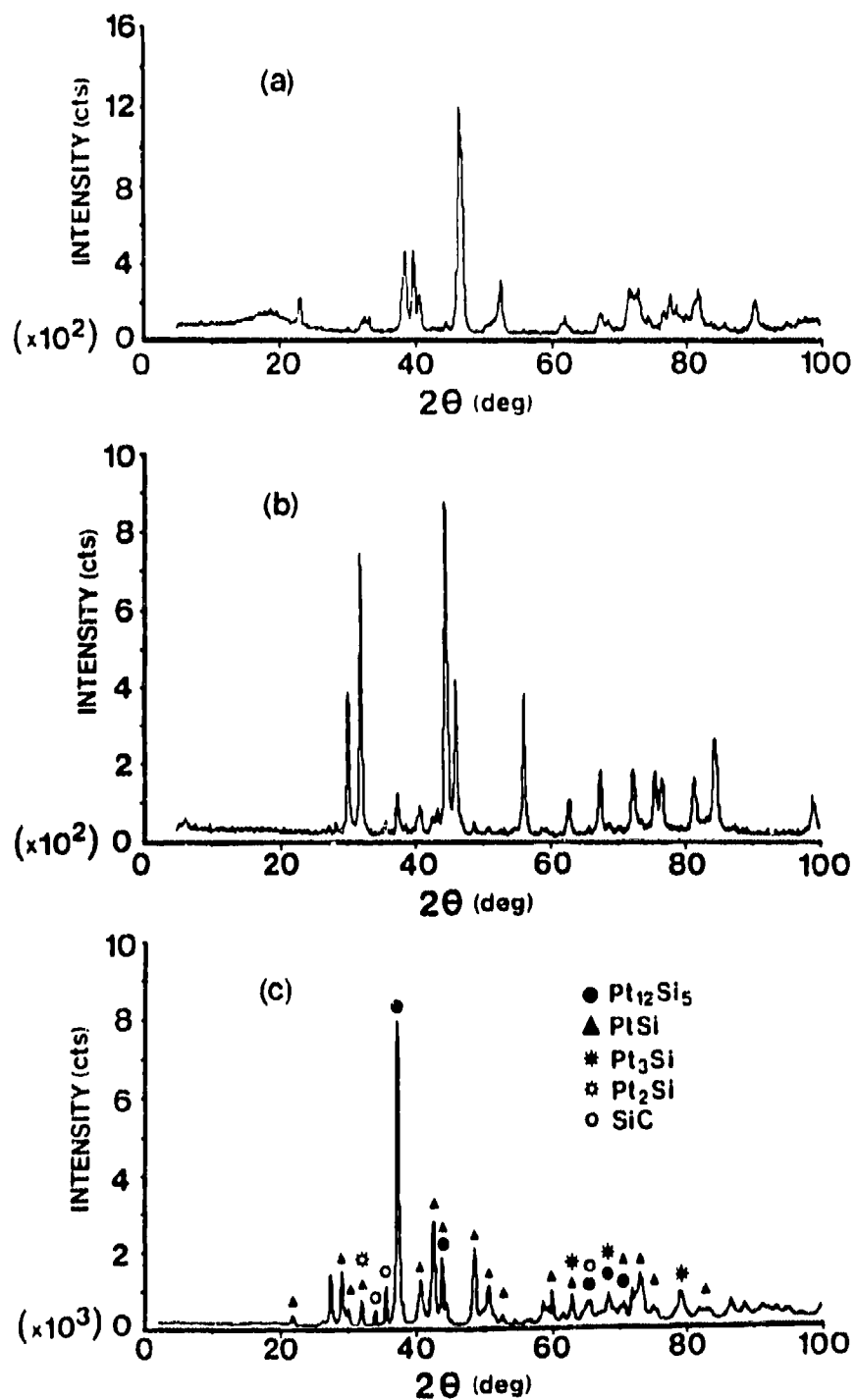


Fig. 5.58 XRD spectra of the Pt/SiC reaction products after (a) 900, (b) 1000, and (c) 1100 °C reactions.



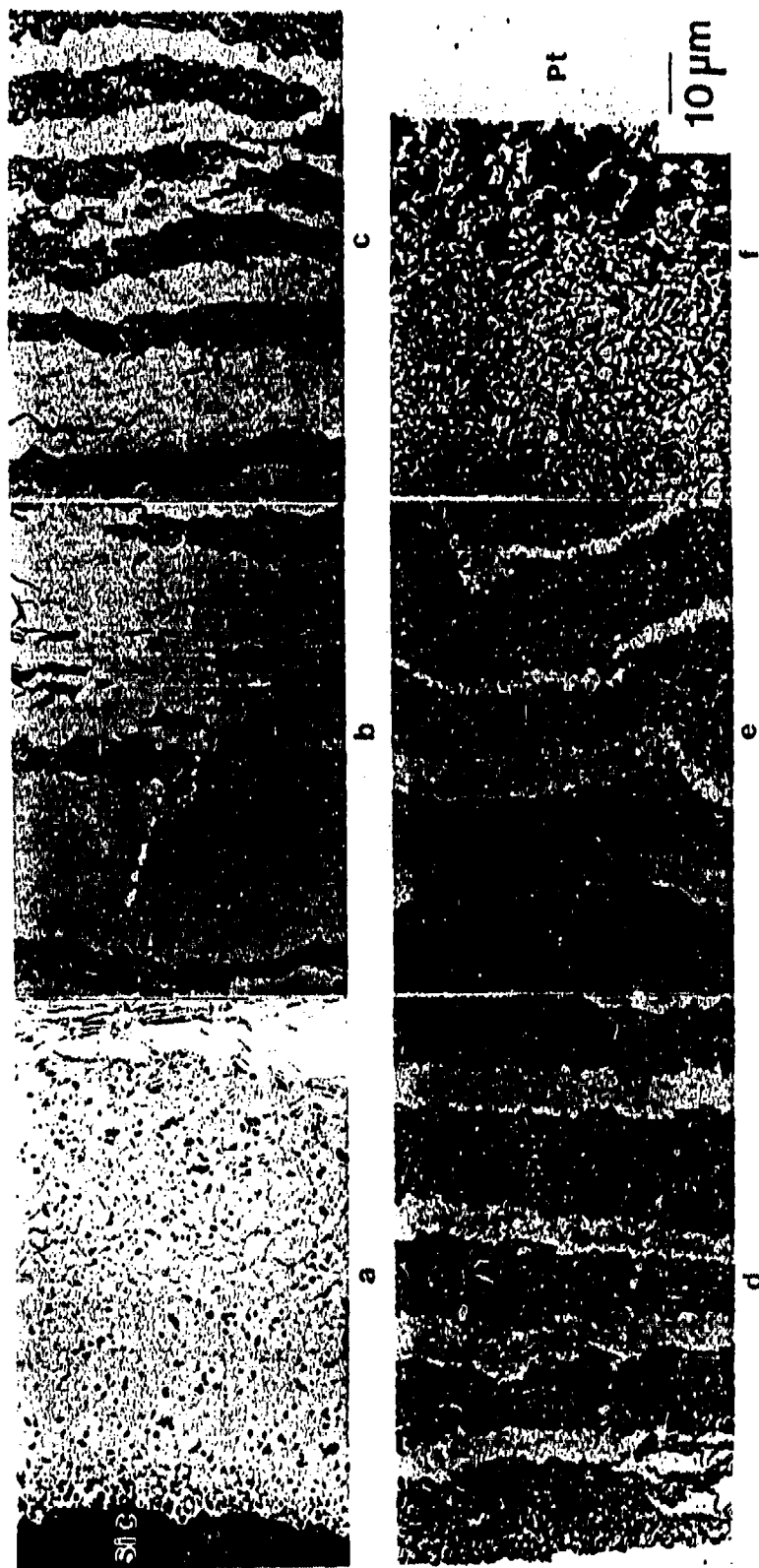


Fig. 5.59 A series of SEM micrographs showing microstructure of the Pt/SiC reaction zone after annealing for 4 hrs at 1100°C.

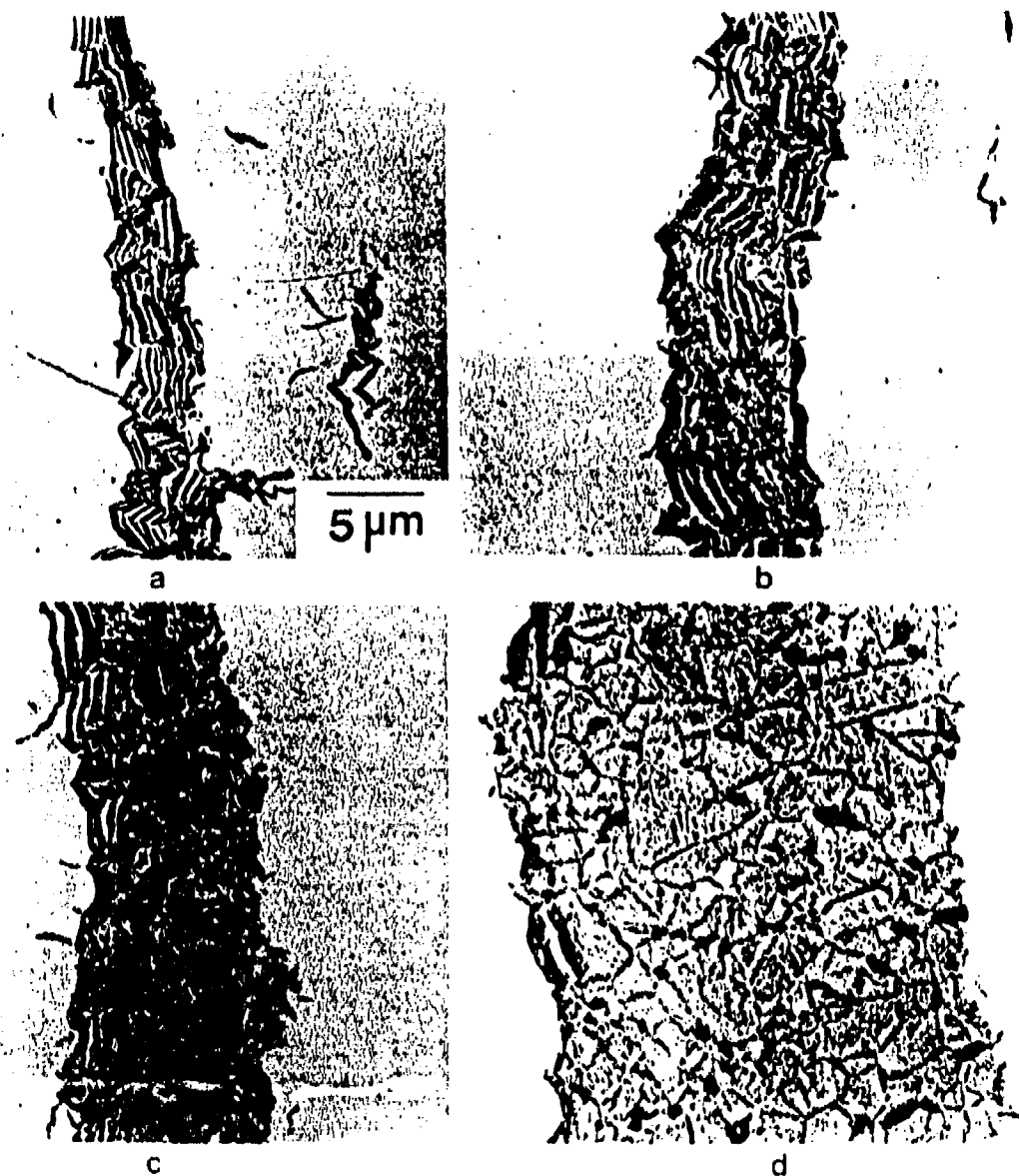


Fig. 5.60

SEM micrographs showing the microstructural change of the C bands, as a function of distance from the SiC reaction interface, from the as-reacted P/SiC diffusion couple after annealing for 4 hrs at 1100°C. As the distance increases, from (a) to (d), the thickness of the clustered C bands increases and the discrete C layers transform into C-decorated, granular Pt-silicide layers.



Fig. 5.61 SEM micrographs showing the microstructural evolution in the reaction zone from the as-reacted Pt/SiC diffusion couple after annealing for 4 hrs at 1100 °C.



Fig. 5.62 A high magnification backscattered electron image showing the microstructure of the 3rd layer, and the morphology of the melted/solidified particulates formed on top from the as-reacted Pt/SiC diffusion couple after reactions at 1100 °C for 4 hrs.

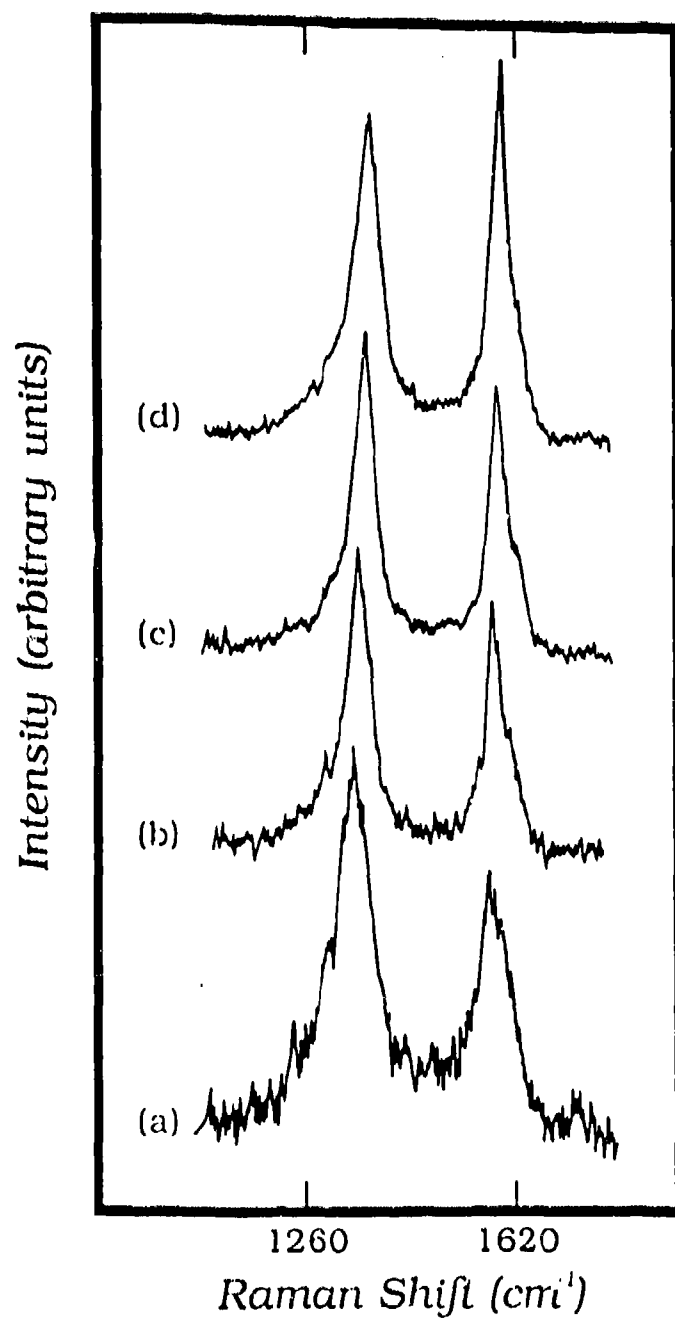


Fig. 5.63

A series of Raman spectra from the modulated C bands precipitated in the the SiC/Pt reaction zone after annealing for 5 hrs at 1000 °C. The spectrum, (a), from the SiC reaction interface indicates the existence of glassy carbon, which is characterized by the presence of a Raman peak at  $1354\text{ cm}^{-1}$ . As the locations of the C bands are farther removed from the SiC interface, from (b) to (d), graphitization of the C occurs, which is characterized by the decrease of the intensity ratio between the  $1354$  and  $1585\text{ cm}^{-1}$  Raman peaks.

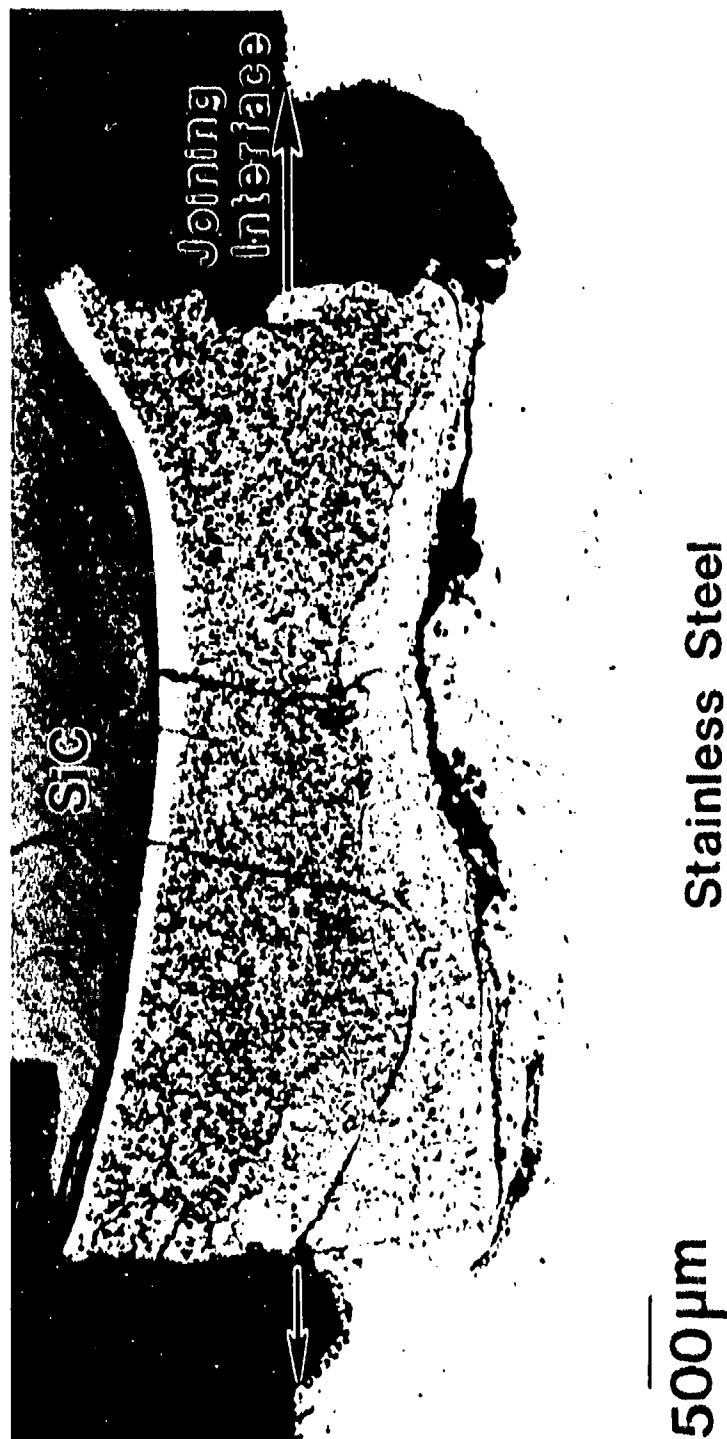


Fig. 5.64 A cross-sectional view SEM micrograph showing the reaction zone of a SS/SiC diffusion couple upon annealing at 1125°C for 8 h.



Fig. 5.65 High magnification SEM micrographs showing the formation of 4 layered reaction zone.  
The four layers are indicated as 1, 2, 3 and 4.

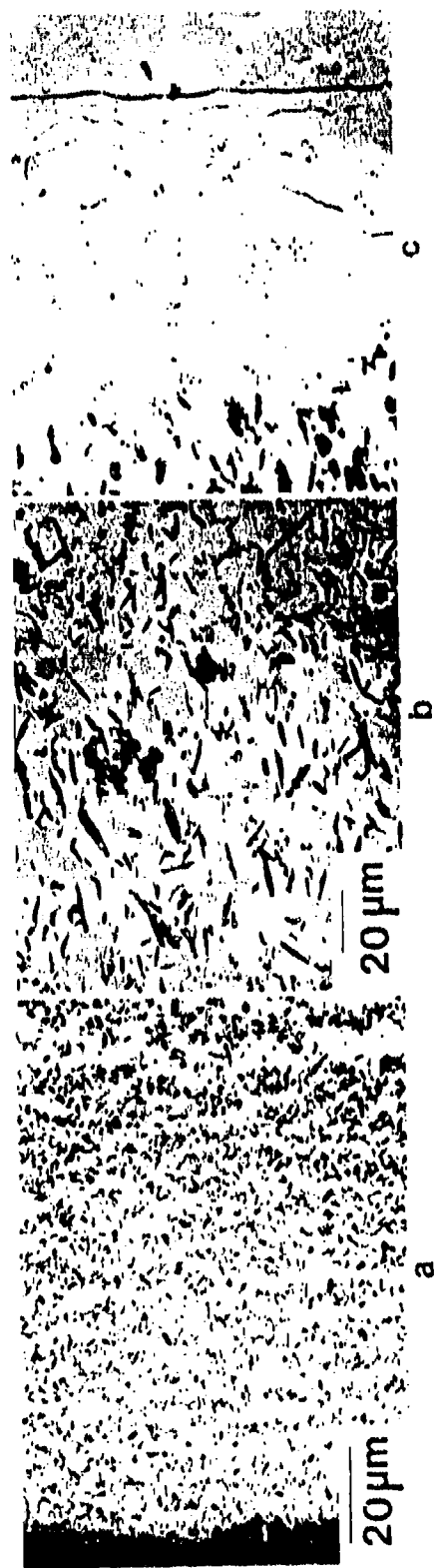


Fig. 5.66 High magnification SEM micrographs showing detailed microstructures in reaction zones 1, 2, and 3. Highly anisotropic C precipitates were observed in reaction zones 1 and 2.



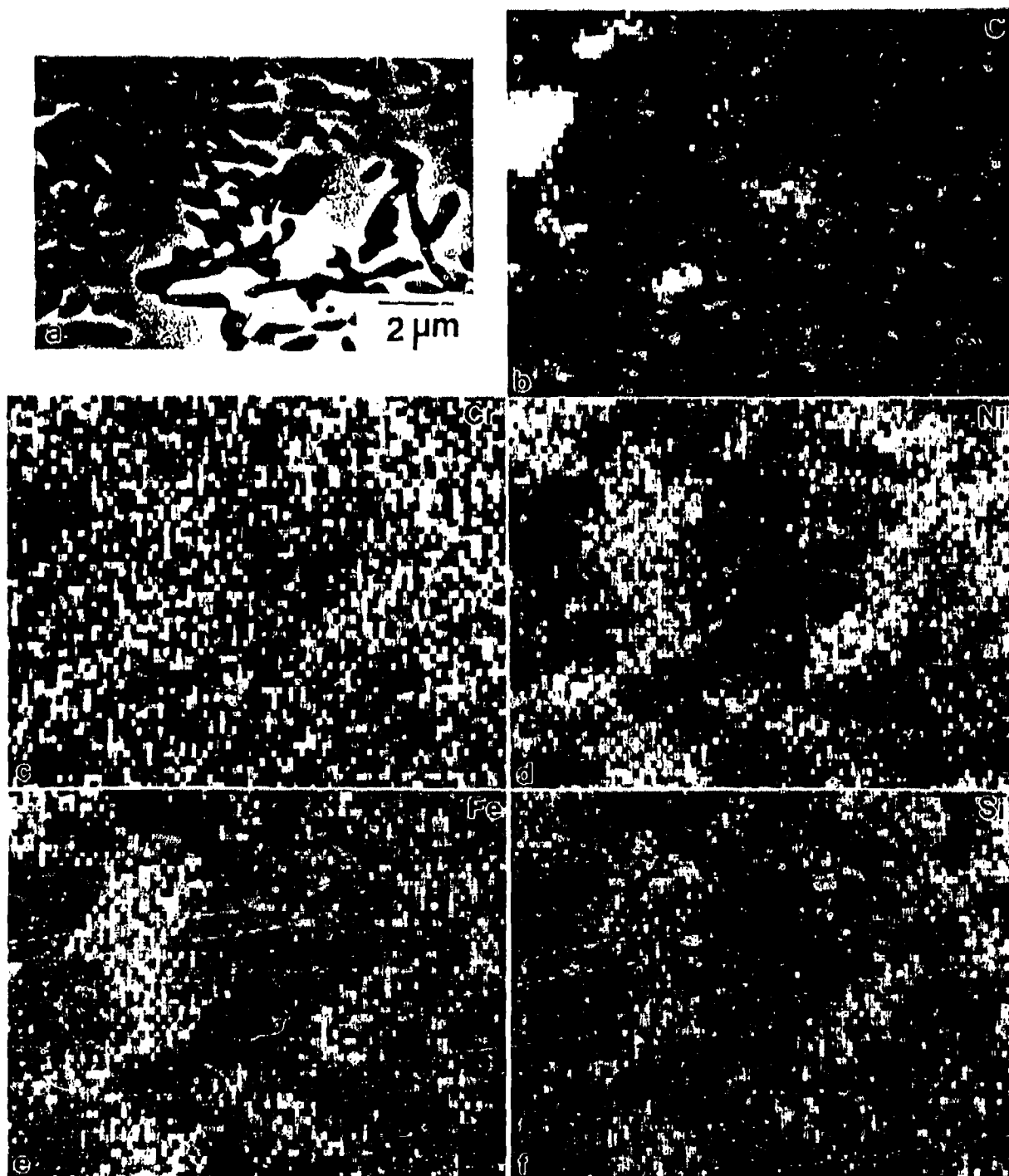


Fig. 5.67 (a) A backscattered electron image, and the corresponding elemental x-ray maps of (b) C, (c) Cr, (d) Ni, (e) Fe, and (f) Si from an area in reaction zone 1.

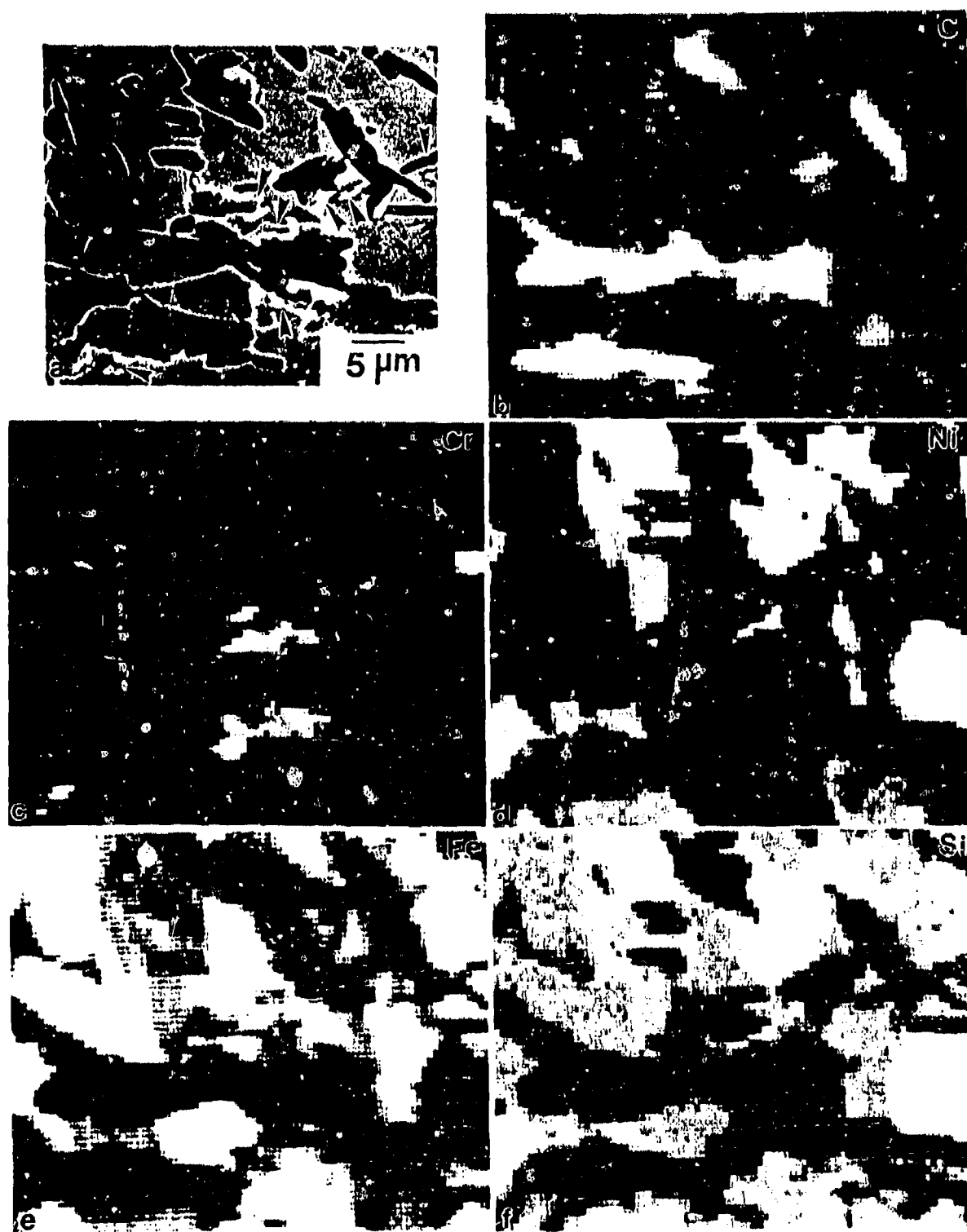


Fig. 5.68 (a) A backscattered electron image, and the corresponding elemental x-ray maps of (b) C, (c) Cr, (d) Ni, (e) Fe, and (f) Si from an area in reaction zone 2.

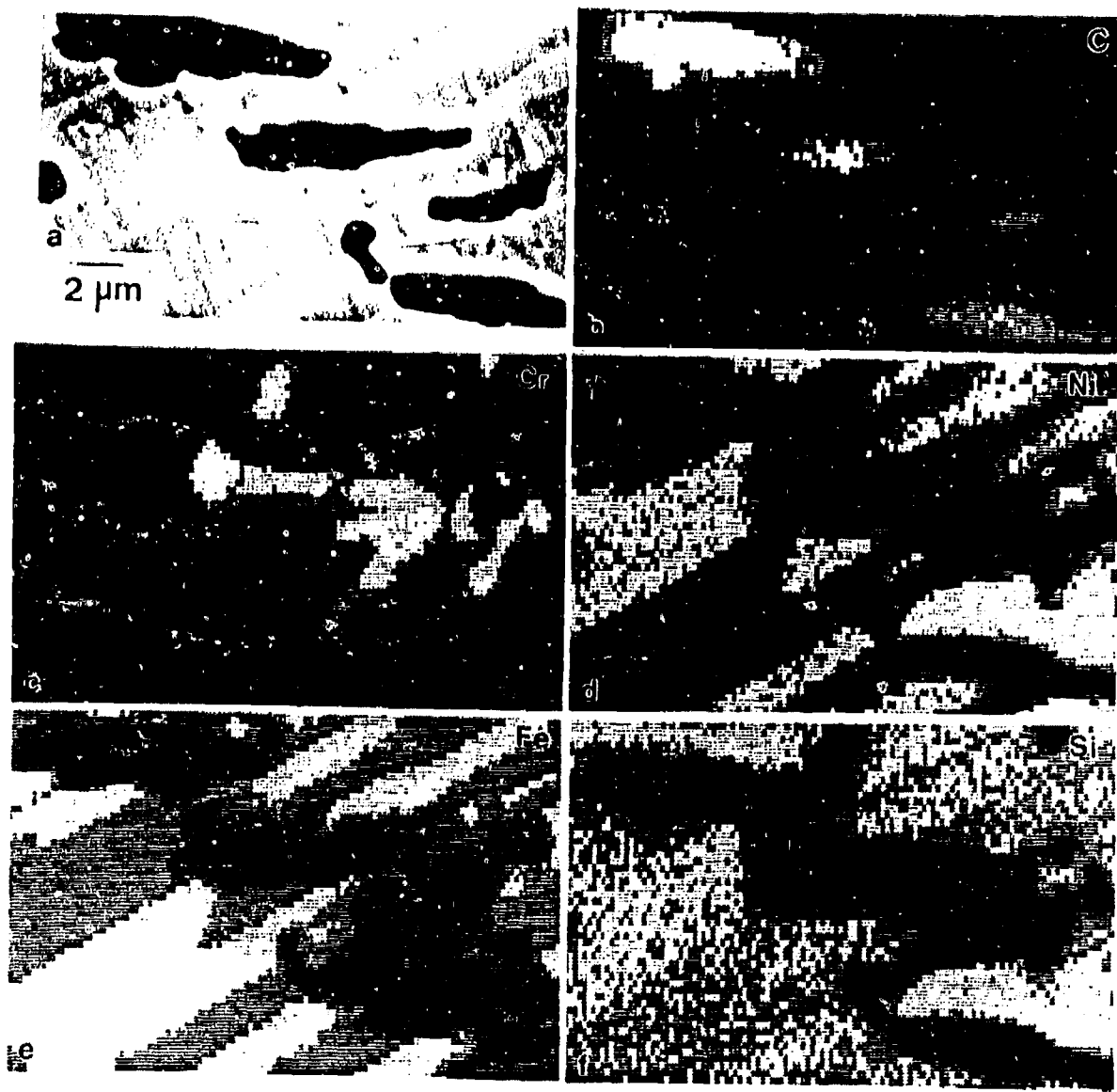


Fig. 5.69 (a) A backscattered electron image, and the corresponding elemental x-ray maps of (b) C, (c) Cr, (d) Ni, (e) Fe, and (f) Si from a farther area in reaction zone 2.

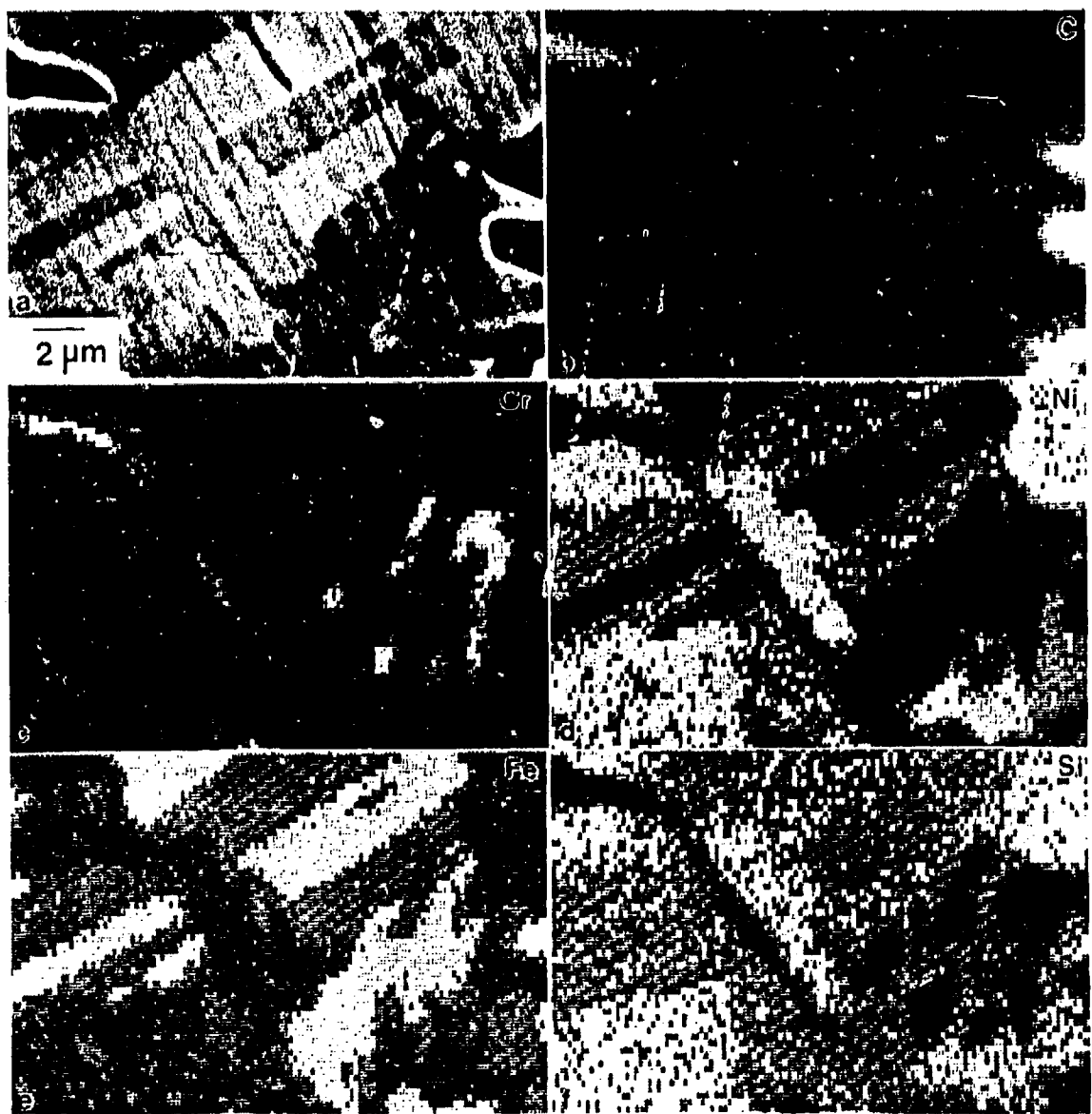


Fig. 5.70 (a) A backscattered electron image, and the corresponding elemental x-ray maps of (b) C, (c) Cr, (d) Ni, (e) Fe, and (f) Si from an even farther area in reaction zone 2.

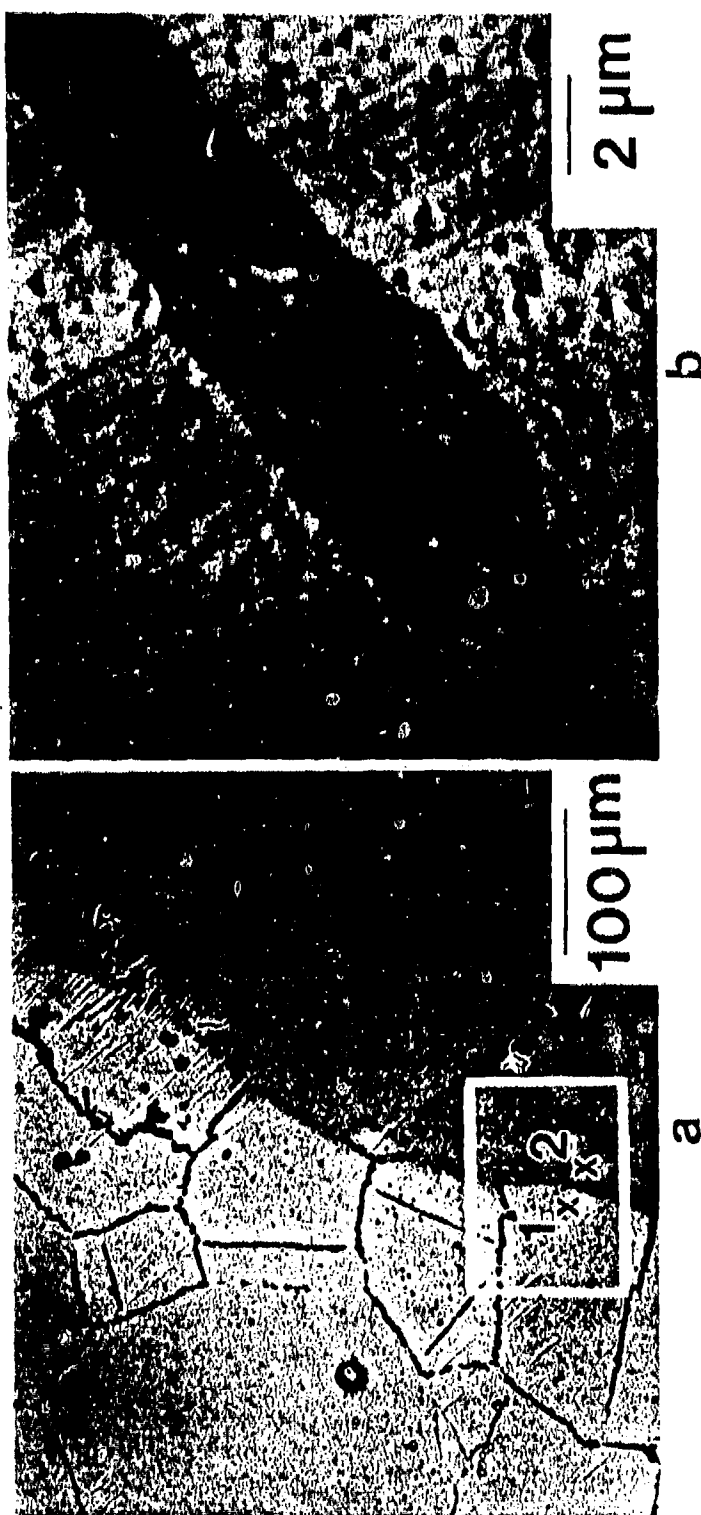


Fig. 5.71 SEM micrographs showing (a) the Si diffusion front and the G.B.-PZ; (b) a high magnification of the grain boundary precipitates. The Si diffusion front is indicated by arrows.

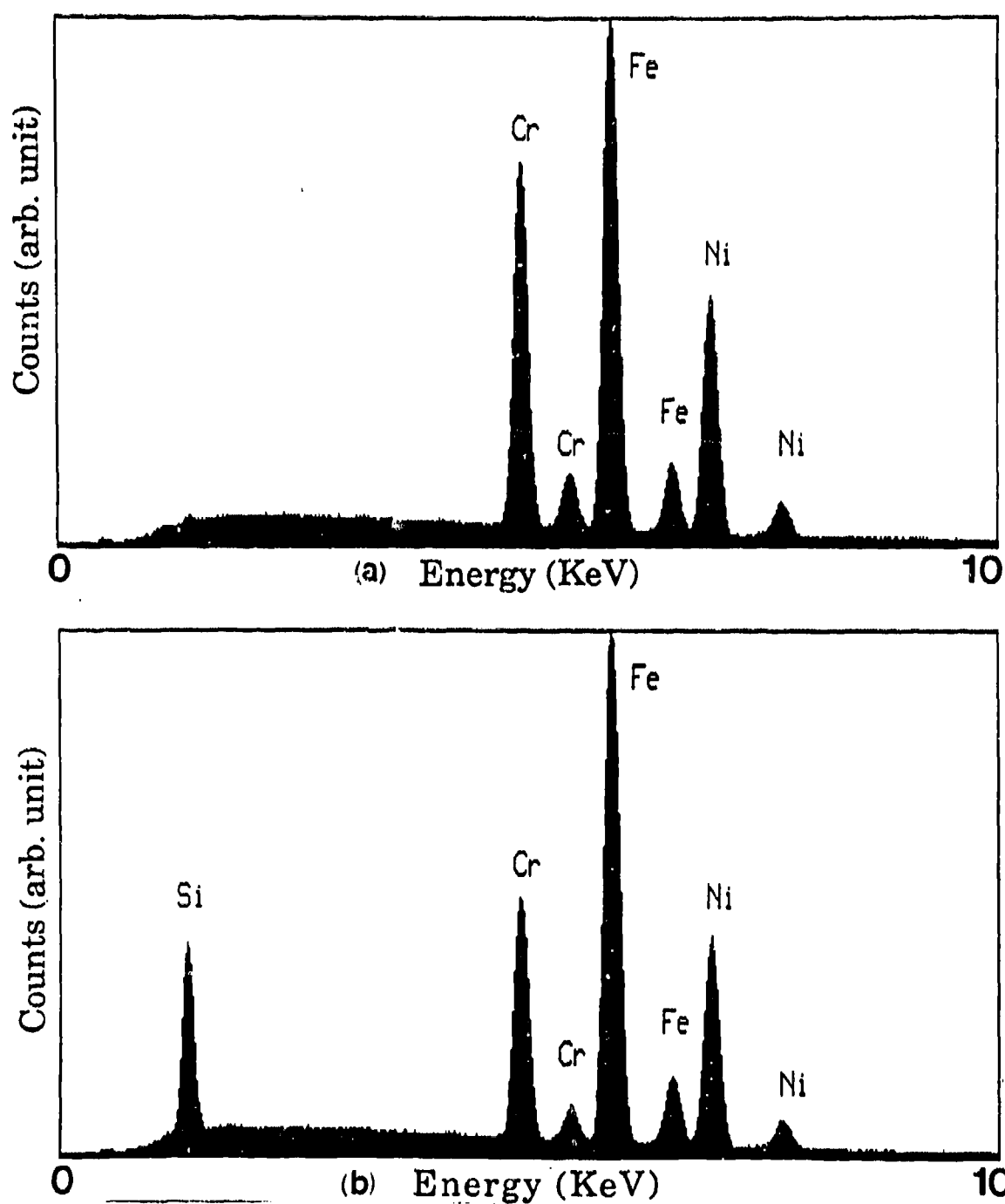


Fig. 5.72 EDS spectra collected from (a) point 1 and (2) point 2, as indicated in Fig. 5.71(a), showing the diffusion of Si is limited by the diffusion front.

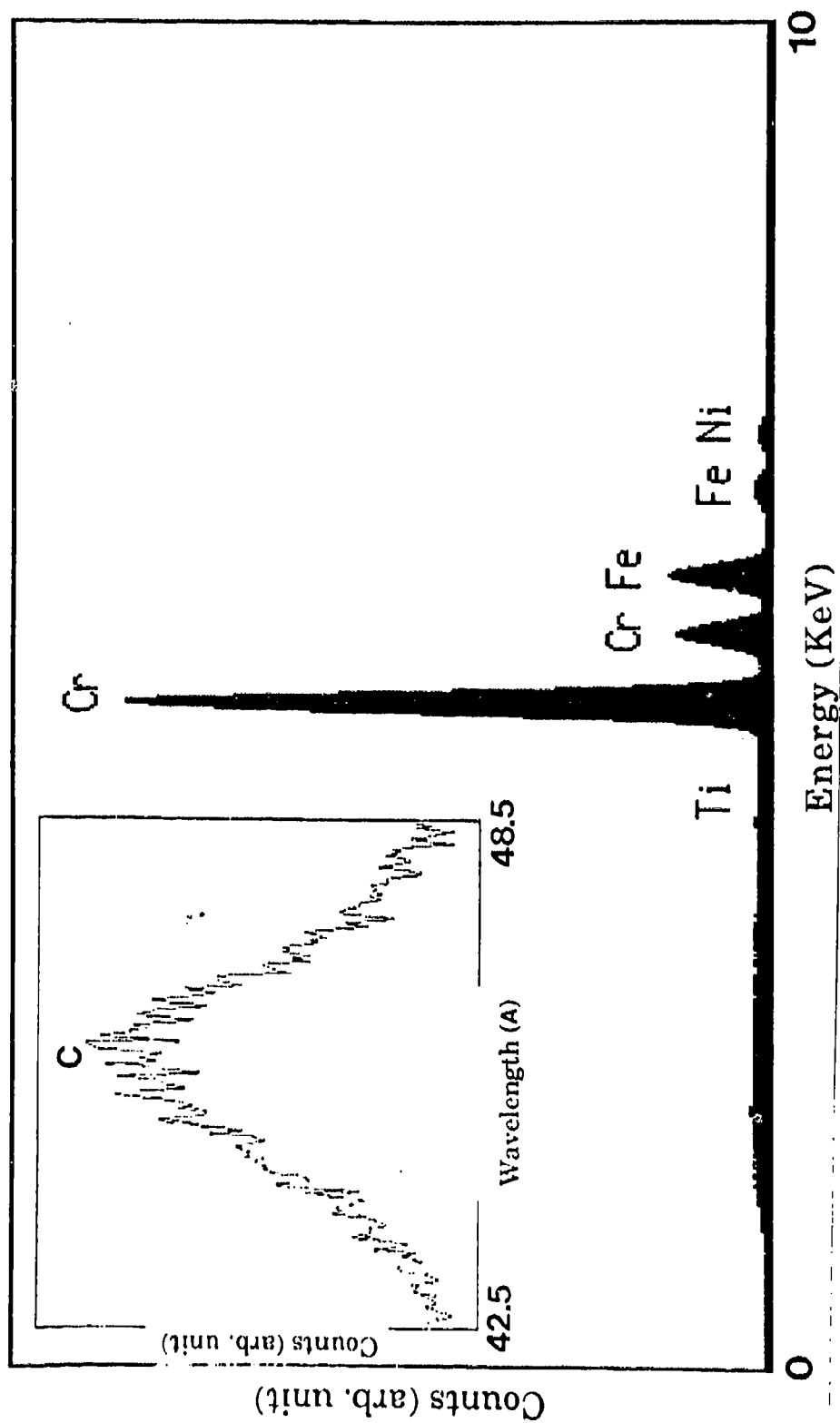


Fig. 5.73 EDS and WDS (the inset) spectra obtained from the grain boundary precipitates, as shown in Fig. 5.71(b), indicating the precipitates are Cr-carbide(s).

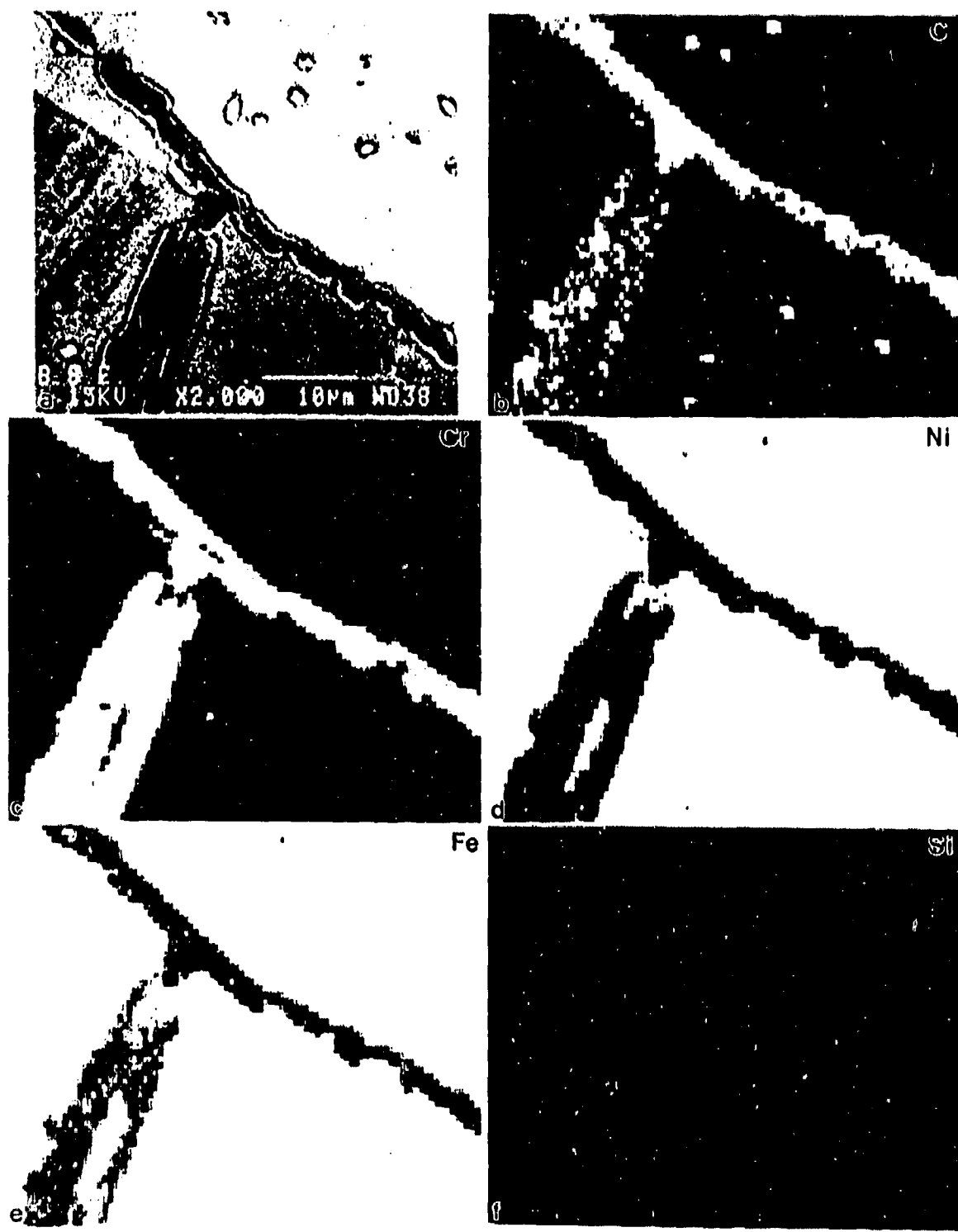


Fig. 5.74 (a) A backscattered electron image, and the corresponding elemental x-ray maps of (b) C, (c) Cr, (d) Ni, (e) Fe, and (f) Si from precipitates located in a triple grain boundary junction.



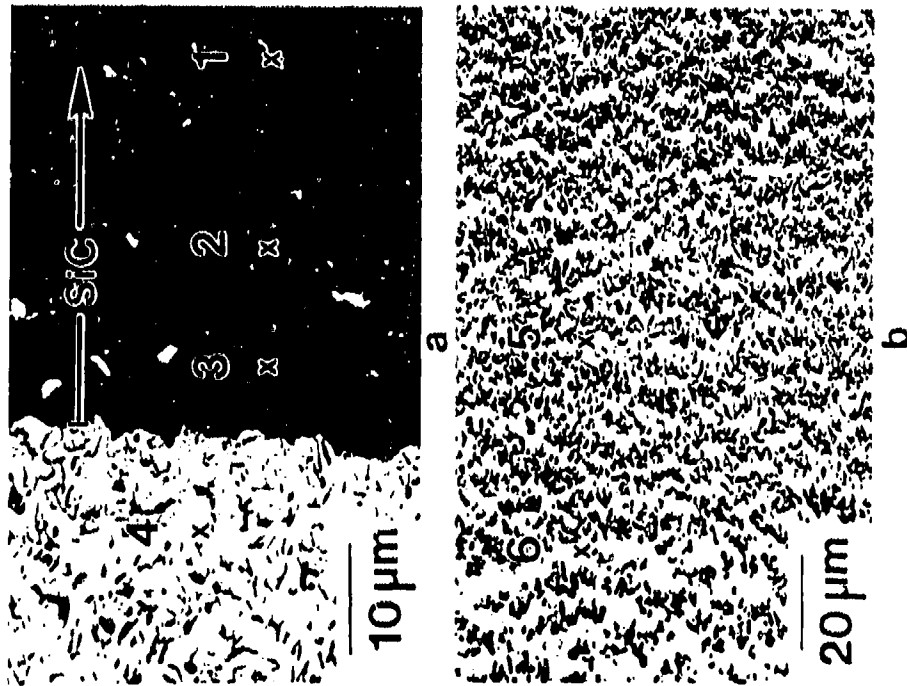


Fig. 5.75 SEM micrographs showing the locations from which systematic EDS analyses were conducted to establish the concentration gradients of Ni, Fe, and Cr.

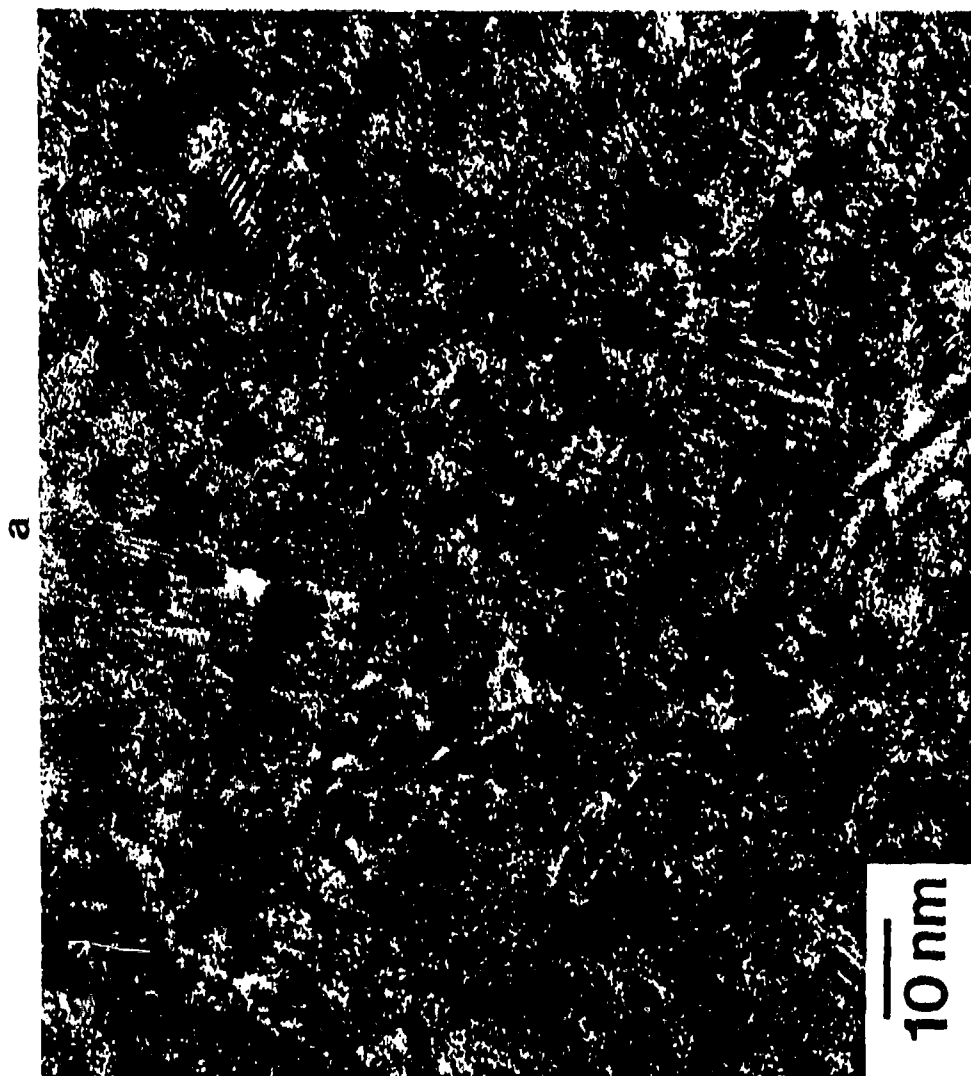
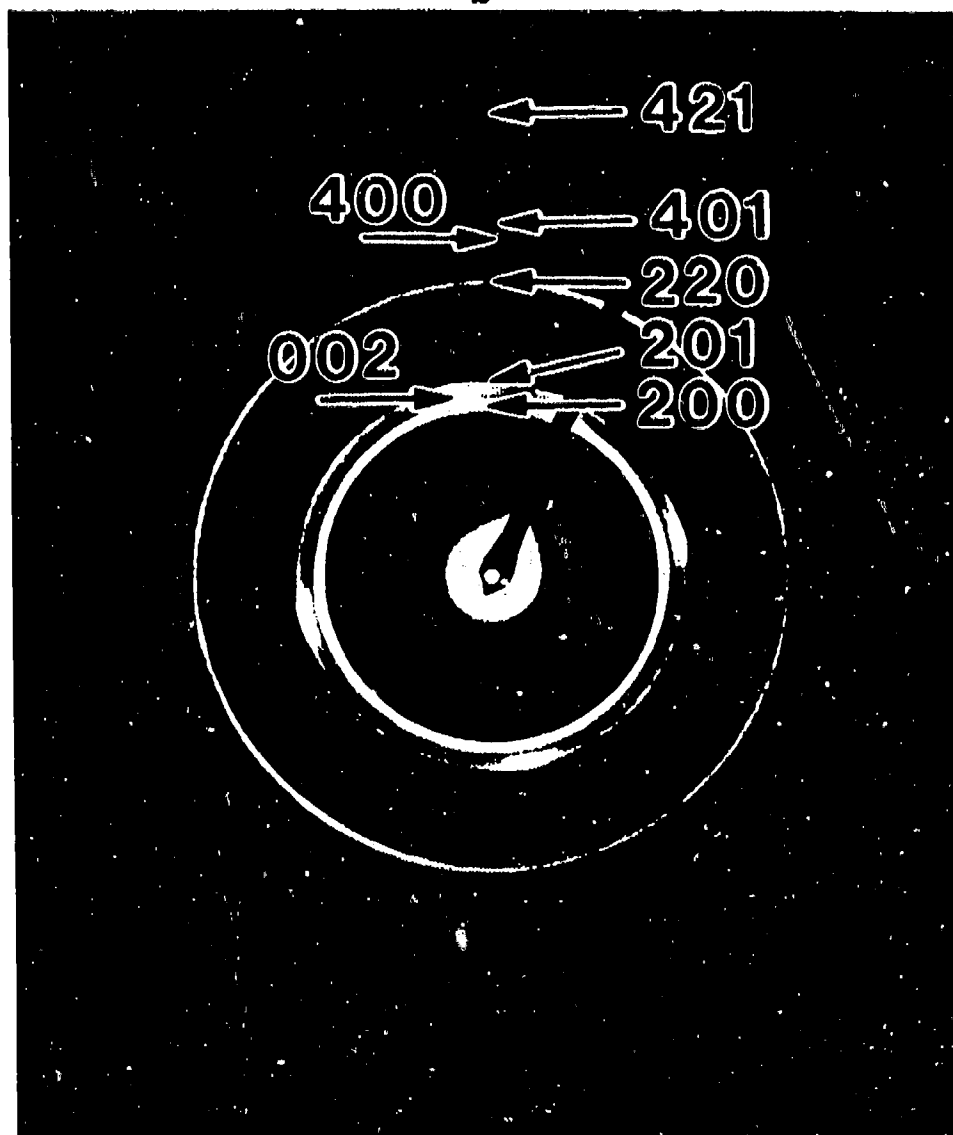


Fig. 5.76 (a) A TEM bright field image and (b) the corresponding electron diffraction pattern showing that the as-deposited film is polycrystalline  $Ti_3Al$ .

b



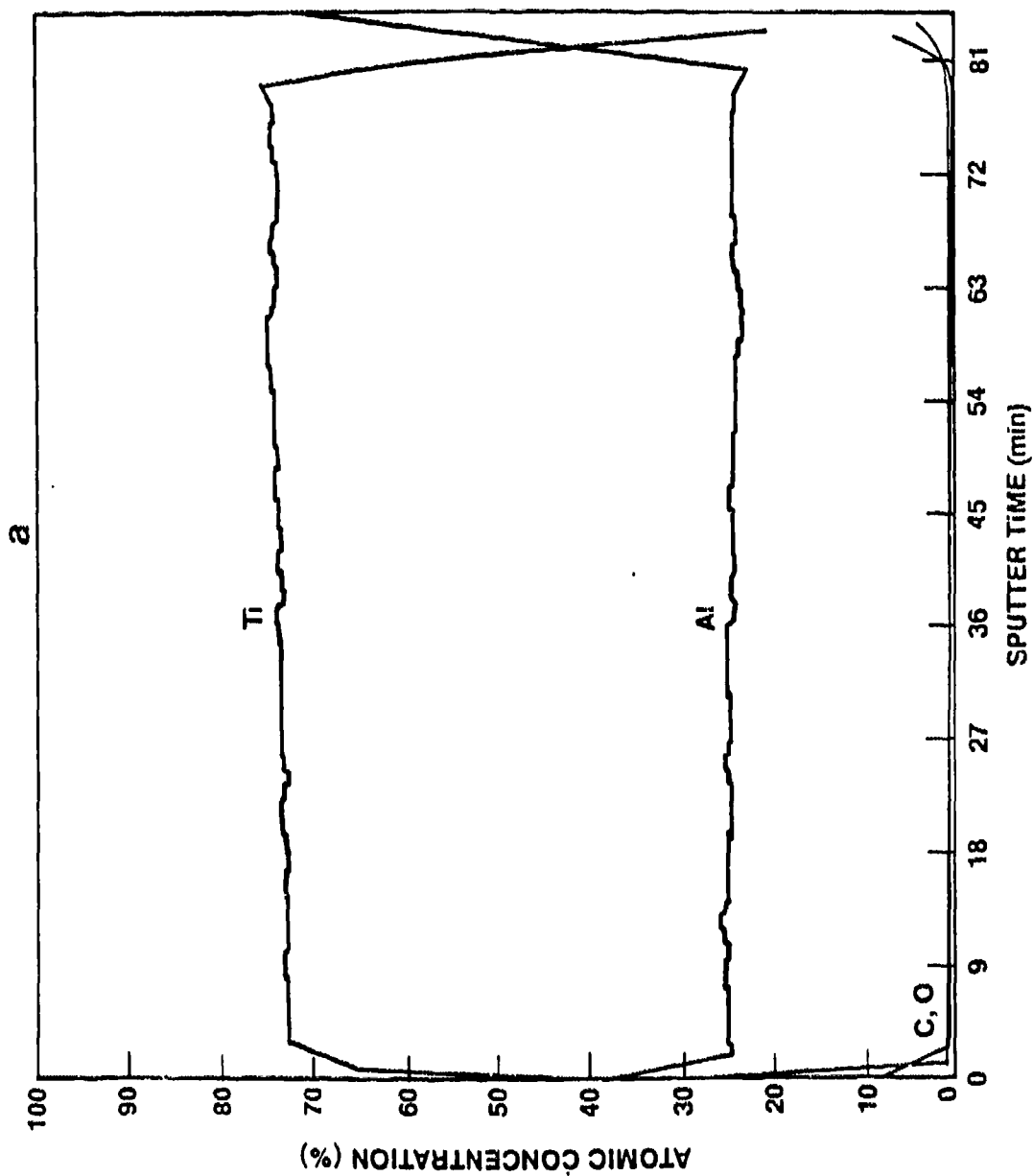
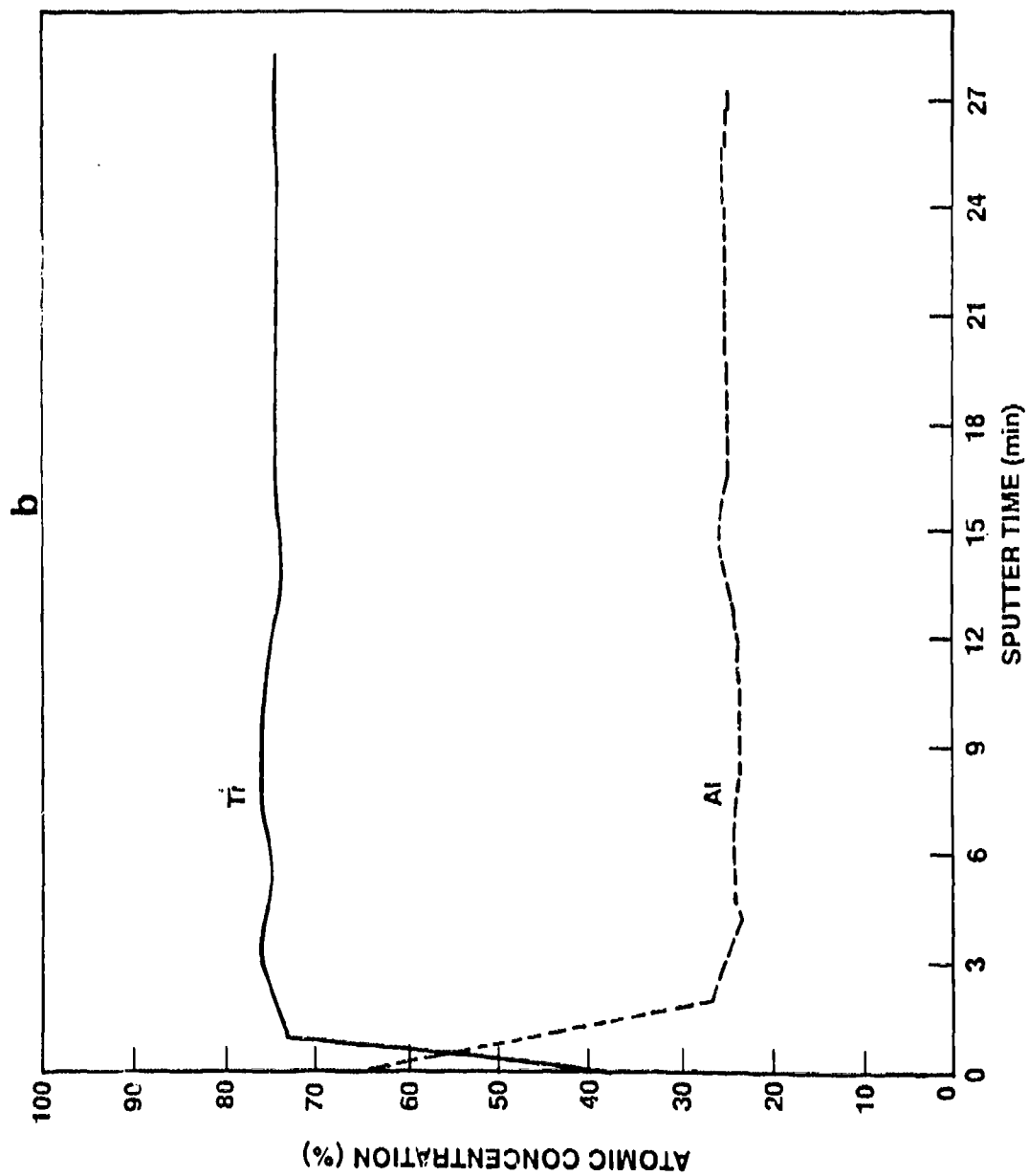


Fig. 5.77 AES depth concentration profiles from (a) an as-deposited  $\text{Ti}_3\text{Al}$  film (on a  $\text{Si}_3\text{N}_4$  substrate) and (b) a bulk  $\text{Ti}_3\text{Al}$  standard.



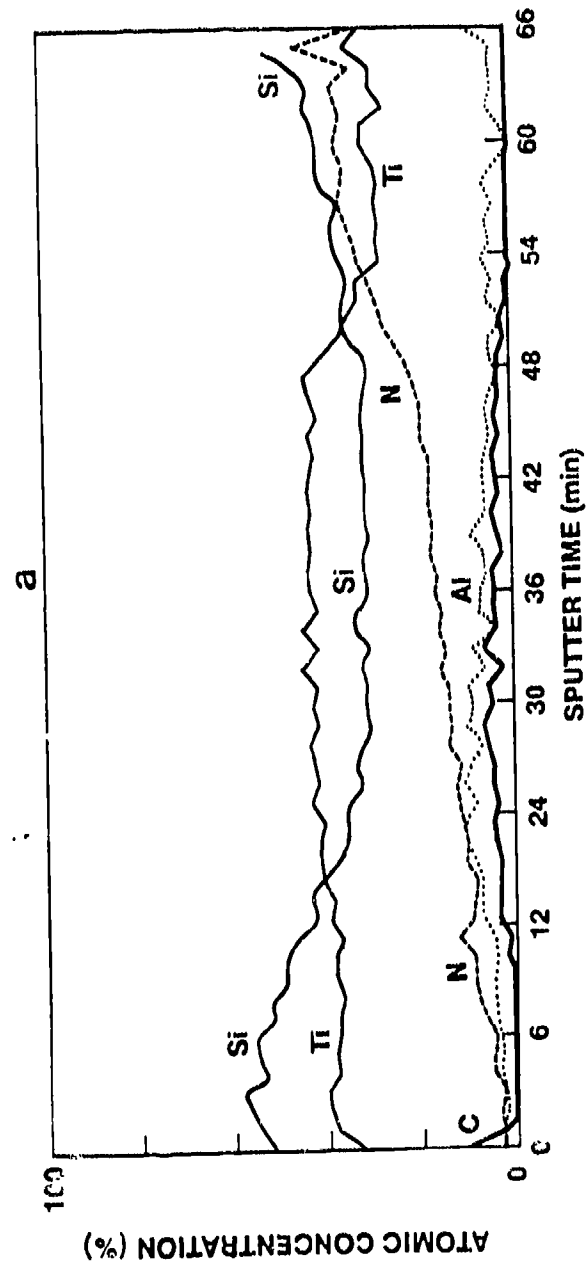
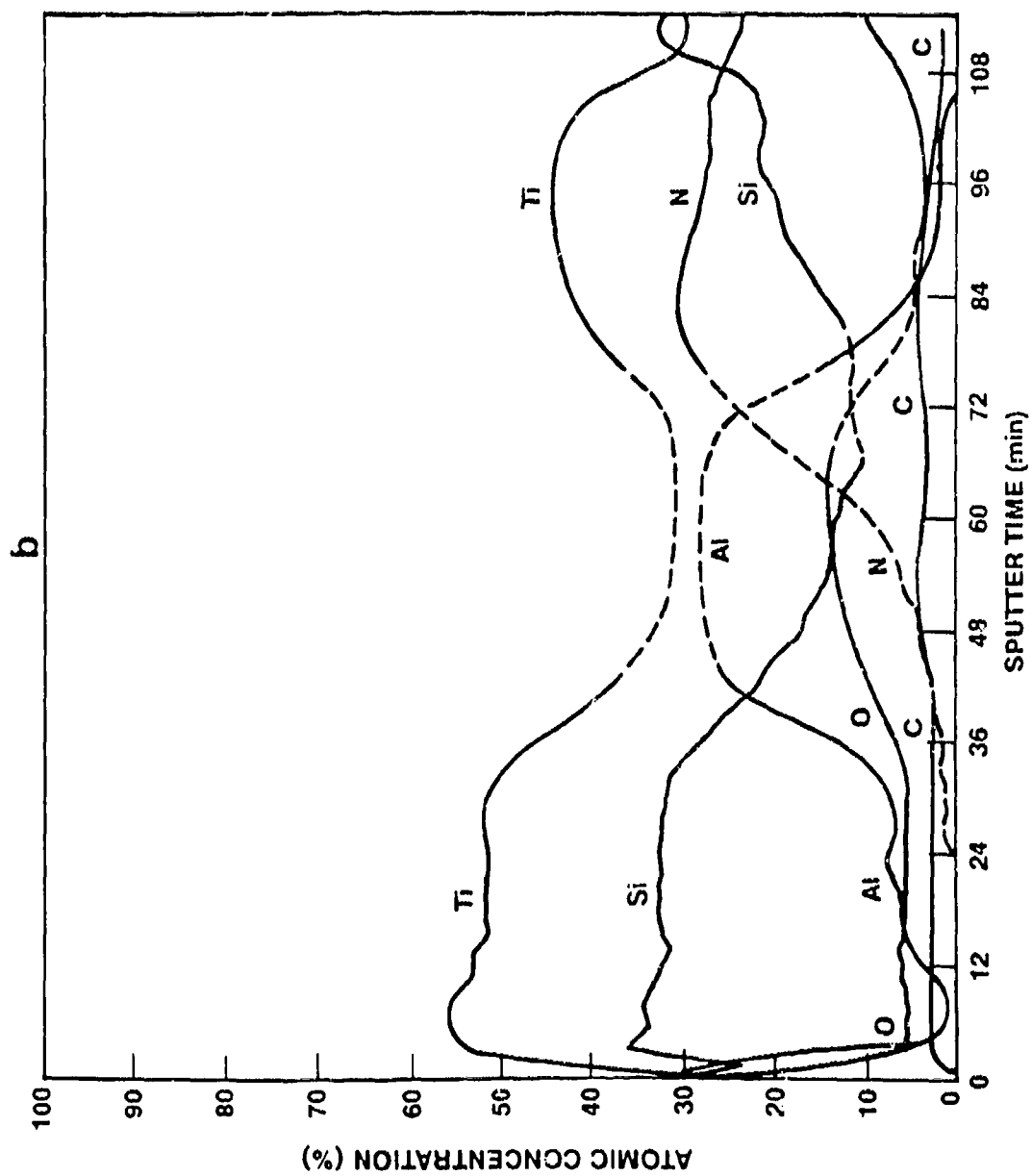


Fig. 5.78 (a) An ESCA and (b) an AES depth concentration profiles of the  $Ti_3Al$  films after reacting with a  $Si_3N_4$  substrate at  $1000^\circ C$  for 4 h.



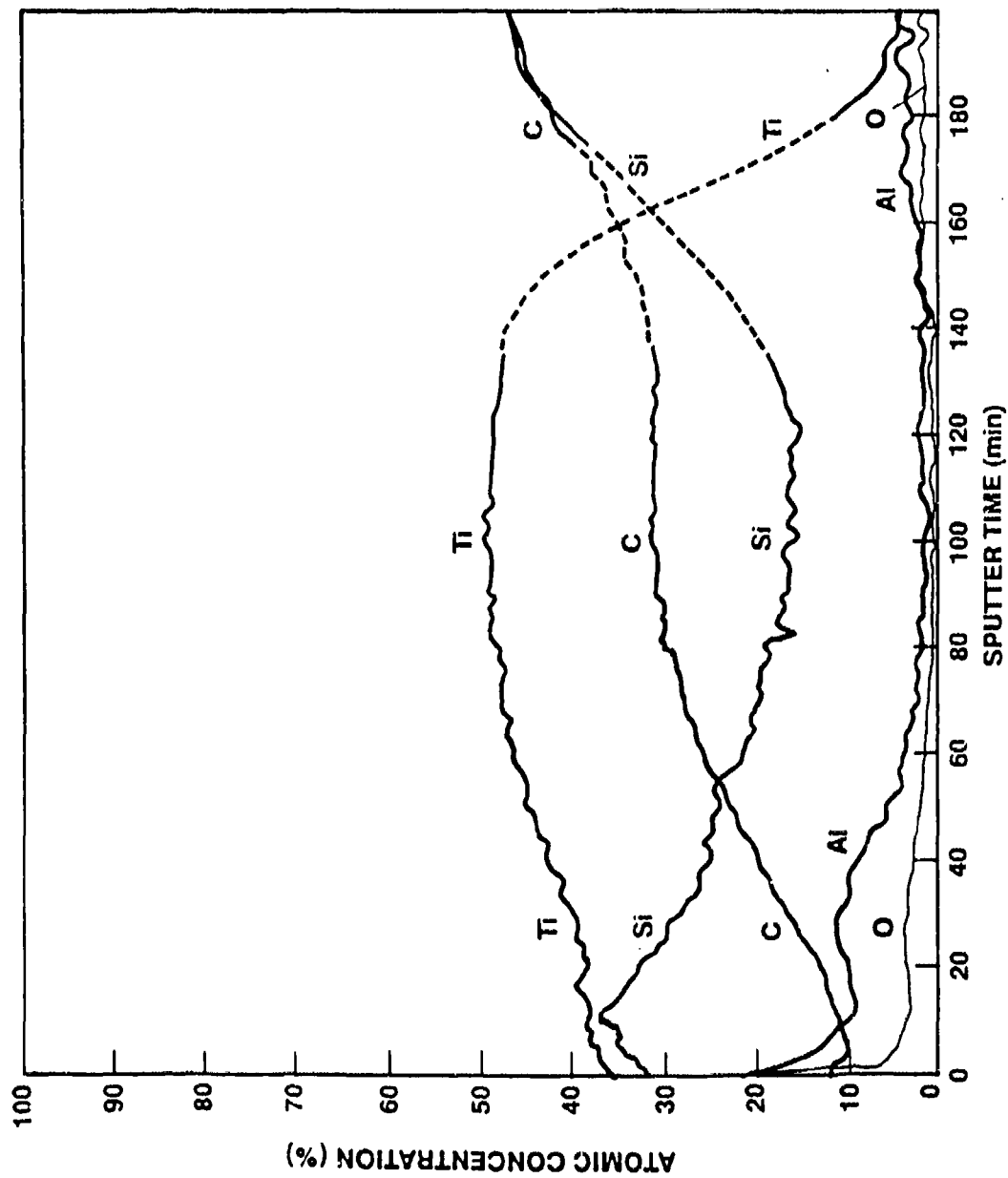


Fig. 5.79 An AES depth concentration profile of the  $\text{Ti}_3\text{Al}/\text{SiC}$  thin film diffusion couples after annealing at  $1000^\circ\text{C}$  for 4 h.



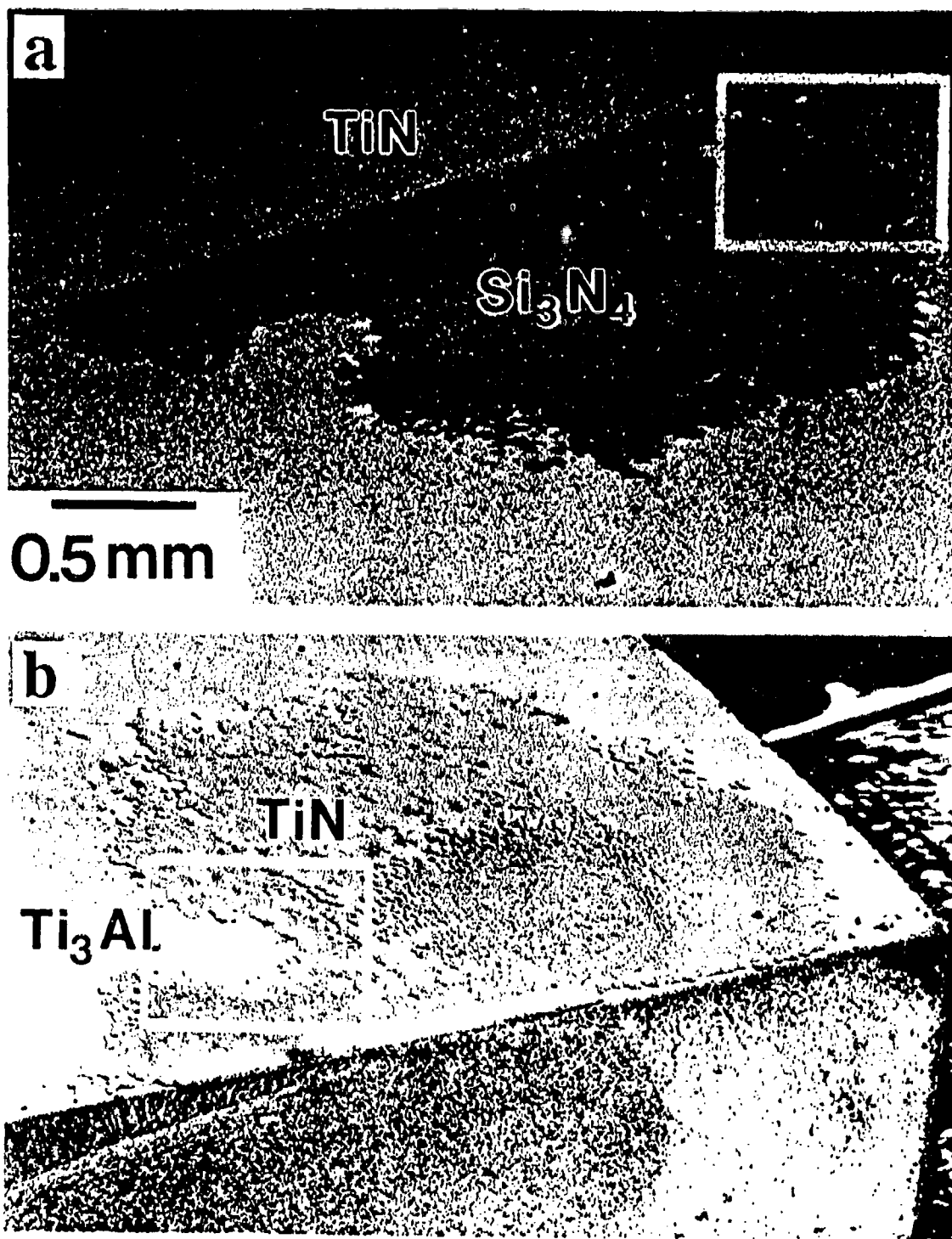
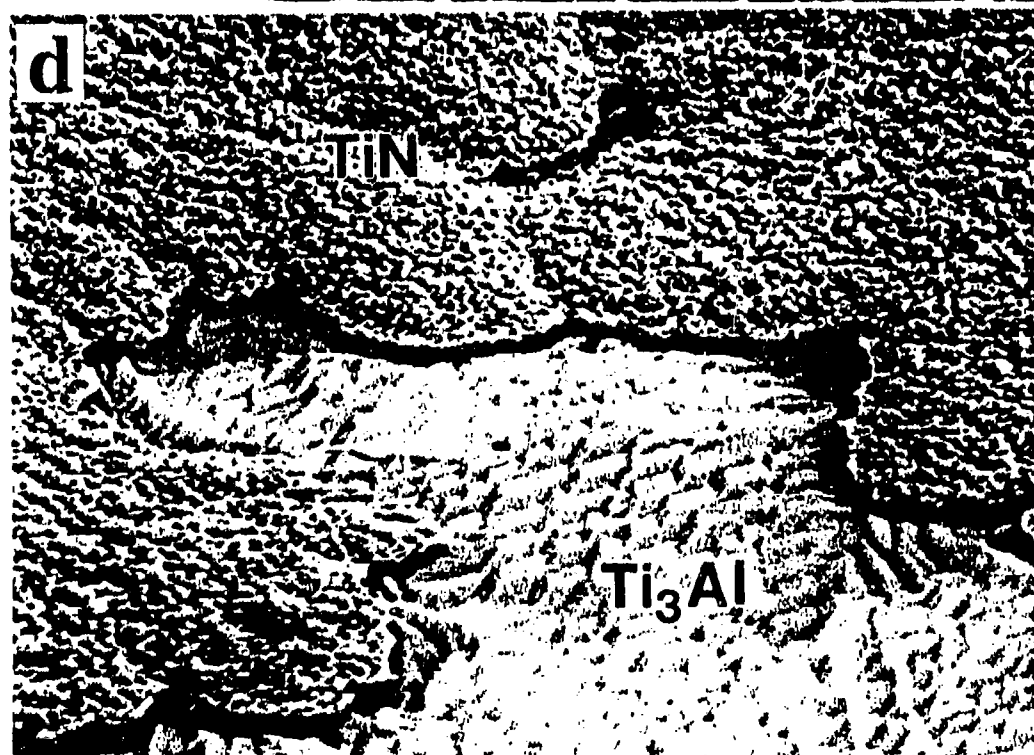
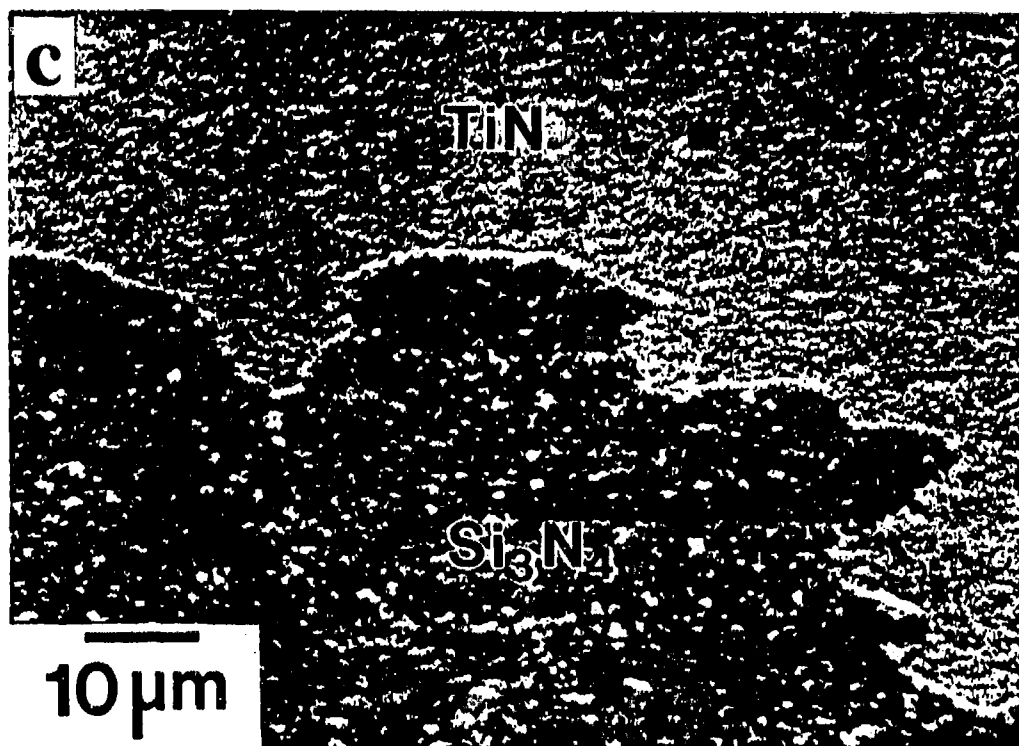


Fig. 5.80

SEM micrographs showing the topographical characteristics of de-bonded reaction interfaces on the  $\text{Ti}_3\text{Al}$  (a and c) and the  $\text{Si}_3\text{N}_4$  (b and d) components.



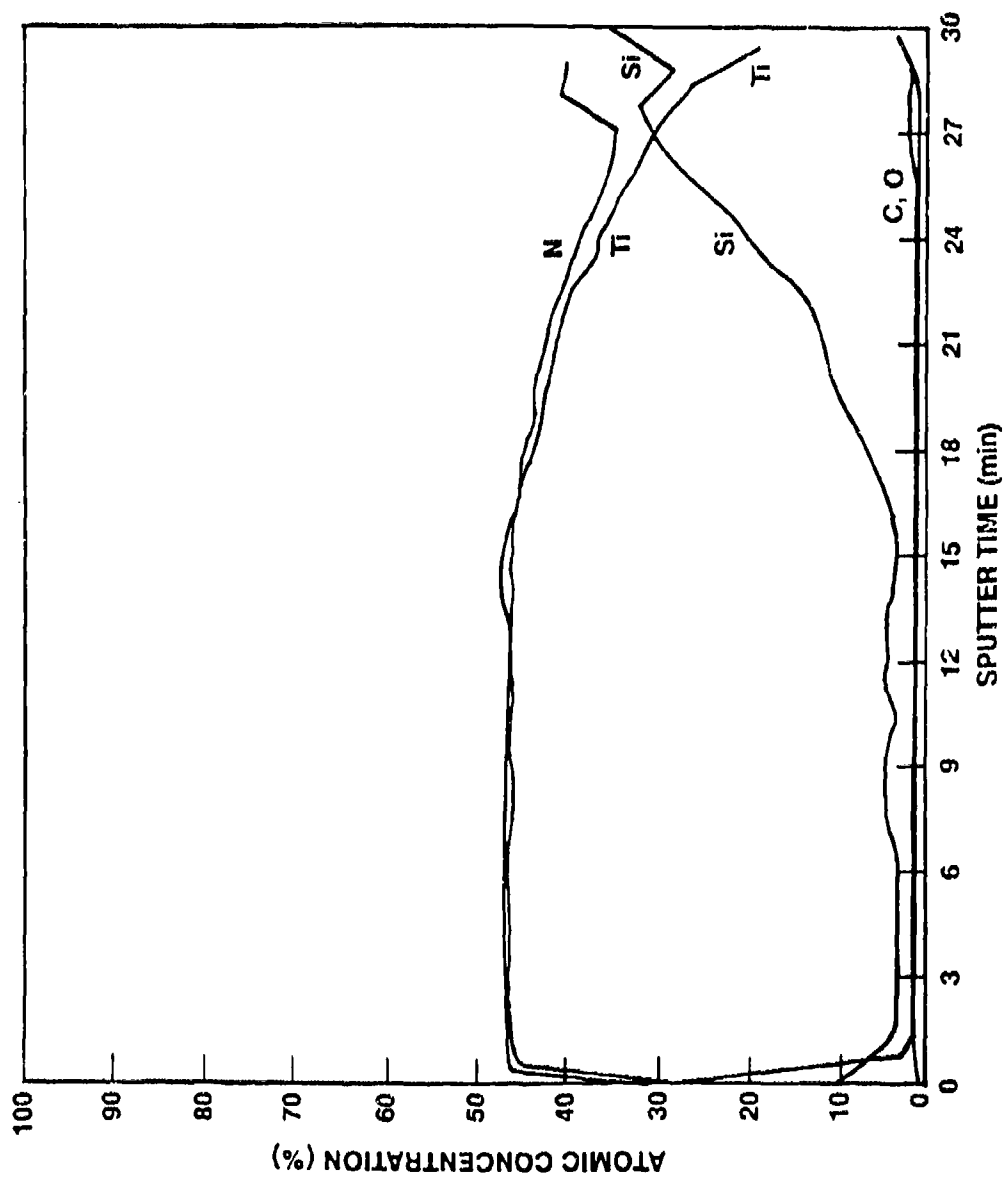


Fig. 5.81 An AES depth concentration profile of the gold-colored layer formed on the  $\text{Si}_3\text{N}_4$  substrate from a bulk diffusion couple after annealing at  $1200^\circ\text{C}$  for 6 h.

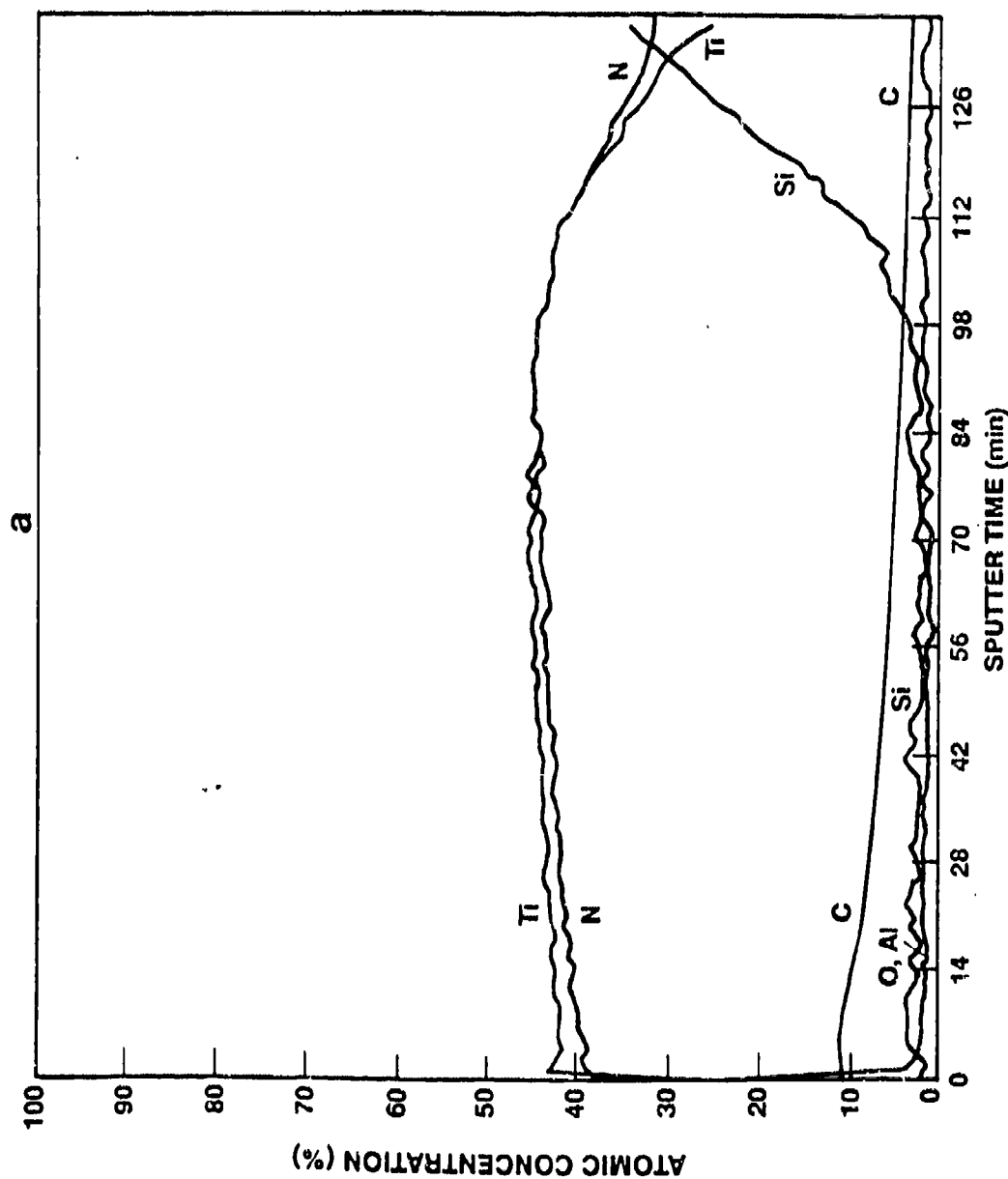
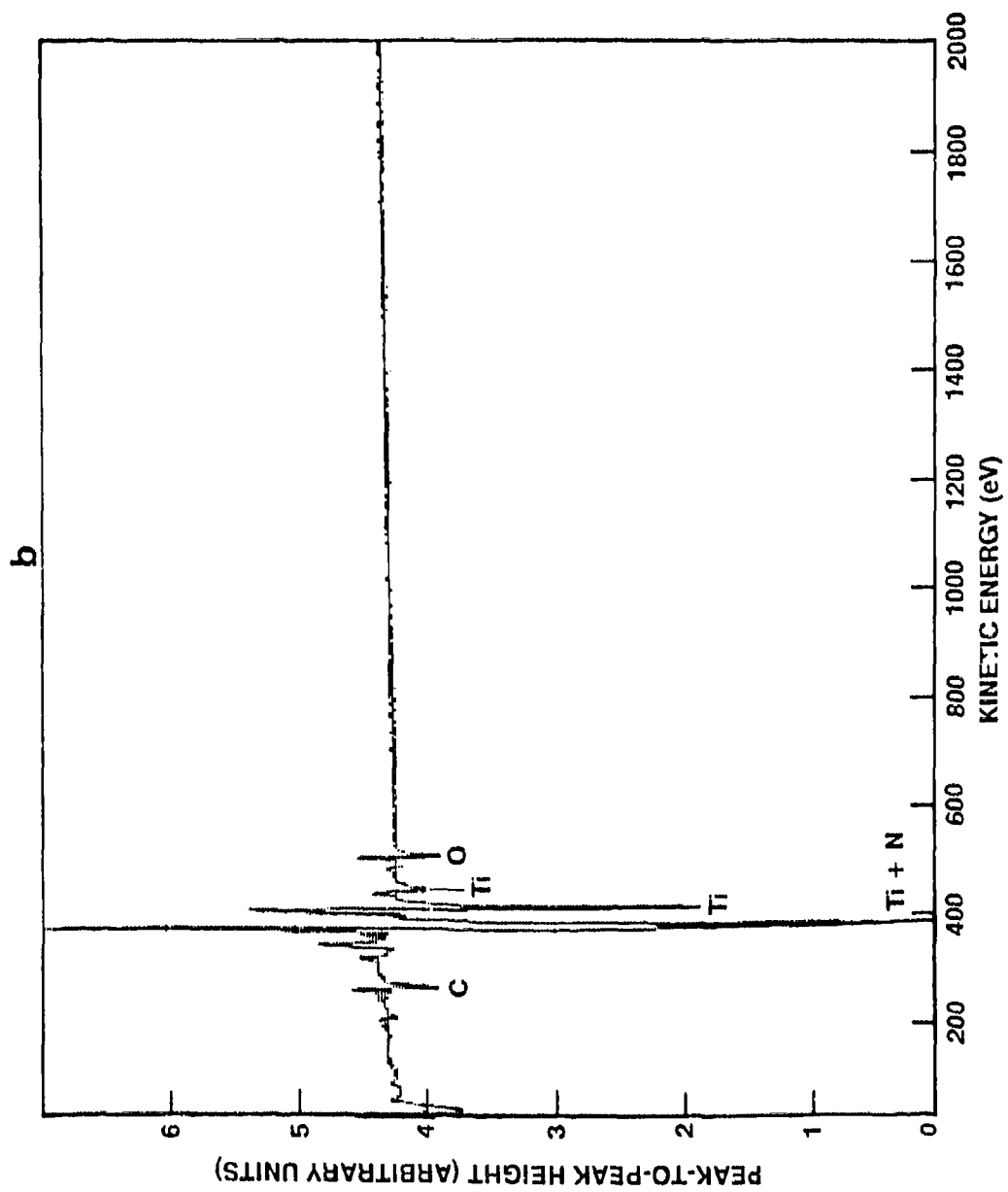
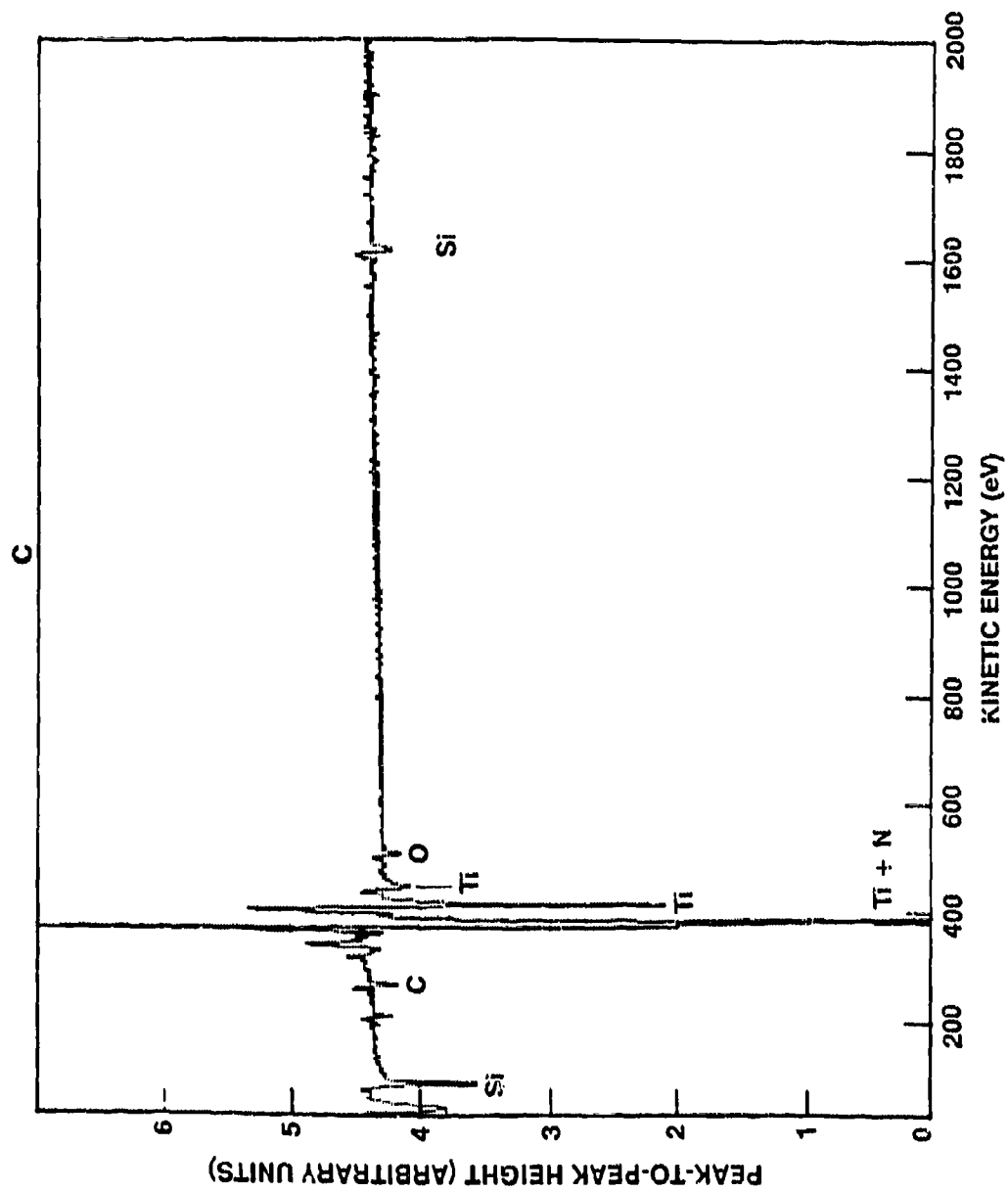


Fig. 5.82 (a) An AES depth concentration profile of the light-brown layer formed on the  $\text{Si}_3\text{N}_4$  substrate from a thin film diffusion couple after annealing at  $1200^\circ\text{C}$  for 6 h. (b) and (c) show AES spectra from the interfaces after 33 and 120 min ion etching, respectively.





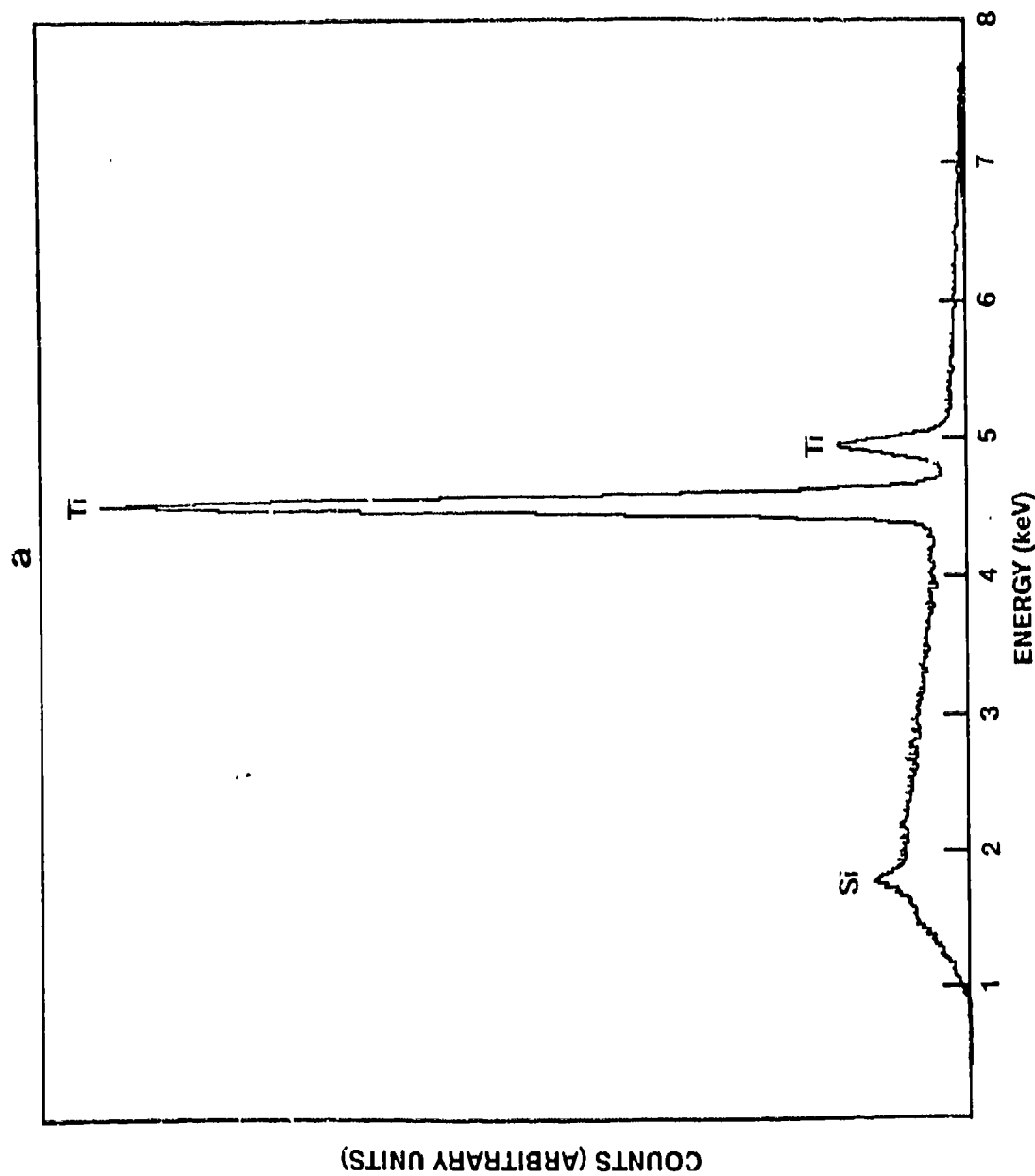
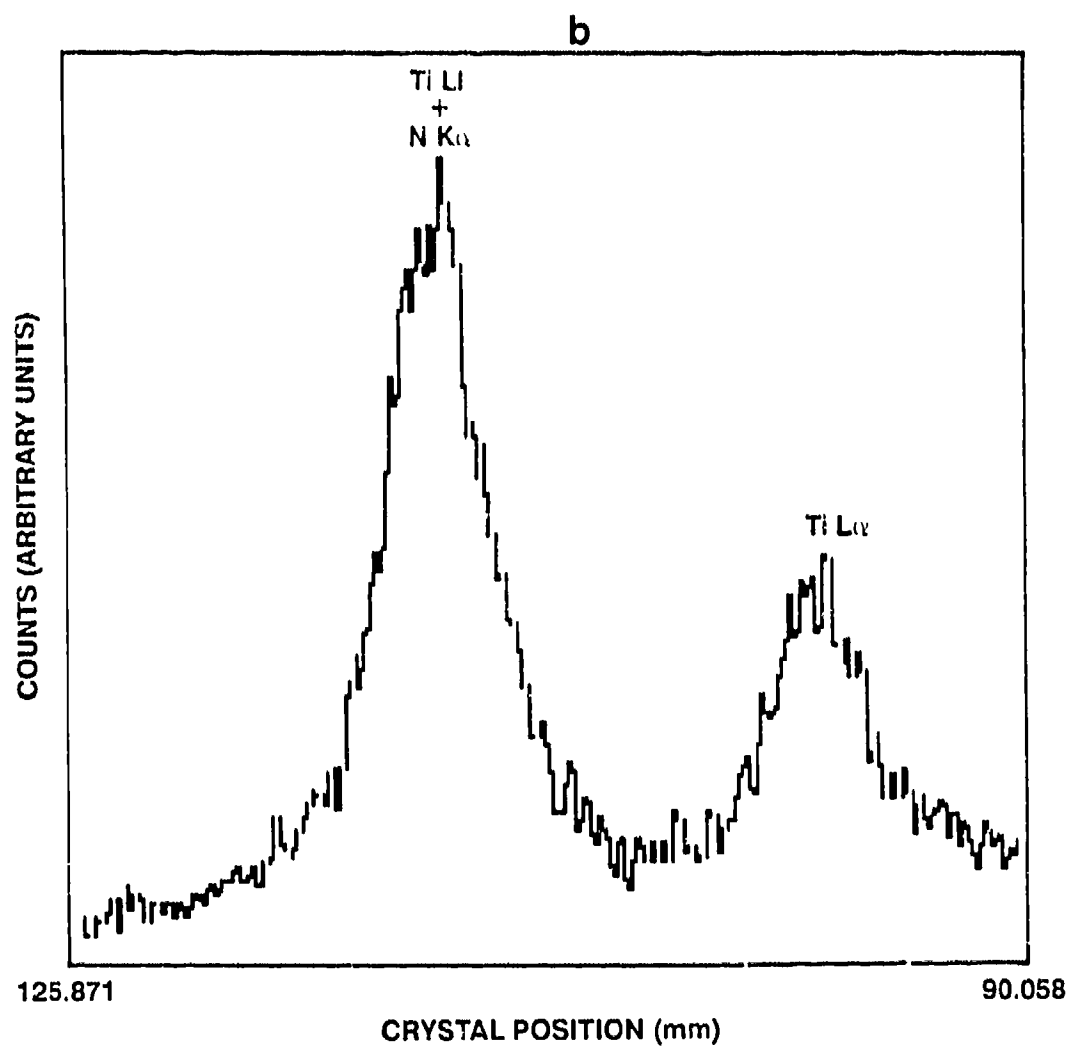
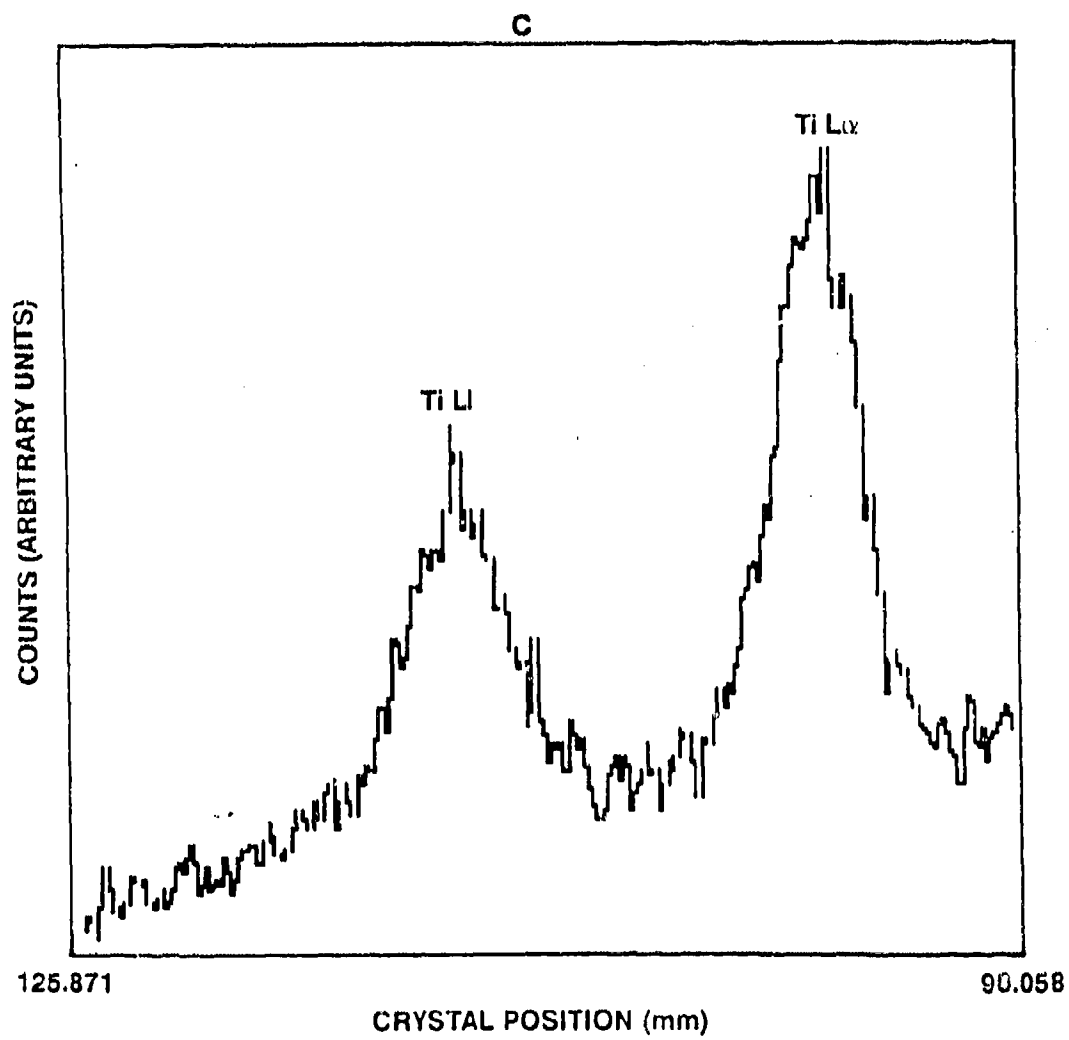


Fig. 5.83 (a) An EDS spectrum taken from the light-brown layer formed on the  $\text{Si}_3\text{N}_4$  substrate from a thin film diffusion couple after annealing at  $1200^\circ\text{C}$  for 6 h. (b) A WDS spectra of Ti-L $\beta$  and L $\alpha$  peaks, and N-K $\alpha$  peak from the light-brown, TiN layer. (c) A WDS spectra of Ti-L $\beta$  and L $\alpha$  peaks, and N-K $\alpha$  peak from an as-deposited  $\text{Ti}_3\text{Al}$  layer.







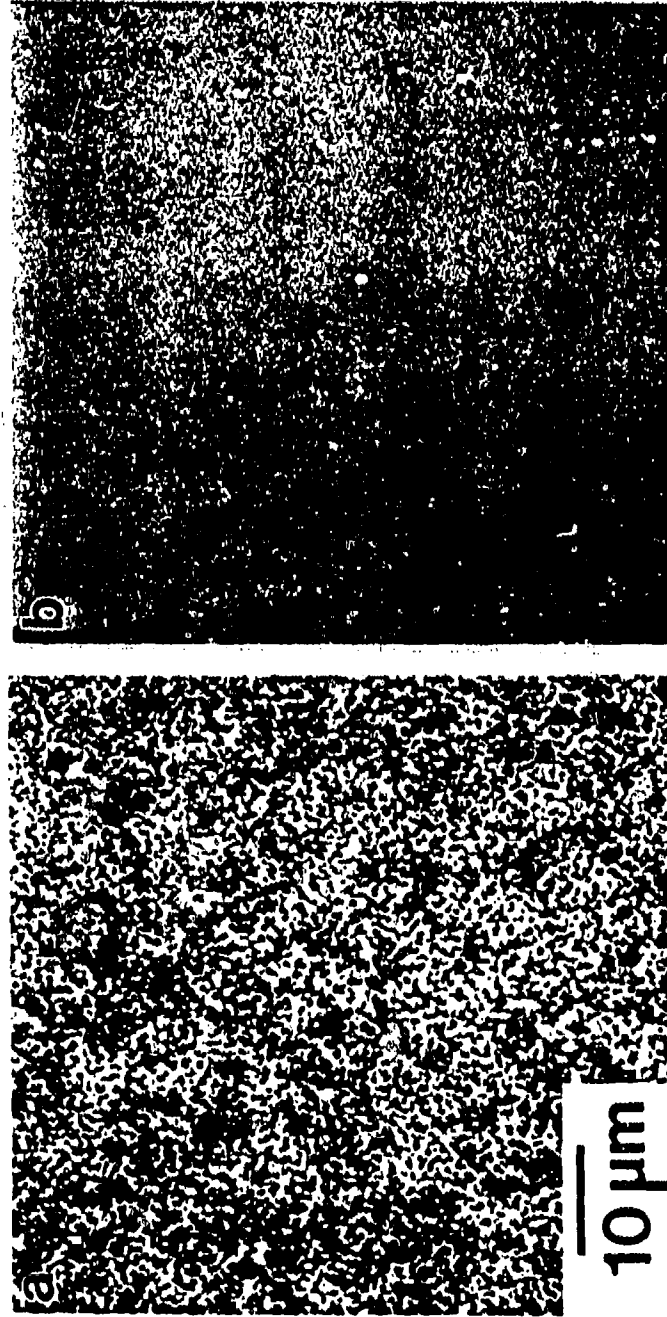


Fig. 5.84 SEM micrographs showing the surface characteristics of  $\text{Ti}_3\text{Al}/\text{Si}_3\text{N}_4$  thin film diffusion couples (a) after and (b) before annealing (at  $1200^\circ\text{C}$  for 6 h).

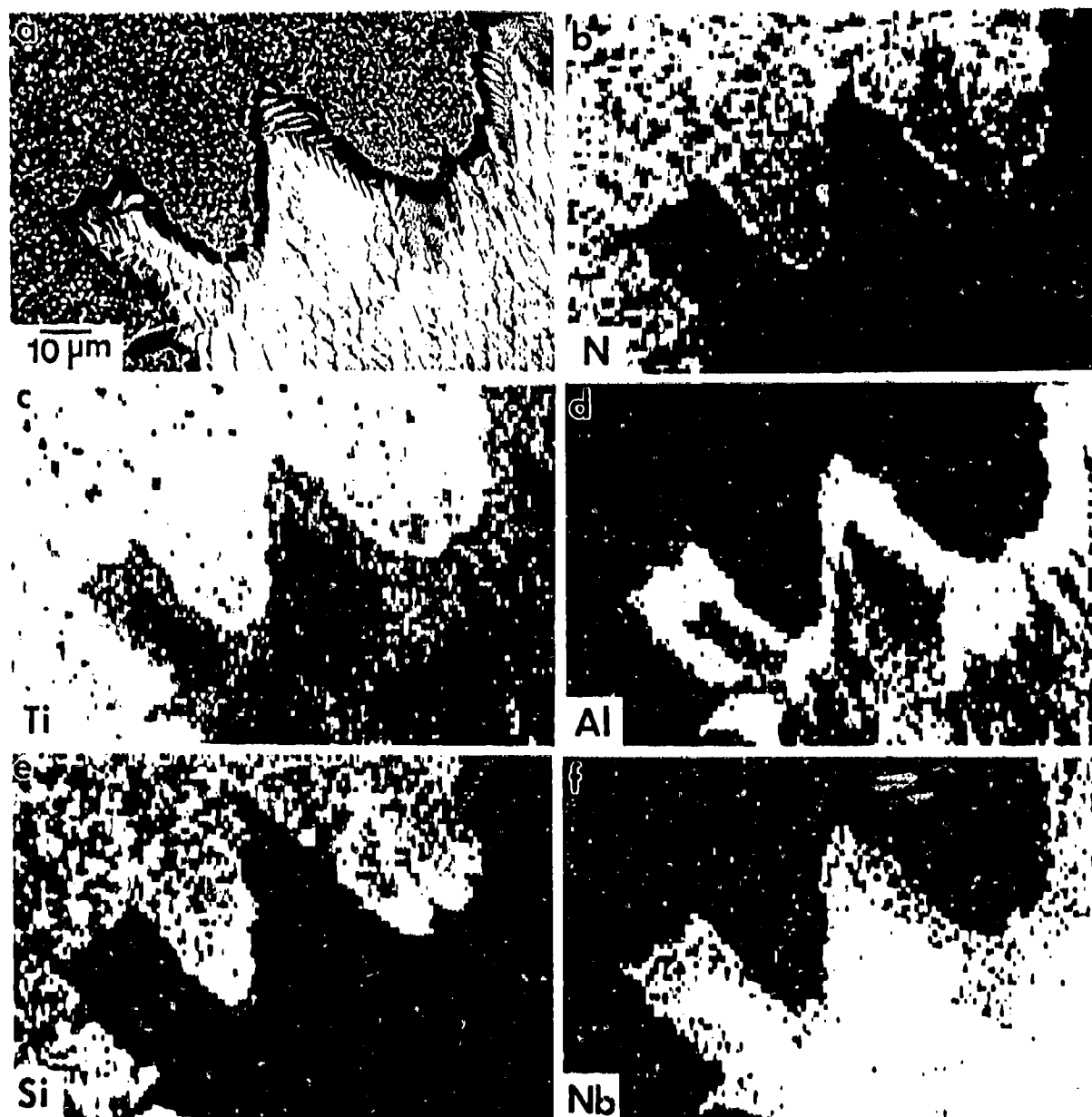


Fig. 5.85 (a) A SEM image and the corresponding x-ray maps of (b) N- $K_{\alpha}$ , (c) Ti- $K_{\alpha}$ , (d) Al- $K_{\alpha}$ , (e) Si- $K_{\alpha}$ , and (f) Nb- $K_{\alpha}$  from an area on the de-coupled reaction interface on the  $Ti_3Al(Nb)$  component after annealing at 1200 °C for 6 h.

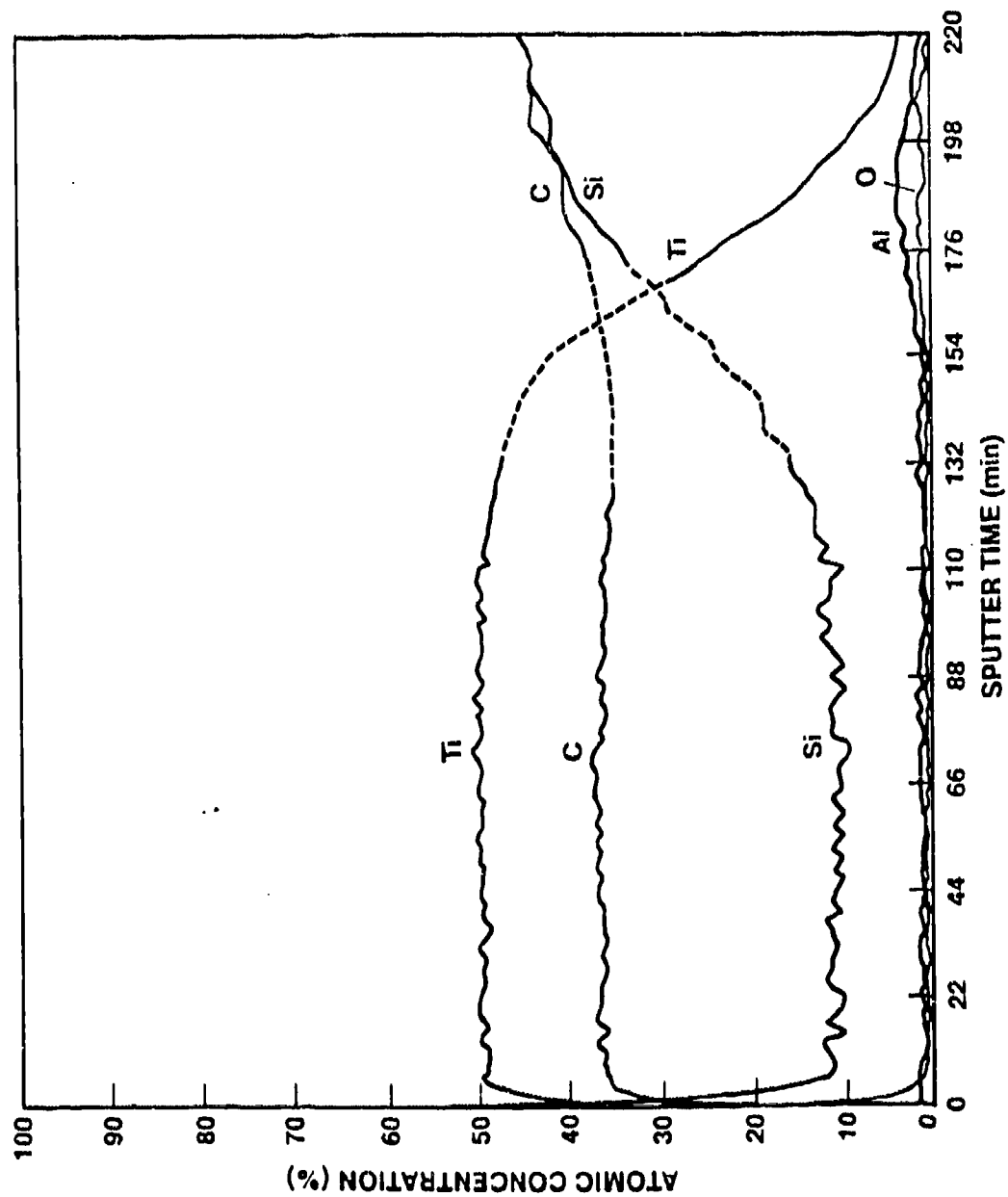


Fig. 5.86 An AES depth concentration profile of the  $\text{Ti}_3\text{Al/SiC}$  diffusion couples annealed at  $1200^\circ\text{C}$  for 4 h.

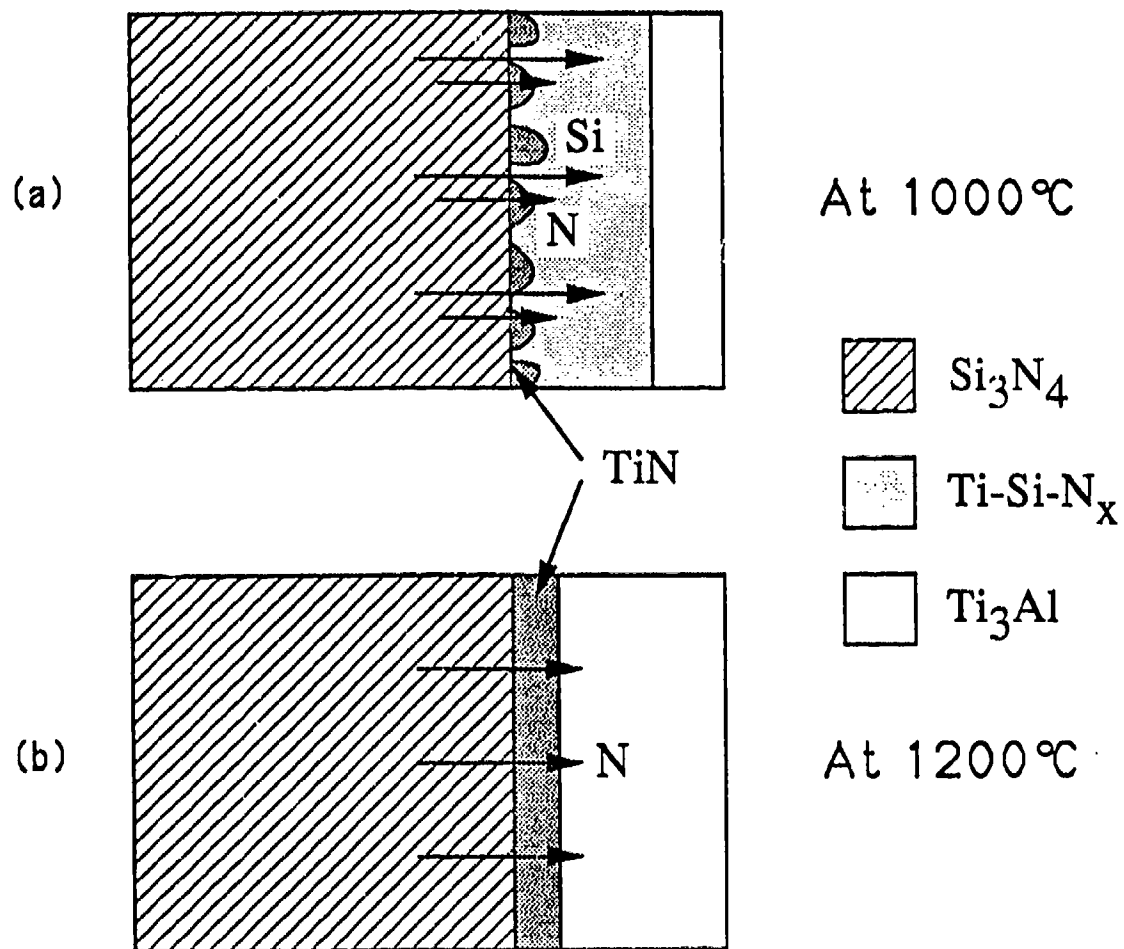


Fig. 5.87

Schematic drawings showing proposed diffusion mechanisms for the  $\text{Ti}_3\text{Al}/\text{Si}_3\text{N}_4$  reactions at (a) 1000°C and (b) 1200°C. At 1000°C, a discontinuous layer of  $\text{TiN}$  is formed and the out-diffusion of Si can effectively take place through the  $\text{TiN}$ -free regions. At 1200°C, a continuous, planar  $\text{TiN}$  layer is formed.

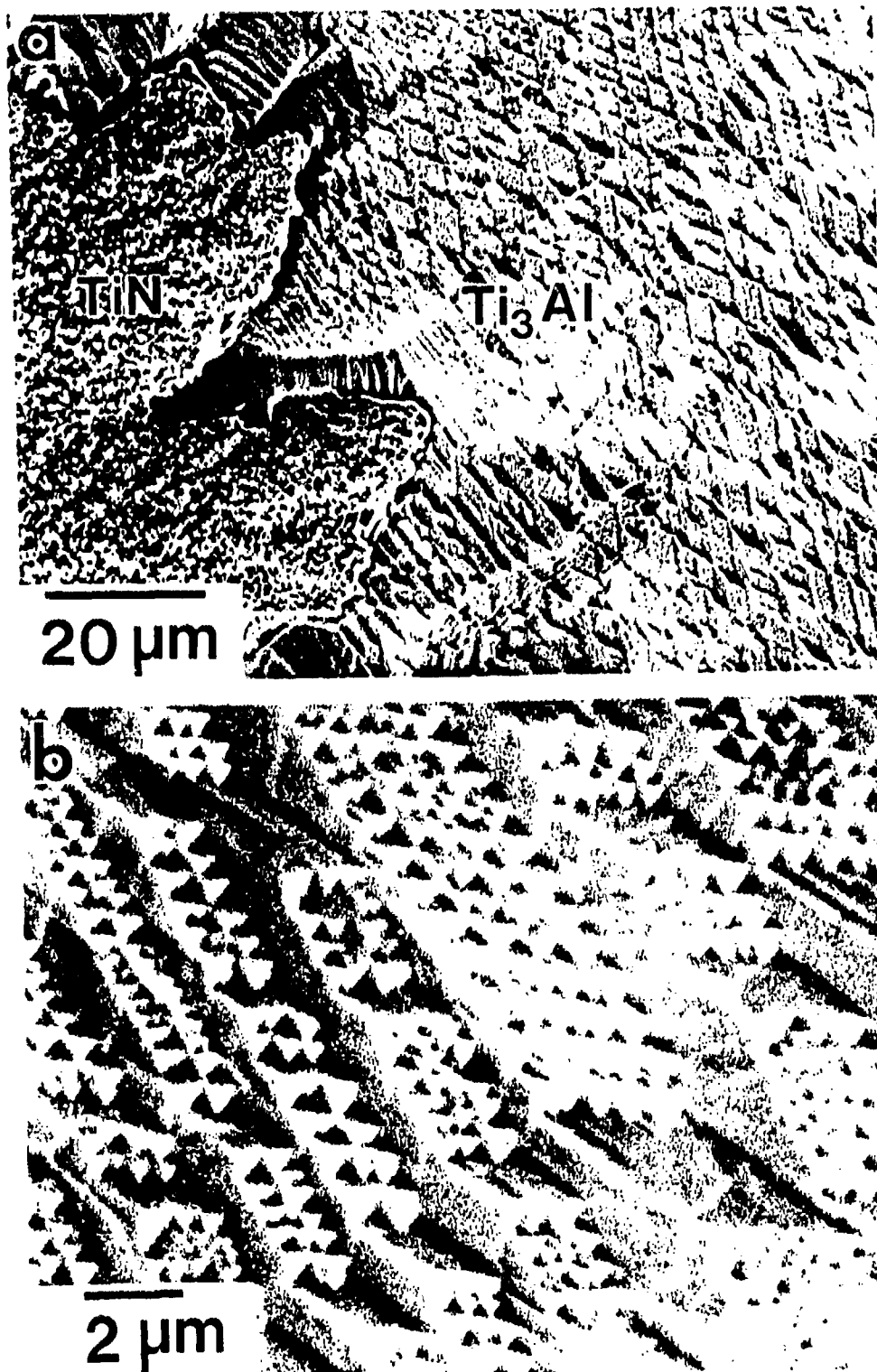


Fig. 5.88

(a) A SEM micrograph showing the surface morphologies of the TiN and the de-bonded Ti<sub>3</sub>Al(Nb). An intriguing pattern is noted on the Ti<sub>3</sub>Al(Nb) surface. (b) A high magnification SEM micrograph indicates the presence of a regular, step-like pattern on the Ti<sub>3</sub>Al(Nb) surface.

## Section 6

SUMMARY

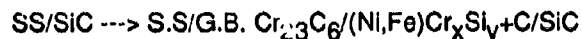
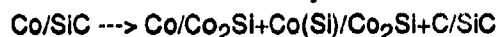
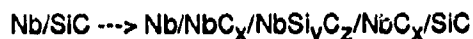
Interdiffusion and interfacial reactions occurring in candidate metal matrix and ceramic reinforcement materials were evaluated using both thin film and bulk diffusion couple specimens. Al, Nb, Ta, Co, Ni, Pt,  $Ti_3Al$ , and stainless steel were among the metals examined, and their reactions with selected ceramic materials SiC,  $Al_2O_3$ , and  $Si_3N_4$  were evaluated. The nature of diffusion, interfacial reactions and microstructural modifications were studied using optical microscopy, scanning electron microscopy, differential scanning calorimetry, Auger electron spectroscopy and transmission electron microscopy.

The reactions of Nb metal with a polycrystalline SiC substrate in the temperature range 800°C to 1300°C lead to the formation of layered structures. Detailed AES and TEM studies suggest a typical reaction sequence to be Nb/Nb<sub>2</sub>C/Nb<sub>5</sub>Si<sub>4</sub>C/NbC/SiC. Variations to this sequence have been observed and were explained based upon extraneous (contaminant) phases present on the SiC surface. Reactions with the substrate resulted in formation of several phases, including NbC, Nb<sub>2</sub>C, Nb<sub>5</sub>Si<sub>3</sub> and Nb<sub>5</sub>Si<sub>4</sub>C. Reactions with the oxygen and carbon present in the vacuum annealing environment resulted in formation of NbO and NbC. Thermodynamic analysis and experimental studies of compatibility of Nb with  $Al_2O_3$  indicate minimal reactions for temperatures up to 1200°C. Based upon this information, a number of specimens were prepared with  $Al_2O_3$  layers in the 100 to 500 nm range at the Nb/SiC interface, and it was shown that  $Al_2O_3$  was an effective diffusion barrier between Nb and SiC up to 2 h at 1200°C. The reactions between SiC and Ta were found to be similar to those between SiC and Nb.

Interfacial reactions of Al with SiC and  $Si_3N_4$  were studied utilizing ~1  $\mu m$  Al films sputter deposited on the ceramic substrates. Reactions of Al/Si, Al-1wt%Si/Si are also being investigated to better understand the driving forces of these reactions and to evaluate the role of Si alloyed in Al on the interfacial reaction. The reaction of Al with SiC annealed for up to 2 h at 600°C was found to be minimal and did not result in the formation of  $Al_4C_3$  or similar interfacial reaction products. In contrast, complete interdiffusion and eutectic reaction occurred in the Al/Si system. The reaction of Al with  $Si_3N_4$  upon annealing for 1 h at 600°C resulted in near-complete disappearance of the Al metal from the surface. It is suspected that Al diffused into the substrate and formed AlN.

Reaction of Ni with SiC and  $\text{Si}_3\text{N}_4$  substrates was evaluated at two temperatures, viz.,  $725^\circ\text{C}$  ( $0.5\times T_m$ ) and  $1160^\circ\text{C}$  ( $0.8\times T_m$ ). Reaction with SiC at both temperatures resulted in formation of a layered structure similar to  $\text{NiSi}_x/\text{NiSi}_xC_y/\text{SiC}$ . The top layer contained little or no carbon and the second layer consisted of an estimated 30 to 40 at.% carbon. Even though the layered structures are similar, the lower temperature annealed specimen exhibited a thinner total reaction zone compared to the high temperature annealed specimen. The ternary phase diagram of Ni-Si-C at  $1150^\circ\text{C}$  does not exhibit any carbon-rich phases, which suggests that the  $\text{NiSi}_xC_y$  region is possibly a physical mixture of carbon with  $\text{NiSi}_x$ . Such a phase would also be required to maintain a thermodynamic equilibrium between Ni and SiC. The interaction of Ni with  $\text{Si}_3\text{N}_4$  at  $1160^\circ\text{C}$  was associated with extensive surface migration and reactions. Numerous  $\text{NiSi}_x$  precipitates were observed on the surface. Nitrogen was observed throughout the film indicating the formation of a ternary phase or formation of islands of  $\text{Si}_3\text{N}_4$  surrounded by  $\text{NiSi}_x$  and Ni.

High temperature interactions of metallic matrices Nb, Co, Ni, Pt and stainless steel with SiC ceramic were examined in the temperature range 800 to  $1200^\circ\text{C}$ . Thin film couples were used in understanding the interfacial reactions of Nb with SiC and in evaluating the effectiveness of  $\text{Al}_2\text{O}_3$  diffusion barriers in minimizing such reactions. It was found that  $\text{Al}_2\text{O}_3$  layers in the 100 to 500 nm range are effective in slowing the interfacial reactions. The reaction products and sequences of metal/SiC reactions can be summarized as follows:



Sequential annealings of Nb/SiC at  $1200^\circ\text{C}$  for 6, 18, 32, and 48 h indicated that the growth kinetics of layered reaction products obeyed a parabolic relationship with respect to annealing time, suggesting that the growth kinetics were limited by diffusion. The growth rate constants for reaction layers 1 and 2 were  $6.7\times 10^{-13}$  and  $5.3\times 10^{-12}$   $\text{cm}^2/\text{sec}$ , respectively. In contrast, no parabolic growth rate was observed in Ni/SiC, Co/SiC, and SS/SiC. In most of the cases, the thickness of the reaction zone on the SiC side was always smaller than that on the metal side, suggesting that the decomposition rate of SiC was slow and may be a rate limiting step for the overall metal/SiC reactions.



The reactions of SiC with Co, Ni, Pt, and stainless steel also resulted in varying microstructure of C precipitates as a function of distance from the SiC reaction front. Typically, C precipitates were coarser at locations farther from SiC. The distribution pattern of the C clusters showed either random or modulated patterns, depending upon the metal system as well as their location from the SiC interface. A model describing discontinuous decomposition of SiC is proposed to explain the formation of modulating C/metal-silicides structures. In general, metal silicide formation is detected in all the systems being studied. The formation of metal-rich silicides gives rise to interfacial melting in Ni/SiC, Co/SiC, and SS/SiC as a result of their relatively low melting points, as compared to the respective annealing temperatures. Non-planar interfaces were produced as a result of surface tension effects in the interfacial melt. The formation of liquid interfacial metal silicide phases is expected to degrade the overall properties of SiC reinforced metal matrix composites that contain Ni, Co and Pt.

Solid state interfacial reactions of  $Ti_3Al$  with  $Si_3N_4$  and SiC were studied at 1000 and 1200°C. At 1000°C, titanium silicide(s), titanium-silicon-aluminide, and titanium-silicon-nitride were formed in the  $Ti_3Al/Si_3N_4$  diffusion couples; titanium silicide(s) (containing some C and Al) and titanium-silicon carbide were formed in the  $Ti_3Al/SiC$  couples. At 1200°C, simple reaction products were formed, TiN in the former system and titanium-silicon-carbide in the latter one. The interfacial reactions of  $Ti_3Al$  with  $Si_3N_4$  and SiC were consistent; Si-enriched surface regions were formed in the reaction zones at 1000°C, while a lesser amount of Si was observed diffusing into the reaction zones at 1200°C. Moreover, the depletion of Al from the reaction product was noted and it exhibited temperature-dependent kinetics. A unified diffusion mechanism is proposed to explain the observed phenomena. It is suggested that the diffusion of N (or C) in the  $Ti_3Al$  and the N/G kinetics of the TiN (or titanium-silicon carbide) reaction product are less effective at 1000°C. As a result, Si can diffuse rather easily through the discontinuous TiN and react with Ti to form titanium silicide(s) in the near surface region. At 1200°C, on the other hand, the diffusion of N (or C) becomes significant and the N/G kinetics of TiN (or titanium-silicon carbide) are effective. As a result, a single-layered reaction product of TiN (or titanium-silicon-carbide) was formed in the near-substrate region. The formation of a planar TiN (or titanium-silicon-carbide) layer may serve as a diffusion barrier which retards the out-diffusion of Si, thereby reducing the amount of Si in the reaction product. The amount of Si that can be present in the TiN may be limited by its solid solubility therein. The depletion of Al in the reaction product is suggested to result from evaporation due to its high vapor pressures at the temperatures studied. According to the interfacial morphologies of the de-bonded  $Ti_3Al(Nb)/Si_3N_4$  bulk diffusion couples, the adhesion of the TiN layer to the  $Si_3N_4$  appears to be better than to the  $Ti_3Al$ ; most of the diffusion couples de-bonded by exposing the

bare  $\text{Ti}_3\text{Al}(\text{Nb})$ . The thermodynamic driving force for the  $\text{Ti}_3\text{Al}/\text{Si}_3\text{N}_4$  solid state reactions at  $1200^\circ\text{C}$  is attributed to the negative Gibbs free energy of the  $\text{TiN}$  formation. Based on the literature thermochemistry data, the overall free energy of the reaction has a negative value.

## Section 7

REFERENCES

1. L.J. Ebert and P.K. Wright, "Mechanical Aspects of the Interface," in Interfaces in Metal Matrix Composites, edited by A.G. Metcalfe, Academic Press, New York, 1974, pp. 31-36.
2. A.G. Metcalfe, "Physical Chemical Aspects of the Interface", ibid., pp. 67-126.
3. J.S. Benjamin, T.E. Volin, and J.H. Waben, "Dispersoids in Mechanically Alloyed Superalloys," High Temperatures - High Pressures, **6**, 443-446 (1974).
4. M. Raychavan, C. Klein, and R. Petkovic-Luton, "Analytical Microscopic Investigation of Commercial Oxide Dispersion Strengthened Alloys," Proceedings of the Thirty-Ninth Annual EMSA Meeting, Atlanta, 1981, pp. 143-145.
5. F.D. Lemkey, H.E. Cline, and M. McClean (eds.), In Situ Composites IV, Materials Research Society Symposia Proceedings, Vol. 12, 1982.
6. T. Ishii, D.J. Duguet, and N.S. Stoloff, "The Low Cycle Fatigue Behavior of Three Advanced Nickel-Base Eutectic Composites," ibid., pp. 59-68.
7. S. Ochual, Y. Murakami, "Theoretical Predictions of the Tensile Strength of Fibers with Brittle Layers on Their Surfaces," Z. Metallkde., **72**, 827-831 (1981).
8. S. Ochula, Y. Irie, K. Osamura, and Y. Murkami, "Room Temperature Tensile Strength of Boron-Aluminum Composite As a Function of Annealing Temperature and Time," Z. Metallkde., **74**, 44-48 (1983).
9. S. Ochula, K. Osamura, and Y. Murakami, "Room Temperature Tensile Strength of Fibers in Boron Aluminum, Boron-Titanium, and Graphite-Aluminum Composites As a Function of Annealing Temperature Time," Z. Metallkde., **74**, 68-73 (1983).
10. A.G. Metcalfe, M.J. Klein, "Effect of Interface on Longitudinal Tensile Properties," in A.G. Metcalfe, op. cit., p. 151.
11. R. Naslain, R. Pailler and P. Martineau, in Physical Chemistry of the Solid State: Applications to Metals and their Compounds, P. Lacombe, Ed., Elsevier, Amsterdam, 1984, pp. 481-499.
12. P. Martineau, R. Pailler, M. Lahaye, R. Naslain, J. Materials Science, **19**, 2749 (1984).
13. M.B. Chamberlain, Thin Solid Films, **72**, 305 (1980).
14. C. Jones, C.J. Kiely and S.S. Wang, J. Mater. Res., **4**, 327 (1989).
15. C.G. Rhodes, R.A. Spurling, in Recent Advances in Composites in the United States and Japan, ASTM STP 864, J.R. Vinson and M. Taya, Eds., 1985, pp. 585-599.

16. R. Pailler, M. Lahaye, J. Thebault and R. Naslain, in Failure Modes and Processing in Composites - IV, J.A. Cornie and F.W. Crossman, Eds., The Metallurgical Society of AIME, New York, 1979, pp. 265-284.
17. D.J. Lloyd, in Composite Science and Technology, 1989, vol. 35, pp.159-179.
18. S.C. Chin and M.H. Richman, Army Materials and Mechanics Research Center Report, AMMRC TR 82-14, 1982.
19. S.R. Nutt and R.W. Carpenter, Materials Science and Engineering, **75**, 169 (1985).
20. L.D. Brown, C.L. Grove and H.L. Marcus, Interfaces in Metal Matrix Composites, Edited by A.K. Dhingra and S.G. Fishman, 1986, pp. 205-210.
21. T.G. Nieh, J.J. Stephens, J. Wadsworth and C.T. Liu, in Interfaces in Polymer, Ceramic, and Metal Matrix Composites, Edited by Hatsuo Ishida, Elsevier, Amsterdam, 1988, pp. 215-224.
22. R. Sherman, Surface and Interface Analysis, **10**, 23 (1987).
23. M. Hansen, Constitution of Binary Alloys, 2nd Edition, New York: McGraw-Hill Book Co., 1958, pp. 230-231.
24. J.W. Christian, The Theory of Transformations in Metals and Alloys, Oxford: Pergamon Press, 1965, Chapter XII.
25. J.A. Snide, F.A. Ashdown, and J.R. Myers, Fiber Sci. Technol., **5**, 61 (1972).
26. M.J. Klein, M.L. Reid, "Compatibility Studies for Viable Titanium Matrix Composites," AFML-TR-69-242, (Oct. 1969).
27. J.L. Ratliff and G.W. Powell, "Research on Diffusion in Multiphase Systems: Reaction Diffusion in the Ti/SiC and Ti-6Al-4V/SiC Systems," AFML-TR-70-42, (March 1970).
28. C.E. Brukl, "Transition Metal-Boron-Carbon-Silicon Systems," Part II, Vol. VII, AFML-TR-65-2, (1965).
29. J.L. Camahort, "Protective Coating by Surface Nitridation of Boron Filaments," J. Composite Materials, **2**, 104-112 (1968).
30. A.E. Vidoz, J.L. Camahort, and F.W. Crossman, "Development of Nitrided Boron Reinforced Metal Matrix Composites," J. Composite Materials, **3**, 254-261 (1969).
31. C.G. Ryder, A.E. Vidoz, F.W. Crossman, and J.L. Camahort, "Mechanical Properties of Nitrided Boron-Aluminum Composites," J. Composite Materials, **4**, 264-272 (1970).
32. M.W. Koop and J.K. Tien, Scripta Metallurgica, **22**, 1527-30 (1988).
33. M.W. Koop, J.K. Tien and D.W. Petrasek, "Reaction Kinetics between Fiber and Matrix Components in Metal Matrix Composites", In Superalloys 1988, Eds. S. Reichman et al., The Metallurgical Society, 1988.

34. J.K. Tien, Annual Technical Report, "A Fundamental Understanding of the Interfacial Compatibility in Hybrid Material Systems", Air Force Office of Scientific Research AFOSR-86-0312, 1988.
35. S.G. Fishman, "Processing Metal Matrix Composites: The State of the Art," ASTM Standardization News, 14, #9, 46-49 (1986).
36. C.G. Levi, G.J. Abbaschian, and R. Mehrabian, "Interface Interactions During Fabrication of Aluminum Alloy - Alumina Fiber Composites," Met. Trans., 9A, 697-711 (1978).
37. J.I. Ralliff and G. W. Powell, Research on Diffusion in Multiphase Ternary Systems: Reaction Diffusion in the Ti/SiC and Ti-6Al-4V/SiC Systems, AFML Techn. Report 70-42, 1970, US Department of Commerce, Nat. Tech. Inf. Serv. Springfield, VA.
38. R. C. J. Schiepers, F. J. I. Van Loo, and G. De With, J. Am. Ceram. Soc. 71, C-284 (1988).
39. C. S. Pal, C. M. Hanson, and S. S. Lau, J. Appl. Phys. 57, 618 (1985).
40. Z. Zhang and K. Wei, Interfaces in Metal-Ceramics Composites, Eds. R. Y. Lin, R. J. Arsenault, G. P. Martins, and S. G. Fishman (TMS, Warrendale, PA, 1990), p.259.
41. S. Krishnamurthy, Interfaces in Metal-Ceramics Composites, Eds. R. Y. Lin, R. J. Arsenault, G. P. Martins, and S. G. Fishman (TMS, Warrendale, PA, 1990), p.75.
42. D. R. Schuyler, M. M. Sohi, and R. Mahapatra, Interfaces in Metal-Ceramics Composites, Eds. R. Y. Lin, R. J. Arsenault, G. P. Martins and S. G. Fishman (TMS, Warrendale, PA, 1990), p.475.
43. C. Jones, C. J. Kiely, and S. S. Wang, J. Mater. Res. 5, 1435 (1990).
44. T. C. Chou, Scripta Met. et Mat. 24, 409 (1990).
45. T. C. Chou and T. G. Nieh, J. Mater. Res. 9, 1985 (1990).
46. E. L. Hall, Y. M. Kouh, M. R. Jackson, and R. L. Mehan, Met. Trans. 14A, 781 (1983).
47. M. R. Jackson, R. L. Mehan, A. M. Davis, and E. L. Hall, Met. Trans. 14A, 355 (1983).
48. C.E. Brukl, Ternary Phase Equilibria in Transition Metal-Boron-Carbon-Silicon Systems, Technical Report No. AFML-TR-65-2, Part II, Vol. VII (Air Force Materials Laboratory, Wright Patterson Air Force Base, Ohio, 1966), p. 44.
49. P. Villars and L.D. Calvert, Pearson's Handbook of Crystallographic Data for Intermetallic Phases (American Society for Metals, Metals Park, OH (1985).
50. Binary Alloy Phase Diagrams, edited by T.B. Massalski, J.L. Murray, L.H. Bennett and H. Baker (American Society for Metals, Metals Park, OH, 1986, V.2), p. 1689.
51. Binary Alloy Phase Diagrams, edited by T.B. Massalski, J.L. Murray, L.H. Bennett and H. Baker (American Society for Metals, Metals Park, OH, 1986, V.1), p. 578.
52. N.C. Birla and M. Hoch, Metall. Trans.A, 6A, 1631 (1975).
53. N. Terao, Jap. J. Appl. Phys., 3, 104 (1964).

54. J. Mansfield, Convergent Beam Electron Diffraction of Alloy Phases (Adam Hilger Limited, Bristol, England, 1984), p. 61.
55. C.E. Wicks and F.E. Block, Thermodynamic Properties of 65 Elements - Their Oxides, Halides, Carbides and Nitrides (U.S. Government Printing Office, Washington, D.C., 1963).
56. I. Barin and O. Knacke, Thermochemical Properties of Inorganic Substances (Springer-Verlag, New York, 1973), pp.562-570.
57. M. Kuwabara, J.C.H. Spence and M. Ruhle, *J. Mater. Res.*, **4**, 972-977 (1989).
58. A.W. Neumann, C.J. van Oss, J. Szekely, *Kolloid - Z.U.Z. Polymere*, **251**, 415 (1973).
59. W.C. Moshier, J.S. Ahearn and D.C. Cooke, *J. Mater. Sci.*, **22**, 115 (1987).
60. T. Ikesi, T. Kameda and T. Maruyama, *J. Mater. Sci.*, **19**, 1692 (1984).
61. Z. Indue, Y. Inomata and H. Tanaka, *J. Mater. Sci.*, **15**, 577 (1980).
62. J. Schoennahl, B. Miller and M. Daire, *J. Solid State Chem.*, **52**, 163 (1984).
63. R. Warren and C-H. Anderson, *Composites*, **15**, 101 (1984).
64. M.R. Jackson, R.L. Mehan, A.M. Davis and E.L. Hall, *Metall. Trans.*, **14A**, 355 (1983).
65. E.L. Hall, Y.M. Kouh, M.R. Jackson, and R.L. Mehan, *Metall. Trans.*, **14A**, 781 (1983).
66. R.L. Mehan and M.R. Jackson, in Surfaces and Interfaces in Ceramic and Ceramic-Metal Systems, Ed. by Pask and Evans (Plenum Press, New York, 1981), pp. 513-533.
67. G. Katagiri, H. Ishida, and A. Ishitani, *Carbon*, **26**, 565 (1988).
68. O. Kubaschewski and C. B. Alcock, Metallurgical Thermochemistry, 5th ed (Pergamon Press, New York, 1979), p.350.
69. P. M. Hansen, Constitution of Binary Alloys (McGraw-Hill, New York, 1958), p.379.
70. T. Yamada, H. Sikiuchi, H. Okamoto, S. Azuma, and A. Kitamura, in Diffusion Bonding of SiC or Si<sub>3</sub>N<sub>4</sub> to Metal, Proceedings of the 2nd International Symposium on Ceramic Materials and Components for Engines, Ed. W. Bunk and H. Hausner (Verlag Deutsche Veramische Gesellschaft, Lubeck-Travemunde, Federal Republic of Germany, 1986).
71. V. M. Bermudez, *Appl. Phys. Letts.* **42** (1983) 70.
72. V. M. Bermudez, *J. Appl. Phys.* **63** (1988) 4951.
73. L. Topor and O. J. Kleppa, *Z. Metallkde.* **77** (1986) 65.
74. J. A. Floro, *J. Vac. Sci. Technol.* **A4** (1986) 631.
75. L. A. Clevenger, C. V. Thompson, and K. N. Tu, *J. Appl. Phys.* **67** (1990) 2894.
76. C. E. Wicksham and J. E. Poole, *J. Vac. Sci. Technol.* **A6** (1988) 1699.
77. T. C. Chou, *J. Mater. Res.* **5**, 601 (1990).
78. T. C. Chou, *Scripta Met. et Mat.* **24**, 63 (1990).
79. I. Barin and O. Knacke, Thermochemical Properties of Inorganic Substances (Springer-Verlag, New York, 1973), pp.240-243.

80. J. S. Marsh, The Alloys of Iron and Nickel, McGraw-Hill, New York, 1938, V.1, Engineering Foundation, pp.58-82.
81. L. Brewer, J. Chipman, and S-G. Chang, Metals Handbook V.8, 8th ed. (Metals Park, OH, 1973), p.413.
82. K. Osinski, A. W. Vriend, G. F. Bastin, and F. J. J. van Loo, *Z. Metallkd.* **73**, 258 (1982).
83. P. C. Patnaik, Ph.D. Thesis, McMaster University (1984).
84. Y. S. Shen, E. J. Zdanuk, and R. H. Krock, *Metall. Trans.* **2**, 2839 (1971).
85. W. Ostwald, *Z. Physik. Chem.* **22**, 365 (1897).
86. T. C. Chou and T. G. Nieh, *Scripta Met. et Mat.* **25**, 2059 (1991).
87. H. A. Lipsitt, *Mat. Res. Soc. Symp. Proc.* **39**, 351 (1985).
88. P. R. Smith and F. H. Froes, *J. of Metals* **36**, 19 (1984).
89. J. Smialek, M. A. Gedwill, and P. K. Brindley, *Scripta Met. et Mat.* **24**, 1291 (1990).
90. J. M. Yang and S. M. Jeng, *J. of Metals* November, **56** (1989).
91. J. M. Yang and S. M. Jeng, *Scripta Met. et Mat.* **23**, 1559 (1989).
92. S. F. Baumann, P. K. Brindley, and S. D. Smith, *Met. Trans.*, **21A**, 1559 (1990).
93. G. Das, *Met. Trans.* **21**, 1571 (1990).
94. C. G. Rhodes, M. S. Vassiliou, M. R. Mitchell, and R. A. Spurling, *Met. Trans.* **21A**, 1589 (1990).
95. J. L. Ratliff and G. W. Powell, AFML Techn. Report 70-42 (US Dept. of Commerce, Nat. Tech. Inf. Ser., Springfield, VA, 1970).
96. L. J. House, Thesis, May 1979, George Washington University, D.C.
97. L. E. Davis, N. C. MacDonald, P. W. Palmberg, G. E. Riach, and R. E. Weber, "Handbook of Auger Electron Spectroscopy," 2nd Ed. (Perkin-Elmer Corporation, Eden Prairie, MN, 1978), pp.31 & 47.
98. Binary Alloy Phase Diagram, V.I and II, Eds. T. B. Massalski, J. L. Murray, L. H. Bennett, and H. Baker, (ASM, Ohio, 1986).
99. C. D. Wagner, W. M. Riggs, L. E. Davis, and J. F. Moulder, "Handbook of X-Ray Photoelectron Spectroscopy," Ed. G. E. Mullenberg (Perkin-Elmer Corporation, Eden Prairie, MN, 1978), pp.50-68.
100. J. I. Goldstein, D. E. Newbury, P. Echlin, D. C. Joy, and E. Lifshin, "Scanning Electron Microscopy and X-ray Microanalysis," (Plenum Press, New York, 1981), p.440.
101. O. Kubaschewski and C. B. Alcock, *Metallurgical Thermochemistry*, 5th ed. (Pergamon Press, New York, 1979), pp.358 & 372.
102. O. Kubaschewski and C. B. Alcock, *Metallurgical Thermochemistry*, 5th ed. (Pergamon Press, New York, 1979), pp.382-383.

103. I. Barin, O. Knacke and O. Kubaschewski, "Thermochemical Properties of Inorganic Substances," (Springer, New York, 1977), pp.752-790.
104. F. R. de Boer, R. Boom, W. C. M. Mattens, A. R. Miedema, and A. K. Niessen, "Cohesion in Metals Transition Metal Alloys," (North-Holland, New York, 1988), pp.126-142.
105. V. V. Samokhval, P. A. Poleshchuk, and A. A. Vecher, Russ. J. Phys. Chem. 45, 1174 (1971).



## Section 8

PUBLICATIONS

1. T. C. Chou and A. Joshi, "Solid State Interfacial Reactions of  $Ti_3Al$  with  $Si_3N_4$  and  $SiC$ ," submitted to Journal of Materials Research.
2. T. C. Chou and A. Joshi, "Selectivity of Silicon Carbide/Stainless Steel Solid-State Reactions and Discontinuous Decomposition of Silicon Carbide," J. of American Ceramic Society **74**, 1364 (1991).
3. T.C. Chou, A. Joshi, and J. Wadsworth, "Solid State Interfacial Reactions of  $SiC$  with Ni, Co and Pt", Advanced Composite Materials, Vol. **19**, 229 (1991).
4. T.C. Chou, A. Joshi and J. Wadsworth, "Solid State Reactions of  $SiC$  with Ni, Co and Pt," Journal of Materials Research **6**, 796 (1991).
5. T. C. Chou, A. Joshi, and J. Wadsworth, "High Temperature Interfacial Reactions of  $SiC$  with Metals," Journal of Vacuum Science and Technology **A 9** (3), 1525 (1991).
6. D. L. Yaney and A. Joshi, "Reaction between Niobium and Silicon carbide at 1373 K", Journal of Materials Research, **5**, 2197, (1990).
7. A. Joshi, H.S. Hu, L. Jesion, J.J. Stephens and J. Wadsworth, "High Temperature Interactions of Refractory Metal Matrices with Selected Ceramic Reinforcements", Metallurgical Transactions **21 A**, 2829, (1990).
8. A. Joshi, H.S. Hu, and J. Wadsworth, "Interfacial Reactions of Refractory Metals Niobium and Tantalum with Ceramics Silicon Carbide and Alumina", Materials Research Society Proceedings **170**, Interfaces in Composites, Eds. C. G. Pantano and E. J. H. Chen, MRS, Pittsburgh, PA, 1990, pp.149-154.
9. A. Joshi, "Interfacial Reactions in Composite Materials", Proceedings of the International Workshops on The Applications of Surface Analysis Techniques", Hong Kong Baptist College, The Commercial Press (H. K.) Ltd., pp.287-298, 1990.